Technische Universität München
TUM School of Computation, Information and Technology

Towards Laboratory Astrophysics in Plasma Wakefield Accelerators

Erwin Walter

Vollständiger Abdruck der von der TUM School of Computation, Information and Technology der Technischen Universität München zur Erlangung eines

Doktors der Naturwissenschaften (Dr. rer. nat.)

genehmigten Dissertation.

Vorsitz: Prof. Dr. Oliver Junge

Prüfende der Dissertation:

1. Hon.-Prof. Dr. Frank Jenko
2. Prof. Dr. Eric Sonnendrücker

Die Dissertation wurde am 20.09.2024 bei der Technischen Universität München eingereicht und durch die TUM School of Computation, Information and Technology am 23.01.2025 angenommen.

TUM SCHOOL OF COMPUTATION, INFORMATION AND TECHNOLOGY

TECHNISCHE UNIVERSITÄT MÜNCHEN

Towards Laboratory Astrophysics in Plasma Wakefield Accelerators

Author:	Erwin Walter
Supervisor:	Hon.-Prof. Dr. Frank Jenko
Advisor:	Dr. John Farmer
Submission Date:	20. September 2024

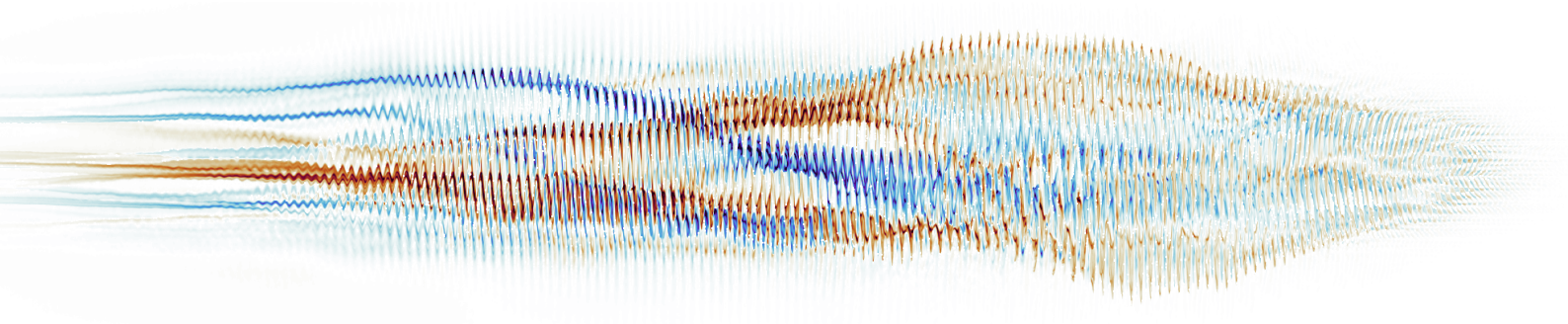

Abstract

From supernovae in distant galaxies to laboratory-based wakefield accelerators, the collisionless interaction of relativistic particles with a plasma medium of ionised gas is relevant to many physical scales. The dynamics are often governed by kinetic instabilities, resulting in electromagnetic field fluctuations. This dissipation of a directed relativistic flow transfers kinetic energy to field energy, which can give rise to collisionless shocks in the astrophysical context. Unprecedented experimental investigations have enabled investigations of plasma instabilities on an accessible scale. Plasma wakefield accelerators, utilised to achieve higher accelerating fields compared to conventional accelerators, are also subject to instabilities and can be adapted to investigate these regimes relevant to astrophysics.

The interaction of a relativistic beam with unmagnetised plasma results in a filamentary structure and can be categorised between the electromagnetic current filamentation instability driven by the plasma return current or two-stream instabilities driven by the electrostatic plasma response. In the latter, the beam excites Langmuir plasma waves, conventionally called wakefields in particle accelerators. The current imbalance in the system defines the regimes of these filamentation instabilities. The electromagnetic instability dominates for a dense beam. For a dilute beam, the plasma current is negligible, and plasma electrons are mainly deflected by the beam charge.

The transverse two-stream instability leads to modulation of the beam along the propagation direction and transverse filamentation. A three-dimensional spatiotemporal two-stream theory for warm beams with a well-defined extent is developed. Diffusion due to a finite emittance gives rise to a non-uniform dominant wavenumber and a cut-off wavenumber above which filamentation is suppressed. Remarkable agreement is found between the theoretical model with fully electromagnetic and quasistatic particle-in-cell simulations. For charged beams, filamentation appears to be suppressed when the predicted distance between filaments is larger than the rms beam width in good agreement with experimental observations. These findings provide a crucial basis for designing laboratory astrophysics experiments investigating filamentation instabilities and for plasma wakefield experiments seeking to avoid them.

A transverse gradient in the beam-generated wakefield deflects the ions in the plasma via the ponderomotive force. In contrast to the amplifying effect on the current-driven instability, the wakefield weakens. Three saturation mechanisms on wakefield-driven instabilities are identified as transverse wavebreaking, transverse decoherence and detuning of the wakefield. These mechanisms are enhanced by the motion of plasma ions. The suppression of the transverse two-stream instability, which takes the form of the self-modulation instability for narrow beams, is observed in good agreement between particle-in-cell simulations and experimental results. The investigation extends the knowledge of the different effects of ion motion on wakefield-driven instabilities and how to avoid the adverse effects.

Keywords: plasma-based accelerators, plasma instability, wakefield-driven filamentation, linear theory, particle-in-cell simulations, ion motion

Kurzfassung

Von Supernovae in fernen Galaxien bis hin zu Kielfeld-Beschleunigern im Labor - die kollisionsfreie Wechselwirkung relativistischer Teilchen mit einem Plasmamedium aus ionisiertem Gas ist für viele physikalische Größenordnungen von Bedeutung. Die Dynamik wird häufig von kinetischen Instabilitäten bestimmt, die zu elektromagnetischen Fluktuationen führen. Diese Dissipation einer gerichteten relativistischen Strömung überträgt kinetische Energie in Feldenergie, was im astrophysikalischen Kontext zu kollisionsfreien Schocks führen kann. Experimentelle Untersuchungen ermöglichen die Erforschung von diesen Plasmainstabilitäten in einem zugänglichen Maßstab. Kielfeld-Beschleuniger, die im Vergleich zu konventionellen Beschleunigern höhere Beschleunigungsfelder erreichen können, sind ebenfalls Instabilitäten unterworfen und können zur Untersuchung dieser für die Astrophysik relevanten Regime angepasst werden.

Die Wechselwirkung eines relativistischen Strahls mit einem unmagnetisierten Plasma führt zu filamentären Strukturen und kann unterteilt werden in die elektromagnetische Strömungsfilamente Instabilität, die durch den Plasma-Rückstrom angetrieben wird, oder in Zwei-Strom Instabilitäten, die durch ein elektrostatisches Feld angetrieben werden. In Letzteren regt der Teilchenstrahl Langmuir-Plasmawellen an, die in Teilchenbeschleunigern üblicherweise als Kielfelder bezeichnet werden. Das Stromungleichgewicht im System definiert die Regime dieser Filamentationsinstabilitäten. Die elektromagnetische Instabilität dominiert für einen dichten Teilchenstrahl. Bei einer geringen Strahldichte werden die Plasmaelektronen hauptsächlich durch die Ladungsdichte des Strahles abgelenkt.

Die transversale Zwei-Strom-Instabilität führt zu einer Modulation des Strahls entlang der Ausbreitungsrichtung und zu transversaler Filamentierung. Eine dreidimensionale raumzeitliche Zwei-Strom-Theorie für warme Teilchenbündel mit gut definiertem Ausmaß wurde entwickelt. Diffusion aufgrund einer endlichen Emittanz führt zu einer nicht einheitlichen dominanten Wellenzahl und einer Grenzwellenzahl, oberhalb derer die Filamentierung unterdrückt wird. Das theoretische Modell stimmt bemerkenswert mit elektromagnetischen und quasistatischen Teilchen-in-Zelle Simulationen überein. Bei geladenen Teilchenbündel scheint die Filamentierung unterdrückt zu werden, wenn der Abstand zwischen den Filamenten größer ist wie die Breite des Bündels, was in guter Übereinstimmung mit experimentellen Beobachtungen steht. Diese Erkenntnisse bieten eine wichtige Grundlage für die Planung von astrophysikalischen Experimenten zur Untersuchung von Filamentierungsinstabilitäten und für Kielfeld-Experimente, die diese meiden.

Ein transversaler Gradient im strahlerzeugten Kielfeld lenkt die Plasmaionen über die ponderomotorische Kraft ab. Im Gegensatz zum verstärkenden Effekt auf die stromgetriebene Instabilität schwächt sich das Kielfeld ab. Drei Sättigungsmechanismen bei Kielfeld-getriebenen Instabilitäten sind identifiziert: Transversales Wellenbrechen, transversale Dekohärenz und Verstimmung des Kielfeldes. Diese Mechanismen werden durch die Bewegung der Plasmaionen verstärkt. Die Unterdrückung der transversalen Zwei-Strom-Instabilität, die für schmale Teilchenbündel die Form der Selbstmodulationsinstabilität annimmt, wurde in guter Übereinstimmung zwischen Teilchen-in-Zelle Simulationen und experimentellen Ergebnissen beobachtet. Die Untersuchung erweitert das Wissen über die verschiedenen Effekte der Ionenbewegung auf Kielfeld-getriebene Instabilitäten und darüber, wie die nachteiligen Auswirkungen vermieden werden können.

Contents

List of Figures

Acronyms

AWAKE Advanced Wakefield Experiment

CFI current filamentation instability

DPS discharge plasma source

LWFA laser wakefield accelerator

OBI oblique instability
OTR optical transition radiation

PIC particle-in-cell
PWFA plasma wakefield accelerator

RF radiofrequency
rms root-mean-square

SMI self-modulation instability
SPS Super Proton Synchrotron

TSI (longitudinal) two-stream instability
TTS transverse two-stream instability

Symbols

Sign	Description	Value
Quantity		
t	time in the lab frame	
$\boldsymbol{x}$	coordinate in configuration space	
$\boldsymbol{k}$	wave vector	
$\boldsymbol{v}$	coordinate in velocity space	
$\boldsymbol{p}$	coordinate in momentum space	
γ	Lorentz/relativistic factor	
$\hat{\boldsymbol{x}}$	unit vector in configuration space	
$f(t, \boldsymbol{x}, \boldsymbol{p})$	distribution function in phasespace	
q	particle charge	
m	particle mass	
n	number density	
ρ	charge density	
$\boldsymbol{j}$	current density	
$\boldsymbol{u}$	particle flux density	
T	temperature	
ω	frequency	
λ	wavelength	
$\boldsymbol{E}$	electric field	
$\boldsymbol{B}$	magnetic field	
$\boldsymbol{W}$	plasma wakefield	
Constant		
c	speed of light	$2.998 \times 10^8\,\mathrm{m/s}$
e	elementary charge	$1.602 \times 10^{-19}\,\mathrm{C}$
m_e	electrons mass	$9.109 \times 10^{-31}\,\mathrm{kg}$
k_B	Boltzmann constant	$1.381 \times 10^{-23}\,\mathrm{J/K}$
n_p	base plasma density	
u_b	beam velocity	
$\lambda_D = [\varepsilon_0 k_B T_e/(e^2 n_p)]^{1/2}$	Debye length	
$\omega_p = [e^2 n_p/(\varepsilon_0 m_e)]^{1/2}$	plasma frequency	
$\omega_\beta = [q_b^2 n_b/(2\gamma_b \varepsilon_0 m_b)]^{1/2}$	betatron frequency of beam	
$k_p = \omega_p/c$	plasma wavenumber	
$k_e = \omega_p/u_b$	beam-driven electron wavenumber	
$E_0 = m_e c \omega_p/e$	cold nonrelativistic wavebreaking field	
σ_y	rms width	
$\sigma_p = [m k_B T]^{1/2}$	rms momentum spread	

Sign	Description	Value
ϵ_n	normalised emittance	
J_n	Bessel function of first kind	
I_n	modified Bessel function of first kind	
K_n	modified Bessel function of second kind	
k_r	transverse wavenumber	
$\eta_u = \frac{(c^2-u_b^2)k_p^2+u_b^2k_r^2}{c^2k_p^2+u_b^2k_r^2}$	spectral two-stream factor	
Operator		
$\cdot'$	normalised quantity	
$\langle\cdot\rangle_V = \int \cdot f \,\mathrm{d}V / \int f \,\mathrm{d}V$	weighted mean	
$\tilde{\cdot}$	envelope of field	
$\dot{\cdot} = \mathrm{d}(\cdot)/\,\mathrm{d}t$	Time derivative	
$\hat{\cdot} = \mathcal{F}\{\cdot\}$	Fourier spectrum	
$\bar{\cdot} = \mathcal{L}\{\cdot\}$	Laplace spectrum	
$\delta\cdot$	linear perturbation	
N	number of exponentiations / e-folding number	
$\nu = \mathrm{d}N/\,\mathrm{d}t$	growth rate	
$\Gamma = \delta \cdot / \delta\cdot_0$	growth factor	
$r_> = \max(r', r)$	maximum between variable and its integration variable	
$r_< = \min(r', r)$	respective minimum	

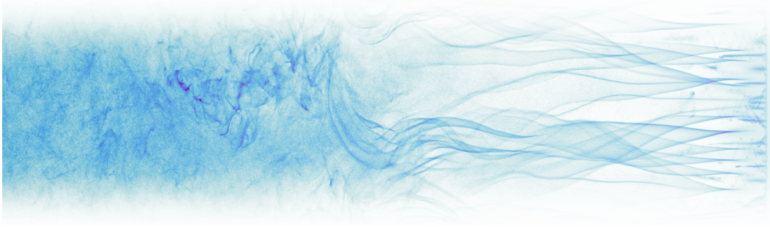

1 Introduction

High-energy physics investigates the fundamental particles and forces under conditions similar to those found in the early universe. These extreme conditions at energy densities beyond $10^{11}\,\mathrm{J/m^3}$ and temperatures above $10^5\,\mathrm{K}$ (Drake, 2006) are found in laboratory experiments designed to probe the fundamental forces of nature and in astrophysical phenomena. Under such conditions, matter is often in the state of plasma – an ionised gas consisting of free electrons and ions. This ionised state makes up to 99.9 % of the visible matter in the universe (Planck Collaboration, 2014), highlighting the importance of plasma-based studies for understanding the behaviour of matter under extreme conditions and the fundamental processes shaping the cosmos.

At these high energies, the interaction between plasma particles is collisionless, meaning they interact collectively through the electromagnetic field instead of over direct collisions. These interactions occur on various physical scales and often yield unstable systems. The arising instabilities dissipate the kinetic energy of the relativistic particles, converting it into fluctuations of the electromagnetic field. This energy transfer can trigger the formation of collisionless shocks, characterised by an abrupt change in density, flow and pressure (Bret, Gremillet, and Dieckmann, 2010; F. F. Chen, 2016; Michno and Schlickeiser, 2010).

Collisionless shocks are extensively studied to understand how energy is redistributed across various astrophysical scales. On the interplanetary scale, for instance, the bow shock forms due to the interaction of the solar wind with Earth's magnetosphere (Turc *et al.*, 2023). On a larger scale, shocks are present in extragalactic environments such as active galactic nuclei (Bohdan *et al.*, 2021), which are regions at the centres of galaxies where supermassive black holes actively accrete matter and emit vast amounts of energy. In galaxy clusters, collisionless shocks occur during mergers of smaller galaxy clusters, which heat the intracluster medium (Bykov *et al.*, 2019).

Cosmic rays, i.e. high-energy particles in space primarily represented by protons and Helium nuclei, are accelerated to TeV energies through diffusive shock acceleration and Landau resonance at the shock front. In Fermi-type diffusive shock acceleration, particles gain energy while being scattered back and forth across the shock front through magnetic turbulence (Fermi, 1954; Spitkovsky, 2008). Particles also gain energy via Landau resonance when the velocity of the plasma wave and its electrostatic field match the velocity of the particles (Iwamoto, Amano, Hoshino, *et al.*, 2019; Landau, 1946; Tajima, Yan, *et al.*, 2020).

1.1 Acceleration from Filamentary Structures

Most shock environments occur in weakly magnetised plasma with magnetic fields of a few microgauss (Heiles and Crutcher, 2005). However, extraordinary regions such as gamma-ray bursts from collapsing stars or merging neutron stars and black holes exist where the background magnetic field is negligible (Medvedev and Loeb, 1999; Perna *et al.*, 2016). The interaction between the stream of relativistic particles with such an unmagnetised plasma medium can be usually categorised between the Weibel-like current filamentation instability (CFI), driven by plasma currents (Fried, 1959; Weibel, 1959), or the two-stream instabilities, driven by the electrostatic plasma response (Bludman *et al.*, 1960; Faĭnberg *et al.*, 1969). In the latter, the stream excites a Langmuir plasma wave (Tonks and Langmuir, 1929), which results in similar filamentary behaviour as CFI (Bret, Gremillet, and Dieckmann, 2010).

The current-driven filamentation in counterstreaming plasmas has been found to achieve magnetic fields perpendicular to the propagation with energy densities ranging from 10^{-5} to 10^{-1} of the kinetic energy density (Medvedev and Loeb, 1999). This magnetic field is strong enough to deflect the streaming particles until the system is thermalised, ultimately forming a collisionless shock. Numerical studies of relativistic shocks in magnetised plasmas by Iwamoto, Amano, Hoshino, *et al.* (2019) and Iwamoto, Amano, Matsumoto, *et al.* (2022) have revealed that electrostatic plasma waves are excited by the interaction of intense electromagnetic waves and reflected particles at a lower density near the shock front. These waves can accelerate particles that are decoupled from the upstream bulk flow. Electrostatic acceleration of this kind may allow ions to reach energies beyond 10^{21} eV for ions (Tajima, Yan, *et al.*, 2020), offering an alternative to Fermi-type acceleration, which is limited by significant synchrotron radiation losses at such high energies (Jackson, 1999).

The current imbalance in the system defines the regimes for the filamentation instabilities. For CFI to dominate, the relativistic stream must have a density of the order greater than the surrounding plasma, such as in the interstellar medium (Bret, Gremillet, and Dieckmann, 2010). The plasma current becomes negligible for a dilute stream, and the plasma electrons are primarily deflected by the electric field driven by the charge imbalance (Katsouleas *et al.*, 1987; Keinigs and Jones, 1987). For dense streams with a smooth gradient rather than a sharp discontinuity, an underdense region exists dominated by the two-stream instability.

The plasma consists of electrons and ions interacting with the particle stream on different time scales, where the motion of the ions has a different effect on the respective instabilities. While plasma electrons quickly thermalise after undergoing CFI, a subsequent ion filamentation enhances the growth of the magnetic field, allowing it to pervade the shock front (Frederiksen *et al.*, 2004; Peterson *et al.*, 2021). Conversely, a collective oscillation of the plasma electrons is disturbed by the motion of ions. As a result, the stability of an electrostatic field weakens, which may suppress the two-stream instabilities (F. F. Chen, 2016; Vieira *et al.*, 2012).

While much of our understanding of the shock formation and the relevant plasma instabilities in the astronomical context comes from spacecraft measurements and simulations, experimental advancements have enabled researchers to recreate and study these processes on a more accessible scale. The experiment led by Fiuza *et al.* (2020) demonstrated with counter-streaming plasmas the formation of turbulent collisionless shocks with an accumulation of plasma and electron acceleration, addressing diffusive shock acceleration. In the

investigation by Zhang *et al.* (2022), a temperature anisotropy was induced into a plasma by a laser, which gave clear evidence of the current-driven filamentation linked to the self-magnetisation in the interstellar plasma medium as a precursor to collisionless shocks. For streams with a transverse extent, Arrowsmith *et al.* (2021) showed the feasibility of generating a dense electron-positron beam from a proton beam and studying its interaction with plasma.

Beam-driven wakefield accelerators are also subject to plasma instabilities and can be adapted to investigate regimes relevant to astrophysics. The experimental studies published by Allen *et al.* (2012) and Verra, Amoedo, *et al.* (2024) revealed that adjusting the parameters of a wakefield accelerator can effectively control the onset and characteristics of beam filamentation.

1.2 Wakefield Accelerators

The achievable centre-of-mass collision energy exponentially increased until recent limitations arose due to radiofrequency (RF) and magnet technologies as shown by Figure 1.1. Further energy improvements require extraordinarily long machines like the Large Hadron Collider (13.6 TeV, 27 km) at CERN (Rosmino, 2022). The most recent plans include the Compact Linear Collider (0.38–3 TeV, 11–50 km) and Future Circular Collider (100 TeV, 98 km) at CERN (*The Compact Linear Collider* 2024; Zimmermann *et al.*, 2020), or the Circular Electron–Positron Collider (240 GeV, 100 km) in China (*The CEPC Project* 2013). While the RF-based technology enables high precision and reliability, the accelerating gradient is limited to around 100 MV/m by the electric breakdown in the cavity structure and limitations of the superconductive magnets (Esarey, Schroeder, *et al.*, 2009).

Plasma wakefield accelerators utilise the electrostatic field corresponding to the Langmuir plasma wave to accelerate charged particle beams (P. Chen *et al.*, 1985; Tajima and Dawson, 1979). The plasma wave can sustain electric field amplitudes substantially higher than RF cavities of conventional accelerators (Adli *et al.*, 2018; Caldwell and K. V. Lotov, 2011; Schroeder *et al.*, 2011). As a possible avenue for next-generation particle accelerators, the

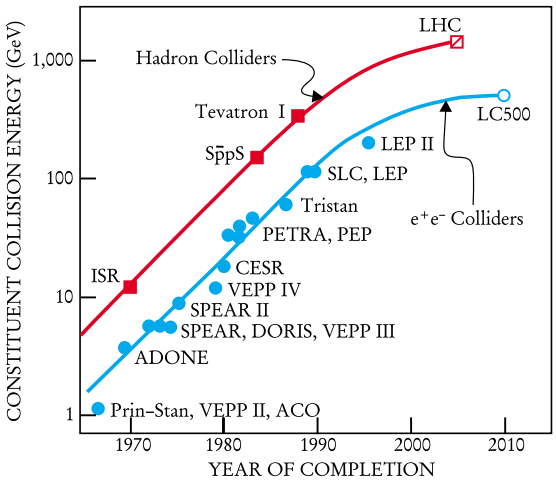

Figure 1.1: Centre-of-mass collision energy of hadron (red) and electron-positron (blue) colliders shown against completion year. Credit: Tigner (2001).

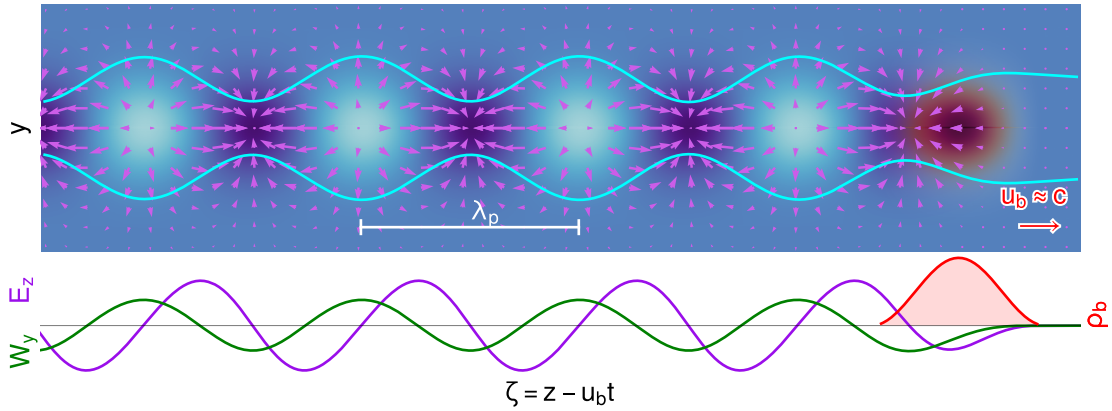

Figure 1.2: Schematic of a beam-driven wakefield. The charged beam (red), the excited plasma density wave (blue), with the electron trajectories shown in cyan, and the wakefield (violet arrows), with lineouts of the on-axis longitudinal and off-axis radial Wakefield component.

limit on the electrostatic field in plasma-based wakefield accelerator increases with the plasma density n_p and is defined by the cold non-relativistic wavebreaking field (Dawson, 1959)

$$E_0 = m_e c \omega_p / e \approx 96 \sqrt{n_p \, [\mathrm{cm}^{-3}]} \, [\mathrm{V/m}]. \tag{1.1}$$

Here, m_e is the electron mass, c is the speed of light and ω_p is the plasma frequency, given by

$$\omega_p = \sqrt{e^2 n_p / (\varepsilon_0 m_e)}, \tag{1.2}$$

with e the elementary charge and ε_0 the vacuum permittivity. It can reach realistic values of $E_z = 1 - 100\,\mathrm{GV/m}$ for plasma densities of $10^{14}\,\mathrm{cm}^{-3}$ to $10^{18}\,\mathrm{cm}^{-3}$, which has the potential to reduce the footprint of future high-energy accelerators. The work by Veksler (1956) and Budker and Naumov (1956) first mentioned the usage of fields sustained in plasma to accelerate particles. Yet, it was the work by Tajima and Dawson (1979) that suggested the first plasma-based accelerator, based on the ponderomotive force of a laser pulse (the gradient in the electromagnetic field) separating the plasma electrons from the ions. Only a few years later, Joshi *et al.* (1981) published the first experimental results. This type of plasma-based accelerator is referred to as laser wakefield accelerator (LWFA). It was found later by P. Chen *et al.* (1985) that a relativistic charged particle beam excites a similar plasma response, referred to as plasma wakefield accelerator (PWFA). The first experimental results were published by Rosenzweig *et al.* (1988). The excited plasma wave is known as Langmuir wave (Tonks and Langmuir, 1929), with the corresponding electromagnetic field referred to as wakefield in the concept of particle accelerators (Dawson, 1959).

Figure 1.2 shows the plasma response to a short beam in its frame, $\zeta = z - u_b t$, where the plasma particles flow to the left. The plasma electrons are displaced relatively to the heavier ions by the space-charge effects of the beam or by the ponderomotive force of a laser pulse. The relative displacement between electrons and ions builds up a net charge and an electrostatic field, which acts as a restoring force. The resulting coherent oscillation of plasma electrons is close to the plasma wavelength. A proportion of the driver's energy is stored in the plasma wave and its resulting longitudinal E_z and transverse $\boldsymbol{W}_\perp$ wakefield

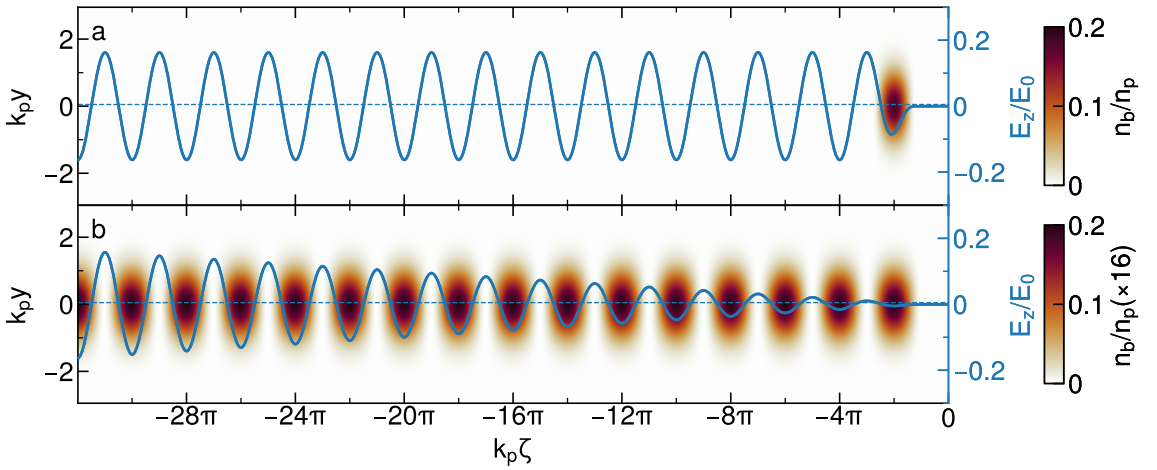

Figure 1.3: The longitudinal on-axis wakefield (blue), excited by a) a short, dense beam or b) a train of microbunches of lower density (red).

component with respect to the propagation direction of the driver. The phase difference between the longitudinal and transverse components is $\pi/(2k_p)$, which enables a focussing and accelerating region within the wakefield.

Usually, the utilised intense laser pulse or dense beam fits within half the wakefield period ($k_p\sigma_\zeta < 1$), sketched in Figure 1.3a), to drive a wakefield (Albert *et al.*, 2021; Clayton *et al.*, 2016). Here, $k_p = \omega_p/c$ is the plasma wavenumber and σ_ζ is the rms length of the driver. For high-intensity laser or high-density beams, usually used in wakefield accelerators, the plasma electrons are fully expelled, leaving a uniform ion column in which injected witness beams are accelerated. A long beam, $k_p\sigma_\zeta \gg 1$, drives a weak wakefield as the plasma electrons only compensate for the beam charge. However, the wakefield acts back on the beam by modulating the beam radius. This allows the wakefield to grow along the beam length, resulting in an instability referred to as axisymmetric self-modulation instability (SMI) (Schroeder *et al.*, 2011). The resulting train of microbunches resonantly drives the wakefield to considerable magnitudes, illustrated in Figure 1.3b).

1.2.1 AWAKE Experiment

The Advanced Wakefield Experiment (AWAKE) at CERN aims to accelerate electron beams in the wakefield resonantly driven by a proton beam up to accelerating field amplitudes of 1 GV/m. The long proton beam undergoes SMI during the first meters it propagates in the plasma. The witness electron beam is injected after $3 - 4$ m into the resonantly-driven wakefield of the beam. The collaboration established a detailed understanding of relevant plasma instabilities and how to control these (K. V. Lotov and Minakov, 2020; Verra, Zevi Della Porta, *et al.*, 2022). In addition to SMI (Adli *et al.*, 2018; Morales Guzman *et al.*, 2021), the beam undergoes hosing, a snake-like amplification of the beam centroid misalignment (Moreira *et al.*, 2023; Nechaeva *et al.*, 2024). The comprehensive overview of achievements is listed in Gschwendtner, K. Lotov, *et al.* (2022).

The proton beam is provided by a staged acceleration process through RF cavities. Hydrogen protons from an electric discharge are bunched and accelerated to 50 MeV by the linear accelerator LINAC4, followed by an acceleration to 1.4 GeV by the Proton Synchrotron Booster, then to 25 GeV by the Proton Synchrotron. After a final acceleration stage at the Super Proton Synchrotron (SPS), the beam at the experiment has an energy of 400 GeV. A witness electron beam is created by a laser pulse hitting a photocathode. The beam is then pre-accelerated up to 20 MeV before it is injected into the plasma cell, extending over 10 m.

The experimental setup of AWAKE during Run 1 in 2018 is shown in Figure 1.4. In this setup, a laser pulse (duration of 120 fs, maximum energy of 450 mJ, wavelength of 780 nm) co-propagates with the proton beam and single ionises the Rubidium vapour in the plasma cell. Rubidium ions have been chosen for the motion of the significantly heavier plasma ions to be negligible. The vapour at the plasma entrance and exit flows into expansion volumes, so the plasma density drops quickly. This provides with the laser an uniform plasma density. Locating the ionisation front of the laser within the beam locks in the phase and initial magnitude of the beam-driven wakefield. This seeds the growth of SMI (Batsch *et al.*, 2021) and enables reproducible electron acceleration, experimentally confirmed up to 2 GeV (Gschwendtner, Turner, *et al.*, 2019).

After the Rubidium cell, the proton beam propagates through a metallic screen (Aluminium coated, 150 μm thick SiO_2), placed 3.5 m behind the plasma exit due to the expansion volume. Optical transition radiation (OTR) is emitted by the screen and imaged onto the entrance slit of a streak camera (Rieger *et al.*, 2017). This enables the time-resolved projection of

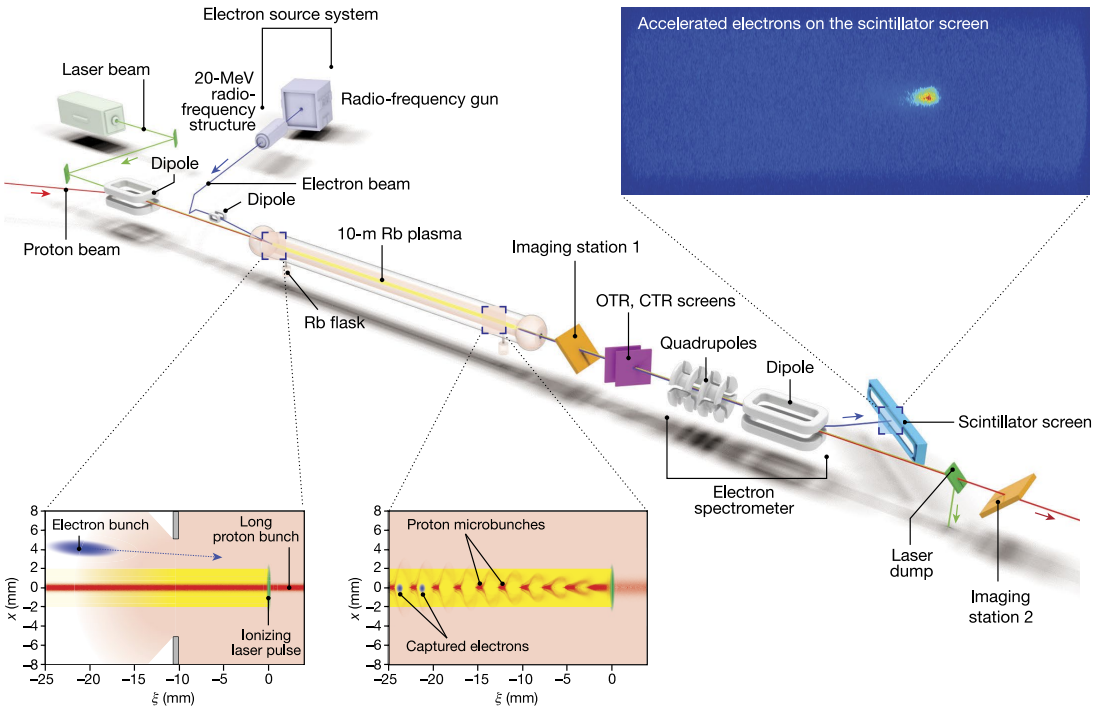

Figure 1.4: Schematic of AWAKE experimental setup during Run 1 (2018). Obtained from Adli *et al.* (2018).

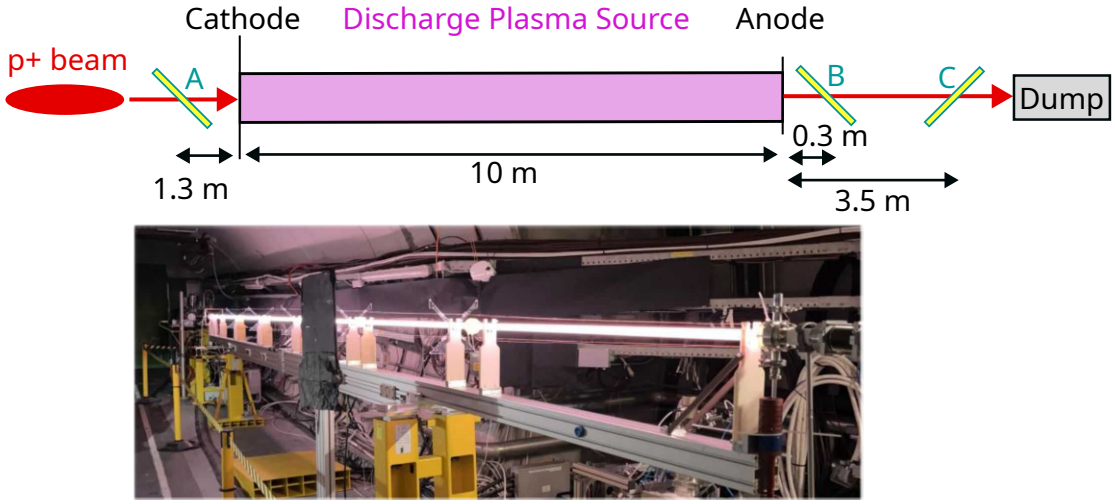

Figure 1.5: Schematic of the AWAKE experiment with the discharge of Helium gas during the DPS run in 2023. Credit to Alban Sublet for the photograph during the commissioning of the plasma source.

the beam at the expense of one projected transverse dimension. Additionally, longitudinal projections of the proton beam can be taken before and after the plasma. Plasma densities are measured by longitudinal, double-pass interferometry or by extracting the modulation frequency of the self-modulated proton beam. The electron beam is focussed by quadrupole magnets and bent by dipole magnets onto a scintillator screen, measuring the energy from the horizontal position.

Future plans involve a staged wakefield acceleration, possibly extending hundreds of meters. Although laser ionisation provides a uniform plasma density, it is not feasible to this extent. One of the alternatives involves the usages of discharge plasma sources (DPSs) in which an electric current ionises the plasma via an applied voltage between two electrodes beyond the striking voltage. This allows for reliable plasma operations with different gases such as Xenon, Argon and Helium at various densities. In the DPS run in May 2023 with the experimental setup sketched in Figure 1.5, the plasma was partially and at most singly-ionised over 3.5, 6.5 or 10 m. The plasma density is adjusted by changing the gas pressure between 8 and 24 Pa, the peak current of the discharge between 300 and 600 A or the time delay between discharge and the arrival of the proton beam (Torrado *et al.*, 2023).

Next to feasibility studies for the self-modulation of the proton beam, the high variability of the beam radius, plasma density, and mass of plasma ions allowed for a detailed study of the filamentation instabilities and investigated the effect of the motion of the plasma ions. The glass window at the entrance of the DPS prevented seeding the instabilities with the laser ionisation front. However, no expansion volume was required, such that a second OTR screen was installed at a distance of 0.3 m behind the plasma exit, enabling unprecedented transverse resolution of the longitudinal projections.

1.3 The Goal of this Project

Most of the literature investigates the plasma dynamics for non-bounded, homogeneous particle streams. In the astrophysical context, however, the stream is usually bounded along the propagation direction, and for laboratory settings, it is additionally confined transversely. This work explores how wakefields arise from the interaction between a relativistic beam with a well-defined extent and plasma and the required parameters. A gradient in the wakefield deflects the ions of the plasma, which was previously found to suppress the SMI. The saturating mechanisms, possibly mitigating wakefield-driven filamentation as well, are being explored in collaboration with the experiment.

These investigations contribute valuable insights into how plasma instabilities, as precursor mechanisms in producing high-energy particles, can be accessed through wakefield accelerators. Specifically, the electrostatic filamentation leads to strong accelerating wakefields, limited only by the wavebreaking threshold. This introduces a complementary acceleration mechanism to Fermi-type particle acceleration in collisionless shocks.

The theoretical aspects of these kinetic instabilities, along with the numerical methods used, are outlined in Chapter 2, establishing the foundation for analytic and numerical studies. Applications of the numerical methods and considerations for investigating relativistic beams with a well-defined extent in plasma are detailed in Chapter 3. The work presented in Chapter 4 and Chapter 5 address the following questions:

- Chapter 4: Laboratory-Relevant Filamentation Instabilities
  - How accurately can the theory for wakefield-driven filamentation of warm beams describe the filamentation growth and dominant wavenumbers observed in simulations and experimental observations?
  - What beam parameters are necessary to access the various beam-plasma instabilities, and how do these instabilities transition between each other?
- Chapter 5: Ion Motion in Wakefield-Driven Instabilities
  - How does the motion of plasma ions influence the wakefield?
  - What is the effect of ion motion on the saturation of wakefield-driven instabilities?

These chapters closely compare analytic models with particle-in-cell simulations and conclude with observations from laboratory experiments in collaboration with the AWAKE experiment at CERN to emphasise the robustness of the simulations and theory. These findings build a crucial basis for designing experiments investigating filamentation instabilities and for beam-driven wakefield accelerators seeking to avoid them. A final summary of these findings is provided in Chapter 6, along with suggestions for future work.

2 Basics of Beam Plasma Physics

Chapter Summary

- Different filamentation instabilities of particle streams in plasma are treated with kinetic plasma theory, and the dominant regimes are discussed. Current-driven filamentation exhibits a dominating magnetic field, while in oblique filamentation instability, the electric field dominates. The growth rate of the filamentation instabilities is well described only for spatially uniform streams and plasmas.
- The beam dynamics of charged beams with a finite extent are presented. The wakefield-driven axisymmetric self-modulation instability modifies the beam radius. A transverse gradient in the wakefield acts as a ponderomotive force, possibly affecting heavy plasma ions.

This chapter introduces the basic principles of plasma in Section 2.1 and the kinetic equations for unmagnetised plasma in Section 2.2. The growth rate derived from these equations for an unstable beam-plasma system describes the different filamentation modes relevant for this work in Section 2.3. In Section 2.4, the dynamics in beam-plasma interactions are described for bounded systems. The utilised numerical methods are listed in Section 2.5.

2.1 Principles of Plasma

Plasma is an ionised gas, referred to as the fourth state of matter beside solid, liquid and gas, in which atoms are (partly) stripped of their electrons due to high energy densities. This results in a quasineutral composition of positively charged ions and negatively charged electrons. The transition to the plasma state is characterized by a continuous and progressive ionisation rather than an abrupt change and occurs if the thermal energy exceeds the ionisation energy of atoms. However, not every ionised gas exhibits plasma properties, widely defined by:

"[Plasma is] a quasineutral gas of charged and neutral particles, which exhibits collective behaviour." - F. F. Chen (2016)

The emphasis lies here on quasi-neutrality and collective behaviour.

Quasi-neutrality: The motion of plasma particles is directed to create electromagnetic fields, which effectively shield any disturbances such as charged particles or photons. If a positive or negative charge is present, a sheath of plasma particles evolves around it to

shield out any potential field, which forms a new equilibrium. For finite thermal energies, the plasma distribution is described by the Boltzmann distribution, $n_e = n_{e0} \exp\left[-e\Phi/(k_B T_e)\right]$, with k_B the Boltzmann constant, and n_e the density and T_e the temperature of the plasma electrons. This distribution can be inserted into Poissons' law for the electrostatic potential, $\nabla^2\Phi = -\rho/\varepsilon_0$ with ρ the charge density. For small potentials, $e\Phi \ll k_B T_e$, the solution to the differential equation is an exponential decaying potential, $\Phi = [\Phi_0/r] \exp(-r/\lambda_D)$, with the screening distance

$$\lambda_D = \sqrt{\varepsilon_0 k_B T_e/(n_e e^2)}, \tag{2.1}$$

referred to as Debye length. The potential field is not negligible within this length defined by the electrons being significantly more mobile than the ions. The potential decreases with fewer particles available to shield the potential and decreases with the plasma temperature as electron fluctuations result in leaks in the shield. The system only remains quasineutral at an extent vastly larger than the Debye length, which is a lower boundary for the density of the ionised gas to be defined as plasma. Further, a statistically meaningful number of particles is required within the Debye shielding sphere, $[4/3] n_e \pi \lambda_D^3 \gg 1$.

Collective behaviour: The collective behaviour of plasma fundamentally differs from gases. The motion of neutral gases is mainly determined by collisions over Brownian motion (Einstein *et al.*, 1915) except for short-range Van-der-Waals interactions. Rather than by locally bounded collision, the plasma motion is dominated by the collectively generated electromagnetic field from local charge and current fluctuations acting on large distances. The long-range interaction can lead to the formation of complex structures such as waves, turbulence and instabilities. If electrons are displaced by δz from a uniform ion background, a potential builds up to restore quasi-neutrality. The resulting electrostatic force results in an oscillation as electrons overshoot their equilibrium position due to their inertia. An analytic description of this oscillation is given by the equation of motion

$$\frac{\mathrm{d}\boldsymbol{p}}{\mathrm{d}t} = \boldsymbol{F}_L = q(\boldsymbol{E} + \boldsymbol{v} \times \boldsymbol{B}), \quad \frac{\mathrm{d}\boldsymbol{x}}{\mathrm{d}t} = \frac{\boldsymbol{p}}{\gamma m} \tag{2.2}$$

with $\mathrm{d}/\mathrm{d}t$ the total time derivative, $\boldsymbol{p} = \gamma m \boldsymbol{v}$, the momentum, $\gamma = [1 + p^2/(mc)^2]^{1/2} = [1 - v^2/c^2]^{-1/2}$ the relativistic or Lorentz factor, $\boldsymbol{x}$ the position and $\boldsymbol{v}$ the velocity of the particles, $\boldsymbol{F}_L$ the Lorentz force, $\boldsymbol{E}$ the electric field and $\boldsymbol{B}$ the magnetic field. Inserting the electric field from Poissons' law into the linearised equation of motion, i.e. neglecting the $\boldsymbol{v} \times \boldsymbol{B}$ term, gives the equation of a harmonic oscillator, $\partial_t^2 \delta z + \omega_p^2 \delta z = 0$. This plasma oscillation due to wave-particle interactions times the mean collision time τ_c separates collisionless and collisional plasma. Collisionless plasma, $\omega_p \tau_c \to \infty$, is relevant to a wide range of phenomena in the astrophysical context and to plasma-based wakefield accelerators.

2.2 Kinetic theory in unmagnetised plasma

In the most basic description, the electric $\boldsymbol{E}$ and magnetic $\boldsymbol{B}$ fields affect the plasma particles via the Lorentz force. Vice versa, the position and momentum of the particles define a charge density ρ and current density $\boldsymbol{j}$ of the plasma, which self-consistently influences the

electromagnetic fields described by Maxwell's equations in vacuum

$$\begin{aligned} \nabla \cdot \boldsymbol{E} &= \rho/\varepsilon_0 && \text{Gauss' law} \\ \nabla \cdot \boldsymbol{B} &= 0 && \text{Gauss' law for magnetism} \\ \nabla \times \boldsymbol{E} &= -\partial_t \boldsymbol{B} && \text{Faraday's law of induction} \\ \nabla \times \boldsymbol{B} &= \mu_0 \left(\boldsymbol{j} + \varepsilon_0 \partial_t \boldsymbol{E}\right) && \text{Ampere's circuital law,} \end{aligned} \tag{2.3}$$

with μ_0 the vacuum permeability, relating to the speed of light c by $\varepsilon_0 \mu_0 = 1/c^2$.

While numerical studies of plasma behaviour in this fundamental description become feasible with the exascale computing power, an analytic description would be daunting. The collective property of plasma enables a kinetic description in phase-space by the distribution $f(t, \boldsymbol{x}, \boldsymbol{p})$, a function of time t, position and momentum. The number of particles within a phase-space volume is $f \,\mathrm{d}\boldsymbol{x}\,\mathrm{d}\boldsymbol{p}$. Relevant macroscopic plasma quantities are derived from the moments of the distribution function, given by

$$\int \boldsymbol{v}^n f(t, \boldsymbol{x}, \boldsymbol{p}) \,\mathrm{d}\boldsymbol{p}. \tag{2.4}$$

The first three moments of the distribution functions link to the number density $n(t, \boldsymbol{x})$, the collective velocity of the plasma $\boldsymbol{u}(t, \boldsymbol{x})$ and pressure tensor $\mathcal{P}(t, \boldsymbol{x})$ given by

$$\begin{aligned} n(t, \boldsymbol{x}) &= \int f(t, \boldsymbol{x}, \boldsymbol{p}) \,\mathrm{d}\boldsymbol{p} \\ n(t, \boldsymbol{x}) \boldsymbol{u}(t, \boldsymbol{x}) &= \int \boldsymbol{v} f(t, \boldsymbol{x}, \boldsymbol{v}) \,\mathrm{d}\boldsymbol{p} \\ n(t, \boldsymbol{x}) \mathcal{P}(t, \boldsymbol{x}) &= \int (\boldsymbol{v} - \boldsymbol{u})^2 f \,\mathrm{d}\boldsymbol{p}. \end{aligned} \tag{2.5}$$

As individual particle interactions are negligible in a collisionless plasma, the distribution function remains constant in phasespace, $\mathrm{d}f(t, \boldsymbol{x}, \boldsymbol{p})/\,\mathrm{d}t = 0$, referred to as Liouville's theorem (Landau and Lifshitz, 1959). The trajectory of the plasma particles in phase-space is defined by the equation of motion given in Equation (2.2). The governing kinetic equation for the time evolution of the distribution function in collisionless plasma, referred to as the Vlasov equation, is given by

$$\frac{\mathrm{d}}{\mathrm{d}t} f = \left(\partial_t + \boldsymbol{v} \cdot \nabla + \boldsymbol{F} \cdot \nabla_{\boldsymbol{p}}\right) f = 0, \tag{2.6}$$

with ∇ and $\nabla_{\boldsymbol{p}}$ the gradient operators on the configuration and momentum space. The Boltzmann equation extends the Vlasov equation by particle collisions such that the distribution function may vary along the particle trajectories, $\mathrm{d}f(t, \boldsymbol{x}, \boldsymbol{p})/\,\mathrm{d}t = (\partial_t f)_c$. Here, $(\partial_t f)_c$ is the rate of change of the distribution function due to collisions where different models exist, such as the Fokker-Planck equation, including Coulomb collisions.

The collisionless evolution of the plasma is self-consistently described by the Vlasov-Maxwell equation

$$\begin{aligned} \left[\partial_t + \boldsymbol{v} \cdot \nabla + (\boldsymbol{E} + \boldsymbol{v} \times \boldsymbol{B}) \cdot \nabla_{\boldsymbol{p}}\right] f &= 0 \\ \nabla \times \boldsymbol{E} &= -\partial_t \boldsymbol{B} \\ \nabla \times \boldsymbol{B} &= \mu_0 \left(\boldsymbol{j} + \varepsilon_0 \partial_t \boldsymbol{E}\right). \end{aligned} \tag{2.7}$$

The electromagnetic field influences the plasma distribution via the Lorentz force, and the macroscopic quantities of the distribution function give the rate of change in the electromagnetic field described by Faraday's law of induction and Ampere's circuital law.

2.3 Filamentation Instabilities in Unmagnetised Plasma

All phenomena in collisionless plasma can be described by the Vlasov-Maxwell equation (Bellan, 2006). The simplest analytic approach is to view the behaviour of the plasma and the electromagnetic field as a composition of harmonic waves. The plasma usually consists of a stable homogeneous background distribution $f_0 = f(\boldsymbol{p})$ which is superimposed by a small time-varying perturbation $\delta f = \delta f(t, \boldsymbol{x}, \boldsymbol{p})$ to $f = f_0 + \delta f$. The Fourier-transformed equations yield a dispersion relation, $\omega = \omega(\boldsymbol{k})$, with $\boldsymbol{k}$ the wavevector, which can be split into an oscillating, $\Re(\omega)$, and growing, $\nu = \Im(\omega)$, part of the waves. Thus, the dispersion relation reveals the dynamical behaviour of a given plasma setup and enables the study of unstable regimes in which the perturbation exponentially grows while $|\delta f| \ll |f|$.

For an unmagnetised plasma, the linearised system is described by

$$\begin{aligned} f_s(t, \boldsymbol{x}, \boldsymbol{p}) &= f_s(\boldsymbol{p}) + \sum_{\omega,k} \delta \hat{f}_s(\boldsymbol{p}) \exp\left(i\boldsymbol{k}\cdot\boldsymbol{x} - \omega t\right) \\ \boldsymbol{E} = \sum_{\omega,k} \delta\hat{\boldsymbol{E}} \exp\left(i\boldsymbol{k}\cdot\boldsymbol{x} - \omega t\right), &\quad \boldsymbol{B} = \sum_{\omega,k} \delta\hat{\boldsymbol{B}} \exp\left(i\boldsymbol{k}\cdot\boldsymbol{x} - \omega t\right) \end{aligned} \tag{2.8}$$

where the subscript s denotes the plasma species. The dispersion relation for the electric field is obtained by combining Faraday's law and Amperes law in Fourier space to

$$\left[(\omega^2/c^2)\boldsymbol{\epsilon}(\omega, \boldsymbol{k}) + \boldsymbol{k} \otimes \boldsymbol{k} - k^2\mathbb{I}\right] \delta\hat{\boldsymbol{E}} = 0. \tag{2.9}$$

The solution are given by the determinant $\left|(\omega^2/c^2)\boldsymbol{\epsilon}(\omega,\boldsymbol{k}) + \boldsymbol{k} \otimes \boldsymbol{k} - k^2\mathbb{I}\right| = 0$, with $\mathbb{I}$ the unit tensor and $\otimes$ the tensor product. The dielectric tensor $\epsilon_{lm}(\omega,k_l) = \delta_{lm} + i j_l/(\varepsilon_0\omega\delta\hat{E}_m)$, with δ_{lm} the Kronecker-Delta, is interpreted as the relative permittivity of the plasma and quantifies the electric field's ability to react to perturbations. The current is expressed by $\boldsymbol{j} = \sum_s [q_s/m_s] \int [\boldsymbol{p}_s/\gamma_s] f_s(\boldsymbol{p})\, \mathrm{d}\boldsymbol{p}$, where the species distribution function f_s can be replaced by the spectral version of Vlasov Equation (2.6) $\delta\hat{f}_s = -i[q_s/\omega]\left[\mathbb{I} + \boldsymbol{p}_s \otimes \boldsymbol{k}/(\gamma_s m_s\omega - \boldsymbol{k}\cdot\boldsymbol{p}_s)\right] \delta\hat{\boldsymbol{E}} \cdot \nabla_{\boldsymbol{p}} f_s(\boldsymbol{p}_s)$. The fully electromagnetic dielectric tensor is expressed by

$$\boldsymbol{\epsilon}(\omega, \boldsymbol{k}) = \mathbb{I} + \sum_s \frac{\omega_s^2}{\omega^2 n_s} \int \frac{\boldsymbol{p}_s}{\gamma_s} \left(\mathbb{I} + \frac{\boldsymbol{p}_s \otimes \boldsymbol{k}}{\gamma_s m_s\omega - \boldsymbol{k}\cdot\boldsymbol{p}_s}\right) \cdot \nabla_{\boldsymbol{p}} f_s(\boldsymbol{p}_s)\, \mathrm{d}\boldsymbol{p}_s. \tag{2.10}$$

For brevity, the index s of the plasma species will be omitted, with quantities referring to any species unless explicitly stated otherwise.

For a cylindrical symmetry in the Fourier space and the equilibrium distribution function, $f(\boldsymbol{p}) = f(p_z)f(p_x^2)f(p_y^2)$, the second transverse dimension can be neglected, $k_x = 0$. Hence, Equation (2.9) reduces to

$$\begin{vmatrix} \omega^2\epsilon_{zz} - c^2k_y^2 & \omega^2 e_{zy} + c^2k_yk_z & 0 \\ \omega^2 e_{zy} + c^2k_zk_y & \omega^2\epsilon_{yy} - c^2k_z^2 & 0 \\ 0 & 0 & \omega^2\epsilon_{xx} - c^2k^2 \end{vmatrix} = 0, \tag{2.11}$$

which results in two branches (Bret, Firpo, *et al.*, 2004).

$$\begin{aligned} \text{I. } 0 &= \left(\omega^2\epsilon_{xx} - c^2k^2\right) \\ \text{II. } 0 &= \left[\omega^2\left(\epsilon_{zy}^2 - \epsilon_{zz}\epsilon_{yy}\right) + c^2\left(k_z^2\epsilon_{zz} + 2k_zk_y\epsilon_{zy} + k_y^2\epsilon_{yy}\right)\right]. \end{aligned} \tag{2.12}$$

The first electromagnetic branch with a dielectric component perpendicular to the direction of the wave propagation $\boldsymbol{k}$ is referred to as the Weibel instability (Weibel, 1959). The second branch includes an electrostatic component with a dielectric component parallel to $\boldsymbol{k}$ driven by space charge and an electromagnetic term driven by the plasma current. This branch is a composition of the two-stream filamentation, also referred to as oblique instability (OBI) (Bret, Firpo, *et al.*, 2004; Landau, 1946), and the CFI (Fried, 1959).

In the perpendicular limit, $k_z = 0$, the second branch simplifies to

$$\left(\omega^2\epsilon_{zz} - c^2k_y^2\right)\epsilon_{yy} = \omega^2\epsilon_{zy}^2. \tag{2.13}$$

The coupled dielectric components ϵ_{zx} on the rhs correspond to space-charge effects (Hao *et al.*, 2008; Tzoufras *et al.*, 2006) and dominate in highly asymmetric systems, where the filaments of the different plasma species are compressed at different rates. The second branch is fully electromagnetic for symmetric systems, $\sum_s \omega_s \boldsymbol{u}_s = 0$. For arbitrary asymmetries in density, mass and collective velocity, space-charge effects result in an electrostatic component.

The evolution of instabilities in the system is segregated into three phases: Seed, unstable loop and saturation. The initial anisotropy in phase space can originate from a driving electromagnetic pulse or a particle beam. Any small-scale fluctuation within the phase space of the driver or plasma results in small currents which generate an electromagnetic field. The feedback loop is closed if the generated field acts to reinforce the perturbation and amplify the currents. This results in exponential growth of the perturbation and the electromagnetic field over time.

2.3.1 Weibel-type Current Filamentation

The pioneering work from Weibel (1959) identified the exponential growth of purely electromagnetic waves from a temperature anisotropy in a single-species plasma at rest, i.e. the momentum spread is higher in one direction. Any current fluctuation along the axis with the higher temperature excites a perpendicular magnetic field, which deflects the particles as shown in Figure 2.1 to enhance the current modulation and results in an increase of the magnetic field. The distribution of the unstable system can be defined by a bi-Maxwellian velocity distribution in a non-relativistic regime

$$f(\mathbf{v}) = \frac{m}{2\pi T_z T_y} \exp\left(-\frac{mv_y^2}{2T_y}\right) \exp\left(-\frac{m(v_z + u_z)}{2T_z}\right), \tag{2.14}$$

with $T_{z,y}$ the plasma temperature linked to a momentum spread by $T_z = \sigma_p^2/m$. Only the purely growing, $\mathrm{Re}(\omega) \to 0$, and transverse, $k_z = 0$, terms are considered. Thus, the space-charge term in Equation (2.13) vanishes and the dispersion relation becomes (R. C. Davidson *et al.*, 1972)

$$0 = c^2k_y^2 - \omega_k^2 + \sum \omega^2[1 - (T_z + mu_z)/T_y] - \sum \omega^2[(T_z + mu_z)/T_y]\xi Z(\xi), \tag{2.15}$$

with $\xi = \omega/[k(2T_y/m)^{1/2}]$ and $Z(\xi) = \pi^{1/2}\int \mathrm{d}x \exp(-x^2)/(x - \xi)$ the plasma dispersion function simplified for small values to $Z(\xi) \approx -2\xi$. For small anisotropies, $|T_z + mu_z -$

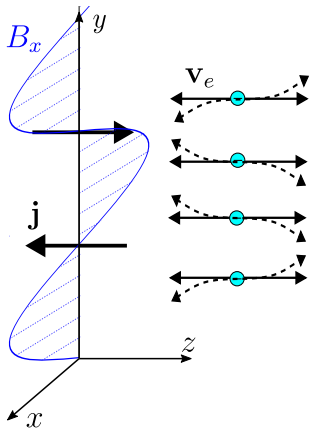

Figure 2.1: Schematic of the Weibel instability. b) The magnetic field growing from anisotropy in the plasma temperature, adapted from Medvedev and Loeb (1999).

$T_y|/T_y \ll 1$, the maximum growth rate of the Weibel instability is (R. C. Davidson *et al.*, 1972)

$$\nu_{\text{weibel}} = \sqrt{\frac{8}{27\pi}\frac{T_y}{m_e c^2}}\frac{T_y}{T_z}\left(\frac{T_z}{T_y}-1\right)^{3/2}. \tag{2.16}$$

The work by Weibel has been extended by Fried (1959) to counterstreaming plasmas, referred to as CFI. The system effectively remains in anisotropy in momentum space, which gives rise to the growth of the electromagnetic field. The Weibel instability coexists with CFI being on different branches of the dispersion relation given in Equation (2.12). Thus, any anisotropy in any of the counterstreaming plasmas increases the growth rate of the field. Considering a stream with non-relativistic temperatures, $T \ll mc^2$, propagating in a cold plasma, the maximum growth rate of the transverse modes is (Bret, Firpo, *et al.*, 2004; Silva, R. A. Fonseca, Tonge, Dawson, *et al.*, 2003; Silva, R. A. Fonseca, Tonge, Mori, *et al.*, 2002)

$$\nu_{\text{cfi}} = \frac{\sqrt{2}\omega_\beta u_b/c}{1+\sigma_p/(m_b c)}, \tag{2.17}$$

with ω_β the betatron frequency of the streaming plasma, defined by

$$\omega_\beta = \sqrt{q_b^2 n_b/(2\gamma_b m_b \varepsilon_0)} \tag{2.18}$$

and n_b the beam peak density summed over all beam species.

In the linear regime, The spectral Poisson equation gives $\boldsymbol{k}\cdot\delta\hat{\boldsymbol{E}} = \delta\hat{\rho}/\varepsilon_0$. The purely electromagnetic transverse mode of the instability, $\boldsymbol{k}\cdot\delta\hat{\boldsymbol{E}} = 0$, can only yield a perturbation in the current density but not in the charge density since $\delta\hat{\rho} = 0$ (Bret, Firpo, *et al.*, 2005). Thus, the Weibel instability and the purely electromagnetic mode of CFI only yield current filamentation. Any charge filamentation during the linear regime must come from space-charge effects excited by the longitudinal mode.

The current perturbation grows exponentially until the magnetic field is strong enough to magnetically trap the particles within the currents. This saturation level for the magnetic field is reached when the betatron frequency of the trapped particles is on the order of the growth rate (R. C. Davidson *et al.*, 1972). Beyond this saturation, rectified current filaments merge with each other. The instability results in a transfer of kinetic energy to thermal energy and an isotropic plasma temperature.

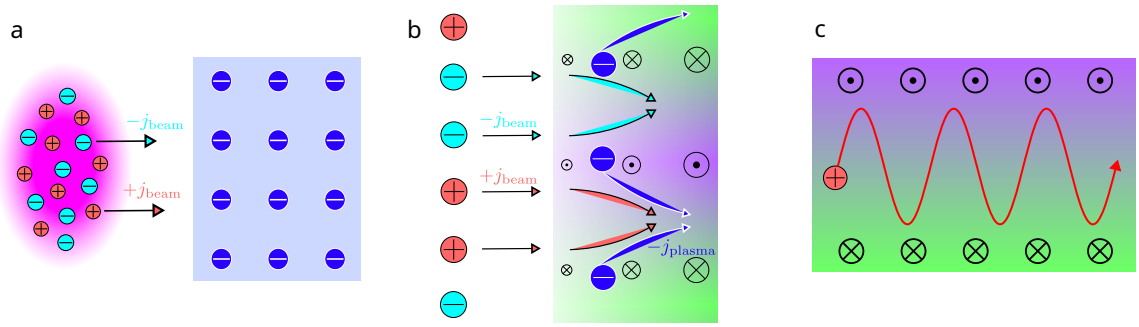

Figure 2.2: Scheme of current driven filamentation for a particle beam. a) Initial setup, where any fluctuation in the beam acts as a driver for the seed of the instability. b) Beam and plasma filamentation result in exponential growth of the perturbation and magnetic field. c) The saturation of the instability as the magnetic field traps the particles of the driver.

For a bounded quasi-neutral beam propagating into plasma, the scheme for CFI varies slightly compared to the periodic system introduced in Section 2.3 and is illustrated in Figure 2.2. The beam propagates from a vacuum into a plasma, where small current fluctuations in the beam result in perpendicular magnetic fields (Figure 2.2a). The return current of the plasma response results in a growing magnetic field, which amplifies the current fluctuation in the beam (Figure 2.2b). The plasma electrons flow with the positive charge of the beam particles such that the plasma return current acts against the growing magnetic field. For a sufficiently strong magnetic field, the beam particles are magnetically trapped and undergo betatron oscillation (Figure 2.2c).

2.3.2 Two-Stream Filamentation

The (longitudinal) two-stream instability is one of the most fundamental instabilities in plasma and only considers the purely electrostatic modes in k_z while neglecting the perpendicular modes. The plasma system becomes two-stream unstable if at least two plasma species with different group velocities $\boldsymbol{u}$ intersect, such that the centre-of-mass moves. First works by Bludman *et al.* (1960), Faĭnberg *et al.* (1969), and Watson *et al.* (1960) considered the growth of electrostatic waves in a two-dimensional spectrum, $\boldsymbol{k} = (k_z,k_y)$, which propagate at an angle to the flow direction of the driver. Due to the finite longitudinal wavenumber, the waves are not purely growing, $\Re(\omega) > 0$. The oblique waves act to amplify both longitudinal and transverse modulations in the charge density due to a finite longitudinal and transverse electric field.

For the kinetic approach, the whole second branch of the dispersion relation in Equation (2.12) has to be considered. The distribution function for a cold (monochromatic $\boldsymbol{k}\Delta\boldsymbol{v} \ll |\omega - k_z u_b|$) stream with velocity u_b is expressed by a delta-distribution, $f(\boldsymbol{v}) = \delta(\boldsymbol{v} - u_b\hat{z})$. For this stream propagating in cold plasma, the dispersion relation is given by (Faĭnberg *et al.*, 1969)

$$0 = \left[1 - \frac{\omega_p^2}{\omega} - \frac{2\omega_\beta^2}{\gamma_b^2(\omega - k_z u_b)^2}\right]\left[(k_z^2 + k_y^2)c^2 + \omega_p^2 + 2\omega_\beta^2 - \omega^2\right] - \frac{2\omega_\beta^2\omega_p^2 k_y^2 u_b^2}{\omega^2(\omega - k_z u_b)^2}. \quad (2.19)$$

The growth rate has a distinct maximum at the electron wavenumber $k_z = k_e = ck_p/u_b$, expressed by (Bludman *et al.*, 1960; Bret, Firpo, *et al.*, 2004)

$$\nu_{\mathrm{obi}} = (\sqrt{3}/2)[\eta_u \omega_\beta^2 \omega_p]^{1/3} \tag{2.20}$$

$$\eta_u = \frac{(c^2 - u_b^2)k_p^2 + u_b^2 k_y^2}{c^2 k_p^2 + u_b^2 k_y^2}, \tag{2.21}$$

with η_u the spectral two-stream factor in two-dimensional geometry. The classical solution for (longitudinal) two-stream instability (TSI) is retrieved in the non-relativistic limit, $u_b \ll c$, neglecting the transverse mode, $k_y = 0$.

For cold streams, the growth rate increases asymptotically with the transverse wavenumber, i.e. fine-scale filaments grow faster. A finite temperature or Landau-damping (resonant wave-particle interaction) damps higher wavenumbers, but the dispersion relation becomes analytically untraceable. The two-dimensional growth spectrum was numerically studied for Heaviside, Maxwellian and Maxwell-Jüttner distribution functions in Bret and Deutsch (2006), Bret, Firpo, *et al.* (2004), and Bret, Gremillet, and Bénisti (2010), respectively. For relativistic stream temperature, $T_b \gtrsim m_b c^2$, OBI becomes dominant over CFI purely due to thermal effects. The growth rate of OBI scales significantly different from the parameters of the streaming plasma by $\omega_\beta^{2/3}$ relative to CFI by $\omega_\beta^{1/2}$, which enables to split the regimes in which the respective instabilities are dominant.

2.3.3 Dominant Regimes

The opposing currents of the plasma species must be comparable for CFI to dominate. For a relativistic stream and a plasma initially at rest relevant in the astrophysical context, this requires a dense stream with a minimum density semi-analytically derived to $0.53\, n_p$ for a Lorentz factor of $\gamma = 2.44$ in Bret, Gremillet, and Dieckmann (2010). For ultrarelativistic streams, this density limit increases to the plasma density. For a stream propagating through overdense plasma, the plasma current is negligible and OBI dominates. Thus, the substantial restriction on the densities is eased for counterstreaming plasmas.

While all filamentation instabilities exhibit a growing wave with a similar finite transverse wavenumber, the physical response of the plasma and the growth of the electromagnetic fields significantly differ, as shown in Figure 2.3. For a single species with anisotropy, strong current filaments within the plasma and a perpendicular magnetic field emerge due to the Weibel-mediated growth. The time-varying magnetic field gives rise to the weak electric field component, which results in a negligible charge separation, $\rho_p \approx 0$.

The charge density vastly differs for a relativistic stream consisting of positrons and electrons, propagating through an equally dense plasma consisting of electrons and immobile ions. A dominantly transverse modulation forms in both the charge density of the stream and the longitudinal current density of the plasma. While a strong electric field emerges, the magnetic field is higher by a factor of 2 and the system is dominated by CFI. Charge separation occurs and couples with the electrostatic, longitudinal modes, which weakens the growth of the electromagnetic mode (Tzoufras *et al.*, 2006).

For a dilute stream prone to OBI, the response of both species shows a clear longitudinal mode at $k_z = k_p$, given by a predominantly electrostatic response of the plasma. The electric

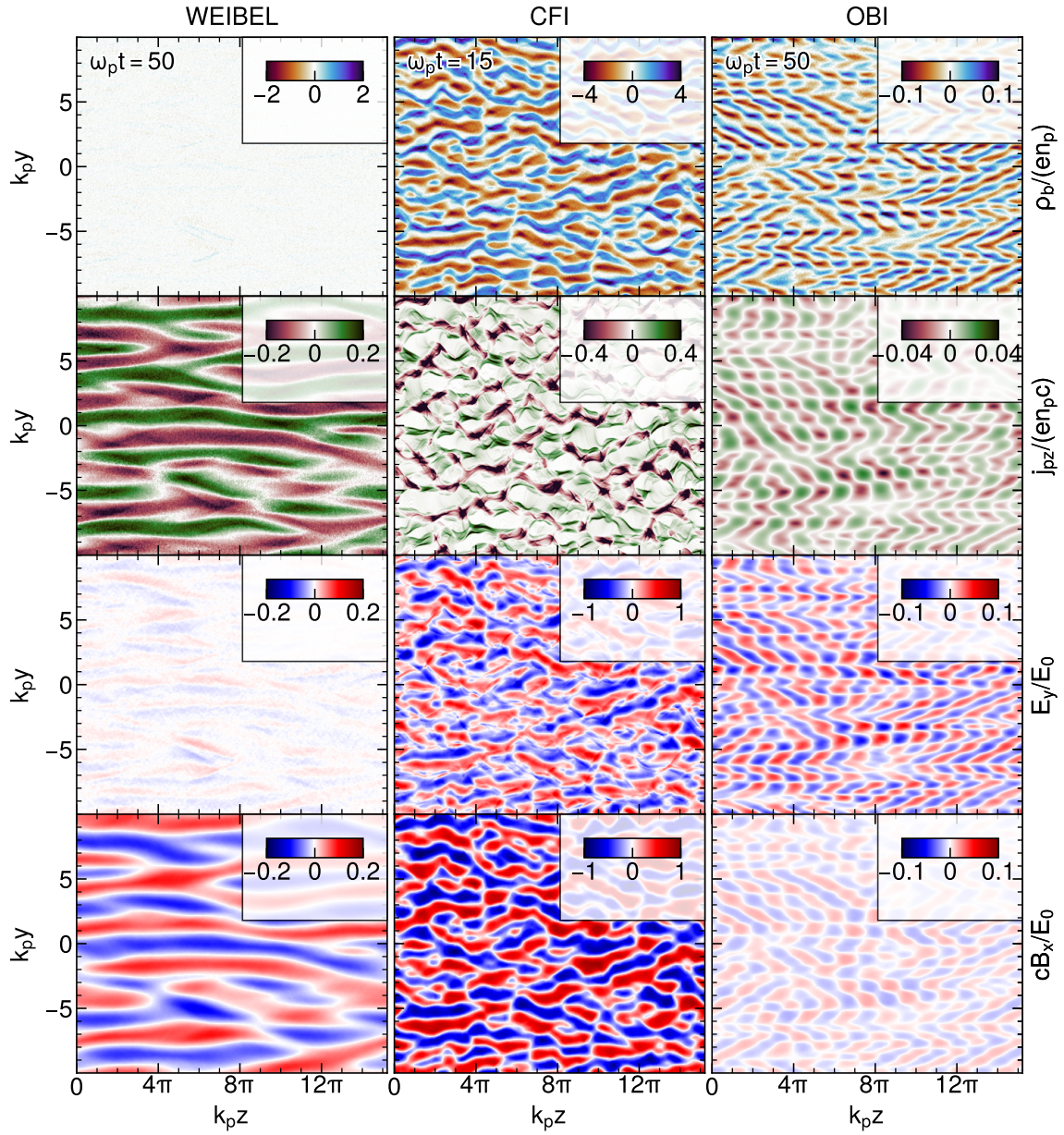

Figure 2.3: Kinetic simulation of the relevant filamentation instabilities. Shown from top to bottom for a system dominated by the Weibel instability (left), CFI (centre) or OBI (right): The charge density of the plasma electrons (Weibel) or streaming positrons (CFI, OBI), the longitudinal current density of the plasma electrons, the transverse electric and magnetic field.

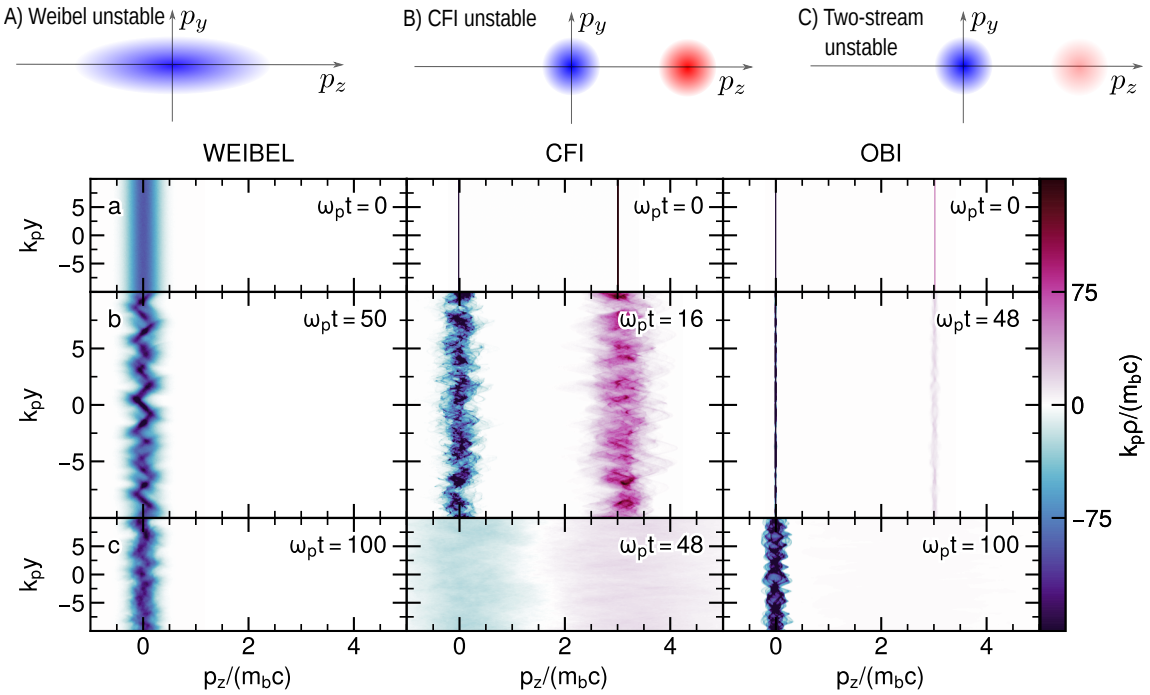

Figure 2.4: Phasespace evolution during the instability growth. The initial phase-space distribution giving rise to A) the Weibel instability, B) the current filamentation instability or C) the two-stream filamentation, adapted from Bret, Gremillet, and Dieckmann (2010). The phasespace in $p_z y$ shown for the simulation in Figure 2.3 at a) $t = 0$, b) towards saturation of the instability, and c) as the system becomes isotropic.

field dominates over the magnetic field by a factor of 4. For lower densities of the stream relative to the plasma, the gap between electric and magnetic field magnitude increases. The motion of the beam particles is predominantly governed by the electric field following previous studies by Li *et al.* (2022) and Shukla, Vieira, *et al.* (2018).

The corresponding phasespace in $p_z y$ of the streaming positrons and plasma electrons in the different instability regimes is shown in Figure 2.4. For the Weibel-dominated regime, small current fluctuations due to the anisotropy in plasma temperature form sinusoidal modulation of the occupied phasespace observed in Figure 2.4b). The resulting magnetic field amplifies the sinusoidal modulation. The wave becomes nonlinear towards the saturation of the instability, and the system converges towards a velocity isotropy in Figure 2.4c). For the CFI-dominated regime, the stream has no longitudinal temperature, but its finite transverse temperature enables the formation of longitudinal current fluctuations. The dense stream results in a substantial fluctuation in the longitudinal momentum of the plasma and, thus, in a strong plasma return current. The modulation of the occupied phasespace by the species is a composition of waves at different phases since both electromagnetic and electrostatic modes drive the instability. For the OBI-dominated regime, the dilute stream results in a weak modulation of the longitudinal momentum of the plasma and the filamentation is driven by the electrostatic transverse oscillation of the plasma electrons instead of the currents of the species.

Next to comparing the growth rates from simulation to theory, the relative partition of the

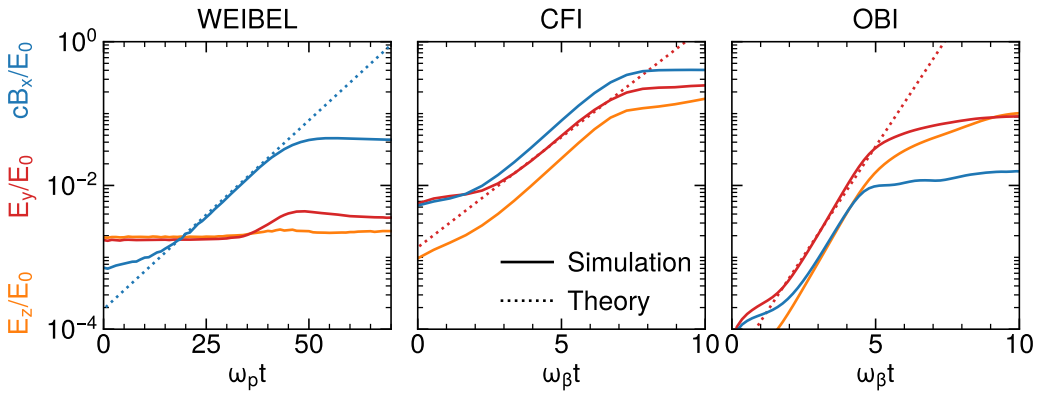

Figure 2.5: The exponential growth of the mean electromagnetic field components for the different regimes in Figure 2.3, compared to theory.

saturated electric and magnetic field magnitude enables to verify whether the evolution of the system is dominated by the purely magnetic Weibel instability, electromagnetic CFI or electrostatic OBI as shown in Figure 2.5. For all instabilities, the evolution in simulation is separated into three intervals: For low times, the current fluctuation increases given by the finite temperature. The system becomes coarse-grained, and the different instabilities compete with each other. One instability dominates, visible by the exponential growth of the magnetic field for the Weibel-dominated regime or electric and magnetic field for CFI and OBI. The field growth from theory agrees with the respective theory, evaluated by $\boldsymbol{E} \sim \exp(\nu t)$. The absolute value for the analytic expression is set to fit the growth from the simulation. The fields grow several orders of magnitude before they deviate from the analytic prediction. This saturation results from magnetic trapping in the Weibel- and CFI-dominated regime or as the perturbation in the density of the stream reaches the order of baseline density for OBI.

Within laboratories, approximating a homogeneous and infinite stream and plasma system is no longer applicable. The beam utilised in plasma-based experiments usually has a finite extent and contains a profile in configuration space, which alters the dynamics of the instabilities and requires a different approach addressed in the next section.

2.4 Beam Dynamics

For a relativistic beam of finite emittance in a vacuum, beam particles propagate ballistically. The transverse evolution of their trajectories can be described by the Courant-Snyder parameters, also referred to as Twiss parameters, where the geometric or rms beam emittance corresponds to the area the beam occupies in the transverse phasespace (x, y, p_x, p_y). The emittance can be linked to the transverse momentum spread of the beam equivalent to its temperature. Here, longitudinal or transverse refers to parallel or perpendicular to the propagation direction of the beam. The rms emittance along each transverse direction is defined by

$$\epsilon_{gy} = \sqrt{|\mathrm{cov}(y, y')|} = \sqrt{\langle y^2 \rangle \langle y'^2 \rangle - \langle y y' \rangle^2}, \tag{2.22}$$

with $y' = \tan(p_y/p_z)$ the propagation angle of the particles and $\langle\cdot\rangle = \int \cdot n_b \,\mathrm{d}y / \int n_b \,\mathrm{d}y$ the weighted average over the beam density. For a laboratory-relevant Gaussian-Maxwellian transverse profile

$$f(y, p_z, p_y) = \frac{1}{2\pi\sigma_y\sigma_{y'}} \exp\left(-\frac{y^2}{2\sigma_y^2}\right) \exp\left(-\frac{y'^2}{2\sigma_{y'}^2}\right), \tag{2.23}$$

with σ_y the rms width and $\sigma_{y'}$ the rms of the propagation angle, the geometric emittance simplifies to $\epsilon_{gy} = \sigma_y\sigma_{y'}$ at the beam waist. The beam waist is usually located at the plasma entrance in plasma-based experiments. For relativistic beams with much larger longitudinal momentum compared to the transverse momentum spread, $p_z \gg \sigma_{py}$, the angle is Taylor approximated to $y' \approx p_y/p_z$ and $\sigma_{y'} \approx \sigma_{py}/\sigma_{pz}$. The momentum spread is a function of the rms emittance, $\sigma_{py} = \epsilon_y p_z/\sigma_y$. The geometric emittance depends on the energy of the beam particles and is, thus, replaced by the normalised emittance, $\epsilon_n = \epsilon_g\gamma_b u_b/c$, which remains invariant under acceleration. The thermal spread in the lab frame can be linked to the normalised emittance of a beam with a Gaussian transverse profile by

$$\sigma_{py} = \epsilon_{ny}/\sigma_y, \tag{2.24}$$

and equivalent for x.

In the presence of an electromagnetic force by the self-fields of a charged beam or the wakefield excited by the beam propagating in plasma, the evolution of the rms beam width is described by (Reiser, 2008)

$$\partial_z^2\sigma_y - \frac{\epsilon_{ny}^2}{\gamma_b^2\sigma_y^3} = \frac{\langle|y|(E_y + u_b B_x)\rangle}{\gamma_b\sigma_y m_b/m_e}. \tag{2.25}$$

The self-fields of a charged beam are given by the electric repulsion from the beam charge and the magnetic field from the beam current. For the relativistic or quasineutral beam, i.e. consisting of equal populations of particles with opposite charges, the self-fields can be neglected as the charge-repulsion term is compensated by the magnetic field. In the absence of self-fields, the beam evolution is described by the beam emittance, and the rms beam width is

$$\sigma_y(z) = \sqrt{\sigma_{y0}^2 + z^2\epsilon_{ny}^2/(\gamma_b^2\sigma_{y0}^2)}, \tag{2.26}$$

with $\sigma_{y0} = \min_z(\sigma_y)$ the rms width at the beam waist at $z = 0$. The range from the beam waist at which the rms width of the beam has increased by a factor of $\sqrt{2}$ is defined by the Twiss beta value

$$\beta_T = \gamma_b\sigma_{y0}^2/\epsilon_{ny} = \gamma_b\sigma_y/\sigma_{py}. \tag{2.27}$$

With this link between the beam width and emittance to the electromagnetic field excited by the beam in plasma, beam-plasma instabilities due to the finite extent of the beam can be investigated.

2.4.1 Self-Modulation Instability

As introduced by Figure 1.2, the beam charge results in an electrostatic plasma response, which gives rise to the wakefield. The wave equation for the electromagnetic field can be

derived from Maxwell's equation, expressed in Equation (2.3), to

$$\begin{aligned}\left(\nabla^2 - \partial_t^2/c^2\right)\boldsymbol{E} &= \mu_0 \partial_t \boldsymbol{j} + \nabla\rho/\varepsilon_0 \\ \left(\nabla^2 - \partial_t^2/c^2\right)\boldsymbol{B} &= -\mu_0 \nabla \times \boldsymbol{j}.\end{aligned} \tag{2.28}$$

and remains linear for dilute beams, $|\rho_b| \ll e n_p$. The low bulk return current of the plasma is negligible for the low beam density, and only the oscillatory current fluctuation is considered. Except for the Bessel functions from the cylindrical geometry, the exact derivation of Green's function is equivalent to the theory for wakefield-driven filamentation in Cartesian geometry, discussed in Section 4.2.

For radially symmetric beam charge density ρ_b, the longitudinal and radial wakefield components are expressed by (Katsouleas *et al.*, 1987; Keinigs and Jones, 1987)

$$\begin{aligned}E_z &= \frac{k_e}{\varepsilon_0}\int_0^\infty \mathrm{d}r' r' I_0(k_e r_<) K_0(k_e r_>) \int_\zeta^0 \mathrm{d}\zeta' \rho_b(\zeta', r') k_e \cos k_e(\zeta - \zeta') \\ W_r &= \frac{1}{\varepsilon_0}\int_0^\infty \mathrm{d}r' r' I_1(k_e r_<) K_1(k_e r_>) \int_\zeta^0 \mathrm{d}\zeta' \partial_{r'}\rho_b(\zeta', r') k_e \sin k_e(\zeta - \zeta'),\end{aligned} \tag{2.29}$$

with I_n and K_n the modified Bessel functions of n^{th}-order, where $r_> = \max(r, r')$ and $r_< = \min(r, r')$ are the maximum and minimum between the variable and its integrand, respectively. In two-dimensional configuration space $(z, r) \to (z, y)$, the terms with the Bessel functions are replaced by exponential functions, $I_n(k_p r_<) K_n(k_p r_>) \to \exp(k_p y_<) \exp(-k_p y_>)$. The radial wakefield has a stronger effect in three-dimensional geometry close to the beam but drops more quickly with radius relative to the two-dimensional geometry. This is in accordance with the beam charge density reducing more quickly with beam width, $\rho_b \sim Q/\sigma_r^2$, in three dimensions relative to $\rho_b \sim Q/\sigma_y$ in two dimensions. The beam current has a higher contribution to the wakefield closer to the axis, which is considered by the definition for the effective slice current of the beam, $I_{\mathrm{eff}}(\zeta) = \int_0^\infty \mathrm{d}r' r' K_0(r') I(\zeta, r')$, with I the beam current. Beams shorter than π/k_p only experience the decelerating wakefield, transferring energy to the plasma. Conversely, the decelerating and accelerating interval of the wakefield interact with long beams, such that the energy in the excited wakefield is transferred back to the beam. Short beams are significantly more effective in driving strong wakefields than long beams.

The schematic of SMI is shown in Figure 2.6a), with the corresponding evolution of the plasma response and excited wakefield at the onset and saturation of the instability illustrated in Figure 2.6b). The plasma electrons are attracted towards the positively charged beam, which results in a higher plasma density on-axis and a transverse wakefield focusing on the whole beam. The longitudinal and transverse wakefield component is superimposed by a small longitudinal modulation at $k = k_e$ in the beam frame due to the transverse oscillation of the displaced plasma electrons. The longitudinal motion of relativistic particles is negligible, such that the transverse wakefield dominantly drives the beam. The transverse wakefield modulates the beam radius, alternating between focussing and defocussing beam particles. The modulation of the beam width enhances the oscillation of the plasma electron and, consequently, the wakefield amplitude. If the beam head is not truncated, e.g. by an ionisation front, the SMI develops from small-scale inhomogeneities within the beam resulting from a finite beam emittance.

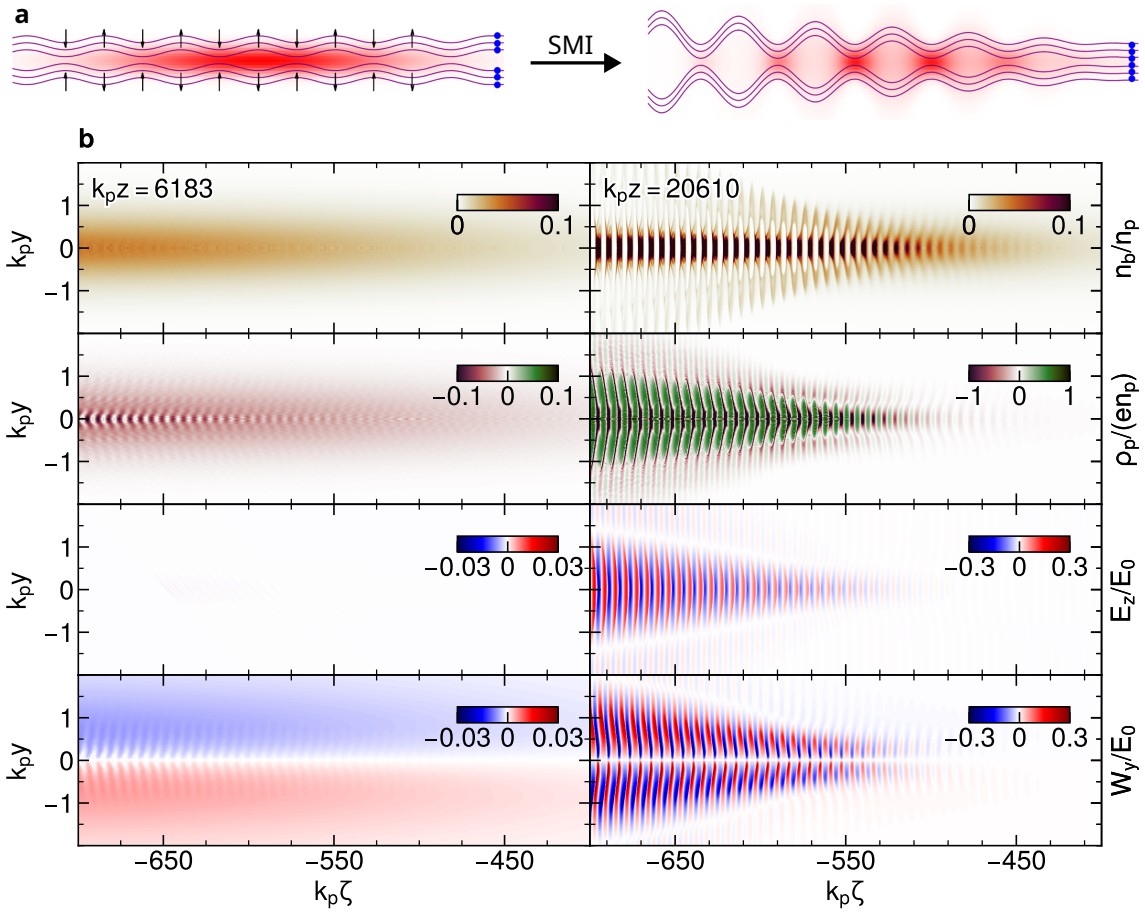

Figure 2.6: The evolution of a long proton beam undergoing self-modulation while propagating in plasma. a) Schematic of SMI, with the beam-induced electron oscillation (violet line) and the resulting wakefield force acting on the beam (black arrows). Credit to John Farmer. b) The growth of SMI at the propagation distance of $z = 6183/k_p = 1.5\,\mathrm{m}$ (left) and $z = 20610/k_p = 5\,\mathrm{m}$ (right) for a plasma density of $n_p = 4.8 \times 10^{14}\,\mathrm{cm}^{-3}$. From top to bottom: The beam density, plasma charge density, and longitudinal and transverse wakefield component.

The SMI saturates if the beam is fully modulated and the focussing force of the wakefield is compensated by the charge-repulsion of the beam. The resulting train of microbunches, equally spaced at the plasma wavelength, resonantly drive the wakefield to amplitudes up to three orders of magnitude higher than the initial wakefield. The longitudinally unmodulated length at the beam head is focussed by the non-oscillatory term of the transverse wakefield. The detailed saturation mechanisms are discussed under the influence of plasma ions with a finite mass in Chapter 5.

The effect of the transverse wakefield on a perturbation δr around the equilibrium width of the beam r_0 is obtained by inserting Equation (2.29) into Equation (2.25). The evolution of the radius envelope along the length of a long beam is described in the beam frame ($\zeta = z - u_b t$, $\tau = z/u_b$) by $(\partial_\zeta \partial_\tau^2 + i\omega_\beta^2 \eta_r)\delta\tilde{\sigma}_r = 0$. Green's function is obtained by a Laplace transform for a narrow beam with a flat top profile along the transverse direction. The

growth of the perturbation radius in the asymptotic limit, $\omega_\beta \tau \to \infty$, is given by (Schroeder *et al.*, 2011)

$$\Gamma_{\mathrm{smi}} = \frac{\delta\tilde{\sigma}_r}{\sigma_{r0}} = \frac{1}{\sqrt{4\pi}} \frac{\exp N_{\mathrm{smi}}}{\sqrt{N_{\mathrm{smi}}}}, \quad N_{\mathrm{smi}} = \frac{3^{3/2}}{2^{5/3}} \left(\eta_r \omega_\beta^2 \tau^2 k_p \zeta\right)^{1/3}, \tag{2.30}$$

with the N the number of exponentiation or e-folding number, i.e. $\Gamma \sim \exp(N)$. The beam shape factor η_r depends on the configuration space by $\eta_{r,3\mathrm{D}} = 4I_2(k_p\sigma_r)K_2(k_p\sigma_r)$ and $\eta_{r,2\mathrm{D}} = [3/(k_p\sigma_r)^2](1 + k_p\sigma_r)\exp(-k_p\sigma_r)[\cosh(k_p\sigma_r) - \sinh(k_p\sigma_r)/(k_p\sigma_r)]$. Since $\eta_{r,3\mathrm{D}} > \eta_{r,2\mathrm{D}}$, the growth rate of SMI is higher in three dimensional geometry. The analytic solution to the instability growth is not purely imaginary and includes an oscillatory part, which reduces the phase velocity of the growing wave relative to the beam velocity by

$$u_\psi = u_b \left[1 - \frac{2}{3^{3/2}} \frac{N_{\mathrm{smi}}}{\omega_p \tau}\right]. \tag{2.31}$$

In beam physics, the betatron frequency ω_β generally refers to the oscillation frequency of the particles in a charged beam around an equilibrium in a magnetic field. In a plasma channel, the beam particles undergo transverse betatron oscillation due to the excited plasma wake (Esarey, Shadwick, *et al.*, 2002). For wakefield-driven instabilities, such as SMI, the inverse of this frequency sets the timescale for the exponential growth.

2.4.2 Nonlinear Force from Heterogeneous Electromagnetic Fields

The beam charge that excites the plasma wake in PWFA is missing in LWFA. The electromagnetic impulse excited by the utilised laser is represented by the high-frequency carrier and its envelope, $\boldsymbol{E}(\boldsymbol{x}) = \tilde{\boldsymbol{E}}(\boldsymbol{x}) \cos \omega_p t$. The response of the plasma particles is too slow to react to the fast oscillation within the electromagnetic pulse. Instead, the particles experience a force away from regions with electromagnetic fields of higher magnitude. This force is referred to as ponderomotive force and can be derived from the Lorentz force for the electrons, $m_e \dot{\boldsymbol{v}} = -e[\boldsymbol{E}(\boldsymbol{x}) + \boldsymbol{v} \times \boldsymbol{B}(\boldsymbol{x})]$, with $\dot{\boldsymbol{v}} = \mathrm{d}\boldsymbol{v}/\,\mathrm{d}t$ (F. F. Chen, 2016). To first order, $m_e \delta\dot{\boldsymbol{v}} = -e\boldsymbol{E}(\boldsymbol{x}_0)$, yields

$$\delta\boldsymbol{v} = \frac{-e}{m_e\omega_p}\tilde{\boldsymbol{E}} \sin \omega_p t, \quad \delta\boldsymbol{x} = \frac{e}{m_e\omega_p^2}\tilde{\boldsymbol{E}} \cos \omega_p t \tag{2.32}$$

in which the average transverse trajectory remains constant. For the second-order terms, $\boldsymbol{E}$ is evaluated to first-order at the actual particle position during its oscillation $\boldsymbol{x}_1$ using Taylor's expansion, $\boldsymbol{E}(\boldsymbol{x}) = \boldsymbol{E}(\boldsymbol{x}_0) + (\delta\boldsymbol{x}\cdot\nabla)\boldsymbol{E}|_{r=r_0} + \cdots$. The nonlinear magnetic term in the Lorentz force, $\delta\boldsymbol{v} \times \delta\boldsymbol{B}$ is obtained via the Faraday's equation $\omega_p \delta\boldsymbol{B} = -\nabla \times \tilde{\boldsymbol{E}}|_{r=r_0} \sin \omega_p t$. The particle trajectory and its finite average over the oscillation period is given to second order by

$$\begin{aligned} m_e\delta^2\dot{\boldsymbol{v}} &= -e\left[(\delta\boldsymbol{x}\cdot\nabla)\boldsymbol{E} + \delta\boldsymbol{v} \times \delta\boldsymbol{B}\right] \\ \left\langle m_e\delta^2\dot{\boldsymbol{v}}\right\rangle_{2\pi/\omega_p} &= \frac{-e^2}{2m_e\omega_p^2}\left[(\tilde{\boldsymbol{E}}\cdot\nabla)\tilde{\boldsymbol{E}} + \tilde{\boldsymbol{E}} \times (\nabla \times \tilde{\boldsymbol{E}})\right], \end{aligned} \tag{2.33}$$

with $\delta^2\cdot$ a second-order perturbation. With $\tilde{\boldsymbol{E}} \times (\nabla \times \tilde{\boldsymbol{E}}) = \nabla\tilde{\boldsymbol{E}}^2 - (\tilde{\boldsymbol{E}}\cdot\nabla)\tilde{\boldsymbol{E}}$ and $\langle \cos^2 \omega_p t\rangle = \langle \sin^2 \omega_p t\rangle = 1/2$, the ponderomotive force, $\boldsymbol{F_p} = m_e\langle\delta^2\dot{\boldsymbol{v}}\rangle$, is derived by

$$\boldsymbol{F}_p = -\frac{e^2}{m_e\omega_p^2}\nabla\tilde{\boldsymbol{E}}^2. \tag{2.34}$$

The exponent of the electric field emphasises that the ponderomotive force is not traceable by linear theory.

2.4.3 Relativistic Fluid Theory

The analytic description for the beam width is insufficient to describe the growth of fine-scale perturbations within the beam density. While the kinetic description of plasma accurately describes a vast regime of waves and instabilities, resolving the 6D + t phase-space usually requires the system to be homogeneous and unbounded to be analytically solvable with linear theory. Spatial approximations only exist for a negligible variation of the distribution function in configuration space (Bers, 1983). The cruder fluid model can explain a substantial amount of observations if a detailed description of the momentum space is not required. Instead, the evolution in momentum space is given by the moments of the distribution function Equation (2.4).

Inserting the macroscopic parameters into the momenta of the distribution function yields the charge continuity and momentum equation in the relativistic regime (Siambis, 1987)

$$\begin{aligned} \partial_t n + \nabla \cdot (n\boldsymbol{v}) &= 0 \\ \partial_t \boldsymbol{p} + (\boldsymbol{v} \cdot \nabla)\boldsymbol{p} + \mathcal{P}/n &= \boldsymbol{F}_L. \end{aligned} \tag{2.35}$$

The pressure tensor $\mathcal{P}$ can be expressed in terms of the temperature along the respective axis via $\nabla \mathcal{P}_{zxy} = k_B T_{zxy} \nabla n$. For a Maxwellian in momentum space

$$f(\boldsymbol{p}) = \frac{1}{(2\pi)^{3/2}\sigma_{pz}\sigma_{px}\sigma_{py}} \exp\left(-\frac{p_z - \gamma m u}{2\sigma_{pz}^2} - \frac{p_x^2}{2\sigma_{px}^2} - \frac{p_y^2}{2\sigma_{py}^2}\right), \tag{2.36}$$

the non-diagonal pressure terms vanish. The diagonal terms, $\mathcal{P}_{aa} = n^{-1} \int (p_a - \langle p_a \rangle)(v_a - \langle v_a \rangle) f(\boldsymbol{p})\, \mathrm{d}\boldsymbol{v}$, allow an analogy to the temperature by

$$k_B T_y = \sigma_{py}^2/(m\gamma). \tag{2.37}$$

For non-relativistic temperatures, $\sigma_{pr} \ll \gamma m u$, the pressure tensor can be closed by a diffusion term (Bret and Deutsch, 2006)

$$\nabla \mathcal{P} = \frac{2}{3}\frac{\sigma_{pr}^2}{m\gamma} \nabla n. \tag{2.38}$$

This not only assumes the pressure tensor to be isotropic but also ignores the dependency on any microscopic event. The postulation of a Maxwellian distribution may be a drastic assumption, but Bret and Deutsch (2006) points out that the instability growth rate in this approximation agrees well with the kinetic formulation. The limit on the beam temperature for which the effect of diffusion can be considered purely diffusive is derived to $\sigma_{pr}/(mc) < [3/2^{10/3}(n/n_p)^{1/3}\gamma^{1/3}(1+\gamma^{-2})^{2/3}/(1+\gamma^{-1})^2]^{1/2}$ in Bret, Gremillet, and Bénisti (2010).

For the analytic studies in Chapter 4, the fluid equations are linearised with

$$n \to n + \delta n \quad \boldsymbol{u} \to u\hat{\boldsymbol{z}} + \delta \boldsymbol{u}, \tag{2.39}$$

with δn the amplitude of the perturbation wave in the density. For relativistic beams or beams with low emittance, the longitudinal momentum is much larger than its transverse momentum spread. In such cases, the linearised gamma factor, $\gamma(\boldsymbol{u}) = [1-(u^2+\delta u^2)/c^2]^{-1/2}$, can be Taylor approximated to

$$\gamma(\boldsymbol{u}) \approx \gamma(\boldsymbol{u}) + \nabla\gamma(\boldsymbol{u}) \cdot \delta\boldsymbol{u} + \frac{1}{2}\delta\boldsymbol{u}^T(\nabla \otimes \nabla)\gamma(\boldsymbol{u}) \cdot \delta\boldsymbol{u} + O(\delta\boldsymbol{u}^3) \tag{2.40}$$

$$\approx \gamma_s(1 + \gamma^2\boldsymbol{u} \cdot \delta\boldsymbol{u}), \tag{2.41}$$

with $\gamma = [1 + p^2/(mc)^2]^{1/2} = [1 - u^2/c^2]^{-1/2}$. The linearised convection term in the momentum equation is formulated by

$$(\boldsymbol{v} \cdot \nabla)\boldsymbol{p} \approx \gamma m(\boldsymbol{u} \cdot \nabla)[\delta\boldsymbol{u} + \gamma^2/c^2(\boldsymbol{u} \cdot \delta\boldsymbol{u})\boldsymbol{u}] = (\gamma^2\delta u_z, \delta\boldsymbol{u}_\perp), \tag{2.42}$$

and the linearised fluid equations are derived to

$$\begin{aligned}(\partial_t + u\partial_z)\delta n &= -n\nabla \cdot \delta\boldsymbol{u} \\ (\partial_t + u\partial_z)\delta\boldsymbol{u} &= \frac{1}{\gamma m}\begin{pmatrix} F_z/\gamma^2 \\ \boldsymbol{F}_\perp \end{pmatrix} + \frac{\nabla\mathcal{P}}{n},\end{aligned} \tag{2.43}$$

with longitudinal F_z and perpendicular $F_\perp$ component of a force acting on the fluid. Applying ∇ to the linearised momentum equation and inserting the linearised continuity equation cancels out $\delta\boldsymbol{u}$ and yields

$$\left[(\partial_t + u\partial_z)^2 + \frac{2}{3}\frac{\sigma_{pr}^2}{m^2\gamma^2}\nabla^2\right]\delta n = \frac{n}{m\gamma}\left(\frac{\partial_z F_z}{\gamma^2} + \nabla_\perp \cdot \boldsymbol{F}_\perp\right), \tag{2.44}$$

with the definition of the pressure term from Equation (2.38). The Lorentz factor lowers the impact of the longitudinal force on the momentum by a factor of γ^{-2}.

The fluid equation in the lab (Eulerian) frame contains the convective term $\partial_t + \boldsymbol{u} \cdot \nabla$, which can be greatly simplified in the Lagrangian frame. Instead of observing a fluid motion from a specific location in space through which the fluid passes, the fluid motion is considered from the individual fluid elements moving through phasespace in the Lagrangian frame. The location and time of the fluid elements are expressed as a snapshot in time by

$$\boldsymbol{\zeta} = \boldsymbol{x} - \boldsymbol{\Lambda}(\boldsymbol{\zeta},\tau), \quad \tau = t \quad \text{with } \boldsymbol{\Lambda}(\boldsymbol{\zeta},\tau) = \int_0^\tau \boldsymbol{u}(\boldsymbol{\zeta},\tau')\,\mathrm{d}\tau', \tag{2.45}$$

where $\boldsymbol{\Lambda}$ is the convective term tracing the fluid motion. The partial derivatives in configuration space and time transform to $\nabla = [1/(1+\nabla_{\boldsymbol{\zeta}}\cdot\boldsymbol{\Lambda})]\nabla_{\boldsymbol{\zeta}}$ and $\partial_t = \partial_\tau - [\boldsymbol{u}(\boldsymbol{\zeta},\tau)/(1+\nabla_{\boldsymbol{\zeta}}\cdot\boldsymbol{\Lambda})]\cdot\nabla_{\boldsymbol{\zeta}}$, such that the convective term rewrites to a co-moving time-derivative

$$\partial_t + \boldsymbol{u} \cdot \nabla \to \partial_\tau. \tag{2.46}$$

For the beam propagating along $+z$, each slice contains the same velocity, $\boldsymbol{\Lambda}(\boldsymbol{\zeta},\tau) = u_b t\hat{\boldsymbol{z}}$ and the Lagrangian frame of the beam as a snapshot in time simplifies to $\zeta = z - u_b t, \tau = t$. In the experimental setup, the image of the beam is taken as a snapshot in position, i.e. each beam slice is measured at the same position at different lab times. The beam frame is then defined by

$$\zeta = z - u_b t, \quad \tau = z/u_b, \tag{2.47}$$

such that each beam slice ζ has propagated the same amount of time τ in plasma. The partial derivatives transform in the beam frame to

$$\partial_t = -u_b \partial_\zeta, \quad \partial_z = \partial_\zeta + \partial_\tau / u_b. \tag{2.48}$$

and the convective term rewrites to $\partial_t + \boldsymbol{u} \cdot \nabla \rightarrow \partial_\tau$, equivalent to the Lagrangian frame given as a snapshot in time.

The existent kinetic theories for the filamentation instabilities provide the foundation to understand the performed simulations throughout the next chapters and verify their numerical convergence. Two simulation methods, listed in the next section, are essential to investigate the nonlinear regimes not traceable by linear theory and validate the three-dimensional analytical model derived in Chapter 4.

2.5 Methods

This doctoral work is conducted at the Group of Plasma Astrophysics within the TOK department at the Max Planck Institute for Plasma Physics in collaboration with the AWAKE experiment at the European Organization for Nuclear Research (CERN). The results are obtained using analytic methods and numerical computations with particle-in-cell (PIC) simulations and compared to experimental measurements at the AWAKE experiment. The simulations are performed with the codes OSIRIS (R. Fonseca *et al.*, 2002), QV3D (built on the VLPL platform) (Pukhov, 1999, 2015) and LCODE (Sosedkin and K. Lotov, 2016) on the MPCDF computing cluster. OSIRIS is a relativistic, fully electromagnetic, massively parallel PIC code developed and maintained by the Osiris consortium, which consists of the Extreme Plasma Physics (EPP) team in the Group of Lasers and Plasmas and the Particle-in-Cell and Kinetic Simulation Software Center (PICKSC) at the University of California, Los Angeles. The fully-electromagnetic PIC method is referred to as full-PIC. QV3D is a quasistatic PIC code for simulations of plasma wakefield acceleration in three-dimensional geometry developed by Alexander Pukhov at the University of Düsseldorf and maintained by John Farmer. LCODE is another quasistatic PIC code developed at the Novosibirsk State University, which is used for the axisymmetric studies in Chapter 5.

The complex nature of plasma motivates computer simulations to extend beyond analytic models. The exascale era allows for in-depth studies of realistic scenarios in laboratories and astrophysical contexts. numerical investigations on plasma were pioneered by works of J.M. Dawson, C.K. Birdsall and A.B. Langdon in the early 60s. Simulations may predict physical phenomena, motivate new research, and aid experimental design. Where good agreement between experiment and simulations occurs, simulations give a deep insight into the evolution and physical phenomena, out of reach for experimental diagnostics or analytic models (Birdsall and Langdon, 2018).

Magnetohydrodynamic approaches are an essential tool to simulate the collective behaviour of plasma and are widely used in astrophysics to nuclear fusion research. The plasma is treated as a single fluid interacting with the electromagnetic field, where the fluid equations are discretised on a grid to solve for the variables. Kinetic approaches are required for systems not in thermal equilibrium or involve detailed particle-wave interactions, such as injection processes or particle acceleration. numerical methods include solving the Vlasov equation

or the elementary PIC algorithm. The Vlasox-Maxwell equation, given in Equation (2.6), is solved with the finite difference or finite element method on an Eulerian grid in phasespace in the Vlasov method. However, the Vlasov method is computationally expensive for multi-dimensional problems as large proportions of the phase space are not occupied by the plasma (Birdsall and Langdon, 2018; Pukhov, 2015).

The Lagrangian Vlasov or PIC method resembles a physical analogy to reality, being the self-consistent evolution between particles and fields. The difference relies on resolving macroparticles, where each macroparticle substitutes for significantly more physical particles. This approximation is possible due to the collective nature of the plasma (Birdsall and Langdon, 2018). The macroparticles propagate within a spatial grid and contain a momentum, i.e. the momentum space is implicitly resolved. This reduces the six-dimensional problem to a three-dimensional problem for the grid. Without the spatial grid, each particle-particle interaction must be evaluated, a N_m^2 problem, with N_m the number of macroparticles. By depositing the current and charge of the particles onto a grid, the particle-mesh interaction only requires N_m evaluations.

2.5.1 Fully-electromagnetic particle-in-cell

Precision errors over many computation steps can be avoided by normalising the numerical plasma and field quantities formulated as

$$\begin{array}{l|ll} \text{Density} & n' = n/n_p & \boldsymbol{j}' = \boldsymbol{j}/(en_pc) \\ \text{Momentum} & \boldsymbol{p}' = \boldsymbol{p}/(mc) & \sigma_p' = \sqrt{k_BT/(mc^2)} \\ \text{Fields} & \boldsymbol{E}' = \boldsymbol{E}/E_0 & \boldsymbol{B}' = c\boldsymbol{B}/E_0 \\ \text{Operators} & \partial_t' = \partial_t/\omega_p & \nabla' = \nabla/k_p, \end{array} \tag{2.49}$$

which rewrites the Maxwell equations without any unit-specific constants to $\nabla' \cdot \boldsymbol{E}' = \rho'$, $\nabla' \cdot \boldsymbol{B}' = 0$, $\nabla' \times \boldsymbol{E}' = -\partial_t' \boldsymbol{B}'$ and $\nabla' \times \boldsymbol{B}' = \boldsymbol{j}' + \partial_t' \boldsymbol{E}'$. The combination of either Faraday's or Ampere's law with Gauss' law results in the charge continuity Equation (2.35) $\partial_t \rho + \nabla \cdot \boldsymbol{j} = 0$, which combined with Gauss' law sets the initial condition for the electromagnetic field in the simulation. The electromagnetic PIC method only utilises Faraday's and Ampere's law, making the algorithm local and, thus, less prone to the usually unphysical boundary conditions (Pukhov, 2015).

The scheme for a fully electromagnetic PIC code with an explicit time advance on a Yee-lattice is shown in Figure 2.7. In the finite-difference scheme, the charge of the macroparticles is deposited onto the grid centre. The relevant current source term is deposited to the grid edges by tracking how much charge has transversed through each cell boundary during a particle push utilising Equation (2.35) (Pukhov, 2015). The obtained current density is used to update the fields on the grid via the Maxwell equations defined in Equation (2.3). The fields are interpolated to the macroparticles, and the momentum and position of the macroparticles are updated via the Lorentz force.

Fully-electromagnetic PIC simulations are required to comply with the Courant-Friedrichs-Lewy condition to avoid non-physical growth of the electromagnetic field. This condition strongly constrains the maximum timestep to $c\Delta t \leq [\sum_n (\Delta x_n)^{-2}]^{-1/2}$, with Δx_n the spatial grid resolution along each dimension (Courant *et al.*, 1928). Simulating systems with plasma species evolving at different spatial and time scales may become computationally expensive.

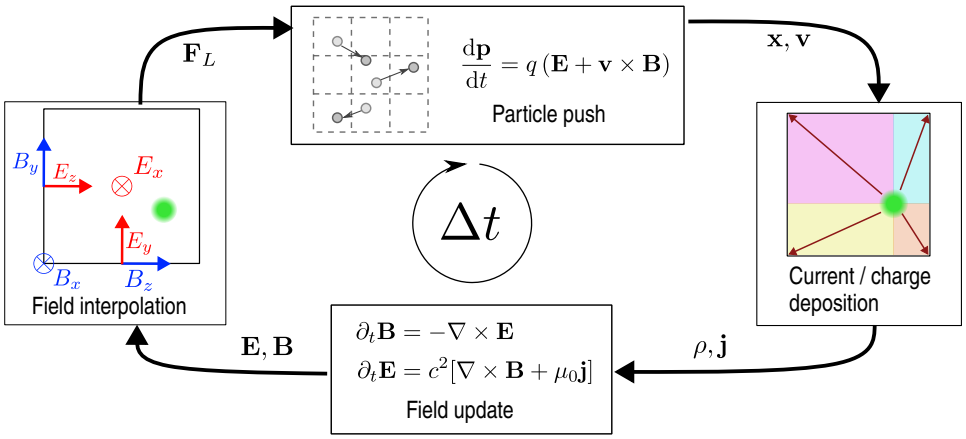

Figure 2.7: Conceptual circle of the PIC method. Macroparticles move within the grid, while the electromagnetic fields and current density of the plasma species are defined on a Yee lattice and nodes, respectively.

This gap in timescale is considerable for a relativistic and heavy beam evolving at the inverse betatron frequency ω_β^{-1} propagating through the plasma with a response time of the inverse plasma frequency ω_p^{-1} (Pukhov, 2015). In experimentally relevant studies, the plasma interacts with the beam over length scales ranging from micrometres to centimetres, which is several orders of magnitude shorter than the acceleration length that can extend up to hundreds of meters.

For fully-electromagnetic simulations, the relativistic beam can be simulated in a frame moving with the beam to reduce the length of the simulation window. To avoid the growth of unphysical waves at the downstream boundary, the window must move at the speed of light. The constraint on the time step remains and requires the quasistatic model.

2.5.2 Quasistatic Particle-in-Cell

The time scales between beam and plasma can be bridged by separating the fast plasma response from the slow beam scale. For the relativistic beam, the beam evolution along its propagation is significantly slower than the response of the plasma electrons along the beam length, expressed by $|\partial_\zeta \delta\rho_p| \gg |\partial_\tau \delta\rho_p / u_b|$ for the plasma quantities and equivalent for the electric and magnetic field. This is known as the quasistatic approximation: The plasma response depends only along the beam, so plasma electrons at different propagation distances copy their motion with a time-delay t (Tuev *et al.*, 2023). Instead of modelling electrons in the simulation volume, a transverse plane of electrons streams along the beam length. This reduces the number of required macroparticles for the plasma.

The propagation step in the quasistatic method is shown in Figure 2.8. The stream of plasma particles propagates along the beam length with the constrain $\Delta\zeta < k_p^{-1}$. The resulting electromagnetic fields from the plasma response push the beam particles via the Lorentz force with a propagation time step only constrained by the physical beam evolution, $\tau < \omega_\beta^{-1}$. For the studies on relativistic proton beam, the speedup of quasistatic simulations relative to the full PIC method is estimated to $\omega_p/\omega_\beta = [2\gamma_b(m_b/m_e)/(n_b/n_p)]^{1/2} \sim 10^4$ to 10^5. The

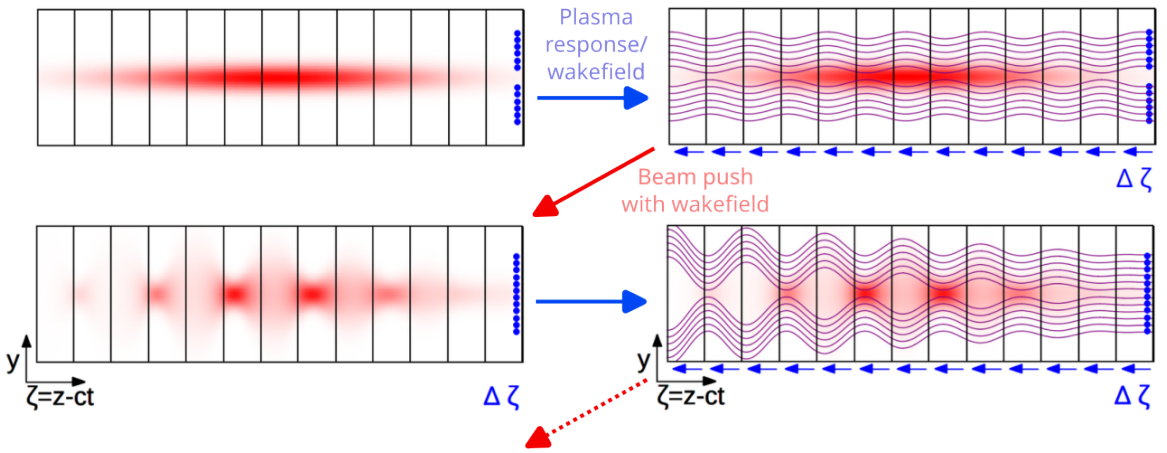

Figure 2.8: Scheme of quasistatic PIC. In the beam frame, a stream of plasma electrons (blue) with step size $\Delta\zeta$ responds to the beam (red). Each transversed beam slice $\Delta\zeta$ is pushed with the propagation step $\Delta z < c/\omega_\beta$ with the resulting wakefield force.

resulting fields are a snapshot at a fixed position along the propagation direction, such that each slice propagated the same amount of time in plasma in analogy to the experimental setup. The resulting fields from full PIC simulations are a snapshot in time, which impacts the field growth, discussed in Section 4.2.2.

Transforming the system to the beam frame and neglecting any partial derivatives with the slow time τ for the plasma response, the wave equation given in Equation (2.28) is expressed by (Tuev *et al.*, 2023)

$$\begin{aligned}\left(\nabla_\perp^2 + \frac{2}{c}\partial_{\tau\zeta}\right)\boldsymbol{E} &= \begin{pmatrix}\partial_\tau/c + \partial_\zeta \\ \nabla_\perp\end{pmatrix}\frac{\rho}{\varepsilon_0} - \mu_0\varepsilon_0\partial_\zeta\boldsymbol{j} \\ \left(\nabla_\perp^2 + \frac{2}{c}\partial_{\tau\zeta}\right)\boldsymbol{B} &= -\begin{pmatrix}\partial_\tau/c + \partial_\zeta \\ \nabla_\perp\end{pmatrix}\times\boldsymbol{j}.\end{aligned} \tag{2.50}$$

The mixed derivatives $\partial_{\tau\zeta}$ include the dynamic electromagnetic waves with a group velocity, which are not included in conventional quasistatic models. The computation of $\partial_\zeta j_z$ can be avoided by the continuity equation in the beam frame $\partial_\zeta\rho = \partial_\zeta j_z + \nabla_\perp\cdot\boldsymbol{j}_\perp$ and gives $(\nabla_\perp^2 + 2\partial_{\tau\zeta}/c)E_z = \nabla_\perp\cdot\boldsymbol{j} + \partial_\tau/c(\rho + j_z/c)$. In the quasistatic model, the equation of transverse motion $\mathrm{d}\boldsymbol{x}_\perp/\,\mathrm{d}t = \boldsymbol{p}_\perp c/(\boldsymbol{p}^2 + m^2c^2)^{1/2}$ for the plasma electrons is set by

$$\partial_\zeta\boldsymbol{p} = (\boldsymbol{F}_L - [v_z/c]\partial_\tau\boldsymbol{p})/(v_z - c) \tag{2.51}$$

The beam particles are pushed with the Lorentz force from the plasma wakefield after the stream of electrons transversed the simulation window.

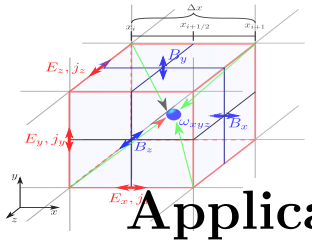

3 Application of Numerical Methods on Beam-Plasma Studies

Chapter Summary

- An analytic model for a non-linear wakefield excited by a dense stream in plasma is developed and compared to fully electromagnetic PIC simulations. The longitudinal wavenumber increases with beam density, where three different effects are identified: The beam charge density increases the oscillation frequency, while relativistic effects for large oscillations decrease the frequency; the plasma return current modifies the wavenumber depending on the beam charge. The model agrees well with the simulations, although non-physical plasma heating occurs.
- Quasistatic simulations of beam filamentation in plasma are compared to fully electromagnetic simulations, where the computing resources are significantly reduced with the quasistatic method. The growth of the field energies for current-driven and wakefield-driven in quasistatic simulations and fully electromagnetic simulations in two-dimensional geometry agree well with fully electromagnetic simulations in three-dimensional geometry. This enables the numerical study of the instabilities in a laboratory-relevant regime.

Plasma instabilities were studied in the most straightforward configuration with one dimension in configuration space in the early years of computers, which reflected realistic scenarios with caveats. This gives a deep insight into the multi-dimensional phase space and nonlinear regimes and verifies existent linear theories. This chapter introduces the nonlinear wakefield response to a charged stream without a transverse modulation in Section 3.1, where the physical increase of the longitudinal wavenumber is evaluated with an excursion to a non-physical increase of the plasma temperature limiting simulation studies. In Section 3.2, the current- and wakefield-driven filamentation of finite beams in three dimensions is discussed and compared between the PIC methods listed in Section 2.5.

3.1 Nonlinear Wakefield

In one dimension, the wakefield excited by a stream from Equation (2.29) reduces to its longitudinal component

$$E_z = \frac{\rho_{b0} k_e}{\varepsilon_0} \int_\zeta^0 \mathrm{d}\zeta' f(\zeta') k_e \cos k_e(\zeta - \zeta'), \tag{3.1}$$

which for a dilute flat-top stream with its head at $\zeta = 0$, $\rho_{b0} = q_b n_b \Theta(-\zeta)$, is a simple sine-wave $E_z = [\hat{\rho}_{b0} k_e/\varepsilon_0] \sin k_e(\zeta - \zeta_0)\Theta(-\zeta)$. The theory introduced in this section considers the effect of the plasma return current and relativistic plasma motion for stream charge densities in the magnitude of $\sim e n_p$.

For a positively-charged stream propagating through plasma, the plasma electron at position z experiences an attractive force towards the head of the stream, $z_{\mathrm{up}} = z_{0e} + \delta z + u_b t$, with z_{0e} the initial electron position and δz the distance between the beam head and plasma electron. From Gauss' law, the force acting on the electron depends on the charge density summed over all species between the beam head and the current electron position

$$E(z) = \frac{1}{\varepsilon_0} \int_z^{z_{\mathrm{up}}} \rho_{pi} + \rho_{pe} + \rho_b \, \mathrm{d}z', \quad E(z_{\mathrm{up}}) = 0. \tag{3.2}$$

With an initially quasineutral plasma, $\rho_{pi} + \rho_{pe} \approx 0$, the electron only witnesses the attractive force due to the positive charge of the beam towards the beam head $E_b(z) = -[e/\varepsilon_0] \int_z^{z_{\mathrm{up}}} n_b \, \mathrm{d}z' = -[e n_b/\varepsilon_0](z_{\mathrm{up}} - z)$. While the electrons accelerate upstream, the ions are stationary. The deficit between electron and ion charge density results in a restoring electric force downstream with $E_i(z) = [e/\varepsilon_0] \int_{z_{0e}}^z n_{pi} \, \mathrm{d}z' = [e n_{pi}/\varepsilon_0](z - z_{0e})$. Due to the two opposing forces, the electron oscillates around a moving equilibrium position z_{eq}, where the force on the electron cancels out, $-eE_b(z_{\mathrm{eq}}) = -eE_{pi}(z_{\mathrm{eq}})$. The equilibrium position and velocity $u_{\mathrm{eq}} = \mathrm{d}(x_{\mathrm{eq}}(t) - x_{0e})/\,\mathrm{d}t$ of the plasma electron are

$$z_{\mathrm{eq}} = \frac{n_b(\delta z + u_b t)}{n_b + n_{pi}} + x_{0e}, \qquad u_{\mathrm{eq}} = u_b \frac{n_b}{n_p + n_b} < \frac{u_b}{c}, \tag{3.3}$$

with the plasma return current $j_{pz} = -e u_{\mathrm{eq}}$.

The boundary value problem from Gauss' law in Equation (2.3) can be reformulated with $E(z_{\mathrm{eq}}) = 0$, and the oscillation of the plasma electrons around their equilibrium positions is

$$E(z) = \frac{e}{\varepsilon_0} \int_{z_{\mathrm{eq}}}^z [n_{pi}(z') + n_b(z')] \, \mathrm{d}z' = \frac{e}{\varepsilon_0}(n_{pi} + n_b)(z - z_{\mathrm{eq}}). \tag{3.4}$$

Defining $\dot{} = \mathrm{d}(\cdot)/\,\mathrm{d}t$, the non-relativistic equation of motion, $m_e \ddot{z} = F(z) = -eE(z)$, gives $\ddot{z} + \omega_n^2(z - z_{\mathrm{eq}}(t)) = 0$, with $\omega_n/\omega_p = (1 + n_b/n_p)^{1/2}$ the total plasma electron frequency. Transforming the equation to the Lagrangian frame for the plasma electrons, $\zeta_e = z - u_e t$ and $\tau = z_{\mathrm{eq}}/u_{\mathrm{eq}}$, results in $\partial_\tau^2 \dot{\zeta}_e + \omega_n^2 \dot{\zeta}_e = 0$, which has the general solution

$$\begin{aligned} \dot{\zeta}_e(\zeta,\tau) &= \dot{\zeta}_{e0}(\zeta) \cos \omega_n \tau + \omega_n \zeta_{e0}(\zeta) \sin \omega_n \tau \\ \zeta_e(\zeta,\tau) &= \int_0^\tau \dot{\zeta}_e(\zeta,\tau') \, \mathrm{d}\tau' = \zeta_{e0}(\zeta_e) * (1 - \cos \omega_n \tau_e) + [\dot{\zeta}_{e0}(\zeta_e)/\omega_n] \sin \omega_n \tau_e, \end{aligned} \tag{3.5}$$

with $\dot{\zeta}_{e0}$ and ζ_{e0} the initial values. This set of equations describes a harmonic oscillation of the individual electrons. For simplicity $\zeta_{e0} = 0$, and the equilibrium velocity of the electrons is $\dot{\zeta}_{e0} = u_{\mathrm{eq}}$. With the initial condition $z_0(\tau) = u_{\mathrm{eq}}\tau_e$, the electron position in the lab frame and the electric field from Equation (3.4) are

$$\begin{aligned} z_e(\zeta_e) &= \zeta_e(\tau_e) + A\sin(k_n\zeta_e) \\ E_z(\zeta_e) &= \frac{\rho_b}{\varepsilon_0} A\sin(k_n\zeta_e), \end{aligned} \tag{3.6}$$

with $k_n = \omega_n/(u_b - u_{\mathrm{eq}})$ the electron wavenumber in the lab frame and $A = \dot{\zeta}_{e0}/\omega_n = 1/k_n$. The harmonic oscillation of the electric field can be transformed to the lab frame by the discrete Fourier transform $\sin(k_n\zeta_e) = \sum_{l=1}^{\infty} c_l \sin(lk_n z_e)$, with the Fourier coefficient $c_l = [k_n/\pi]\int_0^{2\pi} \mathrm{d}z \sin(lk_n x)\sin(k_n\zeta_e) = (-1)^{l+1}[2/(nA)]J_l(lA)$, to

$$E_z(z_e) = \frac{en_p k_p}{\varepsilon_0} \sum_{l=1}^{\infty} \frac{2(-1)^{l+1}}{n} J_l\left(l\frac{\rho_b}{en_p}\frac{k_n}{k_p}\right)\sin(lk_n z_e). \tag{3.7}$$

Relativistic effects must be considered when the kinetic energy of particles is a considerable fraction of the particle's rest energy, $(E - E_0)/E_0 = \gamma - 1 \gtrsim 0.1$. Considering a highly relativistic beam, $u_b \approx c$, and that the maximum velocity during an electron oscillation is approximately double the equilibrium velocity, the beam density applying to the rule is $n_b \gtrsim n_p/4$. In the plasma frame, the equation of motion for the relativistic harmonic oscillator rearranges to

$$\frac{\mathrm{d}}{\mathrm{d}\tau_e}p = \frac{\mathrm{d}}{\mathrm{d}\tau_e}\frac{m_e\dot{\zeta}_e}{\sqrt{1 - \dot{\zeta}_e^2/c^2}} = -\frac{e^2}{\varepsilon_0}(n_b + n_p)\zeta_e. \tag{3.8}$$

In normalised units, $\tau_e' = \omega_n\tau_e$, $\zeta_e' = k_n\zeta_e$ the differential equation rewrites to $0 = \ddot{\zeta}_e{}' + (1 - \dot{\zeta}_e')^{3/2}\zeta_e'$. Further normalising electron momentum, $p_e' = p_e/(m_e c) = \dot{\zeta}_e'/(1 - \dot{\zeta}_e'^2)^{1/2}$, gives $\dot{\zeta}_e = p_e'/(1 + p_e'^2)^{1/2}$ and $\ddot{\zeta}_e = \dot{p}_e'/(1 + p_e'^2)^{3/2}$. These equations are combined to

$$\frac{\dot{p}_e{}' + \zeta_e'}{(1 + p_e'^2)^{3/2}} = 0 \Rightarrow \dot{p}_e' = -\zeta_e'. \tag{3.9}$$

The integral of the time derivative, $\ddot{p}_e' = -\dot{\zeta}_e' = -p_e'/(1 + p_e'^2)^{1/2}$, times $\dot{p}_e'$ results in $\dot{p}_e'^{\,2} = 2[\gamma_{\mathrm{eq}} - (1 + p_e'^2)^{1/2}]$, with $\gamma_{\mathrm{eq}} = (1 - u_{\mathrm{eq}}^2/c^2)^{-1/2}$. The time period $T = 4t_0$ for the periodic motion of p_e', with t_0 the time from zero momentum to the maximum momentum, $p_{\mathrm{eq}}' = p(t_0) = (\gamma_{\mathrm{eq}}^2 - 1)^{1/2}$, is solved by separation of variables

$$I = \frac{T}{4} = \frac{\sqrt{2}}{\pi}\int_0^{p_{\mathrm{eq}}} \frac{\mathrm{d}p_e'}{\sqrt{\gamma_{\mathrm{eq}} - \sqrt{1 + p_e'^2}}} = \frac{\sqrt{2}}{\pi}\int_0^{\operatorname{arsinh}(p_{\mathrm{eq}})} \frac{\cosh p_e'\,\mathrm{d}p_e'}{\sqrt{\gamma_{\mathrm{eq}} - \cosh p_e'}} \approx \frac{p_{\mathrm{eq}}'}{\operatorname{arsinh} p_{\mathrm{eq}}'}. \tag{3.10}$$

The time has to be Lorentz-transformed to the lab frame, $T_{\mathrm{lab}} = \gamma_{\mathrm{eq}}T$. The electron frequency is

$$\omega_{\mathrm{rel}} = \omega_n/(\gamma_{\mathrm{eq}}I) < \omega_n. \tag{3.11}$$

such that relativistic effects result in a lower plasma frequency.

The wavelength is defined by the distance between equal phases, where the beam velocity limits the phase velocity at the beam head. The beam passes the electrons with the upstream velocity u_b, initiating the electron oscillation with $\omega = \omega_{\mathrm{rel}}$. The phase velocity of the plasma wave decreases relative to the beam velocity due to the equilibrium velocity of the electrons u_{eq} towards the beam head. The phase velocity, $u_\psi = \omega/k$, is defined by the ratio between the electron frequency and the wavenumber of the plasma wave excited by the beam, $(u_b - u_{\mathrm{eq}}) = \omega_{\mathrm{rel}}/k_{\mathrm{rel}}$. Combining Equations (3.3) and (3.11), the electron wavenumber is

$$\frac{k_{\mathrm{rel}}}{k_e} = \frac{(1 + n_b/n_p)^{3/2}}{\gamma_{\mathrm{eq}} I} = \frac{n_b}{n_p}\sqrt{1 + \frac{n_b}{n_p}}\frac{\operatorname{arsinh}\left[p_{\mathrm{eq}}/(m_e c)\right]}{p_{\mathrm{eq}}^2/(m_e c)^2}, \tag{3.12}$$

with $p_{\mathrm{eq}}/(m_e c) = 1/\sqrt{[c^2/u_b^2](n_p + n_b)^2/n_b^2 - 1}$. The influence of the plasma return current decreases the wavelength compared to the plasma wavelength λ_p. In previous studies, the increase of the longitudinal plasma wavenumber due to the relativistic time-dilation of the electron oscillation was derived to (Esarey, Schroeder, *et al.*, 2009; K. V. Lotov, 2013)

$$k_e = k_p/[1 + \alpha_\sigma(\tilde{E}_z/E_0)^2], \tag{3.13}$$

where α_σ is an arbitrary factor set by the beam width. The analytic expression from one-dimensional theory, $\alpha = 3/16$, is retrieved for wide beams. This enables semi-analytically obtaining the wavenumber with the electric field known from simulations.

The analytic description of the plasma response is compared to simulations. One-dimensional fully-electromagnetic PIC simulations are used, in which plasma particles have one degree of freedom and $k = k_\zeta$. The relativistic, $\gamma_b = 22.4$ ($u_b/c = 0.999$), cold positron stream has a flat-top profile with extent $k_p\zeta < 1$. The stream propagation through a uniform plasma is considered in the co-moving frame $\zeta = z - ct$. The grid size of the simulation is $k_p\Delta z = 0.05$, and the time step is set to $\omega_p\Delta t = 0.048$. The plasma ions are modelled stationary, and the stream particles propagate with constant longitudinal momentum. The stream and plasma species are represented by one and 256 macroparticles per cell. The boundary conditions are open for the macroparticles and electromagnetic fields. The stream is initialised in a vacuum, and the plasma response after the whole beam enters the plasma is obtained. The fields are solved in the Yee lattice, while the linear interpolation scheme for the shape of the macroparticle is set.

The harmonic oscillation in the plasma frame results in an anharmonic oscillation in the lab frame. Figure 3.1a) shows that plasma electrons remaining equidistant during oscillation in the plasma frame are closer to each other towards $z_e = \mathbb{N}\pi/k_{\mathrm{rel}}$ in the lab frame. The equivalent increase in the plasma density results in the electric field steepening towards a saw-tooth profile. Due to the non-linear profile, the integral form in Equation (3.1) is not applicable. An extension to this model requires non-linear fluid theory for the plasma density and results in a series expression with Bessel functions (R. Davidson and Schram, 1968), comparable to Equation (3.7). The electric field is not unique above the limit $|E_z|/E_0 = k_p/k_{\mathrm{rel}}$ decreasing with the wavenumber of the plasma wake, which is physically interpreted as electrons crossing each other. This phase mixing disturbs the coherent oscillation of the plasma electrons and is referred to as (longitudinal) wavebreaking.

The quasi-linear wakefield excited by the stream with longitudinal flat-top profile is shown in Figure 3.2a). The envelope of the sine-wave remains constant along the length of the

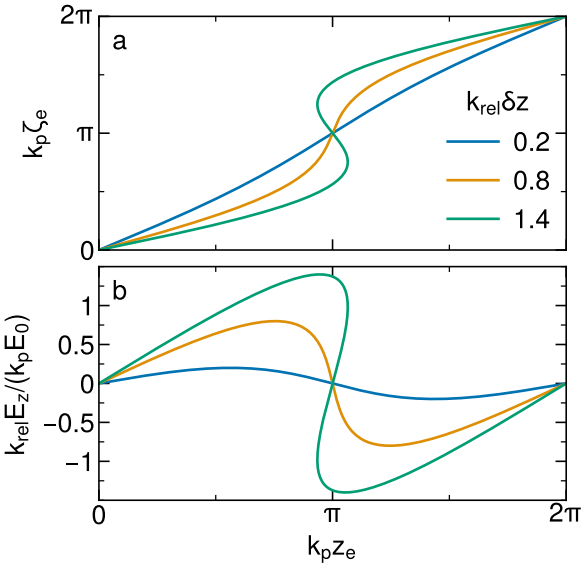

Figure 3.1: The nonlinear wakefield response. a) the electron position in the plasma frame and b) the longitudinal wakefield are shown in the lab frame according to Equation (3.6) for different perturbation amplitudes.

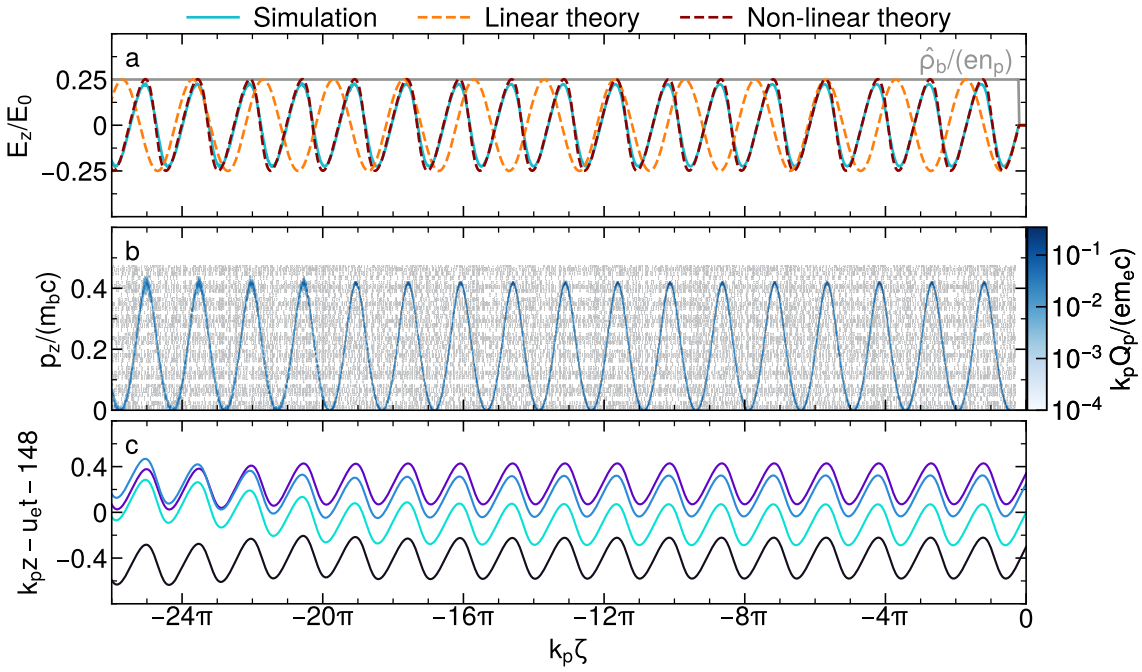

Figure 3.2: The plasma wake driven by a flat-top charged stream with $\rho_b = 0.25\, en_p$. a) The longitudinal electric field excited by the stream (grey) along the beam length from simulation (cyan), linear theory, $k_\zeta = k_p$, (orange-dashed) and the derived non-linear theory (red-dashed). b) The phasespace of the plasma electrons in ζp_ζ. c) The electron trajectories are shown relative to the sum of the moving equilibrium positions with the initial electron positions.

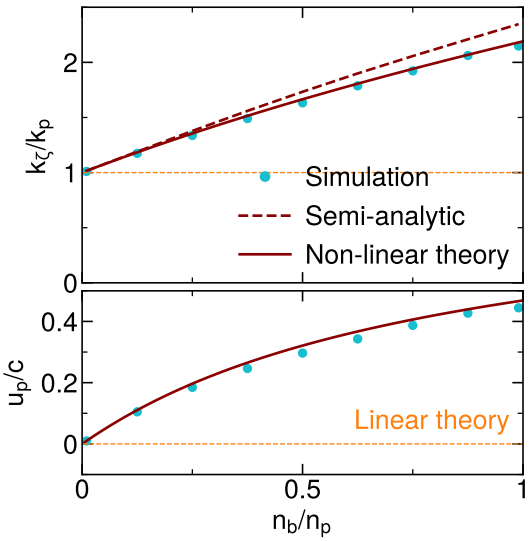

Figure 3.3: The wavenumber and equilibrium velocity of the plasma electrons as a function of the beam density. The cyan dots are from simulation, and the lines are obtained from linear theory (orange), the nonlinear theory derived in Equation (3.12) (red-solid), or solved semi-analytically with the nonlinear theory given by Esarey, Schroeder, *et al.* (2009) (red-dashed).

stream. The semi-analytic solution of the electric field along the beam length from linear theory in Equation (3.1) is expressed in differential form by

$$\partial_\zeta E_{zc}(\zeta) = k_{\mathrm{rel}}[iE_{zc}(\zeta) + \rho_b(\zeta)/(\varepsilon_0 k_p^2)], \tag{3.14}$$

with the physical solution $E_z = \Re(E_{zc})$. The wavenumber from the simulation is higher compared to linear theory, $k_\zeta = k_p$, but agrees well with the semi-analytic solution of Equation (3.14) with the wavenumber from the derived nonlinear theory expressed in Equation (3.12). The envelope from simulation is slightly lower compared to theory, indicating that the wave becomes non-linear.

The amplitude and equilibrium momentum of the longitudinal electron oscillation, shown by the ζp_ζ phasespace in Figure 3.2b), agrees well with the analytic prediction of $p_{\mathrm{eq}} = 0.2$ from Equation (3.3). The momentum spread equivalent to the plasma temperature, $\sigma_{pe} = (T_e/m_e c)^{1/2}$, of the plasma increases for $k_p\zeta < -20\pi$, although no physical heating process is apparent in the cold plasma such as collisions, resistance or neutral particles. This numerical heating, discussed in more detail in Appendix A.1, results in plasma electrons crossing each other in Figure 3.2c) such that electrons witness the electric field from the electron plasma charge density and some electrons are self-injected. Here, the effect of numerical heating is mitigated by obtaining the wavenumber close to the stream head.

The wavenumber of the plasma wake from simulation increases relative to the plasma wavenumber from linear theory with the density of the stream in Figure 3.3. This increase agrees with the derived nonlinear theory given in Equation (3.12), while the semi-analytic solution by evaluating Equation (3.13) slightly overestimates the plasma wavenumber. The equilibrium velocity of the plasma electrons from simulation and nonlinear increases asymptotically with the beam density. The excellent agreement verifies that the following relativistic effects can be safely neglected for this setup: The frequency of the relativistic oscillation depends on the kinetic energy $\omega(z) = \omega_e[1 + E_{\mathrm{kin}}(z)]^{1/2}$ due to the time dilation and remains not constant over the oscillation period. Additionally, the oscillation peak for the electron velocity reduces from u_{eq} due to the non-linear relativistic addition of velocities.

3.2 Filamentation Modes in Quasineutral Beams

Simulations of Weibel-mediated collisionless shocks in the astrophysical context involved counterstreaming pair plasma, i.e. quasineutral electron-positron streams (Spitkovsky, 2008). Therefore, extensive numerical studies of the interaction of quasineutral beams with plasma were performed (Muggli *et al.*, 2013; Shukla, Vieira, *et al.*, 2018) as well as an experimental study planned at the HiRadMat facility at CERN (Arrowsmith *et al.*, 2021). The required computational resources to achieve numerical convergence and bridge the gap between beam and plasma evolution, $\omega_\beta \ll \omega_p$, in full PIC simulations can be significantly higher relative to quasistatic PIC simulations for instability studies of relativistic beams in a low-temperature plasma. While quasistatic simulations are utilised for studies on SMI, it has not been investigated whether quasistatic simulations resolve the physics of CFI and OBI. The quasineutral beam undergoes the filamentation instabilities while suppressing SMI and requires a lower propagation distance and a shorter simulation window relative to a proton beam to track the saturated phase of the instabilities due to its low inertia.

The filamentation of a relativistic, $\gamma_b = 567.5$, electron-positron beam is numerically studied by two- and three-dimensional fully-electromagnetic PIC simulations and compared with three-dimensional quasistatic PIC simulations. The beam has a longitudinally Cosine-squared profile expressed by

$$f(\zeta) = \Theta\left(\sqrt{2\pi}\sigma_\zeta - |\zeta|\right) \cos^2\left[\sqrt{\frac{\pi}{2}}\frac{\zeta}{2\sigma_\zeta}\right], \tag{3.15}$$

to limit the longitudinal extent of the beam. Along each transverse axis, the beam has a Gaussian profile with rms width of $k_p\sigma_r = 2$ and a momentum spread of $\sigma_{pr}/(m_b c) = 0.1$. The total beam charge is constantly set to $Q = 2.92\,\mathrm{nC}$. This corresponds to a total beam peak density of $n_b = n_p$ for a beam with rms length $1/k_p$ and a plasma wavelength of $\lambda_p = 6.43 \times 10^{-2}\,\mathrm{mm}$. The beam evolution is considered in the co-moving frame at the speed of light. The grid size is $k_p\Delta(x, y, \zeta) = (0.05, 0.05, 0.08)$, and each equally-weighted macroparticle represents 143 physical particles for the beam. For the quasistatic simulations, the propagation step is $k_p\Delta z = 10$, and the plasma species with stationary modelled plasma ions is represented by nine macroparticles per cell. For full PIC simulations, the timestep is set to $\omega_p t = 0.03$, and the plasma species is represented by 9 and 27 macroparticles per cell in two- and three-dimensional configuration space, respectively. The field solver is set to fei of type Xu to avoid numerical Cherenkov (Xu *et al.*, 2020). The methods used to mitigate numerical instabilities for the filamentation studies are addressed in Appendix A.2.

The evolution of a filamented short and dense electron-positron beam after propagating $600/\omega_p$ in plasma is shown in Figure 3.4a). The dominantly transverse modulation of the beam grows both along the length of the beam and the plasma and results in beam filaments with the density compressed by an order of magnitude higher compared to the beam peak density. The instability saturates as beam particles get magnetically trapped, undergoing betatron oscillations. During the non-linear phase of the instability, oppositely aligned currents repel from each other while rectified currents merge into larger filaments and generate a strong perpendicular magnetic field. A perpendicular electric field results from both the space charge of the beam and a time-varying magnetic field following Faraday's law $\nabla \times \boldsymbol{E} = -\partial_t \boldsymbol{B}$. The varying magnetic field results in an electric field enclosing it and generates a plasma return current oppositely aligned to the beam current (Muggli, 2020).

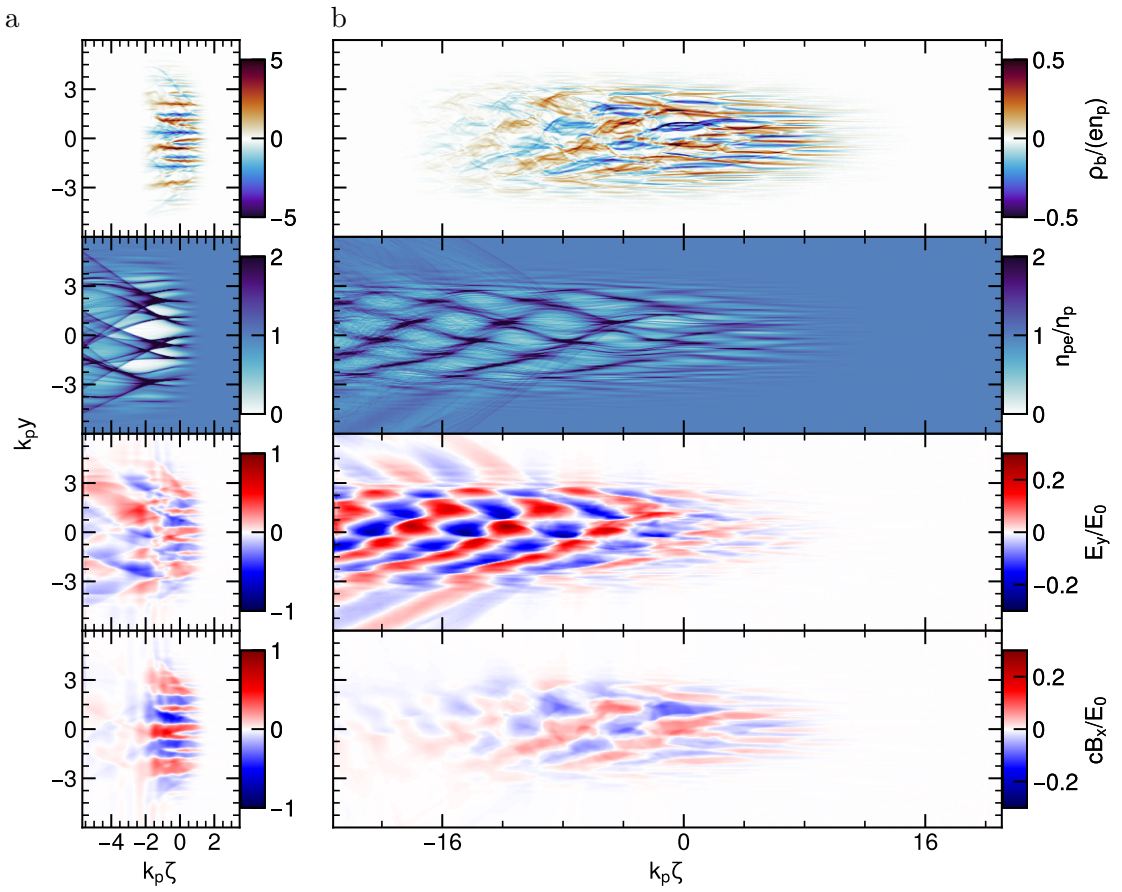

Figure 3.4: Beam filamentation of a) a dense and short $k_p\sigma_\zeta = 1$, and b) a dilute and long, $k_p\sigma_\zeta = 8$, quasineutral beam propagating in plasma. From top to bottom: The beam charge density, plasma electron density, and electric and magnetic field of a filamented beam after a propagation time $600/\omega_p$.

The evolution of a dilute beam with identical parameters from Figure 3.4a), but with the rms length of $k_p\zeta = 8$ is shown in Figure 3.4b). The transverse modulation contains an additional longitudinal modulation at the plasma wavenumber $k_\zeta = k_p$ due to the plasma wakefield component in the transverse electric field excited by the space charge of the beam. After saturation, the beam and its filaments diverge. From theory, the beam modulation is dominantly driven by OBI (Bret, Firpo, *et al.*, 2004). A detailed discussion of the exact mechanism and the connection to transverse two-stream instability (TTS) (Lawson, 1977) is provided in the main Chapter 4.

To quantify the field components, the energy density of the electric or the magnetic field summed within $x^2 + y^2 < 4\sigma_{x,y}^2$ is divided by the initial beam energy, $\epsilon(E_\perp)/\epsilon_b = (E_\perp^2/E_0^2)/[(\gamma_b - 1)(2\pi)^{3/2} n_b \sigma_\zeta \sigma_r^2]$. Figure 3.5a) shows the maximum electric and magnetic field slice energy along the beam length as a function of the propagation distance in plasma. The growth is exponential during the first betatron timescales and quickly decreases as the filamentation instability becomes non-linear. The transverse magnetic field is twice as large as the transverse electric field within the short beam. For the dilute beam, the electric field

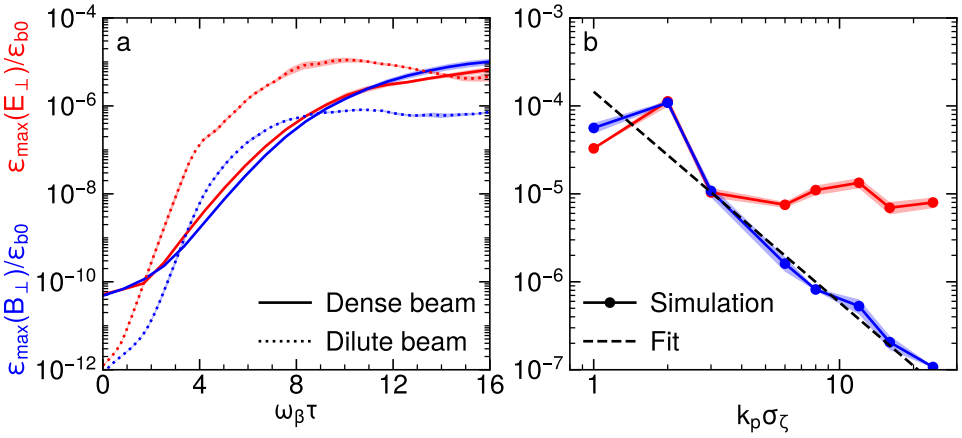

Figure 3.5: The saturation field energy for varying beam densities. a) The growth of the electric (red) and magnetic (blue) field for a dense (solid) or dilute (dotted) beam. The beam shape is indicated by the grey line. b) Maximum electric (red) and magnetic (blue) field energy along the beam length against its rms length at constant beam charge.

dominates the magnetic field by an order of magnitude after a few plasma oscillations, which maintains its magnitude after the beam due to the excited plasma wave. The growth rate as a function of the betatron frequency is higher for the beam with a lower number density, although the total beam charge is constant. As will be shown analytically in Section 4.4.1, the growth for wakefield-driven filamentation is maximum at the tail of the beam and depends on the integrated beam density, $\sim \int n_b \, \mathrm{d}\zeta$. This indicates that the different filamentation instabilities drive the high and low-density beams, respectively.

The transition from the beam evolution dominated by the magnetic field for dense beams to particles driven by the plasma wakefield for low beam densities is investigated by increasing the beam rms length under constant total beam charge. The smooth transition in field energy along the beam length of the transverse electric and magnetic field components is shown in figure Figure 3.5b). The magnetic field energy is only higher for very short rms lengths, $k_p \sigma_\zeta < 2$, while for $2 \leq k_p \sigma_\zeta \leq 4$ the magnetic and electric field equally contribute to the evolution of the beam. For higher beam densities, $k_p \sigma_\zeta > 4$, the magnetic field decreases asymptotically well described by the fit $|B_\perp| \sim (\sigma_\zeta)^{-1.2}$. The saturated magnitude of the magnetic field decreases not only with the lower beam current, predicting $|B_\perp| \sim \sigma_\zeta^{-1}$, but as the beam diverges more quickly. For a beam length $\sigma_\zeta > \lambda_p$, the wakefield is resonantly driven to a maximum magnitude depending on the integrated charge density along the beam length and remains constant for a constant total beam charge.

3.2.1 Benchmark

The parameters have been carefully chosen to be comparable to the work by Shukla, Martins, *et al.* (2020). The beam energy in the reference was $E_b = 29\,\mathrm{GeV}$ ($\gamma_b = 56750$), which is reduced to $\gamma_b = 567.5$ to considerably save computational resources in full PIC simulations. The normalised beam emittance is scaled down accordingly by the factor of $(\gamma_{\mathrm{reduced}}/\gamma_b)^{1/2}$ to achieve identical Twiss beta by $\beta_{\mathrm{Gaus}} = \gamma_b \sigma_r / \sigma_{pr}$. Figure 3.6 shows in a) the linear and the

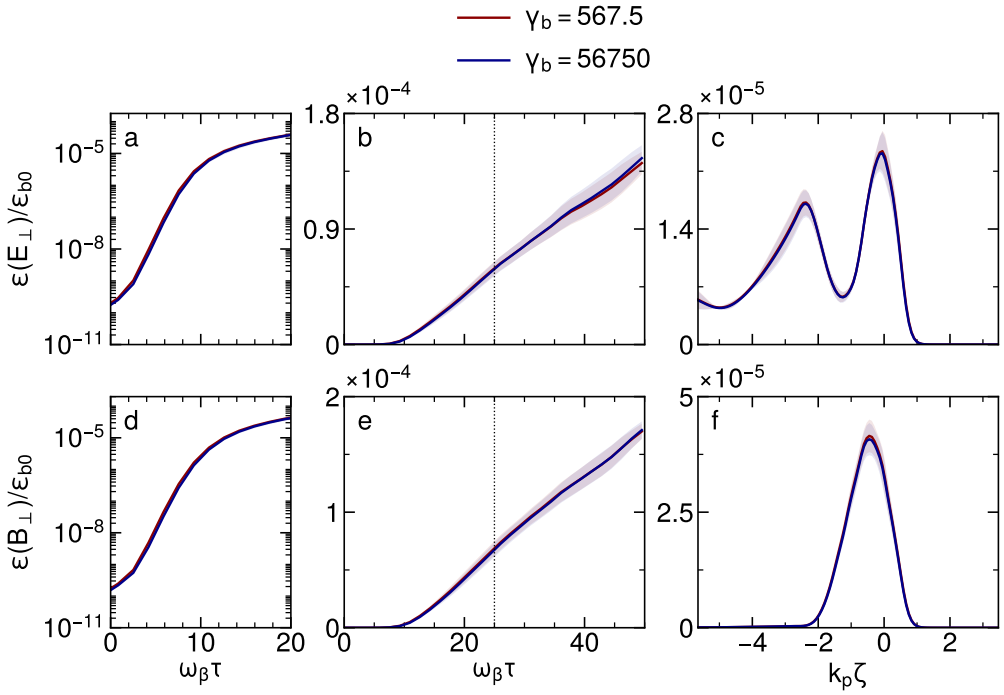

Figure 3.6: The electric and magnetic field energy with respect to the Lorentz factor (in the betatron frequency) of the dense beam. The growth of the electric field is shown along the plasma length in a) logarithmic and b) linear scale summed over the beam length and c) along the length of the beam at $\omega_\beta \tau = 25$. d), e) and f) equivalently show the growth of the magnetic field energy. The beam centre is located at $\zeta = 0$ The statistical mean (solid), and the standard deviation (shaded area) over three runs with different particle seed.

non-linear phase of the filamentation instability along the length of b) the plasma and c) the beam. The growth during the linear and nonlinear regime remains equivalent, considering the growth scaling with the betatron frequency, including the Lorentz factor. Therefore, the beam Lorentz factor is set to $\gamma_b = 567.5$ as the baseline for the benchmark between the PIC methods and the spatial dimensionality.

In addition to reducing the Lorentz factor, beams with reduced mass are often used to lower the computational overhead of simulations. It should be noted that the two-stream instability growth scales with $\omega_\beta \sim 1/(\gamma_b m_b)^{1/2}$ along the propagation time while damping scales with $\sigma_{pr}/(\gamma_b m_b)$, discussed in Section 4.3. Therefore, when scaling the beam mass, the beam momentum spread in units of $m_b c$, $\sigma_{pr}/(m_b c)$, should be scaled by a factor $(m_b/m_{\text{reduced}})^{1/2}$ to maintain the ratio of the growth and diffusion rates.

The electric and magnetic field energies are compared between the quasistatic three-dimensional code QV3D and the full PIC code OSIRIS in two- and three-dimensional geometry. The slice energy from two-dimensional simulations is projected to an area integration by $[\pi/2] \int (E_\perp^2/E_0^2)|y|\,\mathrm{d}y$ to compare to three-dimensional simulations. For the dense beam in Figure 3.7, the exponential growth during the first betatron timescales and the energy at which the fields saturate in a) and d) are equally reflected by all simulations, although the initial field energy is lower in Osiris. The locations and momenta of the beam particles are

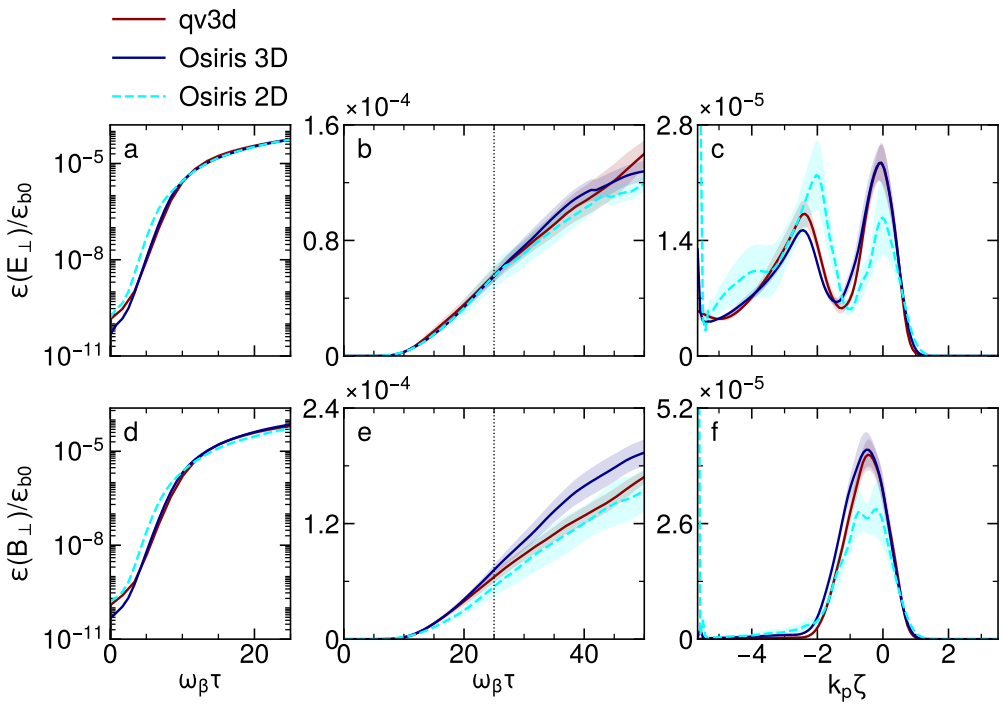

Figure 3.7: The electric and magnetic field energy between quasistatic simulations, and three- and two-dimensional fully-electromagnetic simulations for the dense beam from Figure 3.4a) propagating in plasma. Description as Figure 3.6.

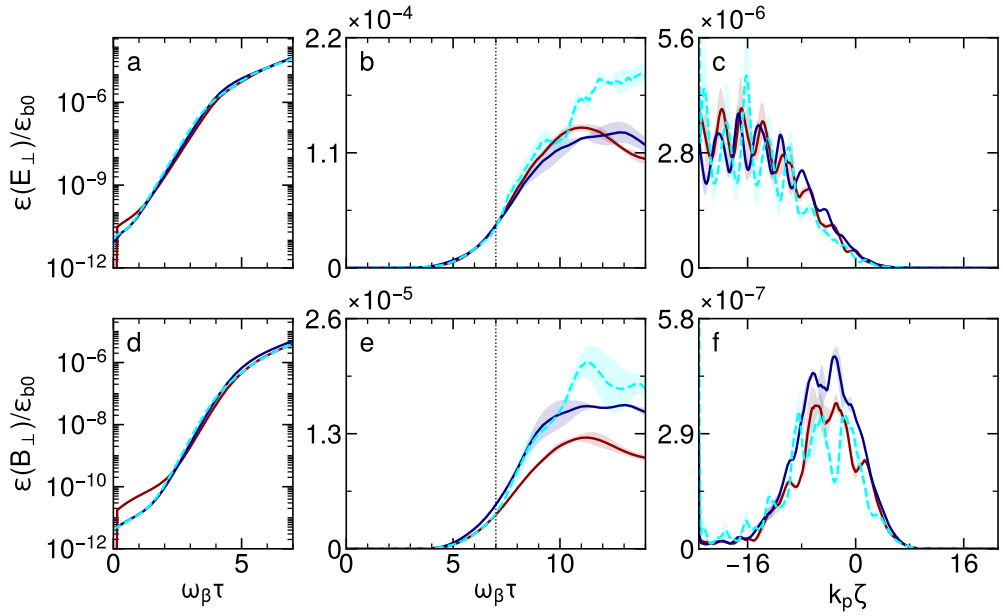

Figure 3.8: The electric and magnetic field energy or the dilute beam from Figure 3.4b) propagating in plasma. Description as Figure 3.7, but the field energy along the beam length is shown at $\omega_\beta \tau = 7$.

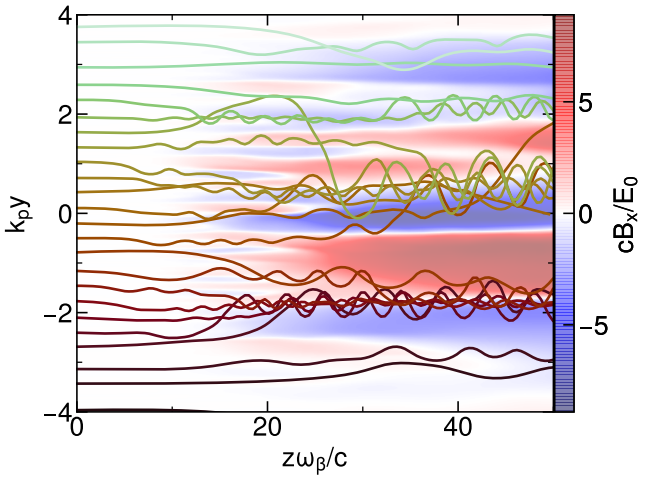

Figure 3.9: Positron trajectories of the dense beam within $|\zeta| < 0.5\,\sigma_\zeta$ and $|x| < 0.3/k_p$ along the propagation in plasma. The particles are equidistant at the plasma entrance and the perpendicular magnetic field is obtained at $\zeta = x = 0$.

equal between the three-dimensional simulations, seeded by an external program, but the current must be smoothed in the fully electromagnetic simulation (see Appendix A.2). During the non-linear phase in which beam filaments merge, the electric and magnetic fields are well reflected within the statistical uncertainties along the length of the beam for long propagation times $\omega_\beta \tau < 40$. The statistical variation is higher for two-dimensional simulations due to the lower number of filaments.

For very long propagation beyond $40/\omega_\beta$, two-dimensional simulations slightly underestimate the fields within the beam as merging rectified currents must flow over opposite currents in plane geometry in contrast to a three-dimensional geometry where rectified current filaments merge while repelling from opposite current filaments. In two-dimensional geometry and quasistatic simulations, the electric field is slightly higher behind the beam. At this stage, the beam filaments merged into one central electron filament undergoing strong betatron frequencies beyond the scope of this work. For unbounded systems, the work by Takamoto *et al.* (2018) showed that the exponential growth is well reflected. For the non-linear regime, however, the magnetic field remains more stable in three-dimensional simulations and the electrostatic component is overestimated in two dimensions.

For the dilute beam in Figure 3.8, the fields also agree well during the exponential growth in the first betatron timescales. The electric field and, thus, the plasma wakefield is comparable between the quasistatic and full PIC simulation. In two-dimensional simulations, the wakefield excited by the beam charge density is overestimated for $\omega_\beta \tau > 10$, since the beam divergence affects the beam density less in two-dimensional geometry, $\sim Q/\sigma_r$, compared to three-dimensional geometry, $\sim Q/\sigma_r^2$. The magnetic field shows a negligible deviation between the PIC methods at the beam centre.

Quasistatic simulations, as well as fully electromagnetic simulations in two-dimensional geometry, resolve not only the exponential growth of the filamentation instabilities but also the non-linear phase governed by magnetically trapped beam particles and filament merging in CFI, or the divergence of beam filaments in OBI, discussed in Section 4.5.1, for very long propagation distances beyond the scope of this work, usually within $\omega_\beta \tau < 6$. The magnetic trapping of beam particles is shown in Figure 3.9 for the quasistatic simulation. For a sufficiently high magnetic field, $|B_\perp| \gtrsim |E_\perp|$, the trajectories of the beam particles oscillate

within the enclosing field lines. Beam particles with high transverse momentum may jump between areas of magnetic trapping.

Quasistatic PIC simulations for relativistic beams in cold plasma significantly reduce computational resources and avoid issues like numerical Cherenkov radiation and grid heating, which may occur in fully electromagnetic simulations. Benchmarks confirm that these simulations accurately track current-driven and wakefield-driven filamentation instabilities for relevant beam and plasma parameters. This enables the investigation of filamentation instabilities in fully three-dimensional geometry over the required time scale. Since quasistatic simulations are limited to the static electromagnetic field, comparisons to two-dimensional fully-electromagnetic simulations remain a vital tool.

4

Laboratory-Relevant Filamentation Instabilities

Chapter Summary

- Dilute beams propagating in unmagnetised plasma are prone to wakefield-driven instabilities; a (longitudinal) two-stream and transverse two-stream. Transverse two-stream results in beam filamentation comparable to CFI, but with a longitudinal modulation at the plasma wavenumber. A finite temperature causes fine-scale perturbations to spread out and reduces the growth for high wavenumbers.
- An analytic model for wakefield-driven filamentation is derived, agreeing with previous research, and extended to warm beams with arbitrary profiles in three-dimensional geometry. The resulting dominant and cut-off wavenumber depend on the beam slice and propagation distance. This analytic model is in remarkable agreement with simulations and experimental observations.
- Beyond the applicability of the model, the field growth saturates when the beam or plasma is fully modulated, and the beam filaments diverge. For a dense beam with a smooth density profile, the two-stream filamentation at the beam head excites a wakefield, which sets the initial condition for current-driven filamentation at the beam centre.

Next to the electromagnetic CFI driven by the plasma return current (Fried, 1959; Weibel, 1959), a relativistic beam can excite an electrostatic plasma wakefield (see Section 2.3), which leads to the two-stream instabilities (Bludman *et al.*, 1960; Faĭnberg *et al.*, 1969), driven by the electrostatic plasma response (see Section 2.3). The beam excites a wakefield, which leads to the TSI and the TTS (Lawson, 1977). The combined influence of TSI and TTS is generally referred to as oblique instability (OBI) (Bludman *et al.*, 1960; Bret, Firpo, *et al.*, 2004; Califano *et al.*, 1998; Chang *et al.*, 2016; San Miguel Claveria *et al.*, 2022; Shukla, Vieira, *et al.*, 2018; Thode, 1976; Watson *et al.*, 1960) and allows dilute beams to undergo a similar filamentary behaviour as CFI.

Previous theoretical work on CFI for cold, spatially uniform streams determined that the temporal growth rate increases with transverse wavenumber (R. C. Davidson *et al.*, 1972). These studies were extended to warm streams, in which diffusion acts to suppress small-scale filamentation, and a dominant wavenumber (Jia *et al.*, 2013; Silva, R. A. Fonseca, Tonge, Mori, *et al.*, 2002) with a growth rate given in Equation (2.17) was calculated. For cold longitudinally bounded streams, CFI was found to exhibit spatiotemporal growth only at

the beam head within the length of $k_e|\zeta| \lesssim [4\eta_\infty\omega_\beta^2/(\gamma_b^2\omega_p)]\tau$. The respective spatiotemporal number of exponentiation within this length (Pathak *et al.*, 2015) or the temporal growth rate beyond this length (R. C. Davidson *et al.*, 1972) are

$$N_{\mathrm{cfi}}(\tau,\zeta) = \sqrt{2\eta_\infty k_e\zeta(\tau/\omega_p)}\omega_\beta, \quad \nu_{\mathrm{cfi}} = \sqrt{2\eta_\infty}\omega_\beta, \tag{4.1}$$

with $\eta_\infty = k_y^2/(k_p^2 + k_y^2)$ the relativistic limit for the spectral two-stream factor given in Equation (2.21).

For two-stream instabilities in cold uniform streams, the growth rate also increases with transverse wavenumber (Bret, Firpo, *et al.*, 2004; Watson *et al.*, 1960). It was predicted that diffusion would suppress the growth of small-scale filaments (Bludman *et al.*, 1960), which was later studied numerically. A threshold above which the system is stable was found analytically (Bret, Gremillet, and Bénisti, 2010). For a localised disturbance in cold bounded systems, TSI (Bers, 1983; Jones *et al.*, 1983) and TTS (San Miguel Claveria *et al.*, 2022) demonstrate a pulse-shaped spatiotemporal growth. However, the effect of a finite beam emittance on the spatiotemporal growth of the filamentation instability has not previously been treated analytically.

This chapter introduces a fully three-dimensional, spatiotemporal theory describing the filamentation of a warm beam due to wakefield-driven two-stream instabilities. This allows limits to be set on the beam temperature for laboratory astrophysics seeking to investigate these instabilities and PWFA experiments seeking to avoid them. The structure is as follows: Wakefield-driven filamentation is introduced in Section 4.1. In Section 4.2, an analytic expression for the growth of wakefield-driven filamentation is derived for a cold beam with arbitrary profile. The theory is extended to warm beams in Section 4.3, which considers the effect of diffusion. This allows the exact value for the dominant wavenumber to be calculated, as well as the cut-off above which no filamentation occurs. The analytic predictions are throughout compared to two and three-dimensional PIC simulations, which show excellent agreement. In Section 4.4, the experimentally observed suppression of beam filamentation is discussed in good agreement with the introduced theory. Considerations beyond the applicability of this model, including the saturation and divergence of the wakefield-driven beam filaments and the transition to a current-driven filamentation, are shown in Section 4.5.

The combined analytic and numerical investigation on wakefield-driven filamentation and a brief comparison to published experimental results has been accepted by *Physical Review E* (Walter *et al.*, 2024). The experimental results on filamentation at AWAKE are published in *Physical Review E* (Verra, Amoedo, *et al.*, 2024).

4.1 Wakefield-Driven Filamentation

The regimes for the two filamentation instabilities are defined by the current imbalance in the system. The beam and plasma currents must be comparable for CFI to dominate. For a relativistic beam propagating in stationary plasma, relevant in the astrophysical context, this requires a dense beam, $n_b \gtrsim n_p$ (Bret, Gremillet, and Dieckmann, 2010). For a dilute beam ($n_b \ll n_p$), the plasma current is negligible, and plasma electrons are mainly deflected by the beam charge. The resulting wakefield leads to TSI and TTS (Bret, Gremillet, and Dieckmann, 2010; Katsouleas *et al.*, 1987; Keinigs and Jones, 1987).

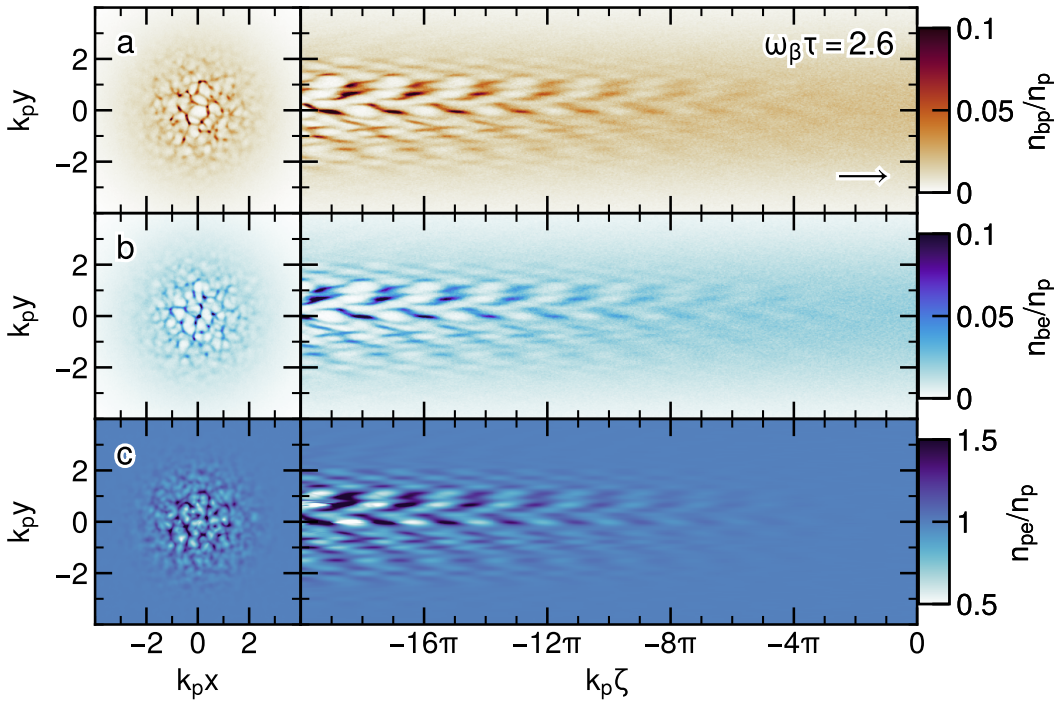

Figure 4.1: Filamentation of a dilute quasineutral beam due to wakefields. Transverse and longitudinal slices of the a) positron and b) electron density of the beam after propagating $\omega_\beta\tau = 2.6$ in an initially uniform plasma. c) The electron density of the corresponding plasma response. The beam propagates to the right, with its head at $\zeta = 0$. The transverse and longitudinal slices are taken at $k_p\zeta = -18\pi$ and $k_px = 0$, respectively.

Plasma wakefield experiments use a charged beam, which is usually dense and short, $k_p\sigma_\zeta < 1$, with σ_ζ the rms length (Albert *et al.*, 2021; Clayton *et al.*, 2016). A dilute and long beam, $k_p\sigma_\zeta \gg 1$, is subject to TTS. For narrow beams, $k_p\sigma_r \lesssim 1$, TTS can take the form of the axisymmetric SMI modulating the beam radius (see Section 2.4.1), or the antisymmetric hosing instability displacing the beam centroid (Moreira *et al.*, 2023). Fully modulated, the beam can resonantly drive a quasi-linear wake with an accelerating field comparable to that driven by a short, dense beam (Gschwendtner, K. Lotov, *et al.*, 2022). Wakefield experiments do not utilise wide beams as they may undergo filamentation due to transverse perturbations (Verra, Amoedo, *et al.*, 2024) and degrade the wakefield. Experiments that investigate filamentation instabilities may operate with quasineutral beams to suppress SMI (Arrowsmith *et al.*, 2021; Shukla, Vieira, *et al.*, 2018).

This filamentation of a quasineutral, dilute beam and the corresponding plasma response is shown in Figure 4.1 after propagating $2.6/\omega_\beta$ in plasma. Both the beam and the plasma response exhibit roughly equidistant filaments, where positrons and electrons are oppositely aligned due to the plasma wakefield that drives the instability. The plasma electrons align with the beam positrons driven by the beam charge. A periodic modulation occurs along the beam, arising due to the oscillation of the wakefield.

The simulation in Figure 4.1 was carried out with the quasistatic PIC method. The relativistic, $\gamma_b = 22.4$ ($u_b/c = 0.999$), warm electron-positron beam has a longitudinally flat-top

profile with extent $-20\pi < k_p\zeta < 0$, along each transverse axis a Gaussian profile with rms width of $\sigma_r = \sigma_x = \sigma_y = 3/k_p$, and a momentum spread of $\sigma_{pr} = \sigma_{px} = \sigma_{py} = 0.05\, m_b c$. The peak density of the beam positrons and electrons is $n_b/2 = 0.02\, n_p$, i.e. n_b is the total peak density of the beam. The grid size is $k_p\Delta(x, y, \zeta) = (0.01, 0.01, 0.1)$, the propagation step is $k_p\Delta z = 2$. The beam species and plasma electrons are represented by 16 and 4 macroparticles per cell, and the plasma ions are stationary. Adding more macroparticles per cell for the cold plasma species has no observable effect. For the beam, the instability growth remains unaffected, although the initial wakefield decreases.

From theory, the filamentation growth rate increases with transverse wavenumber for a cold beam. In simulations, the finite spatial resolution limits the maximum wave number that can be modelled. This leads to a dominant wavenumber determined by the cell size. For the finite emittance considered in Figure 4.1, diffusion results in a physical reduction of the growth rate at higher wavenumbers, yielding a dominant wavenumber well within the resolution limit of the simulation. In the next section, an analytic model is developed for wakefield-driven two-stream instabilities.

4.2 Filamentation of Cold Beams

4.2.1 Wakefield Induced by a Modulated beam

The charge density of the beam drives an electrostatic plasma response, expressed as the longitudinal E_z and transverse $\boldsymbol{W}_\perp$ wakefield (Bret, Firpo, *et al.*, 2004; Katsouleas *et al.*, 1987; Keinigs and Jones, 1987; Lawson, 1977). The plasma is quasineutral, i.e. the plasma ion density equals the initial plasma electron density $n_{pi} = n_{pe} = n_p$ and the plasma ions are stationary, $m_i \to \infty$. Given a dilute beam propagating in the $+z$ direction, the associated fields are E_z, $\boldsymbol{W}_\perp = \boldsymbol{E}_\perp + u_b\hat{\boldsymbol{z}} \times \boldsymbol{B}_\perp$, with $\hat{\boldsymbol{z}}$ the unit vector along z. Only the oscillatory plasma current $\boldsymbol{j}_p$ is considered. The corresponding wave equations of the potential Φ and vector field $\boldsymbol{A}$ in the Lorentz gauge are

$$\begin{aligned}(\nabla^2 - \partial_t^2/c^2)\Phi &= -(\rho_b + \delta\rho_p)/\varepsilon_0 \\ (\nabla^2 - \partial_t^2/c^2)\boldsymbol{A} &= -\mu_0(\boldsymbol{j}_b + \boldsymbol{j}_p),\end{aligned} \tag{4.2}$$

with $\delta\rho_p$ the charge density of the plasma perturbation and $\boldsymbol{j}_b = \rho_b u_b \hat{\boldsymbol{z}}$ the beam current density. The electric field can be obtained by $\boldsymbol{E} = -[\nabla\Phi + \partial_t \boldsymbol{A}]$ and the magnetic field by $\boldsymbol{B} = \nabla \times \boldsymbol{A}$ to the wave equation expressed in Equation (2.28). For a cold unmagnetised plasma, Ohm's law $(m_e/e)\, \mathrm{d}\boldsymbol{u}_p/\,\mathrm{d}t + \boldsymbol{j}_p \times \boldsymbol{B}/n_p - \nabla\mathcal{P}_p/n_p = \boldsymbol{E} + \boldsymbol{u}_p \times \boldsymbol{B}$ reduces to $\mu_0\partial_t \boldsymbol{j}_p = -k_p^2 \boldsymbol{E}$. The magnetic field is found from Faraday's law, $\nabla \times \boldsymbol{E} = -\partial_t \boldsymbol{B}$. The wave equation of the electromagnetic fields are then expressed by

$$\begin{aligned}(\nabla^2 - \partial_t^2/c^2 - k_p^2)\boldsymbol{E} &= \mu_0\partial_t \boldsymbol{j}_b + \nabla(\rho_b + \delta\rho_p)/\varepsilon_0 \\ (\nabla^2 - \partial_t^2/c^2 - k_p^2)\boldsymbol{B} &= -\mu_0 \nabla \times \boldsymbol{j}_b.\end{aligned} \tag{4.3}$$

A link between the plasma perturbation to the beam charge density is expressed by Equation (2.44), $m_e\partial_t^2 \delta\rho_p = -e^2\nabla\boldsymbol{E} = -e^2(\rho_b + \delta\rho_p)/\varepsilon_0$.

Consistent with measurements in the experiments taken at a given position, the beam frame (see Equation (2.47)) is utilised with $\zeta = z - u_b t, \tau = z/u_b$. For relativistic beams, the

quasistatic approximation (see Section 2.5.2) results in $(\partial_z^2-\partial_t^2/c^2)\delta\rho_p \to (1-u_b^2/c^2)\partial_\zeta\delta\rho_p = \partial_\zeta^2\delta\rho_p/\gamma_b^2$. The full set of differential equations is reformulated to

$$\begin{aligned}(\nabla_\perp^2 - \partial_\zeta^2/\gamma_b^2 - k_p^2)E_z &= \partial_\zeta(\rho_b/\gamma_b^2 + \delta\rho_p)/\varepsilon_0\\ (\nabla_\perp^2 - \partial_\zeta^2/\gamma_b^2 - k_p^2)\boldsymbol{E}_\perp &= \nabla_\perp(\rho_b + \delta\rho_p)/\varepsilon_0\\ (\nabla_\perp^2 - \partial_\zeta^2/\gamma_b^2 - k_p^2)\boldsymbol{B}_\perp &= \mu_0 u_b \nabla^\perp\rho_b\end{aligned} \tag{4.4}$$

with $\nabla_\perp = (\partial_x, \partial_y)$ and $\nabla^\perp = (-\partial_y, \partial_x)$.

Defining the three-dimensional Fourier transform

$$\hat\rho_b = \mathcal{F}_{\zeta xy}\{\rho_b\}(k_\zeta, k_x, k_y) = \iiint_{-\infty}^{\infty} \mathrm{d}\zeta\,\mathrm{d}x\,\mathrm{d}y\rho_b \exp\left(-ik_\zeta\zeta - ik_x x - ik_y y\right), \tag{4.5}$$

the spectral form of the plasma fluid in the beam frame is given by $\delta\hat\rho_p = -k_e^2\hat\rho_b/(k_\zeta^2 + k_e^2)$, with $k_e = ck_p/u_b$. The field components transform to

$$\begin{aligned}\hat E_z &= -\frac{i}{\varepsilon_0\sqrt{2\pi}}\frac{k_\zeta(k_\zeta^2/\gamma_b^2 + k_p^2)\mathcal{F}_{\zeta xy}\{\rho_b\}}{(k_\zeta^2 - k_e^2)(k_\zeta^2/\gamma_b^2 + k_p^2 + k_r^2)}\\ \hat{\boldsymbol{E}}_\perp &= \frac{1}{\varepsilon_0\sqrt{2\pi}}\frac{k_\zeta^2\mathcal{F}_{\zeta xy}\{\nabla_\perp\rho_b\}}{(k_\zeta^2 - k_e^2)(k_\zeta^2/\gamma_b^2 + k_p^2 + k_r^2)}\\ \hat{\boldsymbol{B}}_\perp &= \frac{u_b/c^2}{\varepsilon_0\sqrt{2\pi}}\frac{\mathcal{F}_{\zeta xy}\{\nabla^\perp\rho_b\}}{k_\zeta^2/\gamma_b^2 + k_p^2 + k_r^2},\end{aligned} \tag{4.6}$$

with $k_r = (k_x^2+k_y^2)^{1/2}$ the transverse wavenumber in three-dimensional configuration space.

For an ideal cold beam, there is no charge perturbation exciting a wake-field. Therefore, a charge density with a transverse modulation, $\rho_{b0} = q_b\delta n_{b0} f(\zeta)\tilde g(x,y)\cos(k_x x + \varphi_x)\cos(k_y y + \varphi_y)$, is applied to a quasineutral beam. Here, $f(\zeta)$ and $g(x,y)$ are the longitudinal and transverse beam profile, $\tilde f(\zeta)$ and $\tilde g(x,y)$ are the slowly varying envelope, $|\partial_y\tilde g| \ll k_y|\tilde g|$, and $k_{x,y}$ and $\varphi_{x,y}$ are the modulation wavenumbers and phases, respectively. The positron and electron density may be given by $n_{e+,e-} = 0.5[n_b\tilde f(\zeta)\tilde g(x,y) \pm \delta n_b f(\zeta)\tilde g(x,y)\cos(k_x x)\cos(k_y y)]$.

In order to include the self-fields of the beam, it is crucial to evaluate the path integrals in ζ first before addressing the transverse directions. This avoids the branches of the purely electromagnetic mode at $k_\zeta = \pm i\gamma k_p$ for finite γ, sketched in Figure 4.2. A small plasma dissipation $\epsilon > 0$ slightly shifts the singularities to $\pm k_e$. The ideal plasma case is recovered by $\epsilon \to 0$ after the transform inversion (Keinigs and Jones, 1987). The inverse Fourier transforms for $\zeta < 0$ are

$$\begin{aligned}\hat E_z &= \frac{q_b\delta n_b}{\varepsilon_0}\frac{\mathcal{F}_{xy}\{g(x,y)\}}{k_e^2 + k_r^2}\int_{-\infty}^{0}\mathrm{d}\zeta' f(\zeta')\left[k_e^2\cos k_e(\zeta-\zeta') + k_r^2\exp\left(-\gamma_b\sqrt{k_p^2+k_r^2}|\zeta-\zeta'|\right)\right]\\ \hat{\boldsymbol{E}}_\perp &= \frac{q_b\delta n_b}{\varepsilon_0}\frac{\mathcal{F}_{xy}\{\nabla_\perp g(x,y)\}}{k_e^2 + k_r^2}\\ &\quad\times\int_{-\infty}^{0}\mathrm{d}\zeta' f(\zeta')\left[k_e\sin k_e(\zeta-\zeta') - \gamma_b\sqrt{k_p^2+k_r^2}\exp\left(-\gamma_b\sqrt{k_p^2+k_r^2}|\zeta-\zeta'|\right)\right]\\ \hat{\boldsymbol{B}}_\perp &= \frac{\gamma_b u_b}{c^2}\frac{q_b\delta n_b}{\varepsilon_0}\frac{\mathcal{F}_{xy}\{\nabla^\perp g(x,y)\}}{\sqrt{k_p^2+k_r^2}}\int_{-\infty}^{0}\mathrm{d}\zeta' f(\zeta')\exp\left(-\gamma_b\sqrt{k_p^2+k_r^2}|\zeta-\zeta'|\right).\end{aligned} \tag{4.7}$$

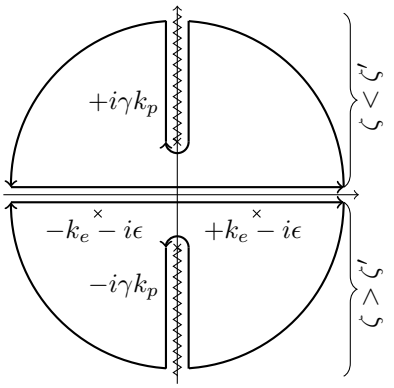

Figure 4.2: Integration path for the inverse Fourier transform in ζ. Adapted from Keinigs and Jones (1987).

The slowly varying transverse envelope $\tilde{g}$ vanishes at the boundaries. Neglecting the small spectral broadening due to $\tilde{g}(x, y)$, the transverse inverse Fourier transform of the transverse electric field gives

$$\boldsymbol{E}_\perp \sim \mathcal{F}_{xy}^{-1}\left\{\frac{\mathcal{F}_{xy}\left\{\nabla_\perp g(x,y)\right\}}{k_e^2+k_r^2}\right\} \approx \frac{\nabla_\perp g(x,y)}{k_e^2+k_r^2} \tag{4.8}$$

and of the longitudinal electric field gives $E_z \sim -[k_e/(k_e^2+k_r^2)]g(x,y)$. The second electromagnetic term in the integral can be split into the contribution of the local beam slice and the inductive, purely decaying fields due to a change in beam shape

$$\begin{aligned}&\int_\zeta^0 \mathrm{d}\zeta' f(\zeta') \exp\left(-\gamma_b\sqrt{k_p^2+k_r^2}|\zeta-\zeta'|\right)\\ &= \frac{f(\zeta)}{\gamma_b\sqrt{k_p^2+k_r^2}} - \int_\zeta^0 \mathrm{d}\zeta' \partial_{\zeta'} f(\zeta') \frac{\exp\left(-\gamma_b\sqrt{k_p^2+k_r^2}|\zeta-\zeta'|\right)}{\gamma_b\sqrt{k_p^2+k_r^2}}.\end{aligned} \tag{4.9}$$

The latter can be safely ignored if the plasma is non-diffusive (Keinigs and Jones, 1987).

In the linear regime, $\delta n_b \ll n_b$ and $|E_z|,|\boldsymbol{W}_\perp| \ll E_0$, and without any limitation on the longitudinal shape, the fields can be expressed by

$$\begin{aligned}E_z &= \frac{q_b\delta n_b}{\varepsilon_0}\frac{k_e g(x,y)}{k_e^2+k_r^2}\int_\zeta^0 \mathrm{d}\zeta' f(\zeta') k_e \cos k_e(\zeta-\zeta')\\ \boldsymbol{E}_\perp &= \frac{q_b\delta n_b}{\varepsilon_0}\frac{\nabla_\perp g(x,y)}{k_e^2+k_r^2}\left[\int_\zeta^0 \mathrm{d}\zeta' f(\zeta') k_e \sin k_e(\zeta-\zeta') - f(\zeta)\right]\\ \boldsymbol{B}_\perp &= -\frac{u_b}{c^2}\frac{q_b\delta n_b}{\varepsilon_0}\frac{\nabla^\perp g(x,y)}{k_p^2+k_r^2} f(\zeta).\end{aligned} \tag{4.10}$$

The integral terms correspond to the wakefield, where each beam slice $f(\zeta)$ drives a plasma response with the amplitude depending on the transverse beam shape. The magnetic field and the second summand in the transverse electric field from the charge-repulsion are the self-fields of the beam. For relativistic beams, $k_e \to k_p$, the self-fields can be neglected since $W_f \sim f(\zeta)(1-u_b^2) = f(\zeta)/\gamma_b^2 \to 0$. Behind the beam, the self-fields disappear while the envelope of the wakefield remains constant. In a vacuum, the wakefield vanishes such that relativistic beam particles move ballistically.

Throughout the analytic treatment, comparisons are initially made to simulations in two-dimensional geometry, consistent with previous analytic and numerical studies. In this

geometry, relativistic beam particles effectively have one degree of freedom, and $k_r = k_y$. The two-dimensional simulations are carried out with the fully electromagnetic PIC method. The grid size of the simulation is $k_p\Delta(y,z) = (0.02, 0.06)$, and the time step is set to $\omega_p\Delta t = 0.0172$. The beam and plasma species are each represented by 384 and 192 macroparticles per cell. The number of particles per cell is significantly higher than that used in the three-dimensional simulations due to the relative decrease in the total number of cells in the two-dimensional simulations. The boundary conditions are open for the macroparticles and electromagnetic fields. The beam is initialised in a vacuum and propagates into plasma. The beam parameters are equivalent to Figure 4.1, but with an initially cold beam. The perturbation in the charge density of the beam has an amplitude of $e\delta n_b = 0.01\, en_p$ and a wavenumber of $k_y/k_p = \pi$.

Figure 4.3a) shows the initial wakefield driven by the transversely modulated beam when each beam slice just entered the plasma, $\tau = 0$. The longitudinal and transverse wakefield exhibit a longitudinal modulation at $k_\zeta = k_e$ and a transverse modulation at the seeded wavenumber $k_y = \pi k_p$. The transverse wakefield is stronger than the longitudinal component in agreement with the theoretical ratio, $\tilde{\boldsymbol{W}}_\perp = \tilde{E}_z \boldsymbol{k}_r u_b/(k_p c)$, from Equation (4.10). For comparison, the wakefield driven by a narrow single-species beam is shown in Figure 4.3b). Unlike the wide beam, the wakefield extends beyond the narrow beam. However, in both cases, the transverse wakefield periodically alternates between focussing and defocussing along the beam, which gives rise to TTS for a transversely modulated beam or SMI for a narrow single-species beam.

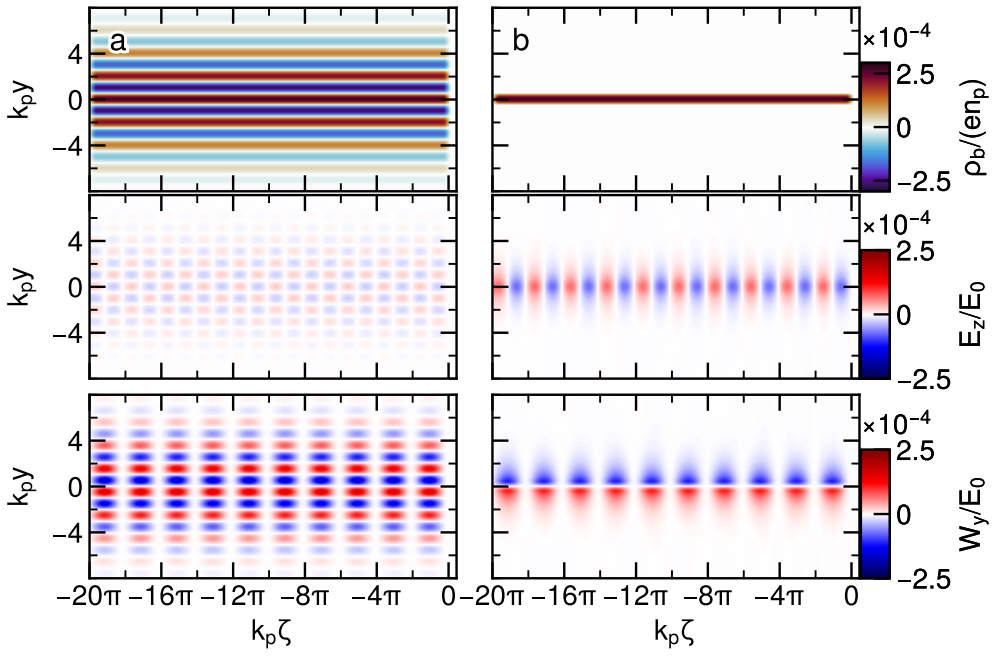

Figure 4.3: Beam-driven wakefield immediately after entering the plasma, $\tau = 0$. The beam charge density and corresponding longitudinal and transverse wakefield are shown for a) the wide quasineutral beam with transverse modulation and b) a narrow single-species beam of identical amplitude δn_b and width k_y.

4.2.2 Growth of Two-Stream Filamentation

Beam particles are accelerated or decelerated by the longitudinal wakefield and focussed or defocussed by transverse wakefield. The evolution of a cold beam is described by the linearised fluid equation (see 2.44)

$$\partial_\tau^2 \delta n_b = (\partial_t + u_b \partial_z)^2 \, \delta n_b = \frac{2\omega_\beta^2}{q_b/\varepsilon_0} \left(\frac{\partial_z E_z}{\gamma_b^2} + \nabla_\perp \cdot \boldsymbol{W}_\perp \right). \tag{4.11}$$

This wakefield reinforces the density modulation causing the wakefield to grow along the beam length, which leads to an instability. By applying the spatial derivative along ζ to Equation (4.11), the spatiotemporal growth from the integral terms in E_z and $\boldsymbol{E}_\perp$ can be analysed. For early-times and long beams, $\omega_\beta \tau \ll k_e \zeta$, the beam perturbation can be described by $\delta n_b g(x,y) \tilde{f}(\zeta)[\exp(ik_e\zeta)/2 + \text{c.c.}]$ (Schroeder *et al.*, 2011), considering the longitudinal wavenumber of the wakefields at $k_\zeta = k_e$. The integral along ζ from Equation (4.10) reduces to

$$\partial_\zeta W_\perp \sim \partial_\zeta \int_\zeta^0 \tilde{f}(\zeta') \frac{\exp(ik_e\zeta')}{2} \sin k_e(\zeta - \zeta') \approx \frac{i}{2} \tilde{f}(\zeta) \exp(ik_e\zeta). \tag{4.12}$$

For a flat-top beam with the head at $\zeta = 0$, $\tilde{f}(\zeta) = \Theta(-\zeta)$, the initial perturbation is given by $\delta n_b(\tau = 0, \zeta) = \delta n_{b0} \Theta(-\zeta)$. The self-fields in Equation (4.10), which only act within a beam slice, $E_{x,y} \sim f(\zeta)$ and $B_{x,y} \sim u_b f(\zeta)$, are negligible compared to the growing wakefield term. For a slowly varying transverse envelope, the transverse gradient simplifies to $\nabla_\perp^2 g(x,y) \approx -k_r^2 g(x,y)$ and the perturbation amplitude follows

$$\left[\partial_\zeta \partial_\tau^2 + i\eta_u k_e \omega_\beta^2 \tilde{g}(x,y) \right] \delta n_b(\tau,\zeta) = 0 \tag{4.13}$$

$$\eta_u = \frac{(c^2 - u_b^2)k_p^2 + u_b^2 k_r^2}{c^2 k_p^2 + u_b^2 k_r^2}, \tag{4.14}$$

with η_u the spectral two-stream factor from Equation (2.21), but in three dimensional geometry. The spectral factor includes the dependency on the beam velocity, where the first and second term represent the respective contribution of the longitudinal and transverse wakefield component and, therefore, of TSI and TTS.

The Green's function can be solved by a double Laplace transform

$$\begin{aligned} \mathcal{L}_{\zeta\tau}\{\delta n_b\}(k_\zeta,k_\tau) &= \iint_{-\infty}^{\infty} \mathrm{d}\tau \, \mathrm{d}\zeta \delta n_b \exp(-k_\zeta\zeta - k_\tau\tau) \\ &= \frac{k_\zeta \mathcal{L}_\zeta \{(k_\tau + \partial_\tau)\delta n_b(\tau = 0,\zeta)\} + \mathcal{L}_\tau \{\partial_\tau^2 \delta n_b(\tau,\zeta = 0)\}}{k_\zeta k_\tau^2 + i\eta_u k_e \omega_\beta^2 \tilde{g}(x,y)}. \end{aligned} \tag{4.15}$$

With a sharp plasma boundary at $\tau = 0$ in accordance to experiments and simulations, the initial condition, $\delta n_b(\tau, \zeta = 0) = \delta n_{b0}$, results in $\partial_\tau \delta n_b(\tau = 0, \zeta) = \partial_\tau^2 \delta n_b(\tau, \zeta = 0) = 0$ and $\mathcal{L}_\zeta\{\delta n_b(\tau = 0, \zeta)\} = \delta n_{b0}/k_\zeta$. The transform in ζ can be readily solved by the Bromwich contour integral shown in Figure 4.4, using the Residue with

$$\mathcal{L}_\zeta^{-1}\{\delta \bar{n}_b\} = \frac{1}{2\pi i} \lim_{T\to\infty} \int_{\alpha - iT}^{\alpha + iT} \mathrm{d}k_\zeta e^{k_\zeta \zeta} \delta \bar{n}_b = \sum_{\zeta_s} \mathrm{Res} \left\{ e^{k_\zeta \zeta} \delta \bar{n}_b \right\} \tag{4.16}$$

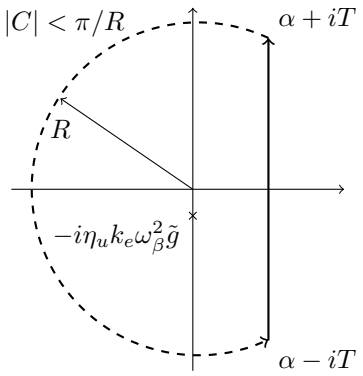

Figure 4.4: Integration path for the inverse Laplace transform in $\tilde{\zeta}$.

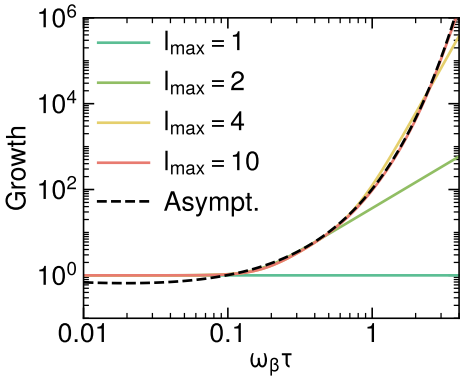

Figure 4.5: Semi-analytic solution of different orders to Equation (4.18) and the asymptotic solution given by Equation (4.20).

at the only singularity $k_\zeta = -i\eta_u \omega_\beta^2 k_e \tilde{g}(x,y)/k_\tau^2$, and gives

$$\delta\bar{n}_b = [\delta n_{b0}/k_\tau]\Theta(\zeta)\exp\left[i\eta_u \tilde{g}(x,y)\omega_\beta^2 k_e \zeta/k_\tau^2\right]. \tag{4.17}$$

Due to the singularity at $k_\tau = 0$, the exponential may be replaced by its series expression $\exp[i\eta_u \tilde{g}(x,y)\omega_\beta^2 k_e \zeta/k_\tau^2] = \sum_n [i\eta_u \tilde{g}(x,y)\omega_\beta^2 k_e \zeta/k_\tau^2]^n/n!$ to calculate the inverse Laplace transform in τ. Using the relation $\mathcal{L}^{-1}\{k_\tau^{-2n-1}\} = \tau^{2n}/(2n)!$ (Abramowitz and Stegun, 1964) gives the solution to Equation (4.15) as a complex power series

$$\delta n_{b,\mathrm{ts}} = \delta n_{b0} \sum_{l=0}^{\infty} \frac{\left[i\eta_u \tilde{g}(x,y) k_e |\zeta| \omega_\beta^2 \tau^2\right]^l}{l!(2l)!}. \tag{4.18}$$

The solution contains a growing imaginary and oscillatory real term, which can be obtained by the absolute, $\Gamma_{\mathrm{ts}} = |\delta n_{b,\mathrm{ts}}/\delta n_{b0}|$, and the phase $\psi(\delta n_{b,\mathrm{ts}})$.

The asymptotic expansion, $\tau \to \infty$, to Equation (4.18) can be obtained by utilising the saddle point method (Oughstun, 2009) to Equation (4.17). The inverse Laplace transform in τ can be approximated by $\int \mathrm{d}k_\tau b(k_\tau)\exp[i\tau h(k_\tau)] \approx [2\pi/(\tau|\partial_{k_\tau}^2 h(\hat{k}_\tau)|)]^{1/2} b(\hat{k}_\tau)\exp[\tau h(\hat{k}_\tau)]$, with $b(k_\tau) = k_\tau^{-1}$, $h(k_\tau) = \eta_u \tilde{g}\omega_\beta^2 k_e \zeta/k_\tau^2$, and $\hat{k}_\tau = [2\eta_u \tilde{g}\omega_\beta^2 \zeta/\tau]^{1/3}\exp(-i\pi/3)$ the dominant saddle-point of $h(k_\tau)$. This gives the asymptotic solution to Equation (4.15)

$$\delta n_{b,\mathrm{ts}} \approx \frac{\delta n_{b0}}{\sqrt{4\pi}} \frac{\exp\{(3/2^{2/3})[i\eta_u \tilde{g}(x,y) k_e |\zeta| \omega_\beta^2 \tau^2]^{1/3}\}}{\sqrt{(3/2^{2/3})[i\eta_u \tilde{g}(x,y) k_e |\zeta| \omega_\beta^2 \tau^2]^{1/3}}}. \tag{4.19}$$

Using Euler's identity, $i^{1/3} = \sqrt{3}/2 + i/2$, the asymptotic growth of the beam perturbation due to the combined two-stream instabilities is

$$|\delta n_{b,\mathrm{ts}}| \approx \frac{\delta n_{b0}}{\sqrt{4\pi}} \frac{\exp N_\infty}{\sqrt{N_\infty}}, \quad N_\infty = \frac{3^{3/2}}{2^{5/3}} \left[\eta_u \tilde{g}(x,y) k_e |\zeta| \omega_\beta^2 \tau^2\right]^{1/3}. \tag{4.20}$$

Figure 4.5 compares the asymptotic solution to including the first N terms for the semi-analytic solution of Equation (4.18),which shows good agreement for $\omega_\beta \tau > 0.1$, $N \geq 10$. In the non-relativistic and ultra-relativistic limit for streams, the asymptotic form simplifies to previous works (Jones *et al.*, 1983; San Miguel Claveria *et al.*, 2022). The transition from spatiotemporal to purely temporal growth of the two-stream mode (San Miguel Claveria *et al.*, 2022), in which the instability saturates in ζ yet continues to grow along τ, becomes relevant if the plasma density gradually increases, and requires an extension of the model presented here. The ratio between the filamentation of beams from Equation (4.20) to unbounded systems from Equation (2.20) is $N_\infty/(\nu_{\mathrm{obi}}\tau) = (3/2^{2/3})[k_e|\zeta|/(\omega_p\tau)]^{1/3}$, such that transverse perturbations in beams grow faster relative to unbounded streams for $k_e|\zeta| > [4/27]\omega_p\tau$.

The oscillatory term yields a phase ψ of the growing electrostatic wave, which is in the asymptotic limit expressed by

$$\psi = \frac{\pi}{4} - k_e|\zeta| - \frac{3}{2^{5/3}}(\eta_u \tilde{g}(x,y) k_e |\zeta| \omega_\beta^2 \tau^2)^{1/3}.$$

The corresponding phase velocity, $u_\psi = -\partial_t\psi/\partial_z\psi$, reduces relative to the beam velocity

$$u_\psi = u_b \left[1 - \frac{1}{2^{2/3}} \left(\eta_u \tilde{g}(x,y) \frac{\omega_\beta^2}{\omega_p^2} \frac{|\zeta|}{c\tau}\right)^{1/3}\right] = u_b \left[1 - \frac{2}{3^{3/2}} \frac{N_\infty}{\omega_p \tau}\right]. \tag{4.21}$$

In addition to the filamentation instability, a single-species beam is subject to the axisymmetric SMI for which the spectral factor η_u is substituted by Bessel functions in the analytic expressions for the growth and phase velocity (Pukhov *et al.*, 2011; Schroeder *et al.*, 2011). The ratio between the analytic growth expressions for a cold beam in Equation (4.20) and (2.30) is $N_\infty(u_b \to c)/N_{\mathrm{smi}} = k_r^{2/3}/[I_2(k_p\sigma_r)K_2(k_p\sigma_r)(k_p^2+k_r^2)]^{1/3}$. For a single-species beam, the growth rate of a transverse modulation within the beam exceeds the rate at which the transverse envelope changes for $\pi/k_r \lesssim \sigma_r$. Although a quasineutral bunch is not subject to SMI, it requires the consideration of the filamentation instability for two species. When the mass of the bunch particles is equal, the introduced theory can be readily applied by defining n_b as the total bunch density summed over all bunch species.

The resulting growth of the filamentation instability from the initial plasma response in Figure 4.3a) is illustrated in Figure 4.6 at a propagation of $2.6/\omega_\beta$ in plasma. The modulation amplitude of the beam charge density in Figure 4.6a) increases along the beam length, and contains a longitudinal modulation at $k_\zeta = k_e$ due to the electrostatic plasma response. The transverse wakefield from Figure 4.6b) and c) alternates between focusing and defocusing, both transversely and along the beam, resulting in alternating positron and electron filaments. The magnetic field in Figure 4.6c) is weaker than the electric field by an order of magnitude and is predominantly due to the local beam current. For a relativistic beam, Coulomb repulsion is compensated by the magnetic field, so the beam evolution is determined entirely by the plasma wakefield.

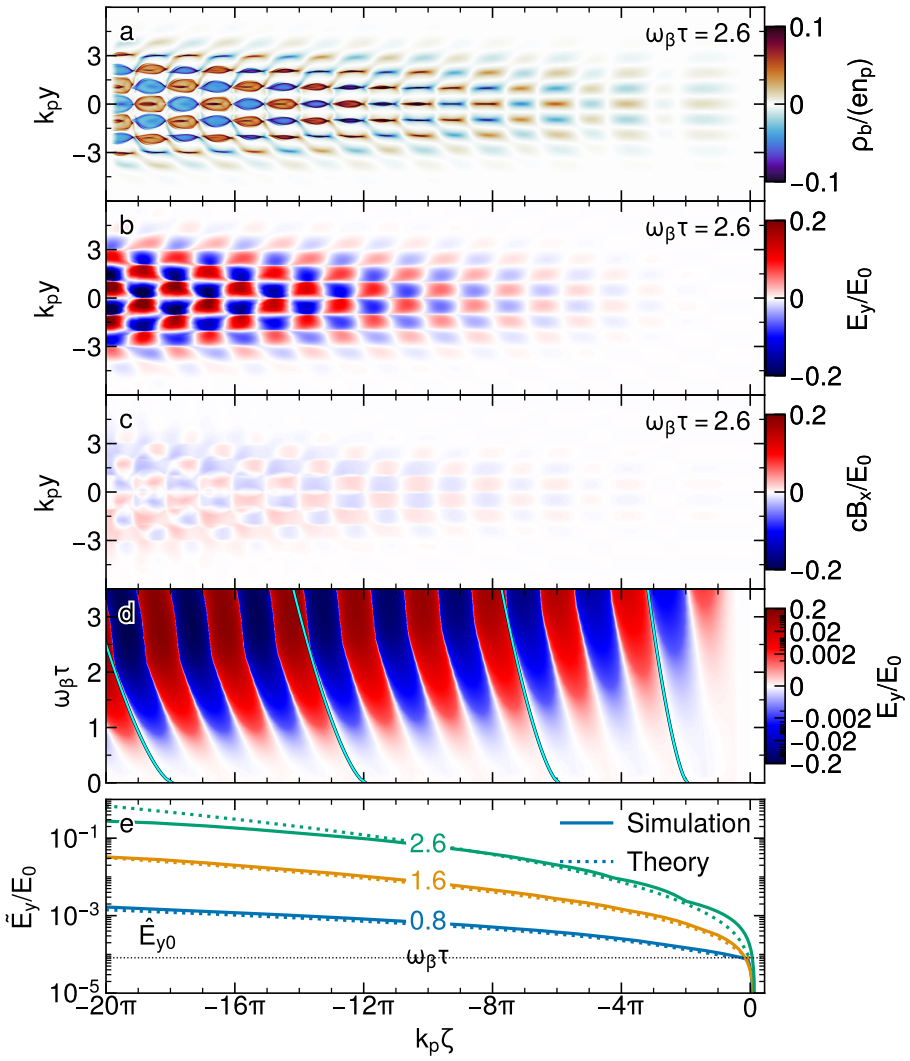

Figure 4.6: The evolution of a modulated beam propagating in plasma. The a) beam charge density, b) electric and c) magnetic field of a filamented beam with a transverse modulation, $k_y/k_p = \pi$, at $\omega_\beta\tau = 2.6$. d) The transversely averaged electric field along the plasma length with the theoretical phase shift superimposed. e) The envelope growth of the electric field $\tilde{E}_y$, along the length of the beam ζ at the propagation times $\omega_\beta\tau = \{0.8,1.6,2.6\}$, showing the simulation and theoretical values by solid and dotted lines, respectively. The black dotted line indicates the seed of the electric field.

The electric field (taken as the average over the range $0 < k_y y < \pi$) in Figure 4.6d) shows the growth along the beam length as the beam propagates in plasma. The modulation shifts backwards, illustrating that the phase velocity is lower than the beam velocity. The superimposed lines represent the integral of the phase velocity from Equation (4.21) over the length of the plasma and agree well with the phase of the wave.

Figure 4.6e) and Figure 4.7a) show the envelope growth of the electric field (averaged over the range $-\pi < k_y y < \pi$) along the beam and the plasma length, respectively. The envelope of the plasma wakefield is calculated as the mean of the absolute peak

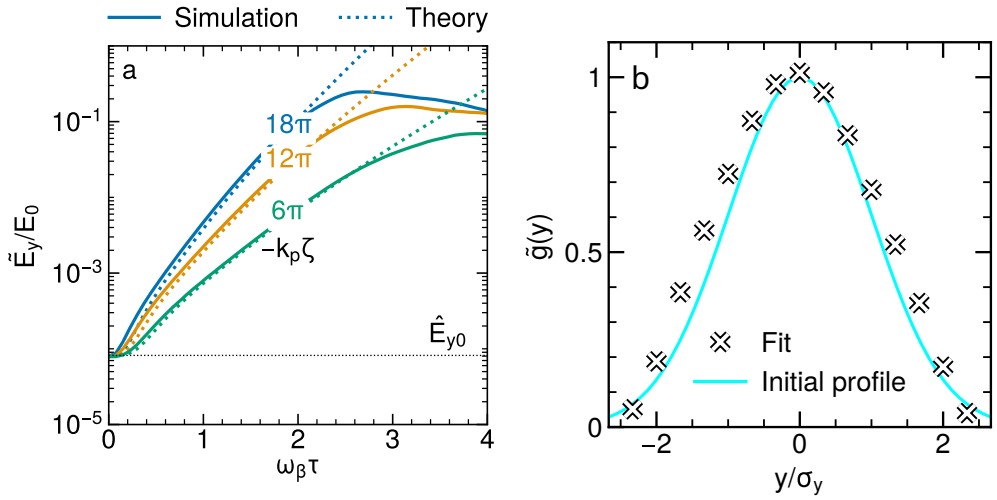

Figure 4.7: The growth along the propagation in plasma and the transverse beam profile. a) Simulated and theoretical envelope growth of the electric field along the propagation τ at equidistant beam slices $k_p\zeta = \{-6\pi, -12\pi, -18\pi\}$. b) beam profile from simulation, obtained by fitting the observed growth to Equation (4.18), compared to the initial beam shape.

and trough values along the beam length, determined using SciPy's peak-finding algorithm. The seed value agrees well with the analytic expression for the Fourier spectrum $\hat{E}_{y0} = \mathcal{F}_\perp\{E_{y0}\} = [e\delta n_{b0}/\varepsilon_0]k_y/(k_p^2 + k_y^2)$, obtained by solving Equation (4.10) for the initial beam profile. The growth of the electric field is compared with the semi-analytic solution to Equation (4.18), including the first ten terms, and shows excellent agreement along the beam up to a propagation time in plasma of $\sim 2/\omega_\beta$. For $\tau > 2/\omega_\beta$, the field growth begins to decrease relative to the analytic predictions (Figure 4.6d,f) while the phase velocity increases (Figure 4.6e). The field growth for $\omega_\beta\tau > 2$ in Figure 4.7a) is lower than the theory. This saturation occurs when the beam is fully modulated, $\rho_b > q_b n_b$, with the electron and positron filaments fully separating as seen in Figure 4.6a) for $k_p\zeta < -10\pi$.

To consider a transverse profile on the beam, Equation (4.18) is fitted to the simulation data along the plasma length at $k_p\zeta = -12\pi$ with $\tilde{g}(y)$ as a free parameter. The fit coefficient agrees well with the Gaussian profile of the beam in Figure 4.7b). In contrast to a longitudinal extent resulting in an increase of the growth along the beam, the growth rate and seed level correlate with the transverse envelope $\tilde{g}(y)$. The growth rate at a given transverse coordinate can be treated as a stream with the local beam density. The curved phase fronts in the beam modulation are due to the dependency of the phase velocity on the transverse envelope, $\tilde{g}(y)^{1/3}$, in Equation (4.21).

The fields from fully-electromagnetic PIC simulations are in the lab frame as a snapshot in time and require the transformation into the beam frame by $\tau = (z+\zeta)/u_b$ to be comparable to experimental observations. The observed evolution of the beam filamentation changes in the lab frame, which is shown for the electric field from Figure 4.6 in Figure 4.8. While the electric field grows along the full length of the beam in the beam frame, shown in Figure 4.8a), the electric field decreases at a given length along the beam in the lab frame

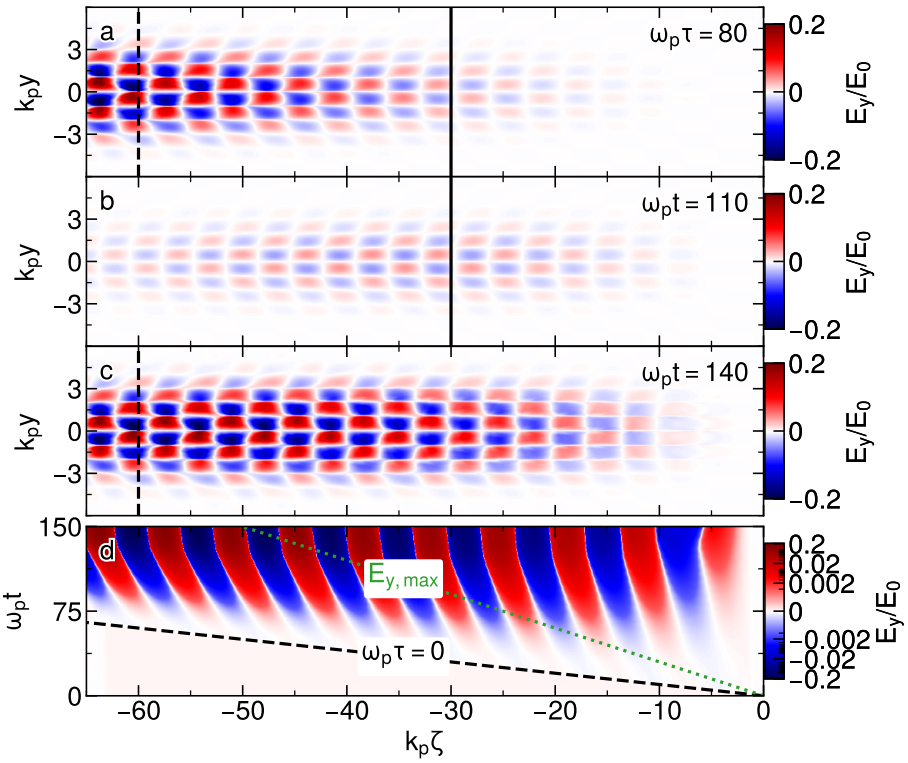

Figure 4.8: Electric field growth in the beam and lab frame. a) A snapshot of the transverse electric field is shown in the beam frame at $\omega_p\tau = 70$, and in the lab frame at b) $\omega_p t = 100$ and c) $\omega_p t = 130$. Vertical lines with the same linestyle show the beam slice of identical propagation time in plasma. d) The transversely averaged electric field from Figure 4.6d) given in the lab frame. The plasma entrance is indicated by the dashed line and the peak of the electric field is given by the green, dotted line.

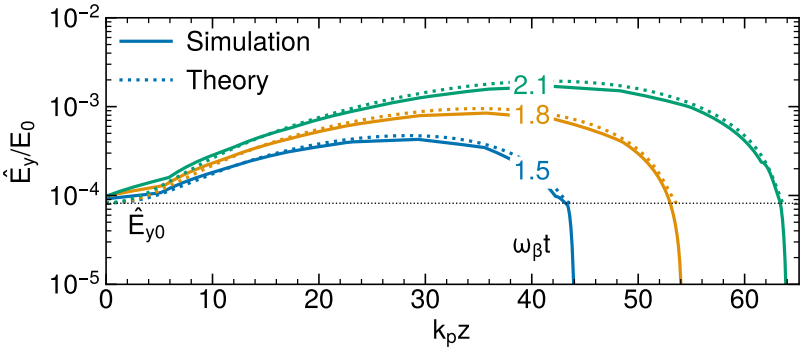

Figure 4.9: The envelope of the electric field in the lab frame at different times. The sharp plasma entrance is located at $z = 0$.

since each beam slice propagated different times within the plasma, shown in Figure 4.8b) and c). The evolution of the electric field along the length of the beam and plasma from Figure 4.6d) is shown for the lab frame in Figure 4.8d). Further along the beam length, the electric field grows later, $t > -\zeta/u_b$.

Figure 4.9 shows the envelope growth of the electric field in the lab frame with a localised initial disturbance at the beam head, $z = 0$, and reveals the pulse-shaped profile. The front

edge of the growing wave moves at the velocity of the beam. The location of the peak electric field is equivalent to the peak of the growth in Equation (4.20) with respect to the propagation distance and propagates at a constant velocity, $\dot{z}_{\max \mathrm{E}} = (2/3)u_b$. The growth is higher in the front vicinity of the pulse in agreement with the analytic prediction from Equation (4.20), where TTS grows more quickly along the length of the plasma relative to the length of the beam, $N_\infty \sim \tau^{2/3}\zeta^{1/3}$. Taking the transformation into account, the growth is well reflected by the semi-analytic expression from Equation (4.18). The instability is not fully convective (Bers, 1983) since no physical effect, such as a finite plasma temperature, damps the plasma wake in this model, and no spatial point returns to its original unperturbed state, $\lim_{t\to\infty} N_\infty \neq 0$.

4.2.3 Initial Perturbation Fields

At early propagation times, the evolution of the beam perturbation and the plasma perturbation are defined by the initial seed rather than its initial growth rate. For short times, the evolution of the perturbation is described by $[\partial_\tau^2 + i\eta_u\omega_\beta^2\tilde{g}(x,y)]\delta n_{b,S} = 0$. With the initial condition $\delta n_{b,S}(\tau = 0) = \delta n_{b0}$, the differential equation can be solved by a Fourier transform, and the purely temporal growth evolves as

$$\delta n_{b,S} = \delta n_{b0}\left[\eta_u\tilde{g}(x,y)\omega_\beta^2\tau^2 + 1\right]. \tag{4.22}$$

This can be observed in Figure 4.10a) and b) along the length of the plasma and in Figure 4.10d) and e) along the length of the beam, where the plasma and beam perturbation are not purely exponential. The same initial field with the bunch perturbation $\delta\hat{n}_b$ as seed dominates their initial growth. The exponentially growing term for the plasma perturbation is seeded by the depth of the beam modulation, and the exponential term for the beam perturbation grows from the wakefield modulating the beam. The exponential terms only dominate after the beam has propagated for some time. This propagation time is higher at the beam head as the growth rate of TTS is lower, shown by the growing gap between the simulation and the semi-analytic term. However, the transverse electric field in Figure 4.10c) and f), proportional to the difference between plasma and beam charge density

$$\frac{\boldsymbol{E}_\perp}{E_0} = \frac{\boldsymbol{k}_r}{k_e^2 + k_r^2}\frac{e\delta n_p - q_b\delta n_b}{n_p}, \tag{4.23}$$

exhibits exponential growth even at early times.

The two-stream filamentation can be analytically described by the evolution of the plasma perturbation, as outlined in the previous work by (San Miguel Claveria *et al.*, 2022), and can be extended to incorporate for a finite plasma temperature. Instead, the beam perturbation is considered here to include the effect of a finite beam emittance on the field growth.

4.3 Filamentation of Warm Beams

The filamentation of the beam depicted in Figure 4.1 results in a dominant wavenumber, a behaviour the theory for cold beams cannot describe. Diffusion of warm beams causes fine-scale perturbations within the beam to spread out, reducing the growth rate of the instability.

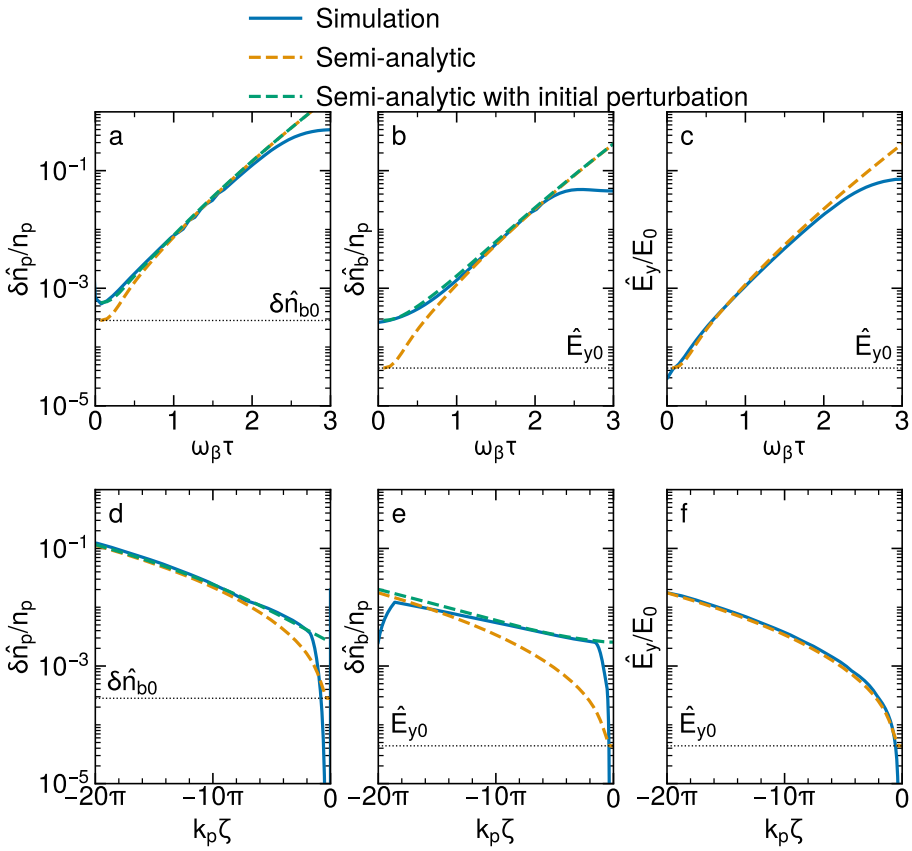

Figure 4.10: Non-exponential growth of the initial perturbation fields. The growth of the spectral a) plasma perturbation, b) beam perturbation and c) electric field shown along the plasma length at $k_p\zeta = -12\pi$ and in d), e) and f) given along the beam length at $\omega_\beta\tau = 1.6$ from simulation and theory for the cold beam with transverse modulation at $k_y/k_p = 2\pi$. The orange dashed lines show the semi-analytic solution to Equation (4.18), and for the green lines the growth from the initial perturbation in Equation (4.22) is added. The dotted lines indicate the seed for the two-stream instability.

For non-relativistic temperatures, $\sigma_{pr} \ll \gamma_b m_b u_b$, the fluid equation in Equation (4.11) can be extended to include the thermal pressure from the momentum spread to

$$\partial_\tau^2 \delta n_b = \frac{2\omega_\beta^2}{q_b/\varepsilon_0}\left(\frac{\partial_z E_z}{\gamma_b^2} + \nabla_\perp \cdot \boldsymbol{W}_\perp\right) + \frac{\nabla^2 \mathcal{P}}{\gamma_b m_b}, \tag{4.24}$$

where the pressure can be described by $\mathcal{P} = (2/3)[\sigma_{pr}^2/(\gamma_b m_b)]\delta n_{b,\mathrm{ts}} g(x,y)$ (Bret and Deutsch, 2006). Diffusion is spatially uniform and can be treated separately from the spatiotemporal growth of the filamentation instability. In the absence of a wakefield, the evolution of the beam perturbation is described by

$$\left[\partial_\tau^2 + \frac{2}{3}\frac{\sigma_{pr}^2}{m_b^2\gamma_b^2}\nabla_\perp^2\right]\delta n_{b,\mathrm{ts}} g(x,y) = 0. \tag{4.25}$$

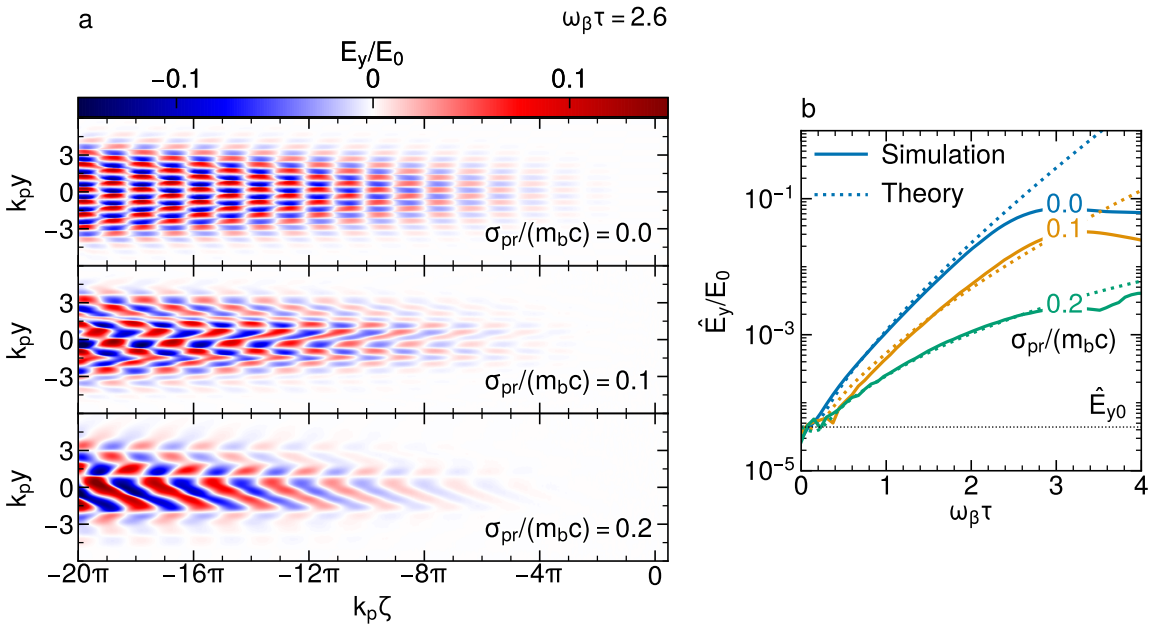

Figure 4.11: Effect of diffusion on TTS. a) The transverse electric field resulting from a cold and warm beam of increasing temperature with a transverse perturbation at $k_y/k_p = 2\pi$. b) The corresponding growth of the spectrum at the seeded wavenumber, $\hat{E}_y = |\hat{E}_y|(k_y)$, obtained from simulation and theory at $k_p\zeta = -12\pi$.

The exponential damping rate ν_d of a transverse perturbation is then

$$\delta n_b = \delta n_{b,\mathrm{ts}} \exp\left(-\nu_d \tau\right), \quad \nu_d = \sqrt{\frac{2}{3}} \frac{\sigma_{pr} k_r}{\gamma_b m_b}. \tag{4.26}$$

The total growth rate is, therefore, the sum of the growth rate from two-stream instabilities with the damping rate from diffusion, expressed by

$$\Gamma_{\mathrm{tot}} = |\delta n_b / \delta n_{b0}| = \Gamma_{\mathrm{ts}} \exp\left(-\nu_d \tau\right) \tag{4.27}$$

The effect of temperature can only be considered as purely diffusive for $\sigma_{pr}/(m_b c) < [3/2^{10/3}(n_b/n_p)^{1/3}\gamma_b^{1/3}(1+\gamma_b^{-2})^{2/3}/(1+\gamma_b^{-1})^2]^{1/2}$ (Bret, Gremillet, and Bénisti, 2010). This corresponds to $\sigma_{pr}/(m_b c) < 0.2$ for the beam parameters in Figure 4.1.

The influence of diffusion on the filamentation instability is examined for beams with different temperatures. Since diffusion has a larger effect at higher wavenumbers, the parameters are as for the beam in Figure 4.6 but with a transverse modulation at $k_y/k_p = 2\pi$. The excited electric field is shown in Figure 4.11a) at $2.6/\omega_\beta$. The field is lower compared to Figure 4.6b) due to the difference in wavenumber, agreeing with $\hat{E}_y \sim k_y/(k_p^2 + k_y^2)$ from Equation (4.10). For the cold beam, the seeded wavenumber continues to dominate along the length of the beam.

For warm beams, the phase fronts deviate from the case of the cold beam. The field reduces with temperature close to the beam head since the filamentation instability grows along the beam while diffusion is spatially uniform. The transverse modulation shifts from the

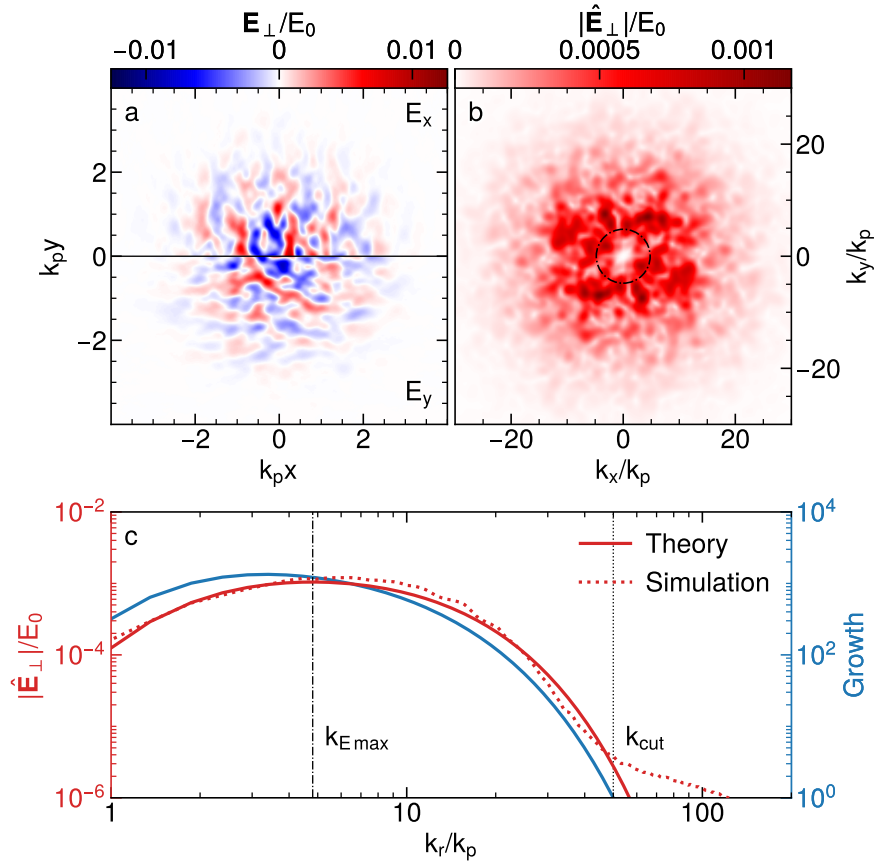

Figure 4.12: Transverse spectrum of the electric field driven by a filamented beam. a) The transverse electric fields are shown as a transverse slice at $\omega_\beta \tau = 2.6$, $k_p\zeta = -12\pi$. b) The corresponding 2D power spectrum, and c) the 1D power spectrum $|\hat{\boldsymbol{E}}_\perp|(k_r)$, showing the results from simulation and theory, as well as the theoretical growth Γ. The dotted and dash-dotted lines indicate the theoretical value for the wavevector of maximum electric field amplitude $k_{E_{\max}}$, and the cut-off wavenumber k_{cut}.

seeded wavenumber, a change that becomes evident further away from the beam head. The growth of the field spectrum along the plasma length from simulation and theory, shown in Figure 4.11b), reveals that damping of the seeded wavenumber increases with the beam temperature. The observation agrees with the analytic description for the effect of diffusion on the growth in Equation (4.27).

The development of filaments with wavenumbers lower than the seeded wavenumber indicates a higher growth rate for larger-scale filaments, such that the whole spectrum of the instability has to be considered. In order to investigate the variation of the filamentation wavenumber, the electric fields corresponding to the transverse slice at $k_p\zeta = -12\pi$ in Figure 4.1 are shown in Figure 4.12a). The transverse component E_y is predominantly modulated along y, and E_x is predominantly modulated along x. However, transverse modulations occur with a broad range of spatial scales and orientations in the transverse plane.

For unseeded beams, the instability grows from fluctuations in the beam due to the finite

temperature, and the resulting electric field is a superposition of all growing transverse modulations. The respective contributions of the wavenumbers can be separated by a Fourier transform. Taking the two-dimensional Fourier transform of the transverse electric field components and plotting the absolute amplitude, i.e. $|\hat{\boldsymbol{E}}_\perp| = |\hat{E}_y| + |\hat{E}_x|$, in Figure 4.12b) reveals a wide range of growing transverse wavenumbers. The spectrum is azimuthally symmetric, showing that growing transverse modulations have no preferred orientation in the transverse plane. The radial symmetry is in agreement with the spectral factor in Equation (4.18), $\eta_1 \to k_r^2/(k_p^2+k_r^2)$, which predicts that the growth rate of the filamentation instability only depends on the absolute value of the transverse wavevector. Thus, the filamentation in transverse planes is coupled, and the transverse modulations in each plane cannot be treated independently.

Averaging the spectrum of the electric field in Figure 4.12b) over all orientations, $(k_x,k_y) \to k_r$, gives the radial spectrum in Figure 4.12c). The spectrum of the electric field grows with transverse wavenumbers up to $k_r/k_p \sim 5$ due to the higher growth rate of the filamentation instability and reduces for higher wavenumbers due to diffusion. The comparison to theory requires an analytic description of the fields at $\tau = 0$, which act to seed the instability. These seed fields are found from simulation to scale as $|\hat{\boldsymbol{E}}_{\perp 0}| \sim (k_r\sigma_{pr}^3)^{1/2}$, with the absolute value determined by the simulation. The wakefield after propagation is the product of the seed spectrum with the theoretical growth spectrum, $|\hat{\boldsymbol{E}}_\perp| = |\hat{\boldsymbol{E}}_{\perp 0}(k_r)|\Gamma_{\mathrm{tot}}(k_r)$, which shows an excellent agreement to the simulation.

The spectrum of the growth exhibits a transverse wavenumber of maximum growth $k_{\Gamma_{\max}}(\tau,\zeta)$ and cut-off wavenumber $k_{\mathrm{cut}}(\tau,\zeta)$ above which the instability is suppressed. In the asymptotic approximation for relativistic beams, the wavenumber of maximum growth can be found by solving $[\mathrm{d}/\,\mathrm{d}k_r]\exp\left[N_\infty(k_r) - \nu_d(k_r)\tau\right]/[4\pi N_\infty(k_r)]^{1/2} = 0$ for $k_r = k_{\Gamma_{\max}}$ and the cut-off wavenumber can be found by solving $\exp\left[N_\infty(k_r) - \nu_d(k_r)\tau\right]/[4\pi N_\infty(k_r)]^{1/2} = 0$ for $k_r = k_{\mathrm{cut}}$, which can expressed by

$$\begin{aligned} 2N_\infty(k_{\Gamma_{\max}}) &= 3(1+k_{\Gamma_{\max}}^2)\nu_d(k_{\Gamma_{\max}})\tau + 1 \\ N_\infty(k_{\mathrm{cut}}) &= \nu_d(k_{\mathrm{cut}})\tau + \ln\sqrt{4\pi N_\infty(k_{\mathrm{cut}})}. \end{aligned} \tag{4.28}$$

The wavenumber of maximum growth scales as $k_{\Gamma_{\max}} \sim \sigma_{pr}^{-1/3}$ and the cut-off wavenumber scales as $k_{\mathrm{cut}} \sim \sigma_{pr}^{-1}$. The cut-off frequency for unbounded systems simplifies to $k_{\mathrm{cut}} \sim (n_b/n_p)^{1/2}u_b/\sigma_{pr}$, and remains a constant over the beam and plasma length (Bret, Gremillet, and Bénisti, 2010). Since the two-stream instability is spatiotemporal, while diffusion is spatially uniform, the characteristic wavenumbers for bounded systems depend on the propagation time in plasma and position within the beam. For the scaling of the seed field, the wavenumber of maximum spectral value $k_{E_{\max}}(\tau,\zeta)$ is obtained from

$$1 + 3k_{E_{\max}}^2 + 4N_\infty(k_{E_{\max}}) = 6(1+k_{E_{\max}}^2)\nu_d(k_{E_{\max}})\tau. \tag{4.29}$$

The predicted wavenumber at which the electric field is maximum, $k_{E\max} \approx 4.9$, from Equation (4.29) aligns well with the simulation data. The electric field above the calculated cut-off wavenumber, $k_r/k_p \gtrsim 50$, is attributed to numerical noise.

The whole scope of the introduced theory is compared to two- and three-dimensional simulations of unseeded warm beams with different temperatures in Figure 4.13. Other parameters are as for the beam in Figure 4.1. The growth spectrum from simulations is obtained by

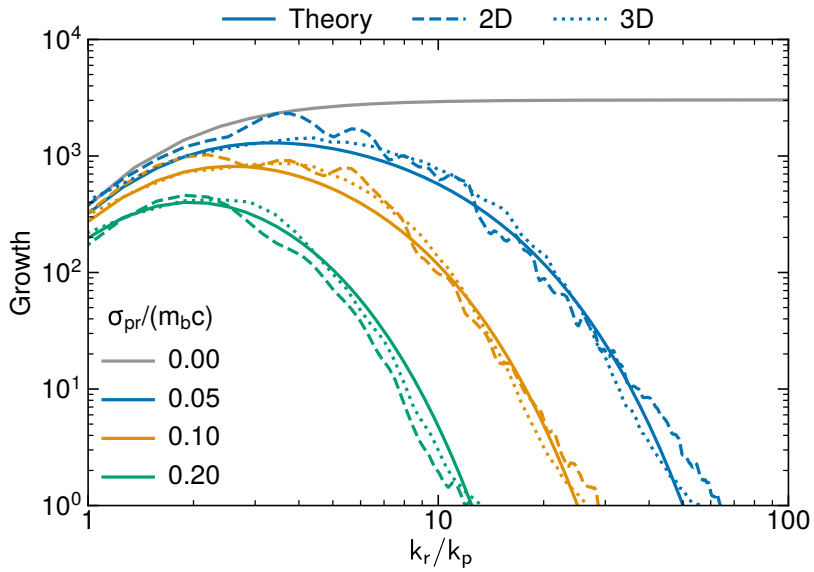

Figure 4.13: The spectral growth dependency on the beam temperature. The theoretical growth for different beam temperatures (solid lines) at $k_p\zeta = -12\pi$ and $\omega_\beta\tau = 2.6$, compared to two-dimensional electromagnetic (dashed lines) and three-dimensional quasistatic (dotted lines) PIC simulations.

taking the ratio between the electric field spectrum after propagation with the scaling of the seed field. This ratio is fitted to the growth spectrum from theory for two- and three-dimensional simulations, respectively. Slight variations in the field spectrum occur when the filamentation instability grows from random fluctuations in the beam. Thus, the growth spectrum is averaged over five two-dimensional runs and three three-dimensional runs for each temperature and compared to the analytic expression for the total growth in Equation (4.27).

Agreement is found for the dependency of the growth spectrum on the temperature for both two- and three-dimensional simulations. The alignment is better in three dimensions since the total number of beam particles is an order of magnitude higher. For cold beams, theory predicts that the growth increases with wavenumber due to the filamentation instability. For warm beams, the growth increases with wavenumber up to $k_{\Gamma_{\max}}$ and then decreases as the influence of diffusion becomes stronger. With higher temperatures, the growth is lower for all wavenumbers and the wavenumber of maximum growth and cut-off wavenumber shift to lower values in good agreement with the predicted values from evaluating Equation (4.28). Thus, transverse modulations in the beam occur at larger scales. The distance between filaments is inversely related to $k_{E_{\max}}$. However, this means that the in-plane distance is higher in three-dimensional simulations with $k_x \sim k_y \sim k_{E_{\max}}/\sqrt{2}$, compared to the distance in two-dimensional simulations with $k_y \sim k_{E_{\max}}$.

A further agreement on the dependency of the growth spectrum is found along the length of the beam, shown in Figure 4.14. Not only does the growth increase along the length of the beam given by the spatiotemporal growth from the two-stream instability, but the dominant wavenumber $k_{\Gamma\max}$ and cut-off wavenumber k_{cut} shift to larger values in agreement to evaluating Equation (4.28). This is in contrast to an unbounded system, where the

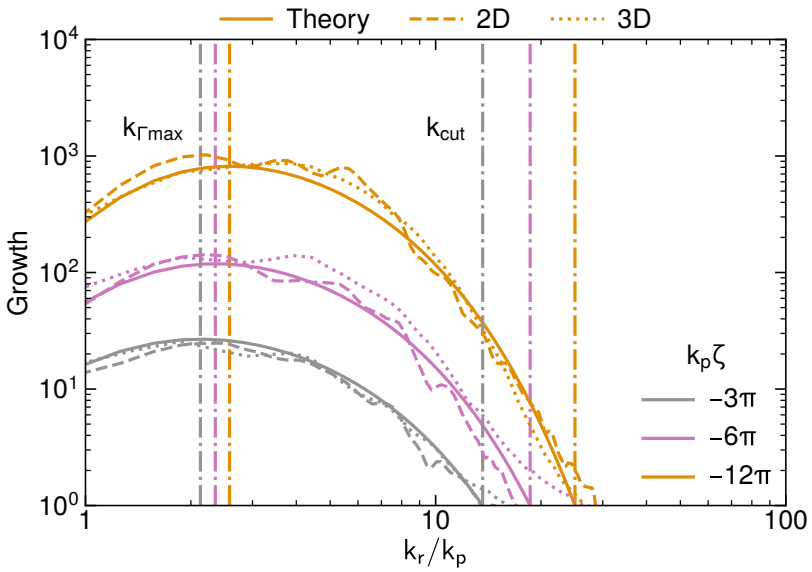

Figure 4.14: The spectral growth along the beam. The spectrum from theory for $\omega_\beta \tau = 2.6$ and $\sigma_{pr}/(m_b c) = 0.1$ (solid lines), compared to two-dimensional electromagnetic (dashed lines) and three-dimensional quasistatic (dotted lines) PIC simulations. The theoretical dominant and cut-off wavenumber are given by dash-dotted lines. The orange line is identical to the orange line in Figure 4.13.

spectrum of the growth rate remains spatially uniform and constant along the propagation time in plasma.

The analytic expression accurately predicts the dependency of the growth from the wakefield-driven filamentation instability and the damping from diffusion. The theory also verifies that the growth of the filamentation instability can be effectively modelled in two dimensions at a lower in-plane wavenumber without losing generality.

4.4 Experimental Observation of the Filamentation Instability

In initial experimental studies with proton beams from the SPS, introduced in Section 1.2.1, the filamentation was studied with the Rubidium plasma from the Run 1 setup. The 400 GeV proton beam with 0.7×10^{11} to 3×10^{11} particles has a profile well approximated by a Gaussian in transverse and longitudinal directions. The beam rms width is variably set between 0.2 to 0.5 mm and rms lengths between 5 to 12 cm at the waist. In this run, the highest plasma density $n_p = 7.3 \times 10^{14}\,\mathrm{cm}^3$ and a beam width of $\sigma_r = 0.46\,\mathrm{mm} = 2.4/k_p$ at the plasma entrance was chosen. Due to the expansion volumes, utilised for the rapid density decrease at the plasma entrance and exit, the OTR screen was placed 3.5 m behind the plasma exit.

However, simulation results for these beam parameters show that visible filaments of the longitudinally projected beam at the plasma exit (Figure 4.15a) are not evident after the beam propagated for an additional 3.5 m in vacuum (Figure 4.15b). Filaments with a small

rms size diverge due to the emittance increase from the filamentation instability, discussed in Section 4.5.1. Thus, transverse modulations smear out in a vacuum, and only a resemblance is observable in the longitudinal projection at 3.5 m in good agreement with the experimental observation shown in Figure 4.15c).

In the DPS studies for the future plans on staged acceleration over hundreds of meters, another screen was placed at a distance of $\sim 0.3\,\mathrm{m}$ behind the plasma exit since no expansion volumes were necessary. Filled with Xenon gas, the DPS could operate at a higher densities up to $n_p = 9.38 \times 10^{14}\,\mathrm{cm}^3$. This gave the unique opportunity at the AWAKE experiment to study the onset of the filamentation instability by varying the plasma density (Verra, Amoedo, *et al.*, 2024). The proton beam had a total charge of 43 nC, an rms length of $\sigma_\zeta/c = 163\,\mathrm{ps}$, an rms width of $\sigma_r = 0.5\,\mathrm{mm}$ and a normalised emittance of 2.5 mm mrad. The plasma length was $c\tau = 10\,\mathrm{m}$.

The experimental observations of the beam filamentation are shown for the close screen in Figure 4.16a), obtained from Verra, Amoedo, *et al.* (2024). At a plasma density of $n_p = 9.38 \times 10^{14}\,\mathrm{cm}^{-3}$ and beam width of $\sigma_r = 0.5\,\mathrm{mm} = 2.9/k_p$, the beam filamentation is evident and consistently observed throughout all datasets, while the transverse envelope of the beam remains bi-Gaussian. The distance between the two filaments indicated by the red line was measured to $\lambda_f = 0.27\,\mathrm{mm}$. Taking the average distance between all filaments of this dataset yields $\lambda_f = 0.33(\pm 0.06)\,\mathrm{mm}$.

Next to the longitudinal projected images, the beam is projected along one transverse direction within the slit of the streak camera (see Section 1.2.1). The time-resolved images, shown in Figure 4.16b), observe the evolution of the instability along the beam length at the screen 3.5 m behind the plasma exit. Multiple filaments were observed at the beam tail, confirming the spatiotemporal growth of the instability in the experiment. No longitudinal modulation in the beam density, predicted from the electrostatic plasma response for TTS, is observed for all measurements.

In roughly half of the dataset at a plasma density of $n_p = 2.25 \times 10^{14}\,\mathrm{cm}^{-3}$ ($k_p\sigma_r = 1.5$), the signature for SMI was observed, given by a single on-axis filament in the longitudinal projection (Figure 4.17a) and a train of microbunches in the time-resolved image (Figure 4.17b).

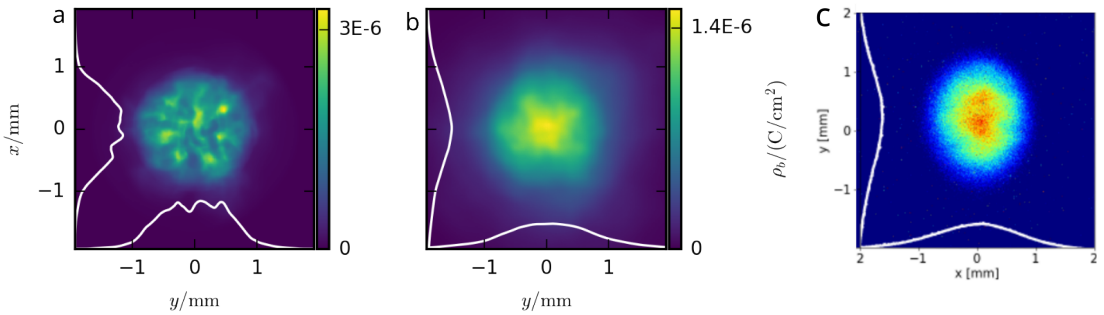

Figure 4.15: Beam projection from simulation and experiment after a long proton beam propagated 10 m in plasma with $n_p = 7 \times 10^{14}\,\mathrm{cm}^{-3}$. The beam from simulation is projected a) at the plasma exit and b) 3.5 m after the plasma exit. c) The beam projection at the screen positioned 3.5 m behind the plasma exit in the experiment, provided by L. Verra, P. Muggli *et al.* (AWAKE collaboration).

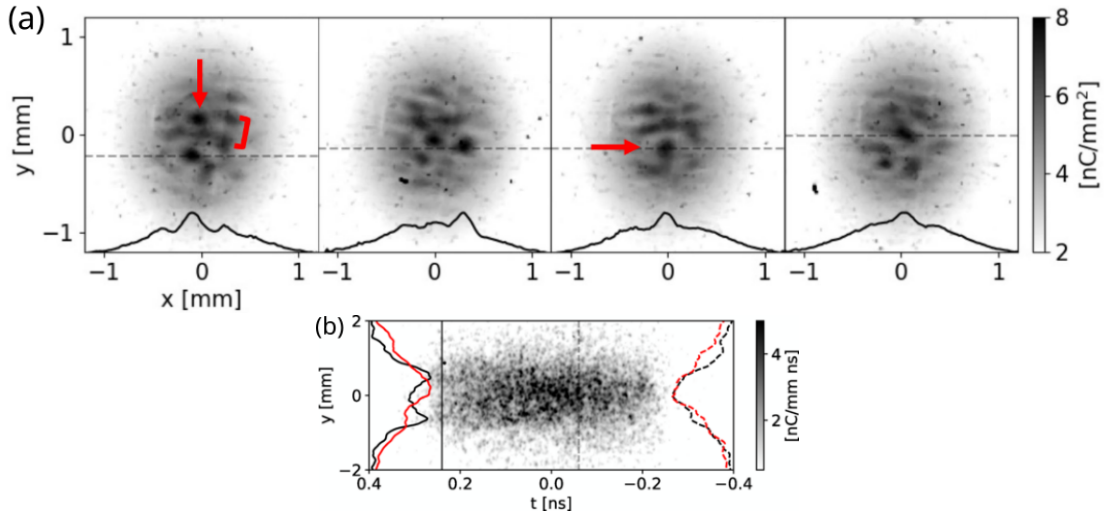

Figure 4.16: Observation of filamentation at the AWAKE experiment with the plasma density at $n_p = 9.38 \times 10^{14}\,\mathrm{cm}^{-3}$. a) The projection and b) the time-resolved image taken of the beam at the screens placed 0.3 m and 3.5 m behind the plasma exit, respectively. The colour scale is saturated to enhance the transverse modulation. Obtained from Verra, Amoedo, *et al.* (2024).

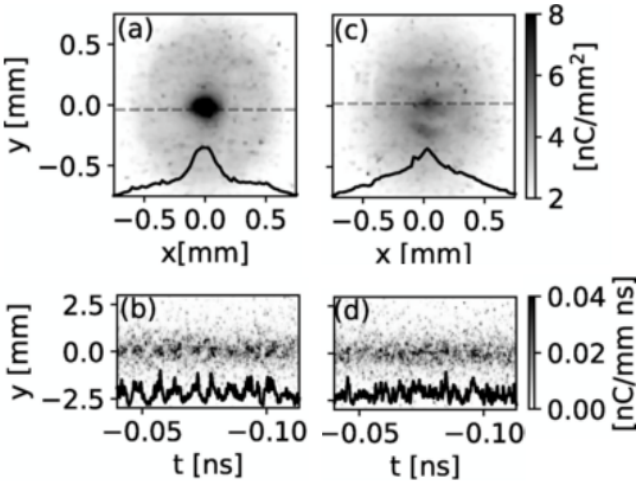

Figure 4.17: Threshold of the beam undergoing TTS or SMI. The measured a) projection and b) time-resolved image of the self-modulated beam, and measured c) projected and d) time-resolved image of a filamented beam at a plasma density of $n_p = 2.25 \times 10^{14}\,\mathrm{cm}^{-3}$. Obtained from Verra, Amoedo, *et al.* (2024).

In the other half, represented by Figure 4.17c) and d), two filaments are observed with no longitudinal modulation. This suggests the threshold for the plasma density and the corresponding beam width for the filamentation instability to occur. No filaments are observed at lower plasma densities.

The onset of filamentation by varying the plasma density was further studied in experiments with electron beams by Allen *et al.* (2012). The 0.06 GeV electron beam had a total charge of 1 nC, an rms length of $\sigma_\zeta/c = 5\,\mathrm{ps}$, an rms width of $\sigma_r = 0.065\,\mathrm{mm}$ and a normalised emittance of 6 mm mrad; the plasma length was $c\tau = 0.02\,\mathrm{m}$. At a plasma density of $n_p = 12 \times 10^{16}\,\mathrm{cm}^{-3}$, beam filamentation was observed with a distance of $\lambda_f = 0.042\,\mathrm{mm}$, although the transverse beam envelope observed in the experiment was significantly modified through its interaction with the plasma and no longer resembles a Gaussian ellipsoid. For

$n_p = 1.6 \times 10^{16}\,\mathrm{cm}^{-3}$, no filamentation was observed. The threshold for the filamentation instability to occur was found to be $\sigma_r = 2.2/k_p$ for the beam width, which corresponds to a plasma density of $3.4 \times 10^{16}\,\mathrm{cm}^{-3}$.

4.4.1 Analytic Extension to Laboratory-Relevant Beam Profiles

Laboratory-relevant beams commonly contain a longitudinally varying beam density. The perturbation growth along the beam length is proportional to the wakefield, which is the integral over the beam length. With the relation expressed in Equation (4.12), the exponent given in Equation (4.17) is extended to account for the arbitrary longitudinal beam profile

$$\frac{\delta\bar{n}_b}{\delta n_{b0}} = \frac{\Theta(\zeta)}{k_\tau}\prod_\zeta \exp\left[\frac{i\eta_u\tilde{g}(x,y)\omega_\beta^2 k_e\tilde{f}(\zeta)|\Delta\zeta|}{k_\tau^2}\right] \to \frac{\Theta(\zeta)}{k_\tau}\exp\left[\frac{i\eta_u\tilde{g}(x,y)\omega_\beta^2 k_e|\int_{\zeta_0}^{\zeta}\tilde{f}(\zeta')\,\mathrm{d}\zeta'|}{k_\tau^2}\right], \tag{4.30}$$

where ζ_0 is the seed position, e.g. due to a ionising laser front. The two-stream growth in the exact Equation (4.18) and asymptotic limit Equation (4.20) reformulates to

$$\Gamma_{\mathrm{ts}} = \frac{|\delta n_{b,\mathrm{ts}}|}{\delta n_{b0}} = \left|\sum_{l=0}^{\infty}\frac{\left[i\eta_u\tilde{g}(x,y)\omega_\beta^2\tau^2 k_e|\int_{\zeta_0}^{\zeta}\tilde{f}(\zeta')\,\mathrm{d}\zeta'|\right]^l}{l!(2l)!}\right| \tag{4.31}$$

$$\approx \frac{1}{\sqrt{4\pi}}\frac{\exp N_\infty}{\sqrt{N_\infty}},\quad N_\infty = \frac{3^{3/2}}{2^{5/3}}\left[\eta_u\tilde{g}(x,y)\omega_\beta^2\tau^2 k_e\left|\int_{\zeta_0}^{\zeta}\tilde{f}(\zeta')\,\mathrm{d}\zeta'\right|\right]^{1/3}. \tag{4.32}$$

The evolution of a beam with a smooth longitudinal profile and the corresponding electric field are shown in Figure 4.18a) and b). Beam parameters are as of Figure 4.6, but with the longitudinal profile reflecting a Cosine-squared function (see Equation (3.15)) with an rms length of $k_p\sigma_\zeta = 30$ and the beam head truncated at $\zeta = 2\sigma_\zeta$. The modulation in the charge density of the beam and the electric field are comparable to the plasma response to the beam in Figure 4.6, although the magnitude of the electric field is the integrated beam density along the beam length. Beam slices with lower density are fully modulated at a lower absolute amplitude of the perturbation, and the electric field from simulation deviates from theory.

Given by the analytic expression for the growth in Equation (4.31), the growth along the beam is proportional to the integrated charge density, $N_\infty \sim [\int n_b(\zeta')\,\mathrm{d}\zeta']^{1/3}$. The semi-analytic solution of Equation (4.31) is in good agreement with the envelope growth of the electric field from simulation up to a propagation time in plasma of $\sim 3/\omega_\beta$, shown in Figure 4.18c) and d). The seed value agrees well with the analytic expression for the Fourier spectrum times the value of the longitudinal beam profile at the truncation, $\hat{E}_{y0}\tilde{f}(\zeta_0)$.

Before saturation, the introduced theory on wakefield-driven beam modulation applies to an arbitrary beam envelope, $\tilde{f}(\zeta)\tilde{g}(x,y)$. The analytic expressions lose their validity at a given transverse point or downstream from a given longitudinal point at which the beam is fully modulated, $\rho_b \gtrsim q_b n_b$. Especially for beams with a low-density tail, this quickly limits the theory to the interval between the beam head and the beam centre.

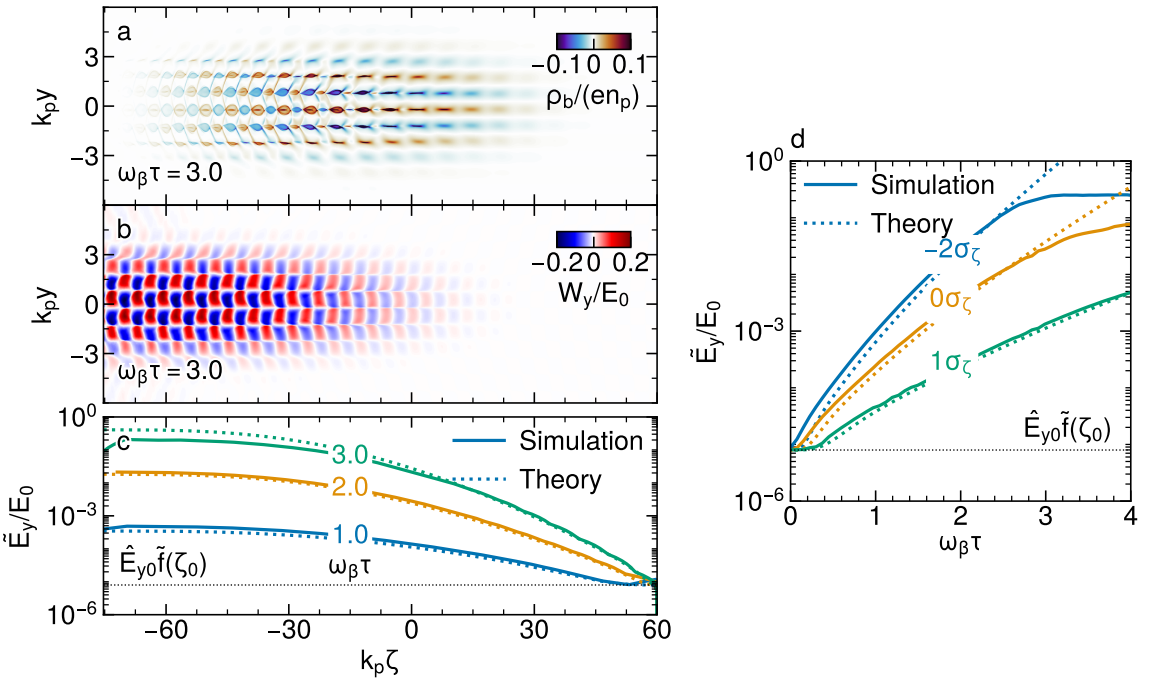

Figure 4.18: The evolution of a beam with longitudinal Cosine-squared profile, truncated at $\zeta/\sigma_\zeta = 2$. The snapshot in a) shows the beam charge density and in b) the electric field. The envelope growth of the electric field is shown along the length of c) the beam and d) the plasma.

4.4.2 Application of the Theory to Experimental Results

The experimental observation of beam filamentation enables the comparison to three-dimensional simulations and the introduced theory with the beam and plasma parameters chosen accordingly to the run for a deeper understanding of the dominating instability. For the simulation, the plasma density is set to $n_p = 7 \times 10^{14}\,\mathrm{cm}^{-3}$ and for the beam the rms length is set to $k_p\sigma_\zeta = 246$ and the rms width is set to $k_p\sigma_r = 2.3$, which gives a beam peak density of $n_b = 0.0026\,n_p$. With a normalised emittance of $\epsilon_n = 2.2\,\mu$m, the momentum spread equals $\sigma_{pr}/(m_b c) = 0.005$. For the numerical parameters, the grid size is set to $k_p\Delta(x, y, \zeta) = (0.02, 0.02, 0.1)$, and the propagation step is $k_p z = 400$. The beam is represented by $\sim 12.3 \times 10^9$ macroparticles, where each numerical particle resembles 24.4 physical particles. Plasma electrons are represented by 9 particles per cell. To avoid a truncated beam head due to the simulation window, the longitudinal profile of the beam resembles the Cosine-squared function (see Equation (3.15)).

The filamentation of the long proton beam after a propagation distance of 6.4 m in plasma is shown in Figure 4.19. The longitudinal and transverse slices show the spatiotemporal growth of the filamentation instability. In addition to transverse modulations, shown in Figure 4.19a), the beam contains a longitudinal modulations at $k_\zeta = k_p$ at varying phases due to the plasma wake. Small wakefields seeded at random phases due to the transverse temperature in the beam compete with the wakefield seeded by the beam shape, e.g. the truncated beam head. These small seeds result in a random phase shift of the dominat-

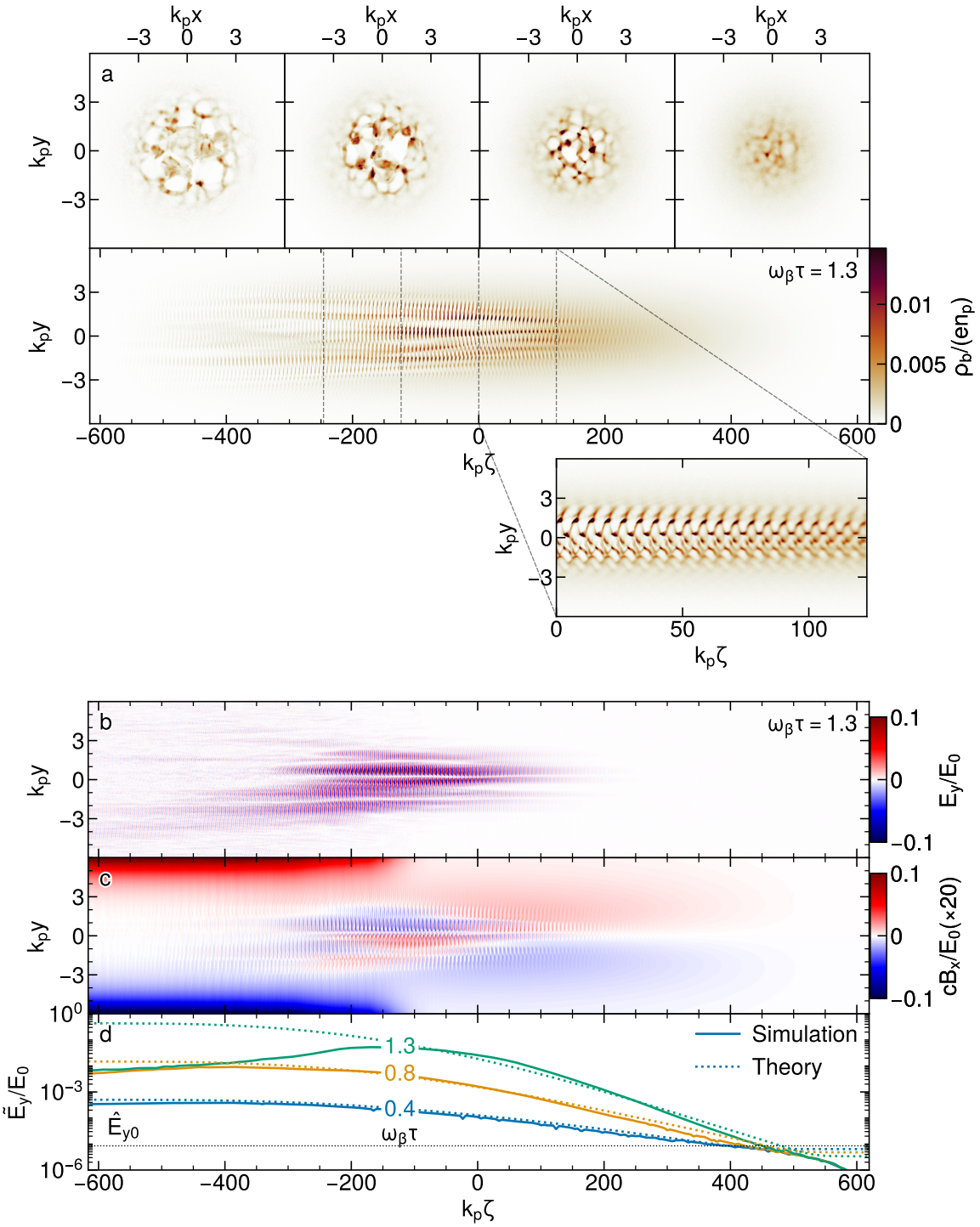

Figure 4.19: Wakefield-driven filamentation of the proton beam after a propagation time of $\tau = 1.3/\omega_\beta = 6.4\,\mathrm{m}/c$ in plasma at $n_p = 7 \times 10^{14}\,\mathrm{cm}^{-3}$. a) The transverse and longitudinal slice taken of the beam charge density. The dash-dotted lines indicate the position of the transverse slices. The b) electric field and c) magnetic field (increased by a factor of 20) excited by the beam. d) The simulated growth and theory of the electric field envelope along the length of the beam at different propagation times.

ing wakefield relative to the cold beam case, shown in Figure 4.11a). The occurrence of longitudinally-modulated filaments cannot be concluded in the experiment since the phase differences are averaged over by the finite resolution of the streak camera.

Due to the high inertia of the beam particles, the instability grows over several hundreds of plasma skin depths. Towards the beam tail, the beam is fully modulated and diverges. This divergence will be discussed for the longitudinal flat-top beam from Figure 4.6 in Section 4.5.1. A lower seed in the experiment would be consistent with the observation of the onset of the filamentation at the beam tail, while in the simulation, the beam tail is fully modulated. The beam is considerably coarser in the simulation with 12.3×10^9 macroparticles relative to $\sim 3 \times 10^{11}$ beam particles in the experiment.

The corresponding electric and magnetic fields are shown in Figure 4.19c) and d), respectively. The electric field dominates the magnetic field by two orders of magnitude with an equivalent longitudinal and transverse signature as discussed in Section 4.2.2. The envelope growth of the electric field along the length of the beam in Figure 4.19e) agrees well with the semi-analytic solution to Equation (4.31), shown by the dotted lines at different propagation times. The simulation and theory show that for these beam and plasma parameters, the beam filamentation is in the wakefield-driven regime.

The expected distance between filaments, $\lambda_f = 2\pi/k_{E_{\max}}$, is shown in Figure 4.20 as a function of the spatiotemporal growth and damping from diffusion. At the back of the beam, where filamentation is strongest, the expected distance between filaments is independent of the beam length, depending instead on the total beam charge, $\omega_\beta^2 \zeta \sim \int n_b \, \mathrm{d}\zeta$, from Equation (4.31).

In experiments carried out with both proton (Verra, Amoedo, *et al.*, 2024) and electron (Allen *et al.*, 2012) beams, the onset of filamentation was studied by varying the plasma density. Taking the experimental parameters Taking the parameters of the experiment with the proton beam from Verra, Amoedo, *et al.* (2024) and varying the plasma density gives the dashed line in Figure 4.20. Point (a) corresponds to a plasma density $n_p = 9.38 \times 10^{14}\,\mathrm{cm}^{-3}$, for which filamentation was observed. The predicted distance between filaments, $\lambda_f = 2/k_p = 0.34\,\mathrm{mm}$, is comparable to the observed average distance of $0.33(\pm 0.06)\,\mathrm{mm}$. Taking the parameters of the experiment with the proton beam from Verra, Amoedo, *et al.* (2024) and varying the plasma density gives the dotted line in Figure 4.20. Point (b) corresponds to a plasma density $n_p = 12 \times 10^{16}\,\mathrm{cm}^{-3}$, for which filamentation was observed. The predicted distance between filaments, $\lambda_f = 2.7/k_p = 0.042\,\mathrm{mm}$ agrees with the observed filamentation distance.

The points (α) and (β) correspond to the cases in Verra, Amoedo, *et al.* (2024) and Allen *et al.* (2012), where the predicted distance between filaments is equal to the rms beam width and agree with the threshold of the rms width of the beam at which filamentation was observed. The plasma density of Point (c) $2.25 \times 10^{14}\,\mathrm{cm}^{-3}$, where the threshold between filamentation and SMI has been found, is close to the plasma density of $2.44 \times 10^{14}\,\mathrm{cm}^{-3}$ for point (α). The observed threshold between one and multiple electron filaments at a beam width of $\sigma_r = 2.2/k_p$ in Allen *et al.* (2012) agrees with the plasma density of $3.4 \times 10^{16}\,\mathrm{cm}^{-3}$ in (β). Point (d), with a plasma density of $1.6 \times 10^{16}\,\mathrm{cm}^{-3}$ is well below point (β), and no filamentation is observed. The distance between filaments for the instability cutoff, $2\pi/k_{\mathrm{cut}}$, corresponds to a plasma density 50–140 times lower than the observed threshold. This dependence of the instability threshold on $k_{E_{\max}}$ and not k_{cut} may be due to the competition

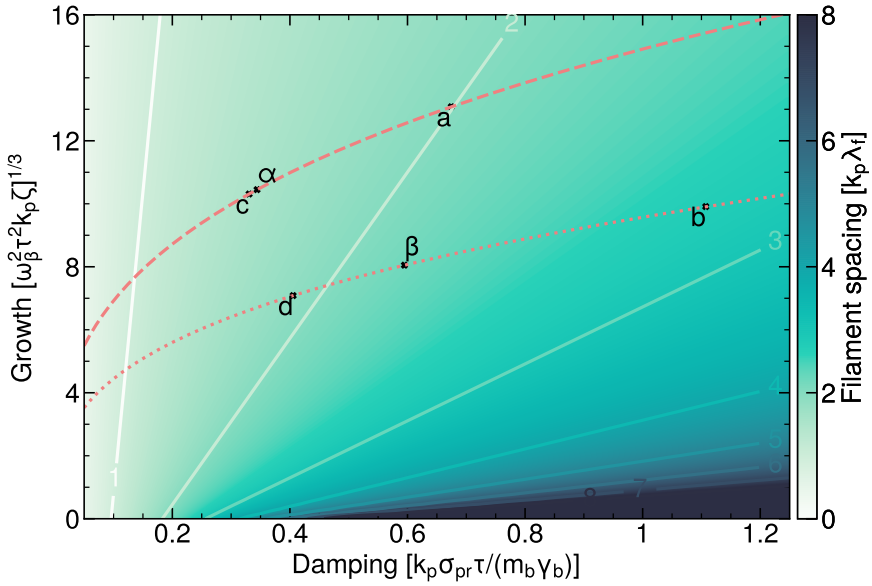

Figure 4.20: The distance between filaments as a function of beam and plasma parameters. The y and x-axis are proportional to the growth of TTS and damping due to diffusion. The dashed line corresponds to the experimental parameters in Verra, Amoedo, *et al.* (2024) for varying plasma density, while the dotted line corresponds to the experimental parameters in Allen *et al.* (2012). Points a, b, c, and d correspond to individual measurements in Verra, Amoedo, *et al.* (2024) and Allen *et al.* (2012), with α and β marking the point at which the distance between filaments is predicted to reach the rms beam width.

of the filamentation instability with SMI of the charged beams used in these experiments. Further experimental and numerical studies would allow this prediction for the instability threshold to be tested across a larger parameter space.

4.5 Considerations Beyond the Model

The theory on wakefield-driven filamentation shows excellent agreement with simulations and published experimental results, although this analytic model based on linearised equations holds limitations towards saturation or for beams of asymmetric composition discussed in this section.

4.5.1 Saturation of Two-Stream Filamentation

As discussed in Section 4.3, the applicability of Equation (4.18) reaches its limit for a fully-modulated beam, $\delta n_b \approx n_b$, or if the plasma is fully modulated, $\delta n_p \approx n_p$. The latter is equivalent to the transverse wakefield reaching the wavebreaking limit $|\boldsymbol{E}_\perp| \approx E_0$. Figure 4.21a) shows the cold beam in Figure 4.6 at a propagation time of $5/\omega_\beta$ beyond the applicability of the analytic model. The beam and the filaments diverge, which decreases

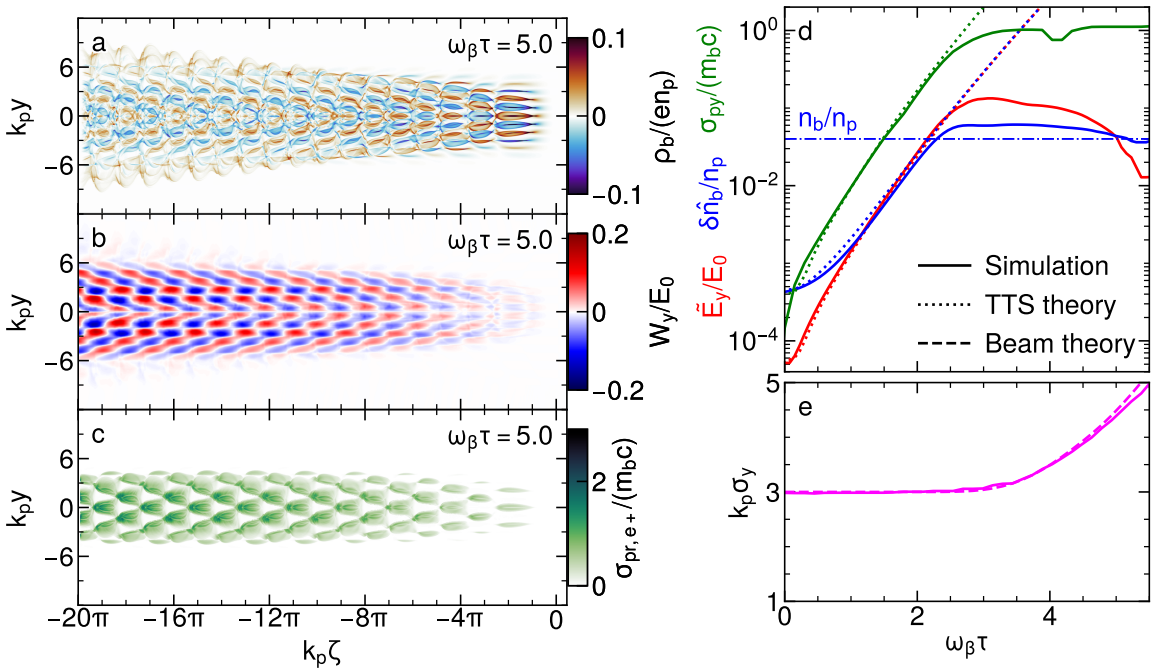

Figure 4.21: Beam divergence after saturation of TTS for the cold beam in Figure 4.6. a) The beam charge density, b) the transverse wakefield and c) the positron momentum spread shown as a snapshot at $\omega_\beta \tau = 5$. d) The envelope taken of the transverse electric field (red), beam perturbation (blue), and transverse momentum spread (green), and e) the evaluated rms width (magenta) at $k_p\zeta = -12\pi$ from simulation and theory.

the beam charge density and, therefore, the response of the plasma wake, shown in Figure 4.21b). The momentum spread in Figure 4.21c) grows with the transverse wakefield, since beam particles are accelerated at different rates along the transverse axis.

The growth of the momentum spread for the beam positrons is shown along the plasma length at $k_p\zeta = -12\pi$ alongside the beam perturbation and transverse electric field in Figure 4.21d). The momentum spread grows proportionally to the transverse wakefield, such that the filaments stay confined. With the initial value defined by $\sigma_{py,0}/(m_b c) = \delta n_{b0}/n_p$, this growth agrees well with the semi-analytic solution to TTS given in Equation (4.18). Equivalent to the transverse wakefield, the growth of the momentum spread deviates from the analytic prediction when the beam is fully modulated, $\delta n_b \approx n_b$. The analytic model allows higher values for the beam perturbation, $\delta n_b > n_b$, which is physically impossible. As the transverse wakefield does not increase further, the beam particles detrap, and the filaments diverge under the influence of the high momentum spread. Consequently, the wakefield amplitude weakens with the beam perturbation and the beam width increases, shown in Figure 4.21e). The increase of the beam width from the initial value $\sigma_{y0} = 3/k_p$ is in good agreement with the semi-analytic solution to $\partial_\tau^2 \sigma_y = u_b^2 \sigma_{py}^2(\zeta, \tau)/(\sigma_y \gamma_b^2 m_b^2 c^2)$, obtained from Equation (2.25) by neglecting the wakefield term.

4.5.2 Sequential Filamentation of Asymmetric Beam Compositions

The analytic model, given by Equation (4.18), assumes beam particles of equal Lorentz factor, charge magnitude and mass. But instead of an electron-positron beam, the beam can also consist of an asymmetric composition of beam species, e.g. an electron-proton beam. For these multi-species beams, the fluid equations of the beam species couple asymmetrically, with the filamentation of the different species developing at different rates (Graw *et al.*, 2022). The corresponding betatron frequency in the analytic expressions is replaced by the total betatron frequency

$$\omega_\beta = \sqrt{\sum_s \omega_{\beta s}^2} = \sqrt{\sum_s \frac{q_s^2 n_s}{2\gamma_s m_s}}, \tag{4.33}$$

with n_s the number density of the respective beam species and q_s, γ_s, m_s the charge, Lorentz factor and mass of its particles. If the betatron frequencies of both species are sufficiently different, $\omega_{\beta e-} \gg \omega_{\beta p+}$, the filamentation of the different species is separable in propagation time.

As shown in Figure 4.22a), the electron beam filaments more rapidly than the proton beam with half the growth rate of the equivalent electron-positron beam. At an extended time scale, the proton beam filaments at a significantly lower rate, shown in Figure 4.22b). When the density modulation of the proton beam becomes relevant, the electron beam has already strongly diverged for $k_e\zeta < -2\pi$, which reduces the plasma wakefield. Further, the beam is no longer quasineutral so that SMI starts to compete with TTS. The density modulation of the electron beam is amplified by the proton filamentation at the beam head.

The envelope of the electric field shows in Figure 4.22c) the two growth regimes for the

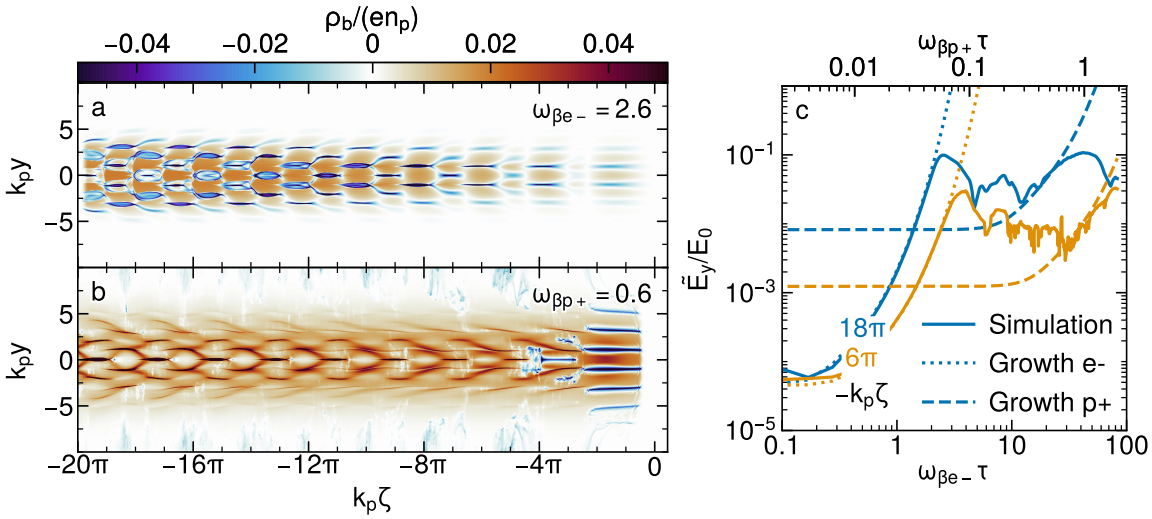

Figure 4.22: The evolution of an electron-proton beam. The beam charge density is shown during a) the electron filamentation at $\tau = 125/\omega_p = 2.6/\omega_{\beta e-}$ and b) the proton filamentation at $\tau = 1250/\omega_p = 0.6/\omega_{\beta p+}$. c) The envelope of the electric field growing along the plasma length (solid) with the semi-analytic solution given for the filamentation of the electron (dotted) and proton (dashed) beam.

respective beam species. The electric field grows quickly due to the electron filamentation and acts as the seed for the proton filamentation for later timescales, which sets the seed level for the analytic prediction of the proton filamentation accordingly. The analytic prediction for the electron beam filamentation agrees with the simulation, while the prediction for the proton beam filamentation slightly deviates. A possible extension of the theory would need to include the saturation and divergence of the beam filaments.

4.6 Transition between Modulation Instabilities

The observations from the experiments give an excellent agreement to the introduced theory on wakefield-driven filamentation referred to as TTS. Yet, the question remains in which parameter space the respective modulation instabilities are dominant and how they transition into each other.

4.6.1 Transition to Longitudinal Two-Stream

To qualitatively compare the dominant regime of the (longitudinal) two-stream and transverse two-stream instability, the spectral parameter from Equation (4.13) can be rewritten to $\eta_u = \eta_{\mathrm{TSI}} + \eta_{\mathrm{TTS}}$. The longitudinal and transverse contributions are provided by

$$\eta_{\mathrm{TSI}} = \frac{(c^2 - u_b^2)k_p^2}{c^2 k_p^2 + u_b^2 k_r^2}, \quad \eta_{\mathrm{TTS}} = \frac{u_b^2 k_r^2}{c^2 k_p^2 + u_b^2 k_r^2}, \tag{4.34}$$

and shown in Figure 4.23a) and b).

As expected, TSI is dominant for non-relativistic beams, and the longitudinal wakefield component predominantly modulates the beam. However, for transverse perturbations with a long scale $k_r/k_p < 1$, TSI remains dominant even in mildly relativistic regimes. This is a

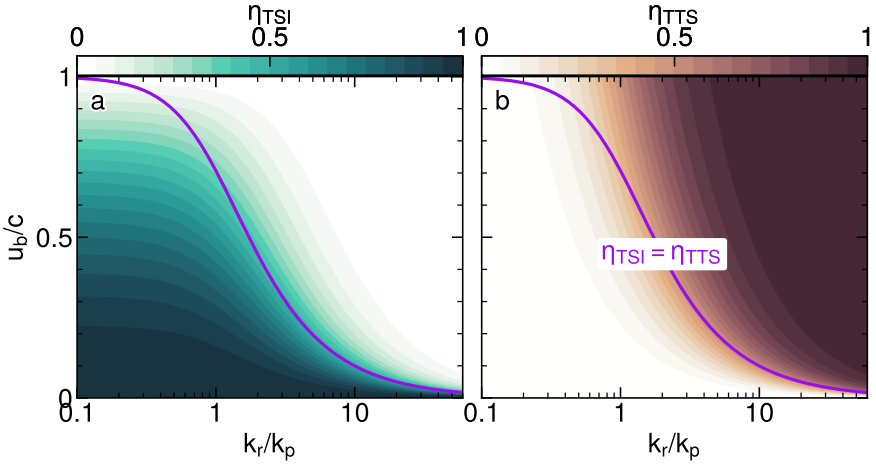

Figure 4.23: The spectral dependency η_u for a) TSI and b) TTS on beam velocity u_b and wavenumber k_r. The purple line indicates where TSI and TTS equally contribute.

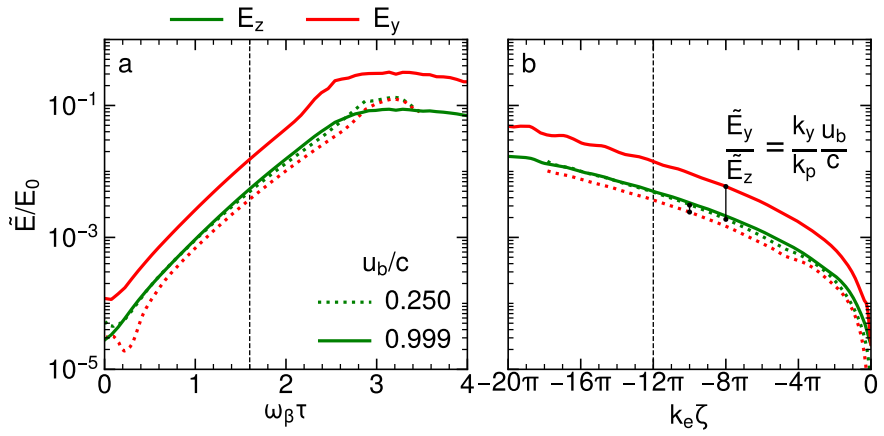

Figure 4.24: The longitudinal E_z (green) and transverse E_y (red) electric field envelope for $u_b = 0.25\,c$ and $0.999\,c$ obtained as a function of a) propagation time and b) position along the beam. The solid vertical lines indicate the theoretical ratio between the field components. The dashed lines indicate the respective slice taken.

consequence of the relative strength between the wakefield components varying as $\tilde{\boldsymbol{E}}_\perp/\tilde{E}_z = \boldsymbol{k}_r u_b/(k_p c)$ according to Equation (4.10). TTS is dominant for highly relativistic beams or high transverse wavenumbers in mildly relativistic beams, such that the transverse wakefield predominantly modulates the beam. Given a negligible energy spread of the beam, the longitudinal wavenumber of the two-stream instability uniformly equals $k_\zeta = k_e = ck_p/u_b$ for the two-stream instabilities. However, CFI, which becomes dominant for overdense beams, represents a different longitudinal wavenumber ($k_\zeta = 0$) and growth scaling as discussed in Bret, Gremillet, Bénisti, and Lefebvre (2008) and Pathak *et al.* (2015).

Figure 4.24 shows the growth of an initial perturbation $k_r/k_p = \pi$ for two different beam velocities. As can be seen, the growth scales with $\omega_\beta \tau$ and $k_e \tau$, in agreement with Equation (4.20), as the spectral parameter η_u remains roughly constant between non-relativistic and relativistic beams for $k_r/k_p \gtrsim 3$. For a constant wavenumber, the transverse wakefield is weaker than the longitudinal wakefield in the non-relativistic limit, given by the theoretical ratio.

4.6.2 Transition to Current-Driven Filamentation

The wakefield- and current-driven filamentation are addressed in Figure 4.25 for the laboratory setup in Section 4.4.2, but with the beam being quasineutral to avoid SMI and pinching. Figure 4.25a) shows the beam evolution with the resulting electromagnetic fields for the dilute beam. Equivalent to the previous sections, the wakefield term in the electric field E_y dominantly drives the beam particles, and each beam filament contains a longitudinal modulation at $k_\zeta = k_p$. The growth of the envelope of the electric field averaged within $|y| < \sigma_r$ (Figure 4.25d) agrees with the analytic solution for TTS, given by Equation (4.31).

The dense beam, shown in Figure 4.25e), also exhibits both transverse and longitudinal modulation at the beam head, and the electric field (Figure 4.25f) dominates. But the response differs towards the beam centre when the magnetic field (Figure 4.25g) surpasses

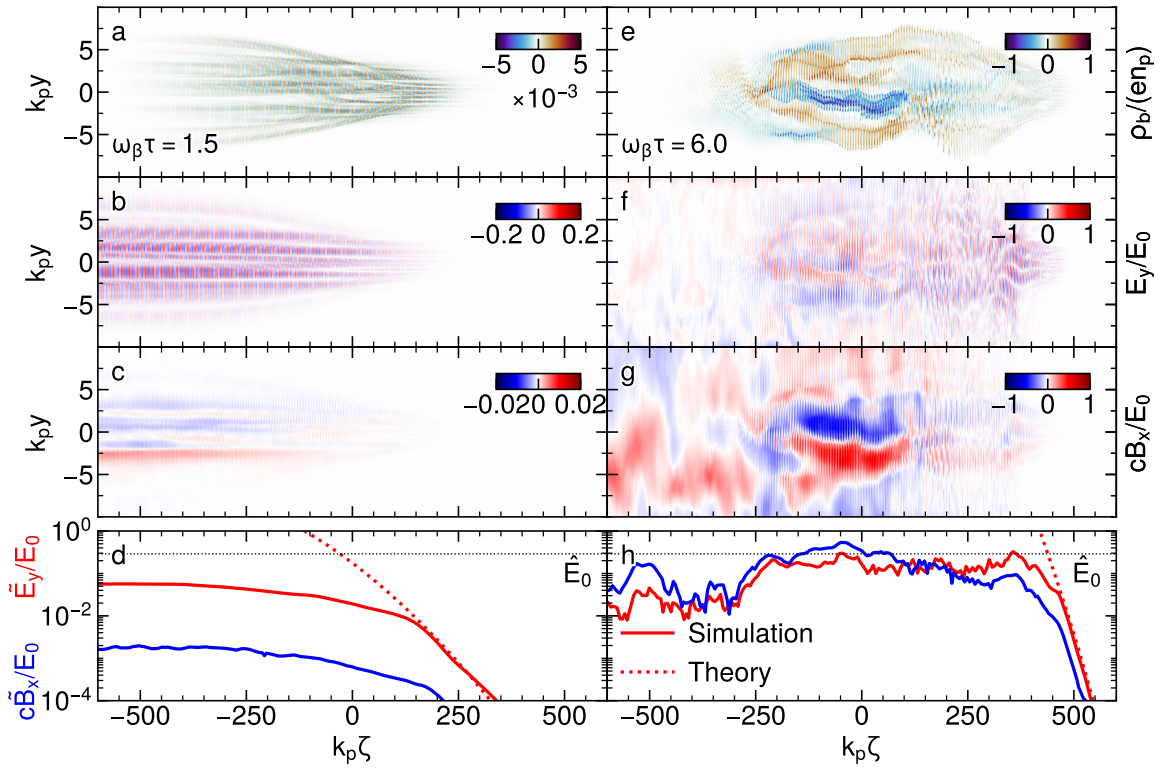

Figure 4.25: Filamentations of a dilute, experiment-like ($n_b/n_p = 0.0026$) and a dense ($n_b/n_p = 0.52$) positron-electron beam. Given for the dilute beam, its a) charge density, and the b) electric field and c) magnetic field (different scale) excited by the beam from simulation, with d) their envelope averaged within $\pm k_p\sigma_r$ (solid) from simulation and theory. The respective quantities for the dense beam are given in e-h).

the electric field. Beam particles bunch together into filaments in which the longitudinal modulation is weaker. The electric field saturates as the plasma is fully modulated, which is equivalent to the wavebreaking number reducing with the transverse wavenumber by $E_0 \sim k_y/(k_p^2 + k_y^2)$. While TTS saturates at the beam head, the magnetic field continues to grow along the length of the beam at a much lower rate and saturates at the beam centre. The transition of different growth rates along the length of the beam indicates that the beam front filaments due to the significantly higher growth of TTS. Further along the beam, TTS sets the initial condition for a second phase of exponential growth from CFI at a considerably lower rate.

The growth of wakefield-driven filamentation can be compared analytically to the growth of CFI. However, CFI exhibits spatiotemporal growth only at the beam head in the mildly relativistic regime (Pathak *et al.*, 2015). For cold streams, the growth ratio between Equation (4.20) and Equation (4.1) is $N_\infty/(\nu_{\text{cfi}}\tau) = (3^{3/2}/2^{5/3})[k_e\zeta/(\eta_1^{1/2}\omega_\beta\tau)]^{1/3}$. Setting the length to the rms length of the beam, $\zeta \to \sigma_\zeta$, and the propagation time from Figure 4.25, gives a ratio of 9.0 for the dilute beam, and TTS dominates over CFI. For the dense beam in Figure 4.25e), the theoretical growth ratio reduces to 5.6, and TTS remains dominant.

As wakefield-driven filaments are modulated at $k_\zeta = k_e$, while current-driven filaments

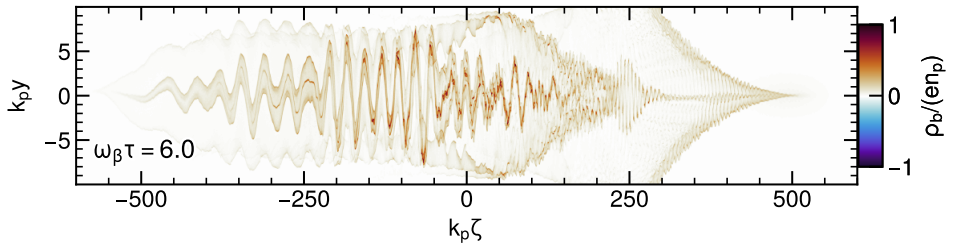

Figure 4.26: Pinching and hosing of a dense single-species beam with parameters from Figure 4.25.

contain no longitudinal modulation ($k_\zeta = 0$), they can grow in parallel (Bret, Gremillet, and Bénisti, 2010). The product of the respective initial seed times the growth, which then determines whether the evolution of the beam is dominated by the wakefield or the magnetic field. Thus, the wakefield may couple with the longitudinal mode of a truncated dense beam, such that TTS remains dominant in a parameter space in which CFI would dominate for unbounded systems. While CFI only dominates for beam densities comparable to the plasma density, TTS remains dominant at the beam head for a smooth longitudinal profile and sets the initial condition for CFI at the beam centre.

The fully-electromagnetic simulations in Figure 4.25 are conducted in two-dimensional geometry. The theory on TTS in Section 4.3 showed in agreement with simulations that the growth is commensurate in two and three dimensions. numerical studies by Takamoto *et al.* (2018) as well as the benchmark studies in Section 3.2 showed similar agreement for the exponential growth of CFI. The spatial grid is set to $k_p \Delta(y, z) = (0.02, 0.08)$, the time step is $\omega_p \Delta t = 0.018$, and the beam and plasma species are represented by 72 and 36 macroparticles per cell. The beam transverse temperature is scaled by $\sqrt{m_b/m_e}$ to $\sigma_{pr} = 0.2$ to maintain an equivalent ratio between filamentation growth and damping from diffusion. To signify the characteristic differences of the wakefield-driven filamentation to CFI, a comparison is drawn to a dense beam ($n_b = n_p/2$), expected to be at the lower bound of CFI at its peak density. Other parameters are identical.

For the beam parameters presented here, the transition from wakefield- to current-driven beam filamentation can be reached by scaling the beam density up by two orders of magnitude. This is feasible for quasineutral beams for which SMI is suppressed. A relativistic charged beam pinches and undergoes hosing before any transverse modulation is observable due to its transverse extent, as shown in Figure 4.26.

The analytic model for wakefield-driven filamentation of warm beams, introduced in this chapter, shows in excellent agreement with particle-in-cell simulations the spatiotemporal growth for arbitrary beam profiles and the spatial dependency of the dominant and cut-off wavenumber. The robustness of the model is undermined with experimental observations in which filamentation appears to be suppressed when the predicted distance between filaments is larger than the rms beam width for single-species beams. Although this section is beyond the applicability of this model, it describes the extreme conditions of a dense beam with a longitudinal profile undergoing wakefield- and current-driven filamentation. This is due to the wakefield excited by the dilute beam head setting the initial condition for CFI at the beam centre, which could be considered in future studies.

5 Ion Motion in Wakefield-Driven Instabilities

Chapter Summary

- A transverse gradient in the beam-generated wakefield gives a ponderomotive force, which deflects heavy ions in the plasma.
- The effect of ion motion on the wakefield and self-modulation instability are studied with simulations and experimental observations.
- Three mechanisms reducing the wakefield and leading to the saturation the self-modulation instability are identified: Transverse decoherence, transverse wavebreaking and detuning. Ion motion enhances each effect depending on the beam shape. The enhanced reduction of the wakefield and suppression of the instability reduces the modulation of the beam tail in agreement with the experimental observations.

In the previous studies on the interaction of electron-positron beams with plasma, the motion of plasma ions is ignored, i.e. $m_i \to \infty$. This approximation results in a uniform plasma wavenumber, $k_\zeta = k_e$, and enables the derivation of the analytic model for wakefield-driven filamentation from linearised fluid equations. The considerations of an electron-proton beam in Section 4.5.2 have shown that the beam species filament at different rates depending on the mass, Lorentz factor and charge of the particles. However, this asymmetric composition is the general case for an electron-ion plasma. Only for plasma ions with significantly higher mass, $m_i \gg m_e$, can the motion of plasma ions be neglected.

In the case of a wakefield excited resonantly by a train of microbunches, the witness beam is typically placed further downstream at a significant magnitude of the growing wakefield. Thus, the effect of ion motion on the accelerating wakefield may cumulate over hundreds of plasma oscillation periods. For such an extended interaction time between the beam and the plasma and sufficiently low ion mass, the effect of ion motion on the plasma wake is no longer negligible. Consequently, the ion density and the plasma wave number are no longer uniform. Numerical studies by Spitsyn *et al.* (2018) and experimental studies by Gilljohann *et al.* (2019) have shown that the ponderomotive force of the wakefield excited by a laser pulse results in a transversely-varying ion density. As a result, the plasma electrons oscillate at different frequencies and transversely cross each other. This disturbs the coherent oscillation of the electrons and, eventually, the plasma wave breaks (Bulanov *et al.*, 1997). This transverse wavebreaking weakens the wakefield (Minakov and K. V. Lotov, 2024; Vieira *et al.*, 2012, 2014).

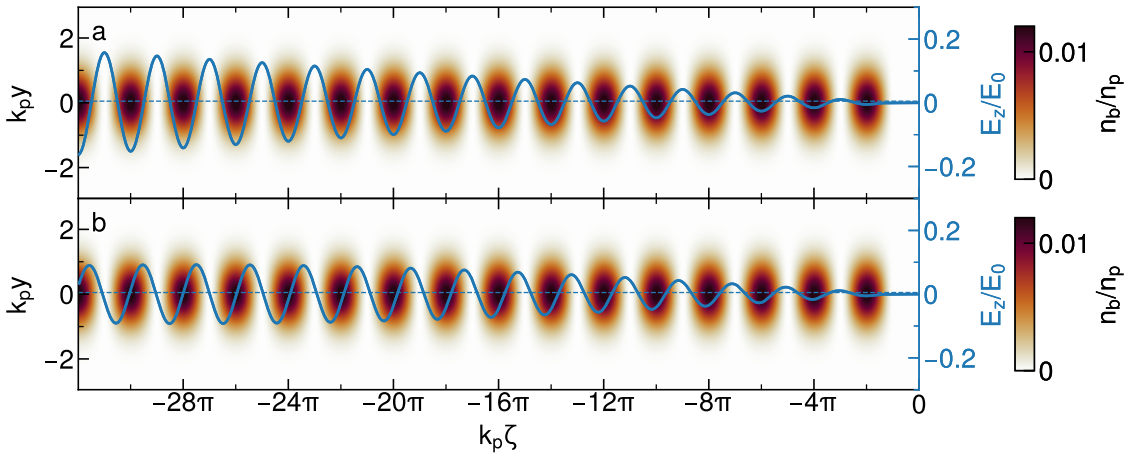

Figure 5.1: Resonantly-driven longitudinal wakefield with a) a constant wavenumber, $k_\zeta = k_p$, and b) a wavenumber depending on the amplitude of the longitudinal wakefield $k_\zeta = k_\zeta(\tilde{E}_z)$. The semi-analytic solution for the on-axis longitudinal wakefield is obtained by solving Equation (2.29).

A wakefield growing from two-stream instabilities, such as the wakefield-driven filamentation introduced in Chapter 4 or the axisymmetric SMI introduced in Section 2.4.1, grows as long as the wavenumber of the electron oscillation remains constant along the length of the longitudinally-modulated beam and along the propagation length in plasma. This is illustrated for a train of microbunches resembling a self-modulated charged beam in Figure 5.1. Yet, the longitudinal wavenumber increases for high wakefield amplitudes due to the relativistic electron oscillation, given by Equations (3.12) and (3.13). On the contrary, the wavenumber reduces towards saturation of SMI as the phase velocity increases, analytically expressed by $u_\psi(\Gamma)$ in Equation (2.31) for SMI and Equation (4.21) for TTS. Due to the increasing wavenumber, the wakefield stops to grow along the length of the beam or even reduces as it detunes from the resonant condition with the self-modulated beam, illustrated in Figure 5.1. Beyond previous studies, the magnitude of the wakefield may also reduce if the phase of the plasma wave is not constant along the transverse direction, referred to as transverse decoherence or the wakefield detunes from the train of microbunches. Two additional saturation mechanisms are amplified by a phase shift in the plasma wakefield due to ion motion.

This chapter investigates the effect of ion motion on the three mechanisms in different setups. In the beginning, the influence on the wakefield is isolated from any temporal evolution of the beam and only the instantaneous plasma response to a short beam in Section 5.1 and a train of microbunches Section 5.2 is studied, resembling the early stage and saturation of SMI. Afterwards, the cumulative effect of ion motion on a self-modulating beam is studied in Section 5.3 and compared to collaborative experimental observations in Section 5.4. This allows limits to be placed on the ion mass for PWFA experiments and extends the physical understanding relevant to these experiments. In Section 5.5, the effect of ion motion is briefly discussed for wakefield-driven filamentation.

The numerical investigation throughout the following sections has been presented at the Annual Meeting of the APS Division of Plasma Physics 2023. The combined experimental

and numerical results of ion motion at the AWAKE experiment at the end of this chapter have been submitted to *Physical Review Letters* (Turner *et al.*, 2024).

5.1 Response to a Short Driver

Equivalent to a long beam before undergoing SMI or a dense laser pule studied by (Spitsyn *et al.*, 2018), a short beam drives a wakefield of constant magnitude and the beam density has a negligible effect on the wavenumber. The beam and plasma parameters are chosen to reach a wakefield magnitude comparable to the resonantly-driven wakefield in accordance with the DPS run at AWAKE. The relativistic, $\gamma_b = 426$, short proton beam consists of 2×10^{10} particles, has a bi-Gaussian profile with rms length $\sigma_\zeta = 0.81\,\mathrm{ps} = 1/k_p$ and radius $\sigma_r = 160\,\mu\mathrm{m} = 0.66/k_p$. The normalised emittance is $\epsilon_n = 2.2\,\mu\mathrm{m}$. The instantaneous plasma response to the short driver is shown in Figure 5.2.

For stationary ions, the ion density in Figure 5.2a) remains spatially uniform. The modulation depth in the plasma charge density in Figure 5.2b) is associated with the amplitude of the electron oscillation and depends on the beam charge density at a given radius, i.e. the modulation depth increases with the charge perturbation from the driver. The phase of the plasma wave is higher on-axis relative to the fringe due to the relativistic oscillation of the plasma electrons described by Equation (3.13). For narrow beams, $k_p\sigma_r \approx 1$, the relativistic dilation reduces, quantified by $\alpha_\sigma \approx 0.1$ (K. V. Lotov, 2013). The longitudinal and transverse wakefield in Figure 5.2c) and d) remain constant as a function of ζ conforms to an ideal system with cold, non-diffusive plasma.

For Helium ions, the ion density varies along the transverse direction with increasing depth downstream, while the average ion density within $k_p r < 1$ reduces. Transversely, the minimum ion density is located at the peak of the radial wakefield, $k_p r \approx 1.2$. The deflected ions form an ion filament on-axis and a cylindrical ring at $k_p r \approx 1.8$. Since the beam is short, the increasing variation in the ion density must dominantly come from the wakefield acting on the plasma ions for an extended time. The plasma wavelength and, thus, the phase of the plasma response increases or decreases at radii of lower or higher ion density, respectively. The plasma wave bends into a 'C' shape within $-300 < k_p\zeta < -200$, referred to as transverse decoherence, which results in a decrease in the longitudinal wakefield and an increase in the transverse wakefield. The plasma wave breaks at $\sim -300/k_p$ but recovers at $\sim -350/k_p$. This transverse wavebreaking coincides with a build-up of a sheath electric field in the radial wakefield component beyond the plasma in agreement with studies by (Gorn *et al.*, 2020). For $-400 < k_p\zeta < -350$, the transverse decoherence amplifies, and both wakefield components decrease. The interaction length in ζ for which the effect of ion motion becomes relevant is $\sim 200/k_p$ at a wakefield amplitude of $W_r \sim 0.2\,E_0$.

The simulations are carried out using the quasistatic PIC code LCODE (Sosedkin and K. Lotov, 2016) in a quasi-three-dimensional cylindrical geometry. While two- and three-dimensional simulations effectively model the exponential growth of TTS, showed in Section 4.3, the growth of the axisymmetric SMI differs depending on the geometry as depicted by Section 2.4.1. The computational resources can be significantly reduced using a quasistatic code, which showed excellent agreement for TTS in the previous chapter. Since SMI is the axisymmetric mode of TTS, the spatial domain can be further reduced by utilising

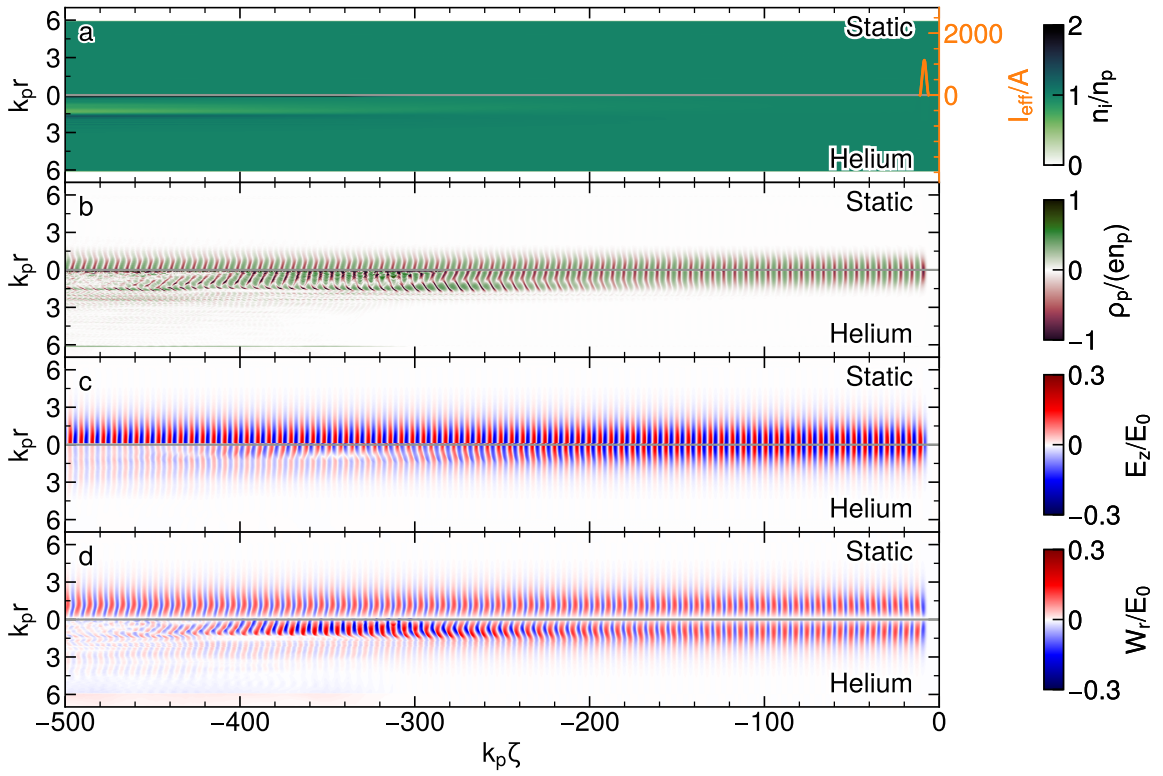

Figure 5.2: The effect of ion motion on the plasma response to a short beam. The a) ion density, superimposed by the effective beam current, the b) plasma charge density, the c) longitudinal and d) radial wakefield component for stationary (upper half) and Helium (lower half) ions.

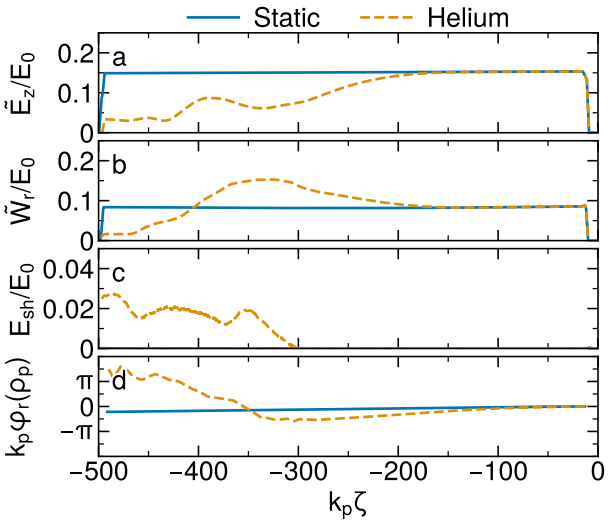

Figure 5.3: The envelope averaged within $k_p r < 1$ of a) the longitudinal and b) the radial wakefield component for the short beam in Figure 5.2. d) The sheath electric field is shown at $k_p r = 6.5$, and e) the difference taken of the phase of the plasma wave at $r = 0.5/k_p$ and $1/k_p$.

cylindrical coordinates. For the short beam and train of microbunches, the beam parameters are chosen to excite a quasi-linear wakefield with amplitudes comparable to the experiment, $W_r \sim 0.2\,E_0$. The initially uniform plasma density is $n_p = 4.8 \times 10^{14}\,\mathrm{cm}^{-3}$ and the plasma ions are chosen between stationary ions and Helium ($m_i/m_e = 7344$). Only the instantaneous plasma response along the length of the beam ζ at a propagation distance of $z = 0$ is retrieved. The spatial resolution is 80 cells per plasma skin depth. Beam and plasma particles are represented by 1 and 100 macroparticles per cell, uniformly spaced on the spatial grid. The low number of beam particles suffices since no beam evolution is retrieved, and the particle weight gives the local beam density.

The envelope of the wakefield components averaged within $k_p r < 1$ (Figure 5.3a-b) are compared to the occurrence of the sheath electric field at $k_p r = 6.5$ (Figure 5.3c) and the phase difference (Figure 5.3d). For stationary ions, the wakefield is constant, and no sheath field occurs. A small phase difference occurs as the wavenumber slightly increases on-axis due to the relativistic electron oscillation. For Helium ions, the increase of the longitudinal wakefield and decrease of the transverse wakefield for $k_p\zeta < -200$ and the decrease of both components for $k_p\zeta < -380$ aligns well with the phase shift of the plasma wave reaching the order of π/k_p and is, thus, correlated to transverse decoherence. A small increase in the sheath electric field due to the plasma wave breaking aligns only with a small additional increase of the radial wakefield at $\sim -300/k_p$ and amplifies the decrease of the wakefield for $k_p\zeta < -380$. For the short beam, the wakefield is dominantly decreased due to the transverse decoherence.

5.1.1 Wakefield-driven Ion Motion

Plasma ions do not experience the fast oscillation of the plasma wave due to their high mass, but experience the envelope of the wakefield. For a radial gradient present in the wakefield envelope, the corresponding ponderomotive force, $\boldsymbol{F}_p = -[e^2/(m_e\omega_p^2)]\nabla\tilde{\boldsymbol{E}}^2$, given by Equation (2.34), deflects ions transversely over an extended time. Although the ponderomotive force is nonlinear, $\boldsymbol{F}_p \sim E^2 \sim (\rho_p - \rho_b)^2$, its effect on the plasma ions remains linear for $\delta n_i \ll n_p$, with δn_i the perturbation density of plasma ions. In the quasistatic regime, $u_b|\partial_\tau \delta n_i| \ll |\partial_\zeta \delta n_i|$, the linearised fluid equation, expressed by Equation (4.11), yields for the plasma ions (Vieira *et al.*, 2012)

$$m_i u_b^2 \partial_\zeta^2 \delta\rho_i = \rho_p \nabla \cdot \boldsymbol{F}_p \tag{5.1}$$

with the ponderomotive force as the only source of momentum change. The equation can be rewritten to

$$\frac{\partial_\zeta^2}{k_e^2}\frac{\delta n_i(\zeta)}{n_p} = -\frac{q/e}{4m_i/m_e}\frac{\nabla^2}{k_p^2}\left(\frac{\tilde{\boldsymbol{E}}^2(\zeta)}{E_0^2}\right). \tag{5.2}$$

For a constant gradient in the electric field excited by the short beam, the solution to Equation (5.2) is given by a double integral in ζ with $\delta n_i(\zeta = 0) = \partial_\zeta \delta n_i(\zeta = 0) = 0$ as initial conditions to

$$\frac{\delta n_i}{n_p} = -\frac{\nabla^2(\tilde{E}^2/E_0^2)}{8m_i/m_e}\zeta^2. \tag{5.3}$$

The envelope of the longitudinal and radial electric field excited by the short beam are shown in Figure 5.4a) and b) for Helium ions. The fields vary radially and contribute to the

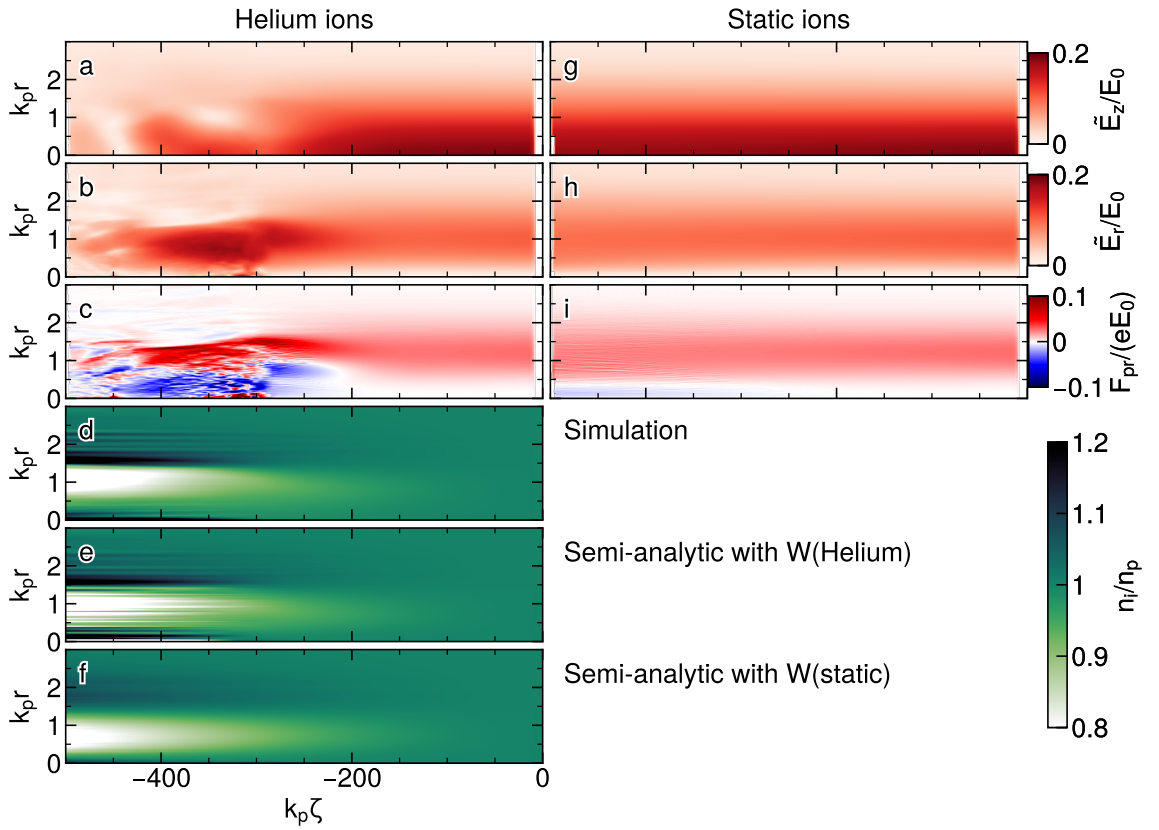

Figure 5.4: The effect of the envelope of the wakefield on the ion density for the short beam in Figure 5.2. The envelope of a) the longitudinal and b) the radial electric field, c) the ponderomotive force. The ion density obtained by d) the simulation and the semi-analytic solution to Equation (5.2) with the wakefield from e) static ions and f) Helium ions. g)-i) Wakefield components and ponderomotive force for static ions.

ponderomotive force shown in Figure 5.4c). Ions are deflected from the peak of the radial wakefield at $\sim 1/k_p$, which results in a reduced ion density around the peak of the radial wakefield. For $k_p\zeta < -200$, the wakefield components and ponderomotive force are affected by the change in ion density (Figure 5.4d). The semi-analytic solution of Equation (5.2) with the electric field from the run with Helium ions (Figure 5.4e) agrees well with the simulation, qualitatively validated in Figure 5.5 along a) the length of the beam and b) the radial axis. In Figure 5.4f) and Figure 5.5b), showing the semi-analytic solution with the wakefield from static ions (Figure 5.4g-i), the agreement to simulation gets worse for $k_p\zeta < -250$. The change in ion density self-consistently reduces the magnitude and gradient in the longitudinal wakefield while it amplifies the radial wakefield and the ponderomotive force.

5.1.2 Transverse Decoherence

Generally, the restoring force on the deflected plasma electrons depends on the ion and beam density. Including the relativistic oscillation of plasma electron, the longitudinal wavenumber

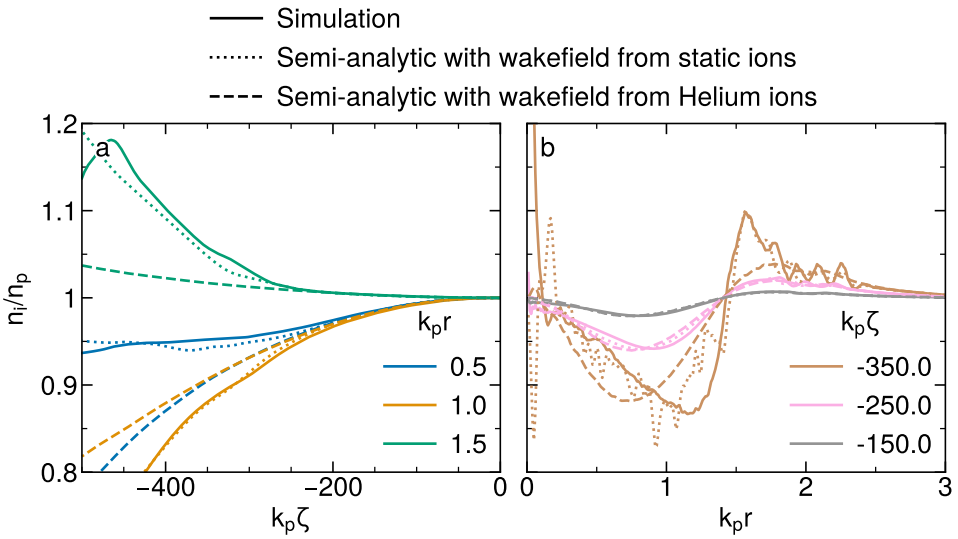

Figure 5.5: Lineouts of the ion density from Figure 5.4. Simulation and theory from solving Equation (5.2) with the wakefield from the simulation with stationary (dashed) and Helium (dotted) ions as a function of a) ζ and b) r.

is expressed by (K. V. Lotov, 2013; Morales Guzman *et al.*, 2021)

$$\frac{k_i}{k_p} = \frac{\sqrt{1 + (\delta n_i + n_b)/n_p}}{1 + \alpha_\sigma (\tilde{E}_z/E_0)^2}. \tag{5.4}$$

The changes in the plasma wavenumber are usually small, $|k_i - k_p| \ll k_p$. However, for a long interaction time between wakefield and ions, the small change in k_i cumulates in the considerable phase difference φ to a wave with a wavelength of λ_p, described by

$$k_p\varphi(\zeta,r) = \int_\zeta^0 \mathrm{d}\zeta' k_i(\zeta',r) - k_p\zeta. \tag{5.5}$$

The plasma wave, illustrated in Figure 5.6a), is shown at different radii in Figure 5.6b) with the location of the zero-crossings, $\rho_p(\zeta_c) = 0$. Due to the phase shift along the transverse axis, oscillating plasma electrons get closer, and the plasma wave within $1 < k_pr < 1.5$ becomes anharmonic. The wavenumber as a function of ζ is then given by $k_\zeta = \pi/\langle\Delta\zeta_c\rangle_\lambda$, where $\langle\Delta\zeta_c\rangle_\lambda$ is the mean difference between three consecutive zero-crossings (required for anharmonic waves). The difference of the phase relative to the phase of a linear wave with $k_\zeta = k_p$ is shown in Figure 5.6c). The simulation agrees with the semi-analytic solution of the phase difference by solving Equation (5.4) for the observed change in ion density. For regions where the wave breaks, e.g. at $k_pr \approx 0.9$ for $k_p\zeta < -300$, Equation (5.4) loses its validity.

The expression for the wakefield in Equation (2.29) assumes a constant longitudinal wavenumber. In the general case of a variable wavenumber, the field equation defined by Equation (4.4) is solved for the relativistic regime without replacing the plasma perturbation

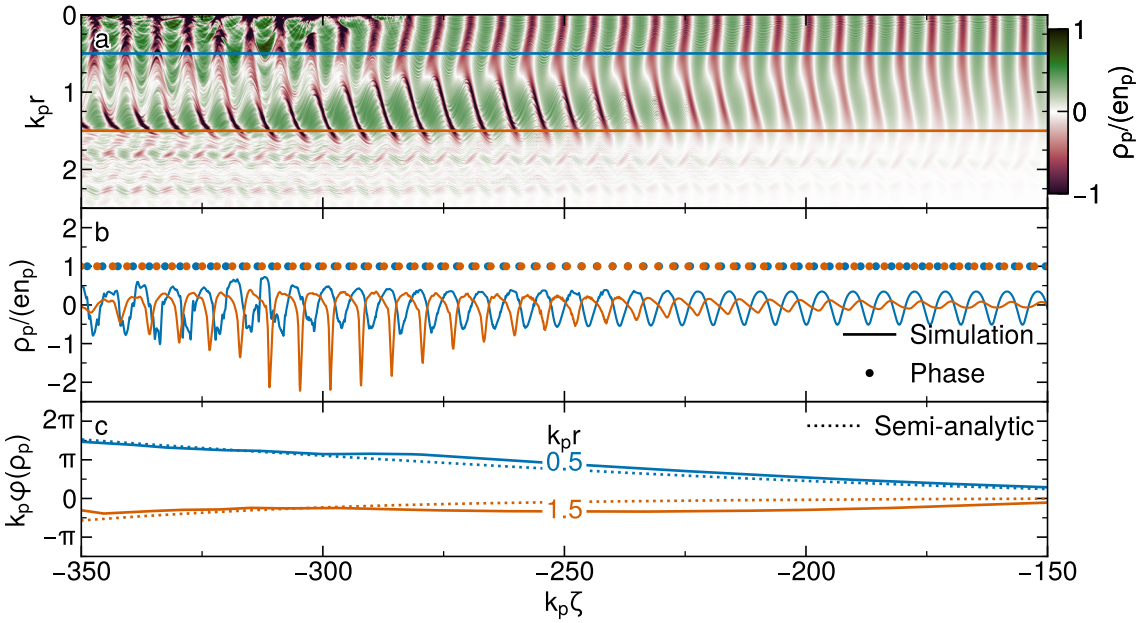

Figure 5.6: Phase variation in the plasma wave for the short beam in Figure 5.2. a) Plasma charge density, where the horizontal lines indicate the radial location for the lineouts in b). The dots mark the zero-crossings of the plasma wave. c) The cumulative phase of the plasma wave from simulation and semi-analytic prediction by solving Equation (5.4).

with its expression from linear fluid theory. The wakefields follow the equation

$$\begin{aligned}(\nabla_r^2 - k_p^2)E_z &= \partial_\zeta \delta\rho_p/\varepsilon_0 \\ (\nabla_r^2 - k_p^2)W_r &= \partial_r \delta\rho_p/\varepsilon_0.\end{aligned} \tag{5.6}$$

Following the wave equations, the wakefield components depend on the respective gradient of the plasma charge density. Under the Hankel transform, $\mathcal{H}_n\{\delta\rho_p\}(k_r) = \int_0^\infty r J_n(k_r r)\delta\rho_p \,\mathrm{d}r$, with J_n the Bessel function, the Laplacian transforms to $\nabla_r^2 \to -k_r^2$. The wakefield is then obtained by the inverse Hankel transform

$$\begin{aligned}E_z &= \iint_0^\infty \mathrm{d}r'r' \,\mathrm{d}k_r [k_r/(k_p^2 + k_r^2)] J_0(k_r r_<) J_0(k_r r_>) \partial_\zeta \delta\rho_p \\ W_r &= \iint_0^\infty \mathrm{d}r'r' \,\mathrm{d}k_r [k_r/(k_p^2 + k_r^2)] J_1(k_r r_<) J_1(k_r r_>) \partial_{r'} \delta\rho_p.\end{aligned} \tag{5.7}$$

With the relation $I_n(k_p r_<)K_n(k_p r_>) = \int_0^\infty \mathrm{d}k_r [k_r/(k_p^2 + k_r^2)] J_n(k_r r_<) J_n(k_r r_>)$ (Abramowitz and Stegun, 1964), the wakefield simplify to

$$\begin{aligned}E_z(\zeta, r) &= \frac{q_b}{\varepsilon_0} \int_0^\infty \mathrm{d}r'r' I_0(k_p r_<) K_0(k_p r_>) \partial_\zeta \delta\rho_p(\zeta, r') \\ W_r(\zeta, r) &= \frac{q_b}{\varepsilon_0} \int_0^\infty \mathrm{d}r'r' I_1(k_p r_<) K_1(k_p r_>) \partial_{r'} \delta\rho_p(\zeta, r').\end{aligned} \tag{5.8}$$

A transverse decoherence in the plasma wave has various effects on the wakefield components, as illustrated in Figure 5.7. For minor variations in the phase of the plasma wave

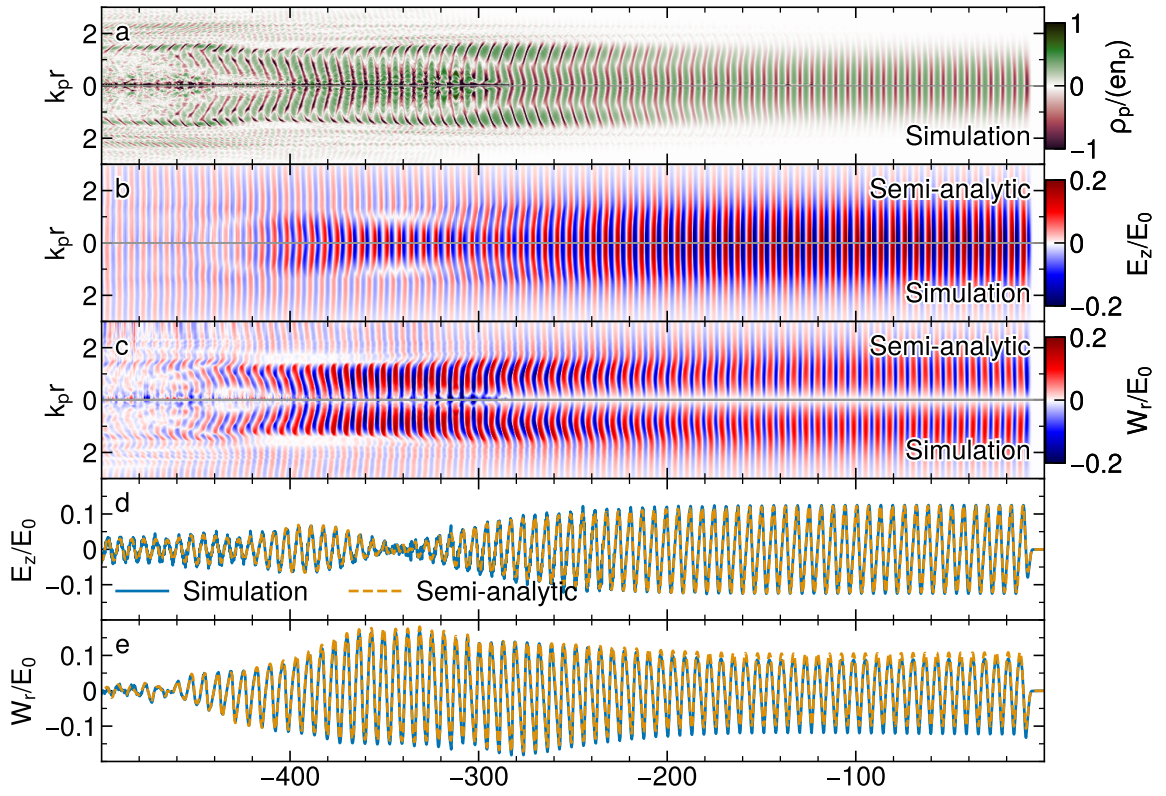

Figure 5.7: The effect of transverse decoherence on the wakefield. a) The plasma charge density, b) the longitudinal and c) the transverse wakefield component from simulation theory, and d) and e) the respective lineouts at $k_p r = 1$.

(Figure 5.7a), $\varphi_r < \pi/k_p$, the longitudinal wakefield decreases (Figure 5.7b), being the transverse integral over the plasma wave decreases. However, the transverse wakefield (Figure 5.7c) increases in magnitude as defined by the integral over the transverse gradient of the plasma charge density. The transverse wakefield decreases for significant variations in the phase, $\varphi_r \approx \pi/k_p$, when the suppressing effect of transverse decoherence dominates the increase in the transverse gradient of the plasma wave. The wakefield from the simulation agrees with the semi-analytic solution by evaluating Equation (5.8) with the plasma charge density from the simulation, quantitatively shown in Figure 5.7d-e).

The sensible choice of the gas utilised for wakefield acceleration experiments relies on how the effect of ion motion scales with the ion mass. Given by Equation (5.3), the interaction length for the change in ion density scales with $m_i^{-1/2}$. Utilising the Taylor-approximation, $(1 + \delta n_i/n_p)^{1/2} \approx 1 + \delta n_i/(2n_p)$, the phase for a constant wakefield scales with $\varphi \sim \zeta^3/(m_i/m_e)$. Thus, the length for which ion motion affects the phase difference provides a weaker scaling of $m_i^{-1/3}$. Figure 5.8a) verifies that the change in the envelope of the wakefield correlates with the phase difference between the radii, $\varphi_r = \varphi(k_p r = 0.5) - \varphi(k_p r = 1)$, shown in Figure 5.8b). Thus, the length for which the wakefield amplitude varies scales accordingly with the ion mass with $(m_i/m_e)^{1/3}$ in agreement with recent theoretical and numerical studies by Spitsyn *et al.* (2018). This weak scaling eases the constraints on the ion mass to avoid the destructive interference of mobile ions with the plasma wave.

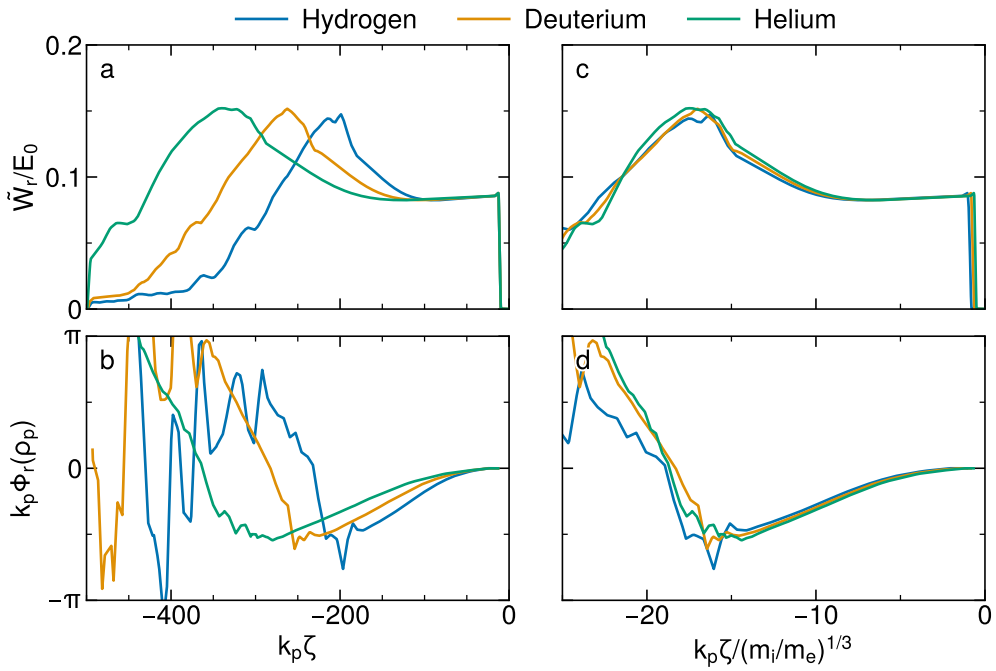

Figure 5.8: Ion mass scaling for the change in wakefield amplitude. a) Phase shift of the plasma wave between $k_p r = 0.5$ and 1, and b) mean envelope of the radial wakefield for $k_p r < 1$. In c) and d) represent a) and b) with the length along the beam divided by $(m_i/m_e)^{1/3}$. The lines are shaded, where the plasma wave is broken.

5.2 Response to a Train of Microbunches

For a train of microbunches equivalent to a fully-modulated long beam towards saturation of SMI, an additional saturation mechanism has to be included: The wakefield detunes from the microbunches. The transverse shape remains Gaussian, while the longitudinal shape of the beam is a simple sine function with wavenumber at k_p and a peak effective current of 75.5 A.

Figure 5.9 shows the effect of ion motion on a resonantly-driven wakefield. For stationary ions, the plasma wave and the longitudinal and radial wakefield, respectively shown in Figure 5.9b), c) and d), are resonantly amplified for $k_p\zeta > -250$. For $k_p\zeta < -250$, the plasma wake saturates and eventually decreases. For Helium ions, the radial modulation of the ion density in Figure 5.9a) is stronger compared to Figure 5.2a), given that the radial wakefield in Figure 5.9c) has grown to a slightly higher amplitude. The plasma wave in Figure 5.9b) and the wakefield reduce for $k_p\zeta < -350$ and for $k_p\zeta < -400$ the plasma is turbulent. No transverse decoherence is apparent in the plasma charge density as the positive charge of the microbunches corrects the phase bending due to a lower ion density.

Equivalent to Figure 5.3, the mean envelope of the wakefield within $k_p r < 1$ is compared to the electric sheath field and the phase difference between $k_p r = 0.5$ and $k_p r = 1$. For stationary ions, the longitudinal and transverse wakefield in Figure 5.10a) and b) increase linearly for $k_p\zeta > -200$. The fields saturate at $k_p\zeta \sim 350$ and decrease further downstream. The wakefield detunes from the resonant condition, defined by the distance between the

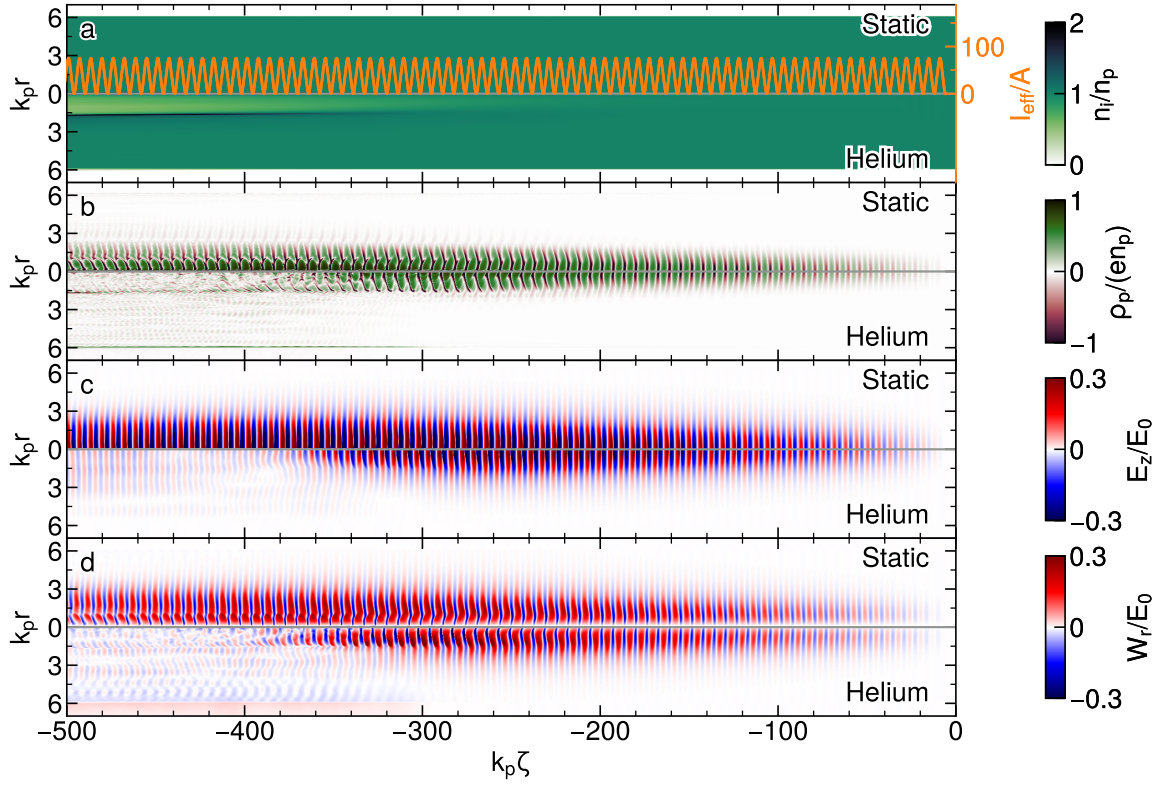

Figure 5.9: a-d) Description as Figure 5.2, but for a train of microbunches. e) Phase difference between wakefield and the train of microbunches relative to the resonant condition.

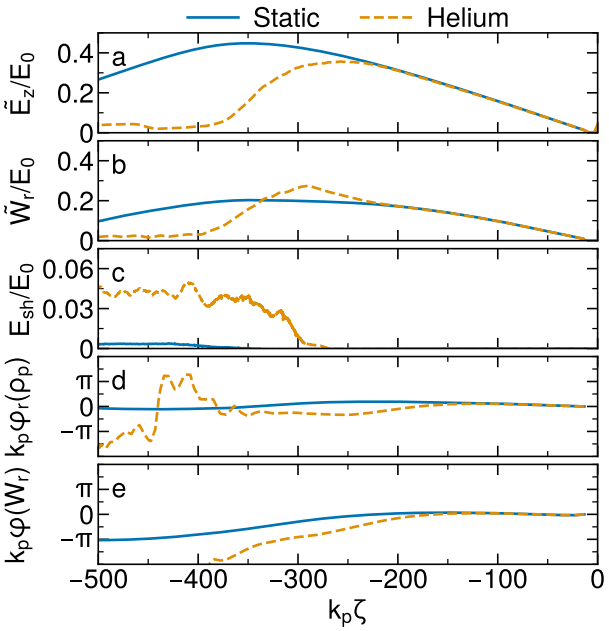

Figure 5.10: The field envelopes for the train of microbunches in Figure 5.9. Description as Figure 5.3.

microbunches since the wavenumber of the relativistic electron oscillation increases for high longitudinal electric fields. The wakefield saturates as it detunes by $\sim \pi/(2k_p)$ and reduces for a higher phase difference. The wakefield reduces at the same rate as it initially increased if the phase difference to the microbunches reaches $\sim \pi/k_p$. The sheath field (Figure 5.10c), the phase difference in the plasma wave between $k_p r = 0.5$ and 1 (Figure 5.10d) and the detuning of the wakefield from the microbunches (Figure 5.10e) remain negligible. The detuning of the wakefield is quantified by the phase difference between the zero-crossing of the wakefield from peak to trough and the microbunch centres. A phase difference of 0 is equivalent to resonant amplification.

For Helium ions, the resonant amplification of the wakefield for $k_p\zeta > -200$ remains comparable to stationary ions. In contrast to the short beam, the decrease of the longitudinal wakefield and increase of the radial wakefield for $k_p\zeta < -250$ due to transverse decoherence (Figure 5.10d) remains negligible. The phase difference at different radii reaches a considerable value for $k_p\zeta < -400$, at which length the wakefield is already suppressed. The initial decrease of both components within $-320 < k_p\zeta < -270$ correlates with the wakefield detuning from the microbunches (Figure 5.10e). The strong decrease of the wakefield for $k_p\zeta < -300$ correlates instead with the sheath electric field (Figure 5.10c). Thus, transverse wavebreaking is the dominant mechanism for decreasing the wakefield excited by a pre-modulated beam.

The dominant effects of ion motion differ in the two limits of a beam undergoing SMI. For a wakefield driven by a non-modulated driver, the transverse decoherence in the plasma response is the dominating effect for the reduced wakefield amplitude. For a resonantly-driven wakefield, the wakefield amplitude is dominantly influenced by transverse wavebreaking, while detuning between the wakefield and microbunches contributes.

5.2.1 Transverse Wavebreaking

The peak amplitude plasma electrons can oscillate is just before they cross paths. For a one-dimensional system, $k_y = k_x = 0$, this is equivalent to the wavebreaking limit of the longitudinal wakefield $E_z = E_0$, discussed in Section 3.1. Transverse wavebreaking is connected to transversely oscillating electrons crossing paths. This generally occurs at much lower wave amplitudes compared to the wavebreaking limit due to a curvature in the plasma wake (Bulanov *et al.*, 1997), observed throughout the previous sections. The transverse distance between oscillating electron trajectories to cross decreases with the phase difference and is at its minimum for a phase difference of $\pi/2$. Transverse wavebreaking is enhanced with increasing amplitude of the transverse wakefield or a stronger curvature in the plasma wake, as is the case for a non-uniform ion density.

The trajectories of neighbouring plasma electrons are shown with the electric field in Figure 5.11 for the pre-modulated beam in Figure 5.9. The trajectories of plasma electrons cross at $\sim -300/k_p$. When they cross, electrons experience an increase in the electrostatic force and are either drawn to the central axis or ejected outward. The plasma is no longer neutral when the outward propagating electron leaves the plasma column. Consequently, a sheath electric field builds up beyond the plasma wall at $k_p r = 6$, drawing the ejected electrons back into the plasma column. Re-entering plasma electrons disturbs the plasma wake, such as the green trajectory at $k_p\zeta = -350$ (Gorn *et al.*, 2020).

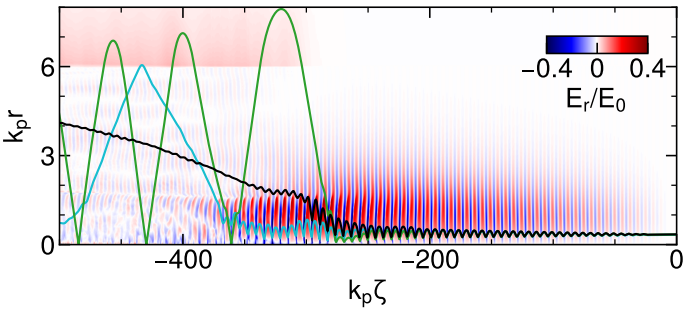

Figure 5.11: Electric field superimposed by neighbour trajectories of the plasma electron for the pre-modulated beam with Helium ions.

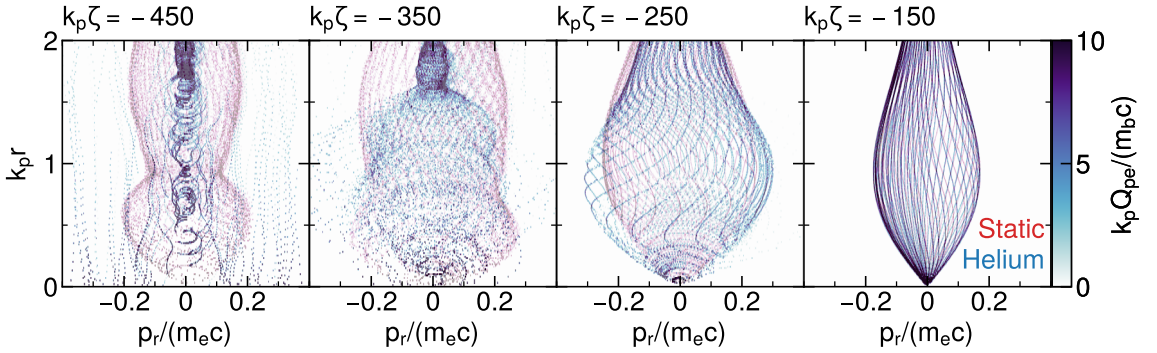

Figure 5.12: Phasespace in rp_r of the plasma electron at chosen intervals $\zeta \pm 10/k_p$ with stationary (red) and Helium (blue) ions for the pre-modulated beam in Figure 5.9

The evolution of plasma electrons under transverse wavebreaking is shown in the rp_r phasespace in Figure 5.12. For stationary ions, the width of the occupied phasespace increases between $k_p\zeta = -150$ and -250, with the peak of the particle momentum at $k_p\zeta \approx 1$. For $k_p\zeta < -350$, the width dominantly decreases at $k_p\zeta = 1$ as the plasma wake detunes from the microbunches. For Helium ions, the occupied volume is squeezed down to lower radii at $k_p\zeta = -250$ and -350 with the peak at $k_p r = 0.9$ and 0.5, respectively. The work by Minakov and K. V. Lotov (2024) has shown that as transverse wavebreaking occurs, coherent electrons are drawn from larger radii to the wavebreaking region such that it temporarily recovers. This results in a transfer of energy and an increase in the plasma wave amplitude close to the wavebreaking region. However, the electrons continue to move radially and draw the energy away from the recovered wavebreaking region and the plasma wave breaks, shown at $k_p\zeta = -350$ and -450. Ejected electrons are separated from the occupied phasespace volume of the plasma wave.

5.3 Response to an Evolving Beam

After unravelling the effect of ion motion on the instantaneous plasma response, the cumulative effect on a self-modulating beam is discussed in this section. The plasma quantities and wakefield at the early stage of SMI are shown in Figure 5.13 at a propagation distance of 1.5 m. The beam density in Figure 5.13a) is weakly modulated and remains comparable between stationary and Helium ions. Due to the low ion mass and the long interaction length,

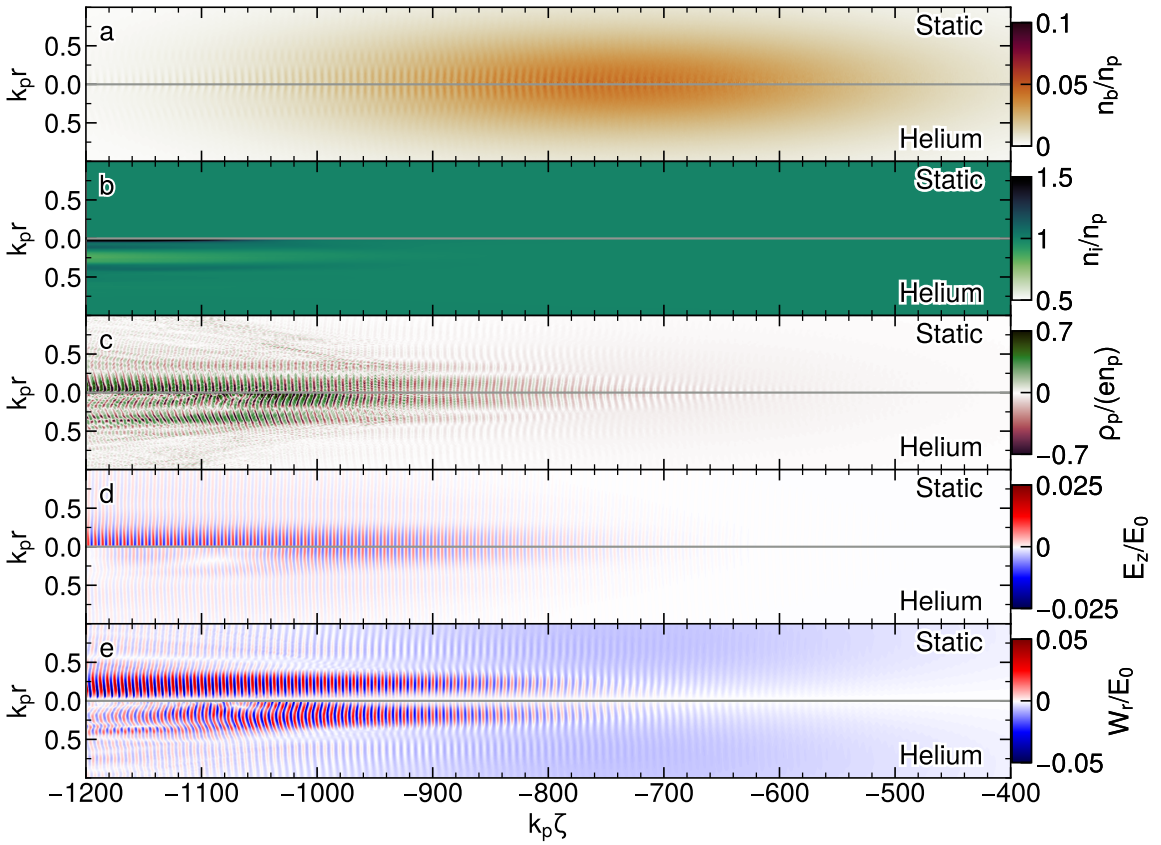

Figure 5.13: The plasma response to a beam undergoing self-modulation at a propagation distance of $z = 1.5\,\mathrm{m} = 6183/k_p$. a) The beam density, b) the plasma ion density, c) the plasma charge density, and d) the longitudinal and e) radial component of the wakefield shown for stationary and Helium ions.

the low wakefield amplitude results in a relevant density modulation of the ion species, as depicted by Figure 5.13b). The plasma charge density in Figure 5.13c) and the radial wakefield in Figure 5.13 increase along the length of the beam due to the spatiotemporal growth of SMI. This growth saturates at $k_p\zeta \approx -1050$ for Helium ions. The phase difference between different radii has to be compared to the run with stationary ions since the beam charge density itself has an effect on the local plasma wavelength, and the growth of SMI results in a reduced phase velocity relative to the beam velocity, as depicted by Equation (2.31). The plasma wave bends into a 'C' shape as the cumulative phase increases for regions with lower ion density. The effect of ions shows equivalent features compared to instantaneous plasma response to a short driver in Figure 5.2.

Consistent with the ion motion studies at the DPS run, the baseline plasma density is set to $n_p = 4.8 \times 10^{14}\,\mathrm{cm}^{-3}$. The long proton beam consists of 2.8×10^{11} particles with an rms length of $\sigma_\zeta = 170\,\mathrm{ps} = 210/k_p$ and an rms radius of $\sigma_r = 160\,\mu\mathrm{m} = 0.66/k_p$ resulting in a peak density of $n_b/n_p = 0.0284$. The propagation distance of the beam in plasma is $z = 10\,\mathrm{m} = 41200/k_p$. The beam in simulations is considerably coarser compared to the experiment, which yields a higher seed for SMI. To achieve numerical convergence and results comparable to the experimental run, the propagation of 10 m is divided into 160 steps. The

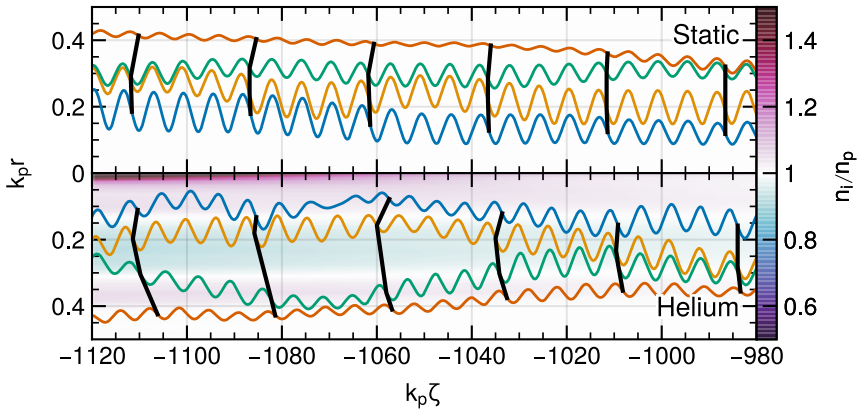

Figure 5.14: Chosen initially equidistant trajectories of plasma electrons for stationary and Helium ions. The oscillation amplitude is magnified by 1.5. Curves of constant phase are shown by black curves, and the ion density is shown in the background.

spatial distribution is bi-Gaussian, with a smooth cut at $3.4\sigma_\zeta$ in the longitudinal direction and a transverse cut at $3\sigma_r$. The beam and plasma species are represented by a relatively high number of 81 and 100 macroparticles per cell, which are uniformly loaded.

Figure 5.14 investigates the effect of the non-uniform plasma wavelength on the electron trajectories. For stationary ions, the electron oscillation remains coherent, and the radial equilibrium position of the electrons remains roughly constant along the beam. For Helium ions, the oscillation phase increases or decreases depending on the local ion density for Helium ions, emphasised by the bending of the curves of equal phases. The radial equilibrium position of the electrons varies attracted by the ions.

The plasma response to a self-modulated beam at a propagation distance of 5 m, where SMI has saturated for a significant length of the beam, is shown in Figure 5.15. The beam density for stationary ions shows the signature for a beam undergoing SMI. Since SMI is spatiotemporal, the beam is fully modulated towards the beam centre into microbunches. This train of microbunches resonantly amplifies the plasma wake while the beam particles between the microbunches diverge under the influence of the defocussing wakefield. The beam head is focused by the non-oscillatory term of the wakefield. For $k_p\zeta < -800$, the wakefield detunes from the microbunches and, consequently, the microbunches dampen the wakefield instead of amplifying it. Vice versa, the microbunches in the focussing phase of the radial wakefield at the early stage of SMI shift to the defocussing interval saturation. This deteriorates the microbunches for $k_p\zeta < -800$ and decreases the effective current of the beam.

For Helium ions, the beam density increases again for $k_p\zeta < -900$ towards the beam tail as the wakefield amplitude decreases earlier along the length of the beam. The beam tail contains a weak longitudinal modulation, which implies that the wakefield is not considerably weakened at the early stage of SMI due to ion motion. Despite the beam shape being significantly different, the variation in the ion density and the reducing envelope of the plasma wave and wakefield for $k_p\zeta < -800$ is equivalent to the instantaneous plasma response from the pre-modulated beam in Figure 5.9.

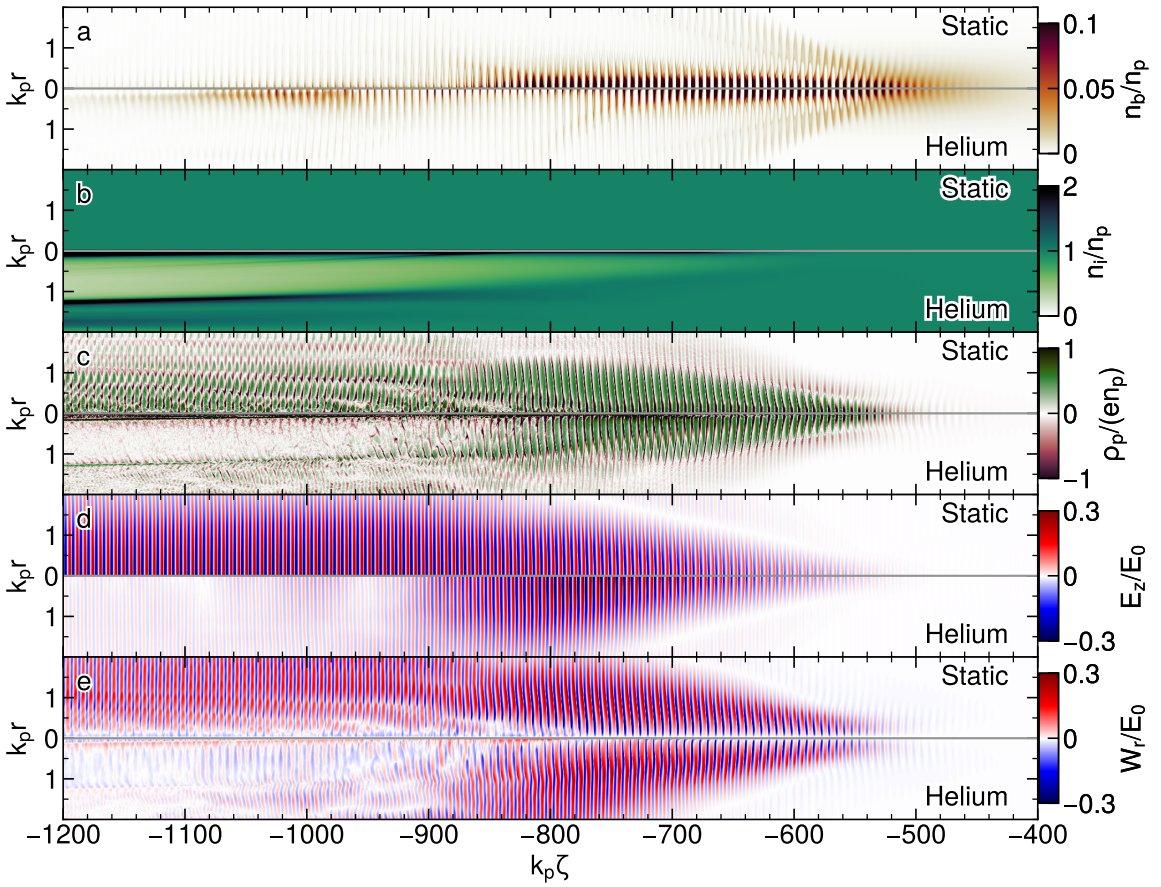

Figure 5.15: Description as Figure 5.13 but after a propagation distance of $z = 5\,\mathrm{m} = 20610/k_p$.

The relative reduction of the longitudinal and radial wakefield at the early stage of SMI is evaluated by the mean value of the envelope within $k_p r < 1$ and outlined in Figure 5.16a) and b). The decrease of the wakefield with Helium ions relative to the wakefield with stationary ions correlates with an increase of the phase difference in the plasma wave, outlined in Figure 5.16d). The sheath electric field (Figure 5.16c) and detuning of the wakefield from the resonant condition (Figure 5.16e) remain negligible. Transverse decoherence remains the dominating effect comparable to the effect of ion motion on the instantaneous plasma response to the short beam.

The beam is, for the most part, fully modulated at $k_p z = 20610$ with stationary ions. The detuning of the wakefield from the resonant condition has only an effect for $-900 < k_p\zeta < -800$ as the beam for $k_p\zeta < -900$, the microbunches strongly diverged. The sheath electric field (Figure 5.16h) increases for $-800 < k_p\zeta < -600$ where the beam self-modulates into microbunches and saturates for $k_p\zeta < -800$ as the radial wakefield stops growing. The high density of the microbunches with a strong radial gradient over hundreds of plasma periods along the beam length results in transverse wavebreaking even with stationary ions.

With Helium ions, the decrease in the wakefield is amplified within $-950 < k_p\zeta < -800$. This reduction is predominantly due to transverse wavebreaking, as shown by the enhanced

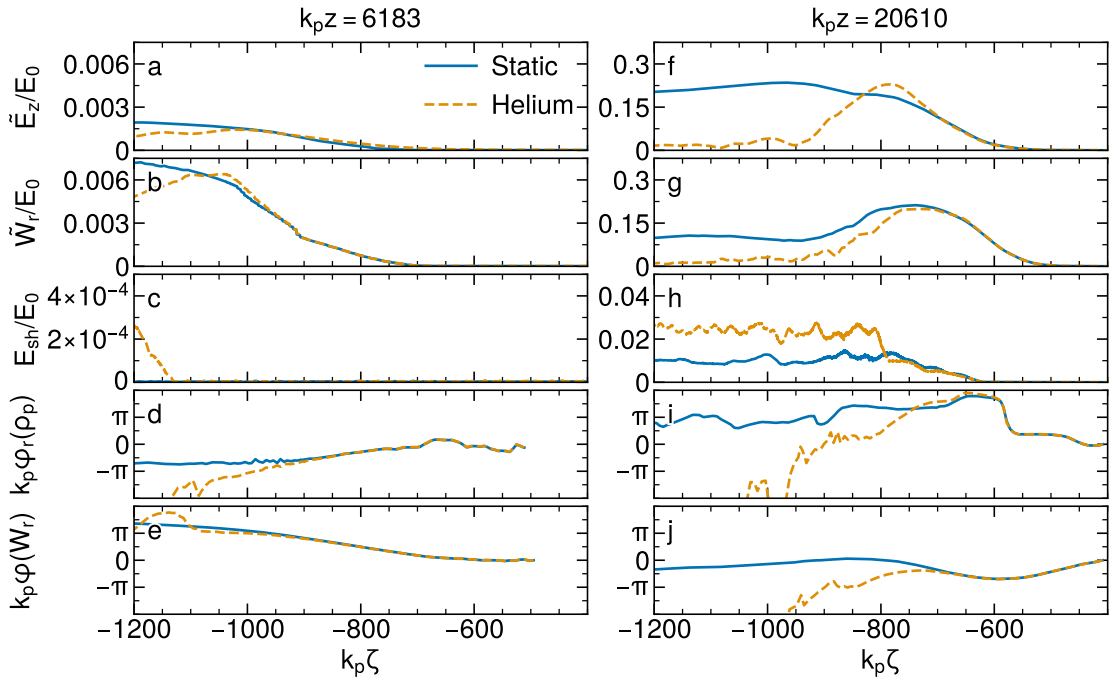

Figure 5.16: a)-e) The field envelopes and phase shift for the self-modulating beam after propagating 1.5 m in plasma (Figure 5.13) and f)-j) after propagating 5 m in plasma (Figure 5.15). Description as Figure 5.3.

build-up of the sheath electric field for $k_p\zeta < -800$. The transverse decoherence in the plasma response (Figure 5.16i) is reduced for Helium ions compared to stationary ions as the microbunches correct for the phase difference from the reduced ion density. Figure 5.15j) shows that the wakefield detunes from the resonant condition for $k_p\zeta < -700$. This has an additional impact within $-800 < k_p\zeta < -700$ next to transverse wavebreaking. While detuning has a minor effect in reducing the wakefield, it results in a shorter beam head as microbunches are defocussed earlier along the beam.

The cumulative effect of plasma ions with finite masses on SMI is shown in Figure 5.17. For stationary ions, the beam effective current and wakefield components in Figure 5.17a), b) and c) show the spatiotemporal growth of SMI. The initial Gaussian beam self-modulates, which increases the peak effective current and results in a spatiotemporal growth of the wakefield. At a propagation distance of ~ 4 m, the instability saturates such that the phase of the radial wakefield increases. The detuning wakefield defocusses the microbunches, which decreases the effective current along the length of the beam and the plasma. Thus, the wakefield saturates earlier along the beam at a higher propagation distance. The envelope of the plasma wave in Figure 5.17e) correlates with the radial wakefield, as both quantities depend on the radial gradient in the phase of the collective electron oscillation. The longitudinal wakefield in Figure 5.17b) is more resilient to the resulting transverse decoherence. Besides detuning, transverse wavebreaking reduces the wakefield for stationary ions, shown by the sheath electric field in Figure 5.17f).

For Helium ions, both the transverse decoherence in the plasma response and transverse wavebreaking due to the transverse variation of the ion density (Figure 5.17d) reduces the

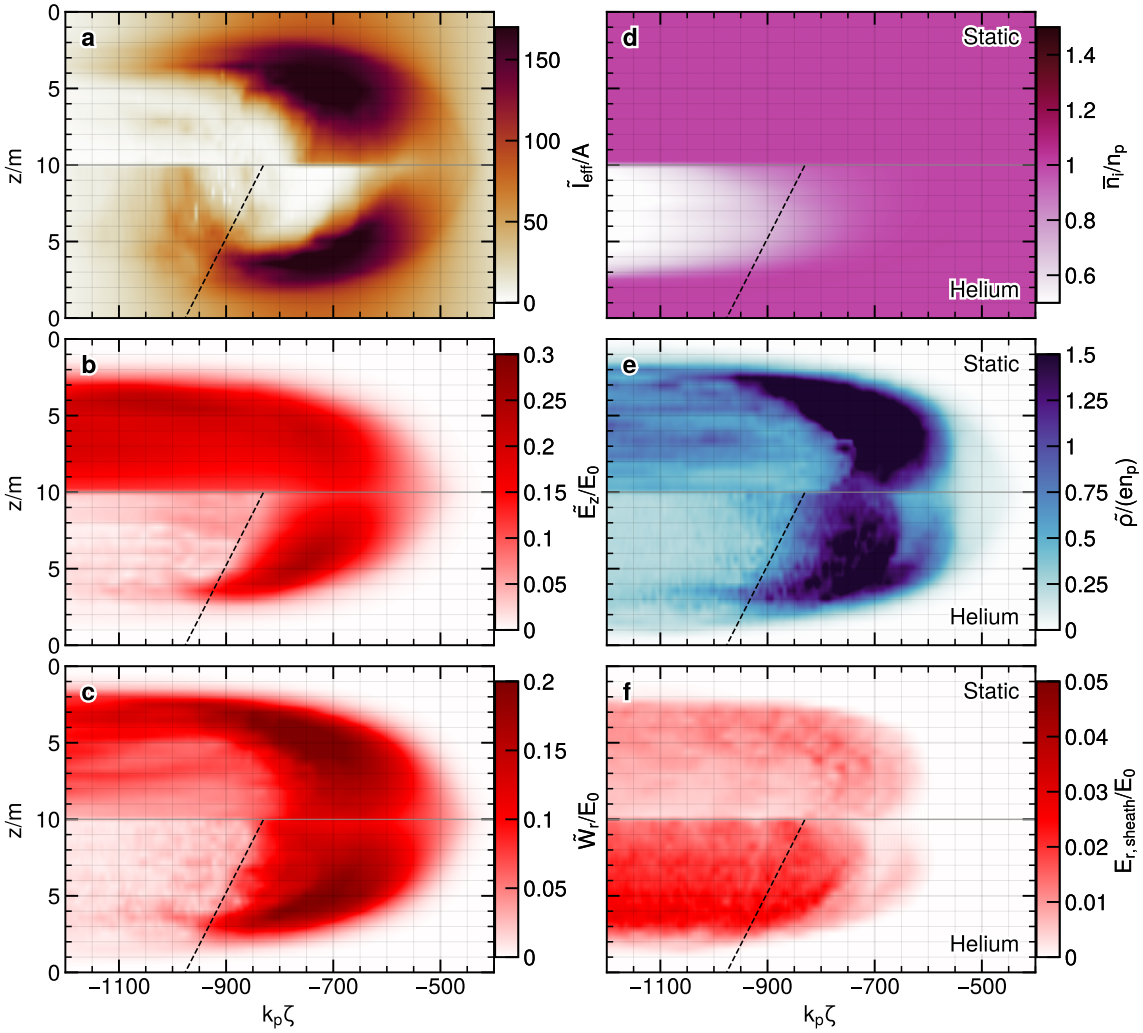

Figure 5.17: Beam undergoing self-modulation along the beam and plasma length for stationary and Helium ions. Mean envelope of the a) beam effective current, the b) longitudinal and c) radial wakefield component, the d) plasma ion density, e) plasma charge density and f) the sheath electric field. Propagation distance on the y-axis and beam slice on the x-axis. The dashed line indicates where the radial wakefield is significantly reduced ($\sim 0.1\,\tilde{W}_{r,\mathrm{peak}}$).

wakefield behind the black dashed line. As a result, the transverse wakefield acts less on the beam tail, which does not undergo self-modulation (Figure 5.17a). Earlier along the beam length relative to the dashed line, the wakefield magnitude remains comparable to the run with stationary ions. The reduced ion density results in the amplified detuning of the wakefield, and thus, the microbunches are defocused earlier along the beam. The sheath electric field (Figure 5.17f) increases by a factor of two due to a higher occurrence of transverse wavebreaking.

5.4 Ion Motion at the Experiment

The mass of plasma ions as the critical parameter for the influence of ion motion was varied at the DPS run, while other parameters were kept constant. The DPS allows for the reliable plasma operation with Xenon (with a density range of $0.68 \times 10^{14}\,\mathrm{cm}^{-3} < n_p < 9.38 \times 10^{14}\,\mathrm{cm}^{-3}$), Argon ($0.1 \times 10^{14}\,\mathrm{cm}^{-3} < n_p < 9.3 \times 10^{14}\,\mathrm{cm}^{-3}$) and Helium ($0.1 \times 10^{14}\,\mathrm{cm}^{-3} < n_p < 4.8 \times 10^{14}\,\mathrm{cm}^{-3}$). The cumulative effect on the self-modulating beam is used as a diagnostic for the suppression of the instability. The simulation parameters are identical to the Section 5.3, but with the mass of the plasma ions set to Xenon ($m_i/m_e = 241048$) or Argon ($m_i/m_e = 73345$). Parts of this section are published in (Turner *et al.*, 2024).

After a propagation distance of 10 m in plasma, the particles from the simulation are ballistically projected for another $\Delta s = 3.5\,\mathrm{m}$. This accounts for the vacuum gap between the plasma exit and the screen for the streak camera in the experiment. The radial position at the slit is given by $r_{\mathrm{slit}} = [(r + \Delta s p_r/p_z)^2 + (\Delta s p_\varphi/(r p_z))^2]^{1/2}$, with r the radial position, p_r the radial momentum and p_φ the azimuthal momentum of the beam particles at the plasma exit. The projection to the slit of the streak camera with a width of $80\,\mu\mathrm{m}$ is realised by randomly assigning an azimuthal angle φ to the beam particles and transforming to Cartesian coordinates, $(x,y)_{\mathrm{slit}} = (r_{\mathrm{slit}} \cos\varphi, r_{\mathrm{slit}} \sin\varphi)$.

Figure 5.18 shows the experimental and numerical observation, averaged over five runs for the beam charge at the streak camera. The beam distribution in vacuum verifies that the experimentally determined beam parameters are correctly reproduced in the simulations. The beam width remains bi-Gaussian with an increased width due to the beam divergence. The beam distributions for stationary ions, Xenon and Argon are qualitatively similar. The beam head is focussed within $200\,\mathrm{ps} < \zeta < 400\,\mathrm{ps}$, while for $\zeta < 200\,\mathrm{ps}$ the beam is self-modulated. The resulting train of microbunches appears as a spine in the simulation and is generally not observed in the streak images due to the finite resolution of the ns timescale shown here. On the ps-timescale, microbunches are observed for all gases within the front half of the beam. The beam particles defocussed by the radial wakefield appear as wings at $\zeta \sim 200\,\mathrm{ps}$.

For the Helium plasma, the beam distribution remains similar to the other gases for $-100\,\mathrm{ps} < \zeta$, such that SMI developed similarly. Beyond that interval, SMI is suppressed beyond that interval, observable by a higher beam charge towards the tail of the beam in good agreement between simulations and experimental observations. The planar profile of the beam is simultaneously measured by two streak cameras with slits that are orthogonally aligned to each other. This enabled to observe $Q_{\mathrm{slit}}(\zeta,y,x=0)$ and $Q_{\mathrm{slit}}(\zeta,y=0,x)$ and verify that the beam is radially symmetric and justifies that the numerical studies in cylindrical geometry are sufficient.

The charge at the slit summed over the transverse plane is compared between all gases for the experimental and numerical results in Figure 5.19. The absolute value for the experiment is chosen for the vacuum profile to match the simulation. It provides an estimate of how much SMI has evolved by the location and height of the peak charge. The peak is further towards the front of the beam and smaller in the simulations. This indicates that SMI is seeded by wakefields at a higher initial level compared to the beam and is coarser in the simulations compared to the experiment. Although the profiles of the charge at slit significantly differ

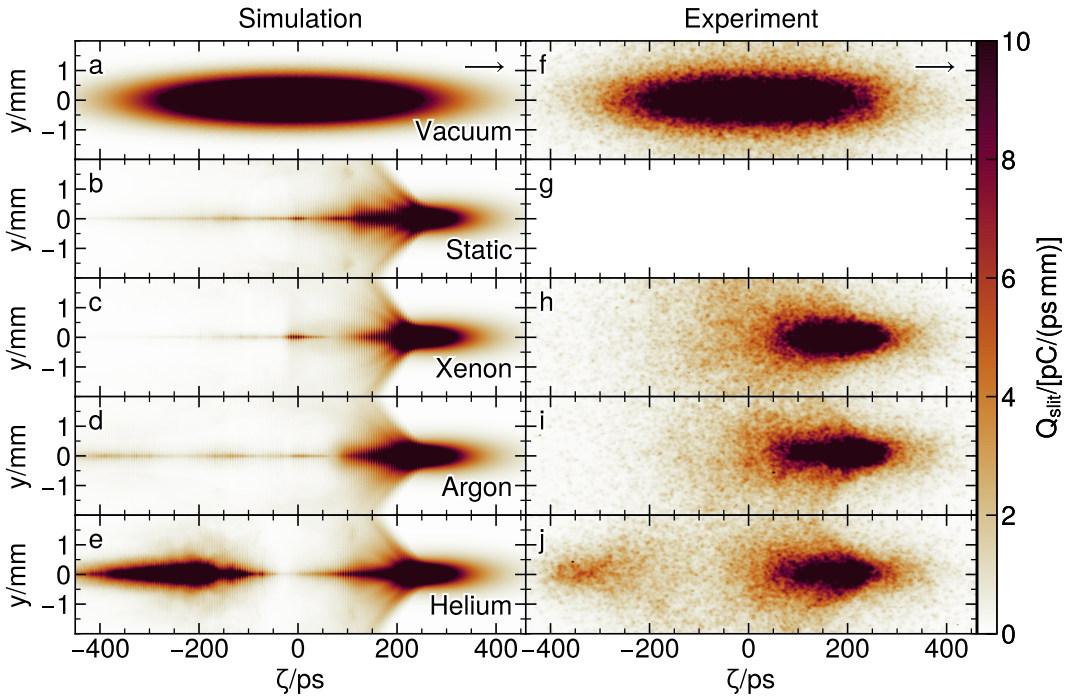

Figure 5.18: The time-resolved beam charge at slit after propagating for 10 m in a) a vacuum, or a plasma at with b) stationary ions, c) Xenon ions, d) Argon ions or e) Helium ions from simulations plus an additional 3.5 m propagation in a vacuum. f-j) respectively show the experimental observations. The distribution is averaged over five experimental or simulation runs, respectively. The plasma density is given by $n_p = 4.8 \times 10^{14}\,\mathrm{cm}^3$ and the colour scale is saturated to highlight the beam tail.

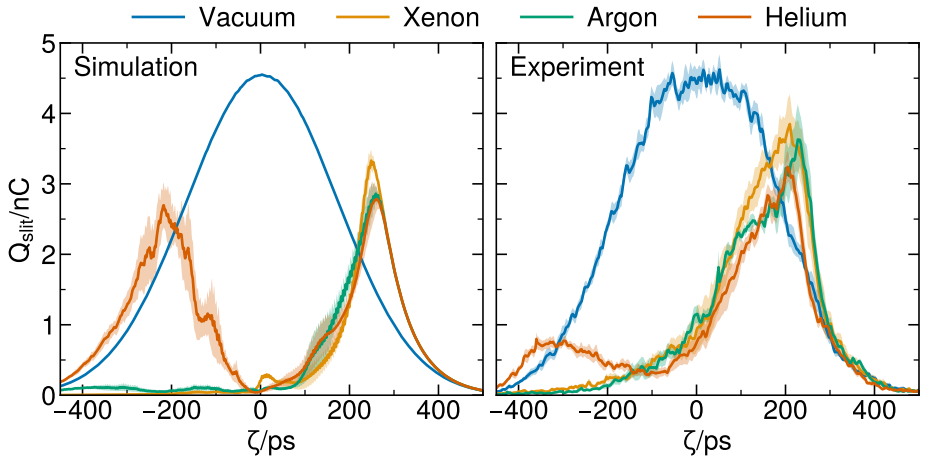

Figure 5.19: The transversely-integrated charge at slit from Figure 5.18. The mean (solid) and standard deviation (shaded area) over five runs.

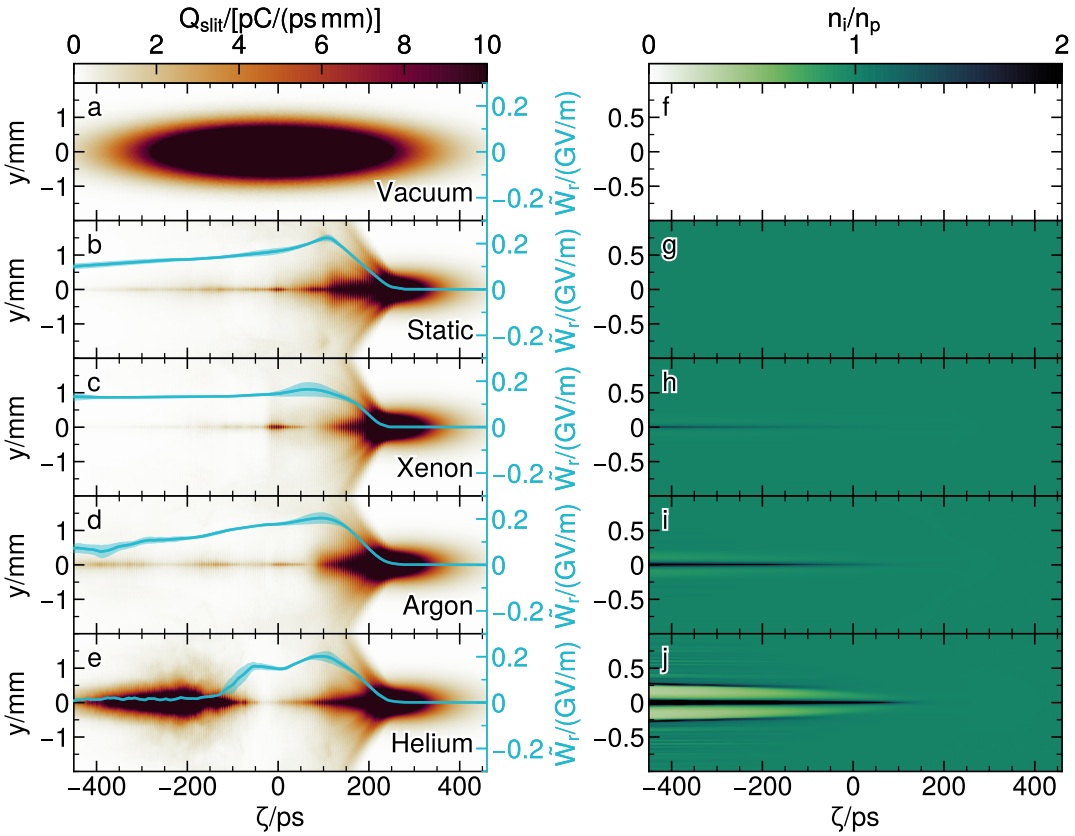

Figure 5.20: a-e) The beam charge at slit from simulation (Figure 5.18a-e), superimposed by the radial wakefield (cyan) at the plasma exit. The respective ion density at the plasma exit is shown in f-j).

between the experiment and the simulations, the physical result remains equivalent for all gases.

Figure 5.20 shows the radial wakefield and ion density, corresponding to the simulation results from Figure 5.18. A modulation in the ion density is apparent for all gases with finite ion mass, given by the appearance of the ion filament. The peak wakefield magnitude at $\zeta \sim 100\,\mathrm{ps}$ is comparable between all gases and the effect of ion motion is negligible. For stationary ions, the wakefield is resonantly driven for $\zeta > 100\,\mathrm{ps}$, but detunes further downstream such that the microbunches damp the wakefield. The wakefield peak in Xenon is slightly lower but remains constant along the beam length. Slight variations in the ion density result in a different beam shape due to the cumulative effect on SMI, but may compensate for the phase shift due to the decrease in phase velocity from the instability growth. For Argon, the ion mass is low enough to affect the wakefield amplitude but does not suppress SMI considerably, such that the beam remains fully modulated in agreement with previous numerical studies (Vieira *et al.*, 2014). For a longer beam in Argon or a higher plasma density, the motion of ions is detrimental enough to result in a higher beam charge towards the tail. For Helium, the results from Section 5.3 are reflected.

The simulations and experimental observations show that plasma ions with a finite mass

enhance not only transverse wavebreaking in agreement with previous studies by Minakov and K. V. Lotov (2024), Spitsyn *et al.* (2018), and Vieira *et al.* (2012, 2014), but also transverse decoherence and detuning of the wakefield from the modulated beam. These effects weaken the wakefield and suppress the SMI earlier along the beam and its propagation in plasma compared to non-evolving ions.

5.5 Ion Motion in Wakefield-driven Filamentation

Since SMI is the axisymmetric form of TTS, the investigations on wakefield-driven filamentation in Chapter 4 are briefly unified with the findings from this chapter on ion motion. The wakefield- and current-driven filamentation of the dilute or the dense beam from Section 4.6.2, but with Helium ions instead of stationary ions, is shown in Figure 5.21.

For the dilute beam, the modulation in the beam charge (Figure 5.21a) is equivalent to the simulation with stationary ions. However, the magnitude of the transverse electric field (Figure 5.21b) reduces for $k_p\zeta < -250 \approx -\sigma_\zeta$, which is in the non-linear regime where the filaments diverge (Section 4.5.1). The envelope of the electric field averaged over $|y| < \sigma_r$

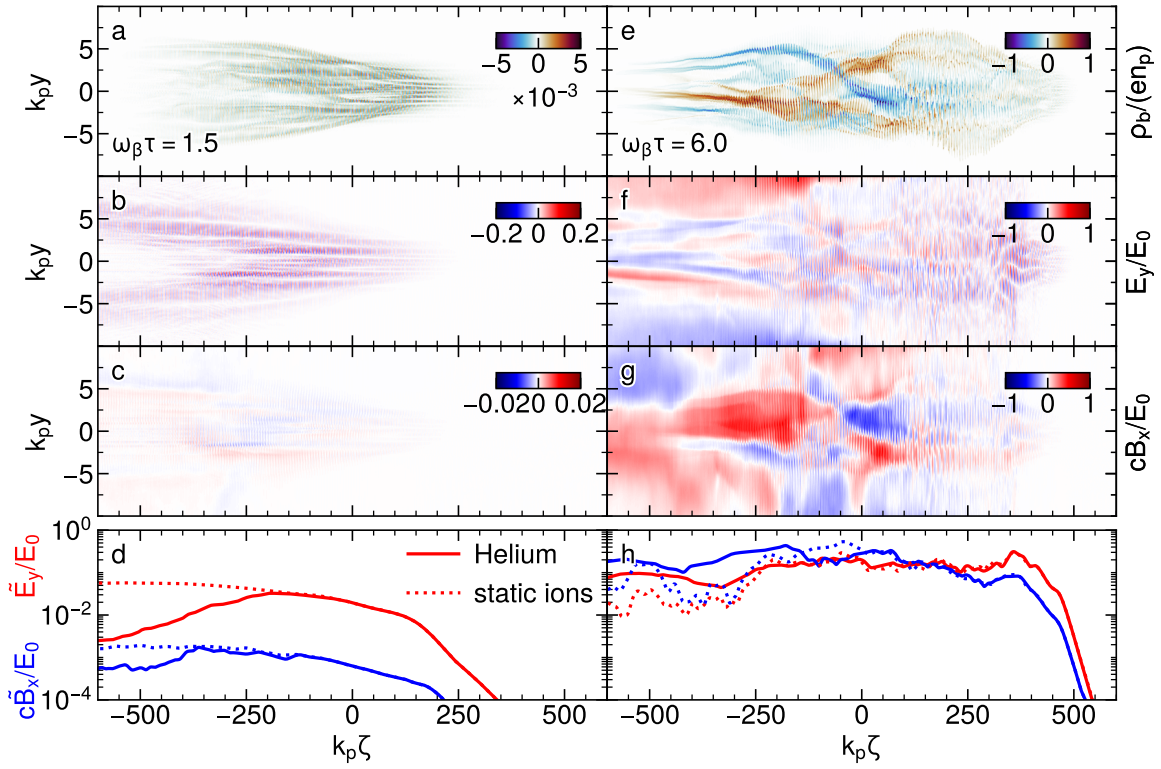

Figure 5.21: The effect of ion motion on wakefield- and current-driven filamentation of the beams in Figure 4.25. For the dilute beam, a) shows the charge density, b) the electric field and c) the magnetic field (different scale) excited by the beam from simulation. d) The field envelope averaged within $|y| < \sigma_r$ for Helium ions (solid) and stationary ions (dotted). The respective quantities for the dense beam are given in e-h).

(Figure 5.21d) shows a comparable growth in Helium and plasma with stationary ions beyond the exponential growth for $200 < k_p\zeta$. The rate at which the electric field reduces for $k_p\zeta < -250$ is similar to the rate at which it grows for $-200 < k_p\zeta < 200$. This trend agrees with the reduction of the wakefield observed for the self-modulating beam in Section 5.3.

For the dense beam, the beam charge density (Figure 5.21a) and electromagnetic fields (Figure 5.21b-c) are comparable for $\zeta > 0$. Over a short length, the beam is driven by the wakefield, and ion motion has no observable effect. As the transition from the wakefield- to current-driven filamentation occurs for $k_p\zeta < -100$, the beam divergence is weaker compared to the evolution in plasma with stationary ions. Further, the beam filaments are more compressed, and the longitudinal modulation is weaker. The electric and magnetic fields sustain their high magnitudes as the ion filaments pervade beyond the beam. This is in agreement with previous analytic and numeric work on the subsequent ion current filamentation by (Frederiksen *et al.*, 2004; Peterson *et al.*, 2021), amplifying the magnetic field.

Both in the TTS and its axisymmetric form, the SMI, the motion of plasma ions reduces the wakefield as the phase of the plasma wave varies transversely. The suppression of the beam modulation depends on whether the wakefield is considerably reduced during the exponential growth of the instability or as it saturates. This is in contrast to the TTS of an asymmetric beam composition, discussed in Section 4.5.2, where the beam species undergoes an additional wakefield-driven filamentation stage of the heavier species, but also to CFI, where the plasma undergoes a subsequent ion filamentation.

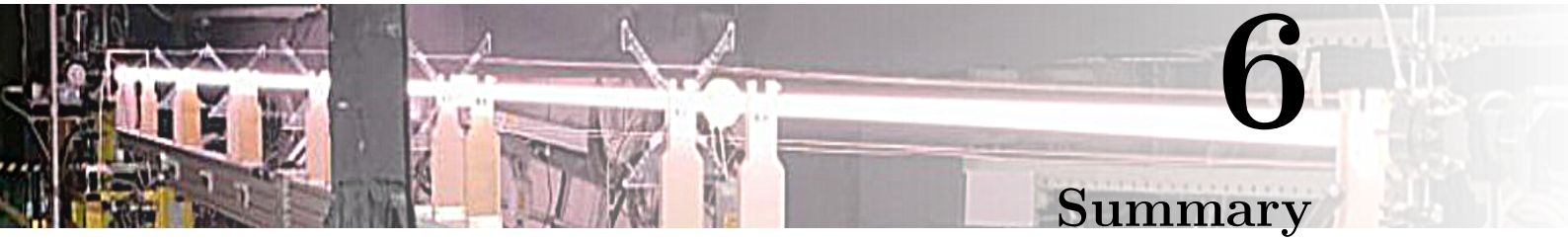

6 Summary

This doctoral work aimed to improve the understanding of filamentation instabilities for beams with well-defined extent in the laboratory and astrophysical context and investigate the feasibility of studying these in currently available PWFA. This was accomplished by a set of analytic and numerical approaches with comparisons made to laboratory studies in collaborative efforts with the AWAKE experiment. Chapter 1 began with an introduction to existing experiments with the potential to study these kinetic micro-instabilities resulting in filamentary electrostatic and electromagnetic fluctuations. Relevant phenomena in the astrophysical framework were briefly listed.

An overview of the relevant kinetic instabilities for unbounded systems and the utilised numerical methods was provided in Chapter 2, where the study was narrowed down to the current-driven filamentation and wakefield-driven two-stream instability. Moving to finite-sized beams, quasistatic simulations of these instabilities were compared to fully-electromagnetic simulations in Chapter 3. The quasistatic PIC method significantly reduced computing resources while not being prone to the non-physical grid heating in a cold plasma. Although previous numerical studies utilised the fully electromagnetic PIC method, the quasistatic model shows the ability to reflect the physics of beam filamentation for relativistic beams. Experimental measurements are generally limited, such that these simulations and analytic models provide a reliable and established method to deepen the physical understanding. With this foundation, the central questions of this work were explored.

6.1 Laboratory-Relevant Filamentation Instabilities

Summary: In Chapter 4, a three-dimensional, spatiotemporal theory for the wakefield-driven filamentation instability was presented for warm beams of finite size. This model extends previously published theories for two-dimensional cold beams and reflects laboratory-relevant configurations. The electrostatic plasma response in TTS leads to the growth of transverse filaments, comparable to CFI, with an additional longitudinal modulation.

The derived theory provides several significant advancements over previous studies and remarkable agreement with PIC simulations:

- The beam profile influences the growth rate and the seed level, with the growth rate at a fixed transverse position equivalent to a stream with the local beam density and the growth at a fixed longitudinal position proportional to the integrated beam density along the beam length.

- For beams with finite emittance, diffusion acts to damp small-scale filamentation. The dependency of the growth spectrum on the temperature is identified for dilute beams. Theory and simulations showed that the filamentation growth rate depends on $k_r = (k_x^2 + k_y^2)^{1/2}$. Explicit expressions for the dominant and cut-off wavenumber are calculated and depend on the propagation time in plasma and position within the beam. This arises as diffusion is spatially uniform while the filamentation instability grows along the beam length.
- Two-dimensional simulations reproduce the behaviour of three-dimensional simulations in the linear regime, with the caveat that $k_r = k_y$ in this reduced geometry, resulting in filaments that are more tightly clustered.

A general trend of the expected distance between filaments and the spectral growth along the beam and plasma length was found with unprecedented accuracy for warm beams with arbitrary spatial profiles. The predicted distance between filaments agreed well with previously published experimental results in Allen *et al.* (2012) and Verra, Amoedo, *et al.* (2024). For single-species beams, filamentation appeared to be suppressed when the predicted distance between filaments is larger than the rms beam width, $2\pi/k_{E\max} > \sigma_r$. These findings provide a crucial basis for designing laboratory astrophysics experiments investigating filamentation instabilities and for PWFA experiments seeking to avoid them.

The chapter compared the recent observation of beam filamentation at the AWAKE experiment to the introduced theory and simulation. With the currently achievable beam and plasma parameters, the proton beam is dominantly driven by the wakefield and not by a magnetic field and, thus, undergoes the transverse two-stream instability. Increasing the beam peak density to $\sim n_p/2$ reveals a spatiotemporal transition from wakefield- to current-driven beam filamentation due to the saturation of the wakefield, which has not been addressed before.

Outlook: One possible extension of this work is to connect the spatiotemporal theory of wakefield-driven filamentation to current-driven filamentation of warm dense beams dominated by the magnetic field instead of the wakefield, which leans on the work by Pathak *et al.* (2015). With a stronger focus on the astrophysical context, analytic investigation of the transition from electrostatic to electromagnetic regime of the filamentation instability is possible, relevant to dense beams with a smooth beam head. This requires including the saturation time and level of the wakefield, setting the initial condition for CFI.

Further, the potential usage of the advanced quasistatic method for simulations of collisionless shocks can significantly reduce computing resources and enable three-dimensional simulations. Investigating beam compositions with different particle masses on the current- and wakefield-driven filamentation is analogous to collisionless shocks of a mixture of plasma species. Further experimental studies would allow the analytic predictions to be tested across a larger parameter space.

6.2 Ion Motion in Wakefield-Driven Instabilities

Summary: The developed linear theory on wakefield-driven instabilities in Chapter 4 does not account for the different effects of the motion of ions. These effects are investigated in Chapter 5 in different experimentally-relevant setups. In agreement with semi-analytic

treatments and experimental observations, simulations verified that plasma ions experience the ponderomotive force from the beam-driven wakefield. The transverse deflection of the ions results in a heterogeneous ion density with the trough ion density at the peak of the transverse wakefield. As a result, the phase of the plasma wave shifts along the transverse coordinate.

Three saturation mechanisms of the SMI were identified to be enhanced by the phase shift, where the previously studied transverse wavebreaking was one of them. Several new aspects were addressed:

- The plasma density wave bows inward, causing transverse decoherence and a reduction of the wakefield strength. Yet, a small bowing temporarily enhances the transverse wakefield. Additionally, the wakefield detunes from the train of microbunches and, thus, from the resonant condition.
- The dominating effect for the wakefield decrease is studied in the cases of a wakefield with a constant magnitude or being resonantly driven, which represents the early stage and saturation of the SMI. The transverse decoherence predominantly reduces the wakefield at the early stage of SMI. When the beam is strongly modulated, the transverse wavebreaking dominates, while the detuning of the wakefield from the resonant condition cuts down the effective current of the beam.

Transverse wavebreaking depends on the transverse variation of the plasma phase. This variation in the plasma phase also leads to a transverse gradient in the plasma charge density, $\nabla_r \rho_p$, resulting in transverse decoherence. The phase shift scales with the cube root of the ion mass and remains negligible for the beam and plasma parameters at AWAKE when using plasma ions heavier than Argon ions in agreement with experimental results. However, the stability of the plasma wake is weakened over long periods, even for higher ion mass, as the detrimental effect of ion motion continues to grow after the beam has passed.

Outlook: Future work may involve the development of a theory which considers the nonlinear change in wakefield amplitude depending on the transverse variation of the phase. A general expression for the decrease in wakefield amplitude based on ion mass and beam charge (or laser intensity) allows the identification of the parameter space where ion motion is negligible. This is a crucial foundation for wakefield experiments aiming to avoid such effects, whether driven by a short beam or resonantly driven by a train of microbunches.

The study focused on the axisymmetric SMI. However, it can be extended to TTS in contrast to the amplifying effect on the current-driven filamentation (Peterson *et al.*, 2021; Ruyer *et al.*, 2015) as depicted in Section 5.5. The dominating saturation mechanism for TTS and how it scales with the transverse wavenumber may also be subject to future work.

6.3 Concluding Remarks

This work investigated the applicability of beam-driven wakefield accelerators to study filamentation instabilities of relativistic particle streams interacting with plasmas in an astrophysical context. Many studies on collisionless shocks linked to Fermi-type accelerated high-energy particles focus on the Weibel or current filamentation instability. Nonetheless, some astrophysical regions exist where the acceleration of particles to ultra-high energies

is connected to the Landau resonance with wakefields, e.g. in active galactic nuclei or the foreshock region. Given the currently achievable parameter space in experiments, the work mainly focused on wakefield-driven instabilities. Ultimately, the remarkable agreement of the analytic model with simulations and experiments proves fertile ground for designing future experiments and for further research in the astrophysical context.

A Numerical Considerations

A.1 Non-Physical Instabilities

The non-physical heating of the plasma, observed in PIC simulations with higher stream densities, occurs due to the spatial discretisation from the grid and a finite number of macroparticles (Pukhov, 2015). Consequently, the plasma phasespace is altered, which may mimic physical phenomena and lead to imprecise conclusions. Grid heating occurs if the Debye wavelength, $k_p\lambda_D = \sigma_{pz}/(m_e c)$, is not resolved by the spatial grid. High-frequency modes of the plasma waves, not resolved by the grid, are aliased to lower frequencies. As a result, the grid adds imaginary roots to the dispersion relation for the warm plasma and the resulting kinetic instability increases the plasma temperature exponentially until the Debye wavelength is resolved by the grid. This limit was predicted to $\lambda_D \approx \Delta z/\pi$ for a streaming plasma without a driver by Birdsall and Langdon (2018).

The plasma temperature for the stream in Figure 3.2 is shown in Figure A.1a) as a function of the grid size. For $k_p\zeta < -12$, the momentum spread of the plasma electrons exponentially heats up by several orders of magnitude independent of the grid size. For very low resolution, high peaks occur for $\sim -12/k_p$ as plasma electrons are self-injected. The saturated temperature $\hat{\sigma}_{p\zeta}$ increases with grid size and is by a factor of two below the limit by Birdsall and Langdon (2018).

The median of the saturated temperature in Figure A.1b) additionally increases with the density of the stream. For low charge densities of the stream $\rho_b \leq 0.3\, e n_p$, the value from simulation agrees well with the fit $\hat{\sigma}_{p\zeta} \sim n_b \Delta z$, with the absolute value of the fit set to align with the dataset from $\rho_b = 0.2\, e n_p$. Within this range, the plasma saturates at lower temperatures than the limit from Birdsall and Langdon (2018) such that the condition is eased. For higher charge densities of the driving stream, $\rho_b > 0.4\, e n_p$, the stability condition for the plasma temperature is worse relative to a non-driven plasma stream. The later is in accordance with the work by Cormier-Michel *et al.* (2008) demonstrating a worse stability condition for a laser-driven plasma wake relative to a non-driven plasma. Self-injection for low resolutions increases with the density and results in the deviation from the fit.

To mitigate grid-heating, the fully-electromagnetic PIC simulations are conducted in two-dimensional geometry and the quasistatic PIC code QV3D is utilised for three-dimensional simulations to reach a sufficiently high grid resolution. Further, the exponential heating can be mitigated by a low-pass filter, generally by choosing a quadratic particle shape and applying a binomial current filter.

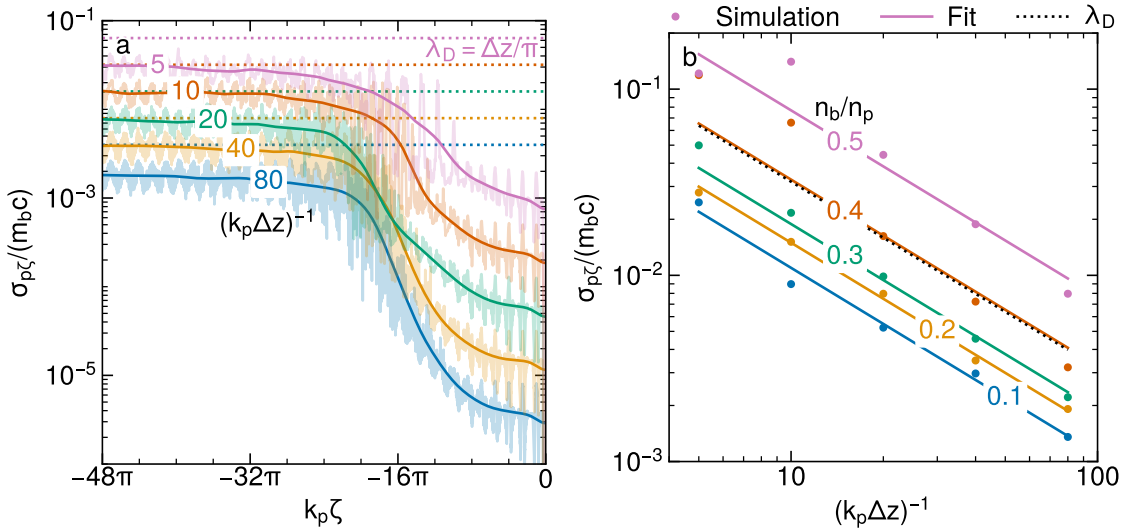

Figure A.1: Non-physical plasma heating due to the discretised configuration space. a) The plasma temperature along the length for the stream in Figure 3.2 for different grid resolutions Δz, and its averaged value over the plasma period. b) The saturated plasma temperature after grid heating from simulation ($\cdot$) and a polynomial fit (–) as a function of the grid resolution at different stream densities. Dotted lines correspond to the saturated Debye wavelength from Birdsall and Langdon (2018).

A.2 Methods to Mitigate Numerical Instabilities

Instead of the commonly used Yee-solver (finite-difference time-domain scheme with a second-order central difference) (Yee, 1966), the custom dispersion-free fei solver of type Xu (Xu *et al.*, 2020) combined with a binomial low-pass filter for the current deposition is used to strongly mitigate for numerical instabilities and avoid the effect of spatial and temporal grid aliasing between the particles with numerical modes of the grid. The numerical growth occurs due to Cherenkov resonance in the Brillouin zone between the streaming beam particles and the grid of the electromagnetic field when the phase velocity of light for the solver has a subluminal phase velocity, $u_\psi < c$ and can lead to particle-wave resonances with the relativistic stream. This may result in transverse deflection of the particles and transverse currents, which imitate the instabilities studied in this work. Additionally, a space-charge field arises when finite-difference errors are larger than $1/\gamma^2$ (Xu *et al.*, 2020), relevant for the ultrarelativistic beams considered here. Most commonly, the relativistic equation of motion is discretised with the finite-difference time-centred Boris algorithm (Boris, 1970). The simulations conducted in this work additionally utilised the Vay pusher (Vay, 2008), an extension of the Boris pusher for relativistic particles, $\gamma_b > 5$.

If no current filter is applied in the fully-electromagnetic simulations, exemplary shown in Figure A.2a), a non-physical seed magnetic field occurs after the short beam propagated $100/\omega_p$ in a vacuum. A 5-pass compensated binomial current smoother is required within the conducted studies to avoid this spurious field behind the beam as illustrated in Figure A.2b). For the quasistatic simulations, no current smoother is required to omit the spurious field behind the beam.

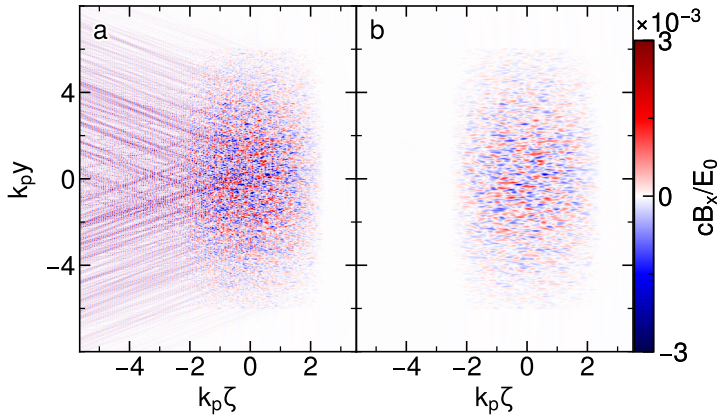

Figure A.2: Effect of current smoothing on the magnetic field for a quasineutral beam propagating $\omega_p t = 100$ in vacuum. The excited magnetic field by applying a) no filter or b) a 5-pass compensated binomial filter on the beam current.

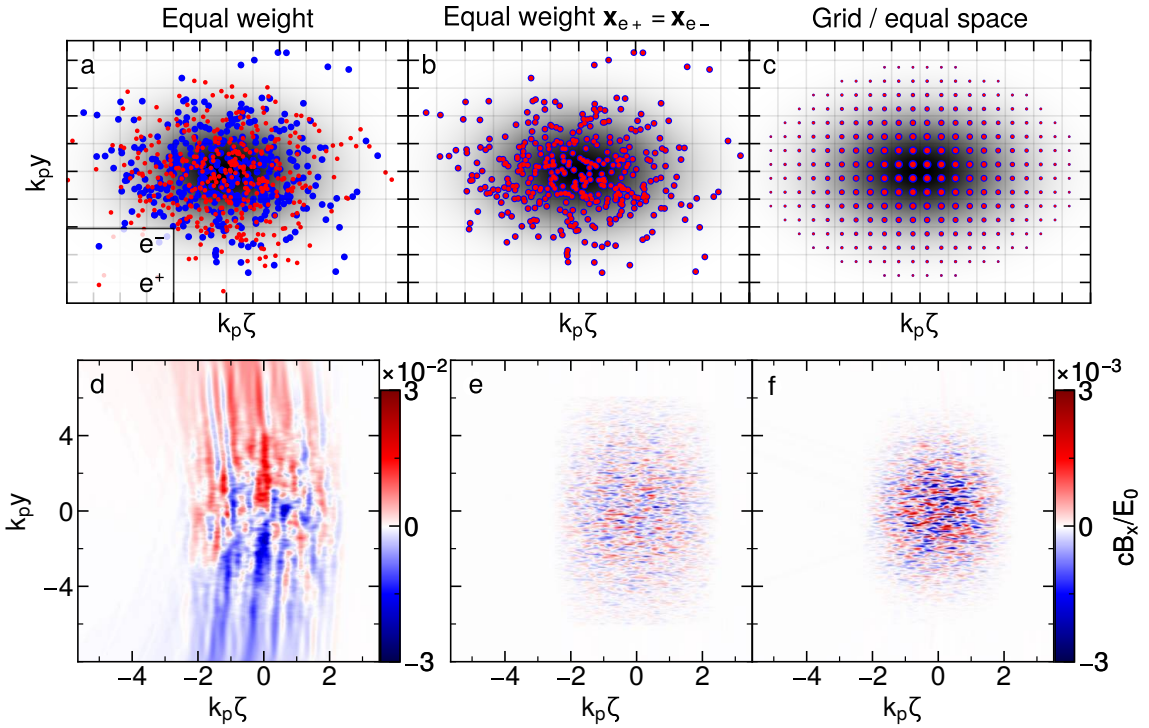

Figure A.3: Seed fields from initialising macroparticles of the quasineutral beam. The negatively (blue) and positively (red) charged particles are initialised a) equally weighted with different positions or b) identical positions, or c) equally spaced. The marker size indicates the weight of the particles. The respective seed magnetic field after the beam propagated for $100/\omega_p$ in a vacuum is shown in d), e) and f).

The instabilities grow from the electromagnetic fields seeded by the macroparticles of the beam, which depends on the number of macroparticles and the initialisation method. The momentum of the particles is randomly sampled from the Maxwell distribution. For equally-weighted particles, the position can be either randomly sampled (Figure A.3a), or with identical initial position between the particles with opposite charge (Figure A.3b). To ensure a uniform resolution of the simulation domain, which becomes essential for a low number of macroparticles, the particles can be loaded equally spaced with different weights (grid-loading), shown in Figure A.3c). Charged beam particles undergo betatron oscillation, which may decrease the phasespace resolution for grid-loaded particles as the few particles at the beam centre with high weight interchange with a high amount of particles with low weight at the beam edge. Most of the conducted studies here are limited to a couple of betatron timescales, $< 6/\omega_\beta$ and particles are grid-loaded.

The initial fields excited by a quasineutral beam after a propagation time of $\omega_p \tau = 100$ is shown in Figure A.3c-e). For equal-weighted particle seeding with random particle position (Figure A.3d), strong fringe fields are excited as the transverse beam slices are not neutral. These fields can be avoided by randomly seeding the position of the positrons and assigning the same positions to the electrons, as illustrated in Figure A.3e). The peak value of the seed field is lower relative to the magnetic field excited by the same total amount of equally-spaced particles in Figure A.3f), but the signal-to-noise ratio varies along the beam. The seed field is higher at the fringe areas of the beam since these areas are poorly resolved by the macroparticles including the beam head where the filamentation instabilities are seeded.

A.3 Spatial Convergence of Filamentation Instabilities

The numerical studies consistently include convergence checks of the resolved phasespace, e.g. of the propagation step, the spatial grid and the number of macroparticles implicitly resolving the momentum space. The results of the simulations vary within the statistical uncertainties when changing the numerical resolution and remain reproducible with a variance much lower than the mean of a quantity.

Figure A.4 shows the dependency of the field energy when decreasing the grid resolution by a factor of four from the baseline, i.e. from $k_p \Delta(x, y) = (0.025, 0.025)$ to $k_p \Delta(x, y) = (0.05, 0.05)$. For a constant number of beam particles, the initial field energy (see Figure A.4a) reduces as each grid is filled with four times more particles relative to the baseline. For a constant number of particles per cell, the initial field energy is slightly higher since the beam is coarser, consisting of four times fewer particles. In both cases, the exponential growth is converged. But during the nonlinear stage in which filaments merge, the electric and magnetic field components are slightly higher. For a negligible change in the field energies within the statistical uncertainties, the total number of beam particles must be scaled by $(\Delta x \Delta y)^{1/2}$ to keep the initial seed comparable. In this example, this corresponds to reducing the number of beam particles by a factor of two.

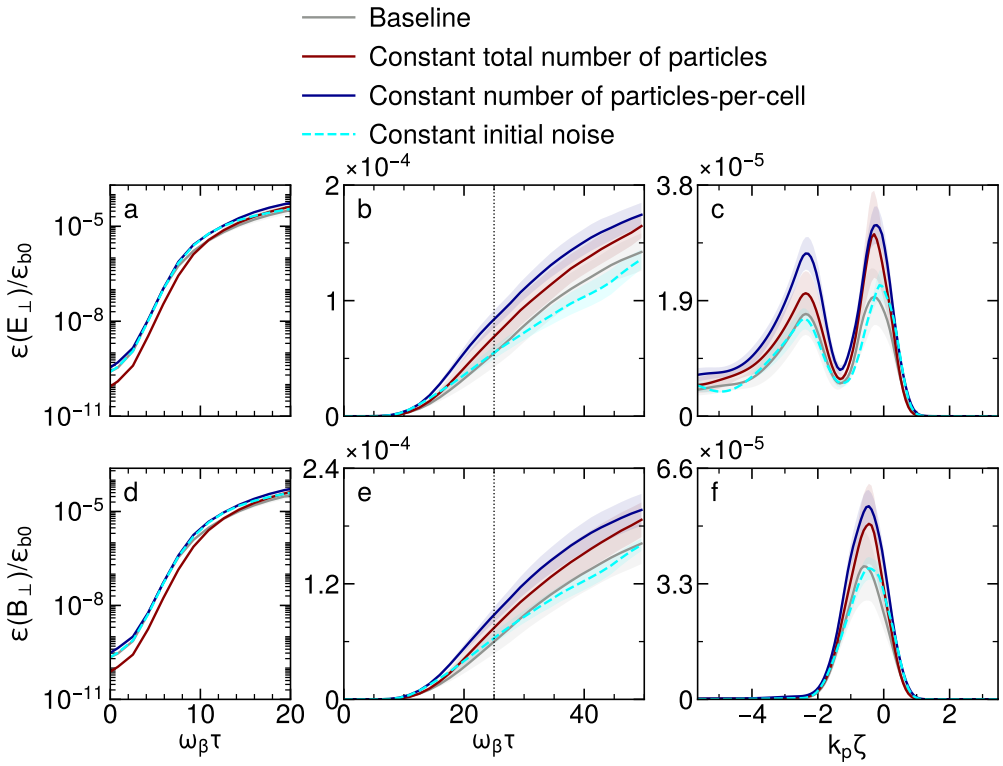

Figure A.4: Convergence in configuration space of the electromagnetic field energy for the short quasineutral beam undergoing CFI, shown in Figure 3.6.

B Contributions Made by the Author

Publications

- E. Walter, J. P. Farmer, *et al.*, 2024. *Wakefield-driven filamentation of warm beams in plasma.* arXiv: 2406.07977. URL: https://arxiv.org/abs/2406.07977 [accepted by Phys. Rev. E]
- M. Turner, E. Walter, *et al.* (AWAKE Collaboration), 2024. *Experimental Observation of Motion of Ions in a Resonantly Driven Plasma Wakefield Accelerator.* arXiv: 2406.16361. URL: https://arxiv.org/abs/2406.16361 [submitted to Phys. Rev. Let.]
- L. Verra, C. Amoedo, *et al.* (AWAKE Collaboration), 2024. "Filamentation of a relativistic proton bunch in plasma". In: *Phys. Rev. E* 109 (5), p. 055203. DOI: 10.1103/PhysRevE.109.055203. URL: https://link.aps.org/doi/10.1103/PhysRevE.109.055203

Conferences

Talks

- Erwin Walter, John Farmer, Martin Weidl, Patric Muggli, Alexander Pukhov, Frank Jenko, *Towards Laboratory Astrophsics in Plasma Wakefield Accelerators*, 65th Annual Meeting APS Plasma Physics (2023).

Posters

- Erwin Walter, John Farmer, Marlene Turner, Frank Jenko. *Ion Motion in Resonantly-Driven Plasma Wakefield Accelerators*, 65th Annual Meeting APS Plasma Physics (2023).
- Erwin Walter, John Farmer, Martin Weidl, Patric Muggli, Alexander Pukhoh, Frank Jenko. *Towards Laboratory Astrophysics in Wakefield Accelerators*, DPG Spring Meeting 2022 (online) and 2023.
- Erwin Walter, Martin Weidl, John Farmer, Patric Muggli, Frank Jenko. *Current Filamentation Instabilities of Proton Beams in Proton Driven Wakefield Accelerators*, 63rd Annual Meeting APS Plasma Physics 2021 and DPG Spring Meeting 2021 (online).

Internal Talks

- Erwin Walter, John Farmer, Martin Weidl, Alexander Pukhov, Frank Jenko, *Wakefield-driven filamentation of warm beams in plasma*, AWAKE Collaboration meeting 2024.
- Erwin Walter, John Farmer, Marlene Turner, Frank Jenko. *Ion Motion in Resonantly-Driven Plasma Wakefield Accelerators*, AWAKE Collaboration meeting 2023.
- Erwin Walter, John Farmer, Martin Weidl, Alexander Pukhov, Frank Jenko, *Filamentation at AWAKE*, AWAKE Collaboration meeting 2021 and HEPP progress talk 2022.

Bibliography

Abramowitz, M. and I. A. Stegun, 1964. *Handbook of Mathematical Functions with Formulas, Graphs, and Mathematical Tables*. ninth Dover printing, tenth GPO printing. New York: Dover.

Adli, E. *et al.*, 2018. "Acceleration of electrons in the plasma wakefield of a proton bunch". In: *Nature* 561.7723, pp. 363–367. ISSN: 1476-4687. DOI: 10.1038/s41586-018-0485-4. URL: https://doi.org/10.1038/s41586-018-0485-4.

Albert, F. *et al.*, 2021. "2020 roadmap on plasma accelerators". In: *New Journal of Physics* 23.3, p. 031101. DOI: 10.1088/1367-2630/abcc62. URL: https://dx.doi.org/10.1088/1367-2630/abcc62.

Allen, B. *et al.*, 2012. "Experimental Study of Current Filamentation Instability". In: *Phys. Rev. Lett.* 109 (18), p. 185007. DOI: 10.1103/PhysRevLett.109.185007. URL: https://link.aps.org/doi/10.1103/PhysRevLett.109.185007.

Arrowsmith, C. D. *et al.*, 2021. "Generating ultradense pair beams using 400 GeV/c protons". In: *Phys. Rev. Res.* 3 (2), p. 023103. DOI: 10.1103/PhysRevResearch.3.023103. URL: https://link.aps.org/doi/10.1103/PhysRevResearch.3.023103.

Batsch, F. *et al.* (AWAKE Collaboration), 2021. "Transition between Instability and Seseded Self-Modulation of a Relativistic Particle Bunch in Plasma". In: *Phys. Rev. Lett.* 126 (16), p. 164802. DOI: 10.1103/PhysRevLett.126.164802. URL: https://link.aps.org/doi/10.1103/PhysRevLett.126.164802.

Bellan, P. M., 2006. "Elementary plasma waves". In: *Fundamentals of Plasma Physics*. Cambridge University Press, pp. 146–173.

Bers, A., 1983. *Handbook of Plasma Physics. Vol. 1*. Ed. by M. Rosenbluth and R. Sagdeev. Amsterdam: North-Holland Publ. Chap. 3.2, pp. 451–517.

Birdsall, C. and A. Langdon, 2018. *Plasma Physics via Computer Simulation*. CRC Press. ISBN: 9781482263060. DOI: 10.1201/9781315275048. URL: http://dx.doi.org/10.1201/9781315275048.

Bludman, S. A., K. M. Watson, and M. N. Rosenbluth, 1960. "Statistical Mechanics of Relativistic Streams. II". In: *The Physics of Fluids* 3.5, pp. 747–757. ISSN: 0031-9171. DOI: 10.1063/1.1706121. eprint: https://pubs.aip.org/aip/pfl/article-pdf/3/5/747/12499127/747_1_online.pdf. URL: https://doi.org/10.1063/1.1706121.

Bohdan, A. *et al.*, 2021. "Magnetic Field Amplification by the Weibel Instability at Planetary and Astrophysical Shocks with High Mach Number". In: *Phys. Rev. Lett.* 126 (9), p. 095101. DOI: 10.1103/PhysRevLett.126.095101. URL: https://link.aps.org/doi/10.1103/PhysRevLett.126.095101.

Boris, J., 1970. "Relativistic plasma simulation-optimization of a hybrid code". In: *Proc. 4th Conf. Num. Sim. Plasmas*, pp. 3–67.

Bret, A. and C. Deutsch, 2006. "A fluid approach to linear beam plasma electromagnetic instabilities". In: *Physics of Plasmas* 13.4, p. 042106. ISSN: 1070-664X. DOI: 10.1063/1.2196876. eprint: https://pubs.aip.org/aip/pop/article-pdf/doi/10.1063/1.2196876/16011061/042106_1_online.pdf. URL: https://doi.org/10.1063/1.2196876.

Bret, A., M.-C. Firpo, and C. Deutsch, 2004. "Collective electromagnetic modes for beam-plasma interaction in the whole k space". In: *Phys. Rev. E* 70 (4), p. 046401. DOI: 10.1103/PhysRevE.70.046401. URL: https://link.aps.org/doi/10.1103/PhysRevE.70.046401.

Bret, A., M.-C. Firpo, and C. Deutsch, 2005. "Characterization of the Initial Filamentation of a Relativistic Electron Beam Passing through a Plasma". In: *Phys. Rev. Lett.* 94 (11), p. 115002. DOI: 10.1103/PhysRevLett.94.115002. URL: https://link.aps.org/doi/10.1103/PhysRevLett.94.115002.

Bret, A., L. Gremillet, and D. Bénisti, 2010. "Exact relativistic kinetic theory of the full unstable spectrum of an electron-beam–plasma system with Maxwell-Jüttner distribution functions". In: *Phys. Rev. E* 81 (3), p. 036402. DOI: 10.1103/PhysRevE.81.036402. URL: https://link.aps.org/doi/10.1103/PhysRevE.81.036402.

Bret, A., L. Gremillet, D. Bénisti, and E. Lefebvre, 2008. "Exact Relativistic Kinetic Theory of an Electron-Beam–Plasma System: Hierarchy of the Competing Modes in the System-Parameter Space". In: *Phys. Rev. Lett.* 100 (20), p. 205008. DOI: 10.1103/PhysRevLett.100.205008. URL: https://link.aps.org/doi/10.1103/PhysRevLett.100.205008.

Bret, A., L. Gremillet, and M. E. Dieckmann, 2010. "Multidimensional electron beam-plasma instabilities in the relativistic regime". In: *Physics of Plasmas* 17.12, p. 120501. ISSN: 1070-664X. DOI: 10.1063/1.3514586. eprint: https://pubs.aip.org/aip/pop/article-pdf/doi/10.1063/1.3514586/16019035/120501_1_online.pdf. URL: https://doi.org/10.1063/1.3514586.

Budker, G. J. and A. A. Naumov, 1956. "Relativistic Stabilized Electron Beam: Ii. Brief Review Of Experimental Work". In: *CERN Symposium on High-Energy Accelerators and Pion Physics*, pp. 76–79.

Bulanov, S. V., F. Pegoraro, A. M. Pukhov, and A. S. Sakharov, 1997. "Transverse-Wake Wave Breaking". In: *Phys. Rev. Lett.* 78 (22), pp. 4205–4208. DOI: 10.1103/PhysRevLett.78.4205. URL: https://link.aps.org/doi/10.1103/PhysRevLett.78.4205.

Bykov, A. M., F. Vazza, J. A. Kropotina, K. P. Levenfish, and F. B. S. Paerels, 2019. "Shocks and Non-thermal Particles in Clusters of Galaxies". In: *Space Science Reviews* 215.1, p. 14. ISSN: 1572-9672. DOI: 10.1007/s11214-019-0585-y. URL: https://doi.org/10.1007/s11214-019-0585-y.

Caldwell, A. and K. V. Lotov, 2011. "Plasma wakefield acceleration with a modulated proton bunch". In: *Physics of Plasmas* 18.10, p. 103101. ISSN: 1070-664X. DOI: 10.1063/1.3641973. eprint: https://pubs.aip.org/aip/pop/article-pdf/doi/10.1063/1.3641973/13613329/103101_1_online.pdf. URL: https://doi.org/10.1063/1.3641973.

Califano, F., R. Prandi, F. Pegoraro, and S. V. Bulanov, 1998. "Nonlinear filamentation instability driven by an inhomogeneous current in a collisionless plasma". In: *Phys. Rev. E* 58 (6), pp. 7837–7845. DOI: 10.1103/PhysRevE.58.7837. URL: https://link.aps.org/doi/10.1103/PhysRevE.58.7837.

Chang, P. *et al.*, 2016. "THE LINEAR INSTABILITY OF DILUTE ULTRARELATIVISTIC PAIR BEAMS". In: *The Astrophysical Journal* 833.1, p. 118. DOI: 10.3847/1538-4357/833/1/118. URL: https://dx.doi.org/10.3847/1538-4357/833/1/118.

Chen, F. F., 2016. In: *Introduction to Plasma Physics and Controlled Fusion*. 3rd ed. Springer Interational Publishing Switzerland 2016. Chap. 7.3, pp. 222–224. DOI: 10.1007/978-3-319-22309-4.

Chen, P., J. M. Dawson, R. W. Huff, and T. Katsouleas, 1985. "Acceleration of Electrons by the Interaction of a Bunched Electron Beam with a Plasma". In: *Phys. Rev. Lett.* 55

(14), pp. 1537–1537. DOI: 10.1103/PhysRevLett.55.1537. URL: https://link.aps.org/doi/10.1103/PhysRevLett.55.1537.

Clayton, C. E. *et al.*, 2016. "Self-mapping the longitudinal field structure of a nonlinear plasma accelerator cavity". In: *Nature Communications* 7.1, p. 12483. ISSN: 2041-1723. DOI: 10.1038/ncomms12483. URL: https://doi.org/10.1038/ncomms12483.

Cormier-Michel, E. *et al.*, 2008. "Unphysical kinetic effects in particle-in-cell modeling of laser wakefield accelerators". In: *Phys. Rev. E* 78 (1), p. 016404. DOI: 10.1103/PhysRevE.78.016404. URL: https://link.aps.org/doi/10.1103/PhysRevE.78.016404.

Courant, R., K. Friedrichs, and H. Lewy, 1928. "Über die partiellen Differenzengleichungen der mathematischen Physik". In: *Mathematische Annalen* 100.1, pp. 32–74. ISSN: 1432-1807. DOI: 10.1007/BF01448839. URL: https://doi.org/10.1007/BF01448839.

Davidson, R. and P. Schram, 1968. "Nonlinear oscillations in a cold plasma". In: *Nuclear Fusion* 8.3, p. 183. DOI: 10.1088/0029-5515/8/3/006. URL: https://dx.doi.org/10.1088/0029-5515/8/3/006.

Davidson, R. C., D. A. Hammer, I. Haber, and C. E. Wagner, 1972. "Nonlinear Development of Electromagnetic Instabilities in Anisotropic Plasmas". In: *The Physics of Fluids* 15.2, pp. 317–333. ISSN: 0031-9171. DOI: 10.1063/1.1693910. eprint: https://pubs.aip.org/aip/pfl/article-pdf/15/2/317/12743024/317_1_online.pdf. URL: https://doi.org/10.1063/1.1693910.

Dawson, J. M., 1959. "Nonlinear Electron Oscillations in a Cold Plasma". In: *Phys. Rev.* 113 (2), pp. 383–387. DOI: 10.1103/PhysRev.113.383. URL: https://link.aps.org/doi/10.1103/PhysRev.113.383.

Drake, R. P., 2006. "Introduction to High-Energy-Density Physics". In: *High-Energy-Density Physics: Fundamentals, Inertial Fusion, and Experimental Astrophysics*. Ed. by L. Davison and Y. Horie. Berlin, Heidelberg: Springer Berlin Heidelberg, pp. 1–17. ISBN: 978-3-540-29315-6. DOI: 10.1007/3-540-29315-9_1. URL: https://doi.org/10.1007/3-540-29315-9_1.

Einstein, A., R. Fürth, and A. Cowper, 1915. "Investigations on the theory of the Brownian movement". In: URL: https://ia801603.us.archive.org/14/items/investigationont0000albe/investigationont0000albe.pdf.

Esarey, E., C. B. Schroeder, and W. P. Leemans, 2009. "Physics of laser-driven plasma-based electron accelerators". In: *Rev. Mod. Phys.* 81 (3), pp. 1229–1285. DOI: 10.1103/RevModPhys.81.1229. URL: https://link.aps.org/doi/10.1103/RevModPhys.81.1229.

Esarey, E., B. A. Shadwick, P. Catravas, and W. P. Leemans, 2002. "Synchrotron radiation from electron beams in plasma-focusing channels". In: *Phys. Rev. E* 65 (5), p. 056505. DOI: 10.1103/PhysRevE.65.056505. URL: https://link.aps.org/doi/10.1103/PhysRevE.65.056505.

Faĭnberg, Y. B., V. D. Shapiro, and V. I. Shevchenko, 1969. "Nonlinear Theory of Interaction between a "Monochromatic" Beam of Relativistic Electrons and a Plasma". In: *Soviet Journal of Experimental and Theoretical Physics* 57, p. 966. URL: http://jetp.ras.ru/cgi-bin/e/index/e/30/3/p528?a=list.

Fermi, E., 1954. "Galactic Magnetic Fields and the Origin of Cosmic Radiation." In: *The Astrophysical Journal* 119, p. 1. DOI: 10.1086/145789.

Fiuza, F., G. Swadling, A. Grassi, and et al., 2020. "Electron acceleration in laboratory-produced turbulent collisionless shocks." In: *Nat. Phys.* 16, pp. 916–920. DOI: 10.1038/s41567-020-0919-4. URL: https://doi.org/10.1038/s41567-020-0919-4.

Fonseca, R. *et al.*, eds. (Apr. 2002). *OSIRIS: A Three-Dimensional, Fully Relativistic Particle in Cell Code for Modeling Plasma Based Accelerators*. Computational Science - ICCS

2002 2331. Springer Berlin Heidelberg. DOI: 10.1007/3-540-47789-6_36. URL: https://doi.org/10.1007/3-540-47789-6_36.

Frederiksen, J. T., C. B. Hededal, T. Haugbølle, and A. Nordlund, 2004. "Magnetic Field Generation in Collisionless Shocks: Pattern Growth and Transport". In: *The Astrophysical Journal* 608.1, p. L13. DOI: 10.1086/421262. URL: https://dx.doi.org/10.1086/421262.

Fried, B. D., 1959. "Mechanism for Instability of Transverse Plasma Waves". In: *The Physics of Fluids* 2.3, pp. 337–337. ISSN: 0031-9171. DOI: 10.1063/1.1705933. eprint: https://pubs.aip.org/aip/pfl/article-pdf/2/3/337/12401439/337_1_online.pdf. URL: https://doi.org/10.1063/1.1705933.

Gilljohann, M. F. *et al.*, 2019. "Direct Observation of Plasma Waves and Dynamics Induced by Laser-Accelerated Electron Beams". In: *Phys. Rev. X* 9 (1), p. 011046. DOI: 10.1103/PhysRevX.9.011046. URL: https://link.aps.org/doi/10.1103/PhysRevX.9.011046.

Gorn, A., M. Turner, E. Adli, and A. collaboration, 2020. "Proton beam defocusing in AWAKE: comparison of simulations and measurements". In: *Plasma Physics and Controlled Fusion* 62.12, p. 125023. DOI: 10.1088/1361-6587/abc298. URL: https://dx.doi.org/10.1088/1361-6587/abc298.

Graw, J. M., M. S. Weidl, and F. Jenko, 2022. "Mildly Relativistic Perpendicular Multiple-ion GRB Shocks". In: *The Astrophysical Journal* 940.2, p. 172. DOI: 10.3847/1538-4357/ac9bf1. URL: https://dx.doi.org/10.3847/1538-4357/ac9bf1.

Gschwendtner, E., M. Turner, *et al.*, 2019. "Proton-driven plasma wakefield acceleration in AWAKE". In: *Philosophical Transactions of the Royal Society A: Mathematical, Physical and Engineering Sciences* 377.2151, p. 20180418. DOI: 10.1098/rsta.2018.0418. eprint: https://royalsocietypublishing.org/doi/pdf/10.1098/rsta.2018.0418. URL: https://royalsocietypublishing.org/doi/abs/10.1098/rsta.2018.0418.

Gschwendtner, E., K. Lotov, *et al.*, 2022. "The AWAKE Run 2 Programme and Beyond". In: *Symmetry* 14.8. ISSN: 2073-8994. DOI: 10.3390/sym14081680. URL: https://www.mdpi.com/2073-8994/14/8/1680.

Hao, B., Z.-M. Sheng, and J. Zhang, 2008. "Kinetic theory on the current-filamentation instability in collisional plasmas". In: *Physics of Plasmas* 15.8, p. 082112. ISSN: 1070-664X. DOI: 10.1063/1.2969432. eprint: https://pubs.aip.org/aip/pop/article-pdf/doi/10.1063/1.2969432/15626437/082112_1_online.pdf. URL: https://doi.org/10.1063/1.2969432.

Heiles, C. and R. Crutcher, 2005. "Magnetic Fields in Diffuse HI and Molecular Clouds". In: *Cosmic Magnetic Fields*. Ed. by R. Wielebinski and R. Beck. Berlin, Heidelberg: Springer Berlin Heidelberg, pp. 137–182. ISBN: 978-3-540-31396-0. DOI: 10.1007/3540313966_7. URL: https://doi.org/10.1007/3540313966_7.

Iwamoto, M., T. Amano, M. Hoshino, *et al.*, 2019. "Precursor Wave Amplification by Ion–Electron Coupling through Wakefield in Relativistic Shocks". In: *The Astrophysical Journal Letters* 883.2, p. L35. DOI: 10.3847/2041-8213/ab4265. URL: https://dx.doi.org/10.3847/2041-8213/ab4265.

Iwamoto, M., T. Amano, Y. Matsumoto, S. Matsukiyo, and M. Hoshino, 2022. "Particle Acceleration by Pickup Process Upstream of Relativistic Shocks". In: *The Astrophysical Journal* 924.2, p. 108. DOI: 10.3847/1538-4357/ac38aa. URL: https://dx.doi.org/10.3847/1538-4357/ac38aa.

Jackson, J. D., 1999. "Radiation by Moving Charges". In: *Classical Electrodynamics*. 3rd ed. John Wiley & Sons, Ltd. Chap. 14, pp. 661–707. ISBN: 978-0-471-30932-1. URL: https://archive.org/details/john-david-jackson-classical-electrodynamics-wiley-1999/page/n3/mode/2up.

Jia, Q. *et al.*, 2013. "Effects of the background plasma temperature on the current filamentation instability". In: *Physics of Plasmas* 20.3, p. 032113. ISSN: 1070-664X. DOI: 10.1063/1.4796052. eprint: https://pubs.aip.org/aip/pop/article-pdf/doi/10.1063/1.4796052/14795548/032113_1_online.pdf. URL: https://doi.org/10.1063/1.4796052.

Jones, M. E., D. S. Lemons, and M. A. Mostrom, 1983. "Space-time evolution of the beam-plasma instability". In: *The Physics of Fluids* 26.10, pp. 2784–2786. ISSN: 0031-9171. DOI: 10.1063/1.864044. eprint: https://pubs.aip.org/aip/pfl/article-pdf/26/10/2784/12495716/2784_1_online.pdf. URL: https://doi.org/10.1063/1.864044.

Joshi, C., T. Tajima, J. M. Dawson, H. A. Baldis, and N. A. Ebrahim, 1981. "Forward Raman Instability and Electron Acceleration". In: *Phys. Rev. Lett.* 47 (18), pp. 1285–1288. DOI: 10.1103/PhysRevLett.47.1285. URL: https://link.aps.org/doi/10.1103/PhysRevLett.47.1285.

Katsouleas, T. C., S. Wilks, P. Chen, J. M. Dawson, and J. J. Su, 1987. "Beam Loading in Plasma Accelerators". In: *Part. Accel.* 22, pp. 81–99.

Keinigs, R. and M. E. Jones, 1987. "Two-dimensional dynamics of the plasma wakefield accelerator". In: *The Physics of Fluids* 30.1, pp. 252–263. ISSN: 0031-9171. DOI: 10.1063/1.866183. eprint: https://pubs.aip.org/aip/pfl/article-pdf/30/1/252/12365569/252_1_online.pdf. URL: https://doi.org/10.1063/1.866183.

Landau, L., 1946. "On the Vibrations of the Electronic Plasma". In: *J. Phys.* 10 (1), pp. 25–34.

Landau, L. and E. Lifshitz, 1959. *Statistical Physics*. Vol. 5. New York: Pergamon Press. URL: https://archive.org/details/ost-physics-landaulifshitz-statisticalphysics/page/n107/mode/2up.

Lawson, J., 1977. *The Physics of Charged-particle Beams*. International series of monographs on physics. Clarendon Press. ISBN: 9780198512783. URL: https://books.google.de/books?id=g9l8AAAAIAAJ.

Li, H.-L. *et al.*, 2022. "Simulation study of coupled two-stream and current filamentation instability excited by accelerator electron beams in plasmas". In: *Physics of Plasmas* 29.5, p. 052101. ISSN: 1070-664X. DOI: 10.1063/5.0086500. eprint: https://pubs.aip.org/aip/pop/article-pdf/doi/10.1063/5.0086500/16592211/052101_1_online.pdf. URL: https://doi.org/10.1063/5.0086500.

Lotov, K. V., 2013. "Excitation of two-dimensional plasma wakefields by trains of equidistant particle bunches". In: *Physics of Plasmas* 20.8, p. 083119. DOI: 10.1063/1.4819720. eprint: https://doi.org/10.1063/1.4819720. URL: https://doi.org/10.1063/1.4819720.

Lotov, K. V. and V. A. Minakov, 2020. "Proton beam self-modulation seeded by electron bunch in plasma with density ramp". In: *Plasma Physics and Controlled Fusion* 62.11, p. 115025. DOI: 10.1088/1361-6587/abba42. URL: https://dx.doi.org/10.1088/1361-6587/abba42.

Medvedev, M. V. and A. Loeb, 1999. "Generation of Magnetic Fields in the Relativistic Shock of Gamma-Ray Burst Sources". In: *The Astrophysical Journal* 526.2, p. 697. DOI: 10.1086/308038. URL: https://dx.doi.org/10.1086/308038.

Michno, M. J. and R. Schlickeiser, 2010. "ON THE MAGNETIZATION OF COSMIC OUTFLOWS: PLASMA MODES AND INSTABILITIES OF UNMAGNETIZED PLASMA BEAMS". In: *The Astrophysical Journal* 714.1, p. 868. DOI: 10.1088/0004-637X/714/1/868. URL: https://dx.doi.org/10.1088/0004-637X/714/1/868.

Minakov, V. A. and K. V. Lotov, 2024. "Transformer ratio growth due to ion motion in plasma wakefield accelerators". In: *Physics of Plasmas* 31.3, p. 034503. ISSN: 1070-664X.

DOI: 10.1063/5.0197176. eprint: https://pubs.aip.org/aip/pop/article-pdf/doi/10.1063/5.0197176/19840220/034503_1_5.0197176.pdf. URL: https://doi.org/10.1063/5.0197176.

Morales Guzman, P. I. *et al.* (AWAKE Collaboration), 2021. "Simulation and experimental study of proton bunch self-modulation in plasma with linear density gradients". In: *Phys. Rev. Accel. Beams* 24 (10), p. 101301. DOI: 10.1103/PhysRevAccelBeams.24.101301. URL: https://link.aps.org/doi/10.1103/PhysRevAccelBeams.24.101301.

Moreira, M., P. Muggli, and J. Vieira, 2023. "Mitigation of the Onset of Hosing in the Linear Regime through Plasma Frequency Detuning". In: *Phys. Rev. Lett.* 130 (11), p. 115001. DOI: 10.1103/PhysRevLett.130.115001. URL: https://link.aps.org/doi/10.1103/PhysRevLett.130.115001.

Muggli, P., 2020. *Beam-Driven Systems, Plasma Wakefield Acceleration.* DOI: 10.48550/ARXIV.2007.05226. URL: https://arxiv.org/abs/2007.05226.

Muggli, P., S. F. Martins, N. Shukla, J. Vieira, and L. O. Silva, 2013. *Interaction of Ultra Relativistic e- e+ Fireball Beam with Plasma.* DOI: 10.48550/ARXIV.1306.4380. URL: https://arxiv.org/abs/1306.4380.

Nechaeva, T. *et al.* (AWAKE Collaboration), 2024. "Hosing of a Long Relativistic Particle Bunch in Plasma". In: *Phys. Rev. Lett.* 132 (7), p. 075001. DOI: 10.1103/PhysRevLett.132.075001. URL: https://link.aps.org/doi/10.1103/PhysRevLett.132.075001.

Oughstun, K. E., 2009. "Asymptotic Methods of Analysis using Advanced Saddle Point Techniques". In: *Electromagnetic and Optical Pulse Propagation.* 1st ed. Springer New York, NY. Chap. 10, pp. 98–103. DOI: 10.1007/978-1-4419-0149-1.

Pathak, V. B., T. Grismayer, A. Stockem, R. A. Fonseca, and L. O. Silva, 2015. "Spatial-temporal evolution of the current filamentation instability". In: *New Journal of Physics* 17.4, p. 043049. DOI: 10.1088/1367-2630/17/4/043049. URL: https://dx.doi.org/10.1088/1367-2630/17/4/043049.

Perna, R., D. Lazzati, and B. Giacomazzo, 2016. "SHORT GAMMA-RAY BURSTS FROM THE MERGER OF TWO BLACK HOLES". In: *The Astrophysical Journal Letters* 821.1, p. L18. DOI: 10.3847/2041-8205/821/1/L18. URL: https://dx.doi.org/10.3847/2041-8205/821/1/L18.

Peterson, J. R., S. Glenzer, and F. Fiuza, 2021. "Magnetic Field Amplification by a Nonlinear Electron Streaming Instability". In: *Phys. Rev. Lett.* 126 (21), p. 215101. DOI: 10.1103/PhysRevLett.126.215101. URL: https://link.aps.org/doi/10.1103/PhysRevLett.126.215101.

Planck Collaboration, 2014. "Planck 2013 results. XVI. Cosmological parameters". In: *A&A* 571, A16. DOI: 10.1051/0004-6361/201321591. URL: https://doi.org/10.1051/0004-6361/201321591.

Pukhov, A., 1999. "Three-dimensional electromagnetic relativistic particle-in-cell code VLPL (Virtual Laser Plasma Lab)". In: *Journal of Plasma Physics* 61.3, pp. 425–433. DOI: 10.1017/S0022377899007515.

Pukhov, A., 2015. *Particle-in-Cell Codes for plasma-based particle acceleration.* arXiv: 1510.01071 [physics.plasm-ph].

Pukhov, A. *et al.*, 2011. "Phase Velocity and Particle Injection in a Self-Modulated Proton-Driven Plasma Wakefield Accelerator". In: *Phys. Rev. Lett.* 107 (14), p. 145003. DOI: 10.1103/PhysRevLett.107.145003. URL: https://link.aps.org/doi/10.1103/PhysRevLett.107.145003.

Reiser, M., 2008. "Linear Beam Optics with Space Charge: Sections 4.1 - 4.4". In: *Theory and Design of Charged Particle Beams.* John Wiley & Sons, Ltd. Chap. 4, pp. 163–232.

ISBN: 9783527622047. DOI: https://doi.org/10.1002/9783527622047.ch4a. eprint: https://onlinelibrary.wiley.com/doi/pdf/10.1002/9783527622047.ch4a. URL: https://onlinelibrary.wiley.com/doi/abs/10.1002/9783527622047.ch4a.

Rieger, K., A. Caldwell, O. Reimann, and P. Muggli, 2017. "GHz modulation detection using a streak camera: Suitability of streak cameras in the AWAKE experiment". In: *Review of Scientific Instruments* 88.2, p. 025110. ISSN: 0034-6748. DOI: 10.1063/1.4975380. eprint: https://pubs.aip.org/aip/rsi/article-pdf/doi/10.1063/1.4975380/13576608/025110_1_online.pdf. URL: https://doi.org/10.1063/1.4975380.

Rosenzweig, J. B. *et al.*, 1988. "Experimental Observation of Plasma Wake-Field Acceleration". In: *Phys. Rev. Lett.* 61 (1), pp. 98–101. DOI: 10.1103/PhysRevLett.61.98. URL: https://link.aps.org/doi/10.1103/PhysRevLett.61.98.

Rosmino, C., 2022. *LHC neu gestartet: Mit 13,6 Tera-Elektronenvolt auf der Jagd nach dem unendlich Kleinen*. Accessed: 2024-09-16. URL: https://de.euronews.com/2022/07/06/lhc-neu-gestartet-mit-136-tera-elektronenvolt-auf-der-jagd-nach-dem-unendlich-kleinen.

Ruyer, C., L. Gremillet, A. Debayle, and G. Bonnaud, 2015. "Nonlinear dynamics of the ion Weibel-filamentation instability: An analytical model for the evolution of the plasma and spectral properties". In: *Physics of Plasmas* 22.3, p. 032102. ISSN: 1070-664X. DOI: 10.1063/1.4913651. eprint: https://pubs.aip.org/aip/pop/article-pdf/doi/10.1063/1.4913651/15898337/032102_1_online.pdf. URL: https://doi.org/10.1063/1.4913651.

San Miguel Claveria, P. *et al.*, 2022. "Spatiotemporal dynamics of ultrarelativistic beam-plasma instabilities". In: *Phys. Rev. Res.* 4 (2), p. 023085. DOI: 10.1103/PhysRevResearch.4.023085. URL: https://link.aps.org/doi/10.1103/PhysRevResearch.4.023085.

Schroeder, C. B., C. Benedetti, E. Esarey, F. J. Grüner, and W. P. Leemans, 2011. "Growth and Phase Velocity of Self-Modulated Beam-Driven Plasma Waves". In: *Phys. Rev. Lett.* 107 (14), p. 145002. DOI: 10.1103/PhysRevLett.107.145002. URL: https://link.aps.org/doi/10.1103/PhysRevLett.107.145002.

Shukla, N., S. F. Martins, P. Muggli, J. Vieira, and L. O. Silva, 2020. "Interaction of ultra relativistic fireball beam with plasma". In: *New Journal of Physics* 22.1, p. 013030. DOI: 10.1088/1367-2630/ab60f0. URL: https://dx.doi.org/10.1088/1367-2630/ab60f0.

Shukla, N., J. Vieira, *et al.*, 2018. "Conditions for the onset of the current filamentation instability in the laboratory". In: *Journal of Plasma Physics* 84.3, p. 905840302. DOI: 10.1017/S0022377818000314.

Siambis, J. G., 1987. "Relativistic fluid equations for intense electron beams". In: *The Physics of Fluids* 30.3, pp. 896–903. ISSN: 0031-9171. DOI: 10.1063/1.866343. eprint: https://pubs.aip.org/aip/pfl/article-pdf/30/3/896/12611274/896_1_online.pdf. URL: https://doi.org/10.1063/1.866343.

Silva, L. O., R. A. Fonseca, J. W. Tonge, J. M. Dawson, *et al.*, 2003. "Interpenetrating Plasma Shells: Near-Equipartition Magnetic Field Generation and Nonthermal Particle Acceleration". In: *The Astrophysical Journal* 596.1, p. L121. DOI: 10.1086/379156. URL: https://dx.doi.org/10.1086/379156.

Silva, L. O., R. A. Fonseca, J. W. Tonge, W. B. Mori, and J. M. Dawson, 2002. "On the role of the purely transverse Weibel instability in fast ignitor scenarios". In: *Physics of Plasmas* 9.6, pp. 2458–2461. ISSN: 1070-664X. DOI: 10.1063/1.1476004. eprint: https://pubs.aip.org/aip/pop/article-pdf/9/6/2458/19097722/2458_1_online.pdf. URL: https://doi.org/10.1063/1.1476004.

Sosedkin, A. and K. Lotov, 2016. "LCODE: A parallel quasistatic code for computationally heavy problems of plasma wakefield acceleration". In: *Nuclear Instruments and Meth-*

ods in Physics Research Section A: Accelerators, Spectrometers, Detectors and Associated Equipment 829. 2nd European Advanced Accelerator Concepts Workshop - EAAC 2015, pp. 350–352. ISSN: 0168-9002. DOI: https://doi.org/10.1016/j.nima.2015.12.032. URL: https://www.sciencedirect.com/science/article/pii/S0168900215016034.

Spitkovsky, A., 2008. "Particle Acceleration in Relativistic Collisionless Shocks: Fermi Process at Last?" In: *The Astrophysical Journal* 682.1, p. L5. DOI: 10.1086/590248. URL: https://dx.doi.org/10.1086/590248.

Spitsyn, R. I., I. V. Timofeev, A. P. Sosedkin, and K. V. Lotov, 2018. "Characterization of wavebreaking time and dissipation of weakly nonlinear wakefields due to ion motion". In: *Physics of Plasmas* 25.10, p. 103103. ISSN: 1070-664X. DOI: 10.1063/1.5048549. eprint: https://pubs.aip.org/aip/pop/article-pdf/doi/10.1063/1.5048549/15624540/103103_1_online.pdf. URL: https://doi.org/10.1063/1.5048549.

Tajima, T. and J. M. Dawson, 1979. "Laser Electron Accelerator". In: *Phys. Rev. Lett.* 43 (4), pp. 267–270. DOI: 10.1103/PhysRevLett.43.267. URL: https://link.aps.org/doi/10.1103/PhysRevLett.43.267.

Tajima, T., X. Q. Yan, and T. Ebisuzaki, 2020. "Wakefield acceleration". In: *Reviews of Modern Plasma Physics* 4 (1). DOI: 10.1007/s41614-020-0043-z. URL: https://doi.org/10.1007/s41614-020-0043-z.

Takamoto, M., Y. Matsumoto, and T. N. Kato, 2018. "Magnetic Field Saturation of the Ion Weibel Instability in Interpenetrating Relativistic Plasmas". In: *The Astrophysical Journal Letters* 860.1, p. L1. DOI: 10.3847/2041-8213/aac6d6. URL: https://dx.doi.org/10.3847/2041-8213/aac6d6.

The CEPC Project (2013). Accessed: 2024-09-16. Institute of High Energy Physics, Chinese Academy of Sciences. URL: http://cepc.ihep.ac.cn/intro.html.

The Compact Linear Collider (2024). Accessed: 2024-09-16. CERN. URL: https://home.cern/science/accelerators/compact-linear-collider.

Thode, L. E., 1976. "Energy lost by a relativistic electron beam due to two-stream instability". In: *The Physics of Fluids* 19.2, pp. 305–315. ISSN: 0031-9171. DOI: 10.1063/1.861441. eprint: https://pubs.aip.org/aip/pfl/article-pdf/19/2/305/12638730/305_1_online.pdf. URL: https://doi.org/10.1063/1.861441.

Tigner, M., 2001. "Does Accelerator-Based Particle Physics Have a Future?" In: *Physics Today* 54.1, pp. 36–40. ISSN: 0031-9228. DOI: 10.1063/1.1349610. eprint: https://pubs.aip.org/physicstoday/article-pdf/54/1/36/11109441/36_1_online.pdf. URL: https://doi.org/10.1063/1.1349610.

Tonks, L. and I. Langmuir, 1929. "Oscillations in Ionized Gases". In: *Phys. Rev.* 33 (2), pp. 195–210. DOI: 10.1103/PhysRev.33.195. URL: https://link.aps.org/doi/10.1103/PhysRev.33.195.

Torrado, N. E., N. C. Lopes, J. F. A. Silva, C. Amoedo, and A. Sublet, 2023. "Double Pulse Generator for Unipolar Discharges in Long Plasma Tubes for the AWAKE Experiment". In: *IEEE Trans. Plasma Sci.* 51.12, pp. 3619–3627. DOI: 10.1109/TPS.2023.3337314.

Tuev, P. V., R. I. Spitsyn, and K. V. Lotov, 2023. "Advanced Quasistatic Approximation". In: *Plasma Physics Reports* 49.2, pp. 229–238. ISSN: 1562-6938. DOI: 10.1134/s1063780x22601249. URL: http://dx.doi.org/10.1134/S1063780X22601249.

Turc, L. *et al.*, 2023. "Transmission of foreshock waves through Earth's bow shock". In: *Nature Physics* 19.1, pp. 78–86. ISSN: 1745-2481. DOI: 10.1038/s41567-022-01837-z. URL: https://doi.org/10.1038/s41567-022-01837-z.

Turner, M. *et al.* (AWAKE Collaboration), 2024. *Experimental Observation of Motion of Ions in a Resonantly Driven Plasma Wakefield Accelerator*. arXiv: 2406.16361. URL: https://arxiv.org/abs/2406.16361.

Tzoufras, M. *et al.*, 2006. "Space-Charge Effects in the Current-Filamentation or Weibel Instability". In: *Phys. Rev. Lett.* 96 (10), p. 105002. DOI: 10.1103/PhysRevLett.96.105002. URL: https://link.aps.org/doi/10.1103/PhysRevLett.96.105002.

Vay, J.-L., 2008. "Simulation of beams or plasmas crossing at relativistic velocitya)". In: *Physics of Plasmas* 15.5, p. 056701. ISSN: 1070-664X. DOI: 10.1063/1.2837054. eprint: https://pubs.aip.org/aip/pop/article-pdf/doi/10.1063/1.2837054/14087346/056701_1_online.pdf. URL: https://doi.org/10.1063/1.2837054.

Veksler, V. I., 1956. "Coherent principle of acceleration of charged particles". In: DOI: 10.5170/CERN-1956-025.80. URL: https://cds.cern.ch/record/1241563.

Verra, L., C. Amoedo, *et al.* (AWAKE Collaboration), 2024. "Filamentation of a relativistic proton bunch in plasma". In: *Phys. Rev. E* 109 (5), p. 055203. DOI: 10.1103/PhysRevE.109.055203. URL: https://link.aps.org/doi/10.1103/PhysRevE.109.055203.

Verra, L., G. Zevi Della Porta, *et al.* (AWAKE Collaboration), 2022. "Controlled Growth of the Self-Modulation of a Relativistic Proton Bunch in Plasma". In: *Phys. Rev. Lett.* 129 (2), p. 024802. DOI: 10.1103/PhysRevLett.129.024802. URL: https://link.aps.org/doi/10.1103/PhysRevLett.129.024802.

Vieira, J., R. A. Fonseca, W. B. Mori, and L. O. Silva, 2012. "Ion Motion in Self-Modulated Plasma Wakefield Accelerators". In: *Phys. Rev. Lett.* 109 (14), p. 145005. DOI: 10.1103/PhysRevLett.109.145005. URL: https://link.aps.org/doi/10.1103/PhysRevLett.109.145005.

Vieira, J., R. A. Fonseca, W. B. Mori, and L. O. Silva, 2014. "Ion motion in the wake driven by long particle bunches in plasmasa)". In: *Physics of Plasmas* 21.5, p. 056705. ISSN: 1070-664X. DOI: 10.1063/1.4876620. eprint: https://pubs.aip.org/aip/pop/article-pdf/doi/10.1063/1.4876620/15924094/056705_1_online.pdf. URL: https://doi.org/10.1063/1.4876620.

Walter, E., J. P. Farmer, M. S. Weidl, A. Pukhov, and F. Jenko, 2024. *Wakefield-driven filamentation of warm beams in plasma*. arXiv: 2406.07977. URL: https://arxiv.org/abs/2406.07977.

Watson, K. M., S. A. Bludman, and M. N. Rosenbluth, 1960. "Statistical Mechanics of Relativistic Streams. I". In: *The Physics of Fluids* 3.5, pp. 741–747. ISSN: 0031-9171. DOI: 10.1063/1.1706120. eprint: https://pubs.aip.org/aip/pfl/article-pdf/3/5/741/12499098/741_1_online.pdf. URL: https://doi.org/10.1063/1.1706120.

Weibel, E., 1959. "Spontaneously Growing Transverse Waves in a Plasma Due to an Anisotropic Velocity Distribution". In: *Phys. Rev. Lett.* 2 (3), pp. 83–84. DOI: 10.1103/PhysRevLett.2.83. URL: https://link.aps.org/doi/10.1103/PhysRevLett.2.83.

Xu, X. *et al.*, 2020. "On numerical errors to the fields surrounding a relativistically moving particle in PIC codes". In: *Journal of Computational Physics* 413, p. 109451. ISSN: 0021-9991. DOI: https://doi.org/10.1016/j.jcp.2020.109451. URL: https://www.sciencedirect.com/science/article/pii/S0021999120302254.

Yee, K., 1966. "Numerical solution of initial boundary value problems involving maxwell's equations in isotropic media". In: *IEEE Transactions on Antennas and Propagation* 14.3, pp. 302–307. DOI: 10.1109/TAP.1966.1138693.

Zhang, C. *et al.*, 2022. "Mapping the self-generated magnetic fields due to thermal Weibel instability". In: *Proceedings of the National Academy of Sciences* 119.50, e2211713119.

DOI: 10.1073/pnas.2211713119. eprint: https://www.pnas.org/doi/pdf/10.1073/pnas.2211713119. URL: https://www.pnas.org/doi/abs/10.1073/pnas.2211713119.

Zimmermann, F., M. Benedikt, and A.-S. Müller, 2020. "The Future Circular Collider Study". In: *Proc. IPAC'20* (Caen, France). International Particle Accelerator Conference 11. JACoW Publishing, Geneva, Switzerland, MOVIR01, pp. 6–10. ISBN: 978-3-95450-213-4. DOI: 10.18429/JACoW-IPAC2020-MOVIR01. URL: https://jacow.org/ipac2020/papers/movir01.pdf.

Acknowledgments

Awake, but at what cost? - Towards the end of the most interesting, although intense time of my life so far, I look back and wonder how so many students complete a PhD. The answer is as simple as it can get: It most importantly requires a community consisting of strongly supportive colleagues, family and friends. The lines often blur between the roles.

First and foremost, my deepest gratitude goes to John 'PIC' Farmer, the person who challenged me the most and guided me through the second half of my PhD. His humor and insight kept me grounded, and without him, this thesis simply would not exist. I owe particular thanks for his mentorship during my first manuscript, which was a defining moment in my academic journey. His vast knowledge in numeric and analytic methods wasn't given freely but earned through light-hearted teasing. Ironically, while he is the colleague I worked most closely with, I know the least about his personal life—his wife's name remains a mystery. What could have been a daunting experience, switching supervisors midway through my PhD worked out well. Another huge thanks goes to my first supervisor Martin Weidl, who gave me a smooth and interesting transition into plasma research and has become a good friend. A great thanks also belongs to Marlene Turner, who has been a strong collaborator and initiated the fruitful studies on ion motion.

I would like to extend my sincere thanks to my formal supervisors, Prof. Frank Jenko at IPP and Edda Gschwendtner at CERN. Despite their demanding roles leading large teams, they always found time to offer guidance and support. Most significantly, they provided me with the extraordinary opportunity to spend a year at CERN, a dream realized from my school yearbook's prediction of where I'd be in five years. Working as a physicist at CERN, especially with the AWAKE Collaboration, gave me countless unforgettable experiences.

Then there are these colleagues and friends, which give the greatest support, although not necessarily on a professional basis. The emotional support I have received from so many persons were the key to keep on going during the most difficult times. The cake-offs, initiated by Rohan's disbelief I could bake, started small and ended with half of the IPP students joining them. Many thanks also go to Jonas, Pablo and Nils who I spent many coffees and necessary distracting conversations with. In the final stretch of my PhD, I am grateful for the coffee breaks spent with Artem, Daniel, Camille, Nathan, Christian, Frank and Valentine from the plasma astrophysics group.

On the CERN side, I must give a special shout-out to Fern for her unwavering German accent, Jan for joining me on via ferratas and Arthur for being Arthur. To my office mate Livio, thank you for tolerating my frequent prayers to the PhD gods for the strength to finish this thesis. Yet, I cannot express enough gratitude to Mrs. van Gils, an entity who speaks more than eight languages and became my closest friend showing me around Switzerland. One day, we will make that long-promised horseback ride across the Andes.

Outside of the work environment, I am greatly thankful for my flat mates and volleyball team members including Ivan, Jean Baptiste and Giulia, as well as my military-style climbing

group including Frolain and Mirka. Another warm gratitude goes to my Swedish-speaking Finns Carolina, who once taught me in the heart of the Bolivian Amazon filled with poisonous spiders and alligators: 'Det finns ingen orsak att gråta över spilld mjölk.'

Das allerwichtigste kommt zum Schluss: Der tiefste Dank geht an meine liebste Familie, ohne welche ich es niemals geschafft hätte. Mama, Papa und Schwesterherz, ihr wart immer für mich da, habt mich durch all die diversen Phases von Glück zu Trauer begleitet und immer an mich geglaubt. Ihr seid für so viel mehr dagestanden, wie ich mir jemals wünschen könnte. Ihr werdet immer die wichtigsten Plätze in meinem Herzen haben.

This work was funded by the Deutsche Forschungsgemeinschaft (DFG, German Research Foundation) under Germany´s Excellence Strategy – EXC 2094 – 390783311. The simulations were conducted on the Cobra and Raven HPC system of the Max Planck Computing and Data Facility (MPCDF).